NASA SP-219

CASE FILE
COPY

STATUS OF PASSIVE INFLATABLE FALLING-SPHERE TECHNOLOGY FOR ATMOSPHERIC SENSING TO 100 km

A symposium held at
LANGLEY RESEARCH CENTER
Hampton, Virginia
September 23–24, 1969

FEB 1970
RECEIVED
NASA STI FACILITY
INPUT BRANCH

NATIONAL AERONAUTICS AND SPACE ADMINISTRATION

NASA SP–219

STATUS OF PASSIVE INFLATABLE FALLING-SPHERE TECHNOLOGY FOR ATMOSPHERIC SENSING TO 100 km

A symposium held at
Langley Research Center
Hampton, Virginia
September 23-24, 1969

Scientific and Technical Information Division
OFFICE OF TECHNOLOGY UTILIZATION 1969
NATIONAL AERONAUTICS AND SPACE ADMINISTRATION
Washington, D.C.

For sale by the Clearinghouse for Federal Scientific and Technical Information
Springfield, Virginia 22151 – Price $3.00

PREFACE

The number of meteorological rocket soundings to altitudes between 30 and 100 km has now passed the 10,000 mark. One of the key elements in the success of these soundings is the sensor, or the means of obtaining useful measurements of the temperatures, densities or pressures, and winds for studies of the structure and behavior of the upper atmosphere. The types of sensors used in these soundings have varied, reflecting the ingenuity of the experimenters in devising a means for deriving data on the upper atmosphere. A rough count indicates that 800 or more of the soundings made in the past ten years have involved falling-sphere experiments. The use of a falling sphere as the primary sensor has appealed to many experimenters because of the seeming simplicity of the concept – that is, the fall rate of a sphere of given size and weight and at a given altitude is a function of the density of the atmosphere at that altitude and the drag coefficient of the sphere for the conditions at hand. Despite this apparent simplicity, perhaps no method of sounding the upper atmosphere has required so much study for interpreting the data as the falling-sphere technique.

In order to examine the meteorological sounding rocket problem in some detail and to guide further research and development activity, a study was recently undertaken by the NASA Langley Research Center to define the most feasible system for sounding the upper atmosphere from 30 km to about 100 km. The recommended system included a passive falling sphere as a payload, on the basis of its simplicity, reliability, and cost effectiveness for use in network types of operations. This recommendation has been received with skepticism by some who question whether a falling sphere and the required precise ground tracking equipment really constitute the most effective atmospheric sounding system.

As a follow-up to the feasibility study, a symposium was held to bring together the various groups who are concerned with the use of falling spheres for obtaining high-altitude meteorological measurements. The purpose of the meeting was to provide a forum for direct exchange of information and ideas between Government, industry, and university personnel who are actively engaged in falling-sphere experiments, and to form a basis for evaluating the current state of the art of falling-sphere technology, pinpointing the critical areas requiring further research and development effort, and coordinating such effort among the user agencies. The size of the meeting was kept small to encourage informal discussions among the attendees.

The symposium was framed around a number of invited papers on the topics of experience with falling-sphere systems, the aerodynamics of falling spheres, the techniques which have been developed for reducing sphere tracking data, and the characteristics of the atmospheric data derived from falling-sphere experiments. The papers are presented in this document.

CONTENTS

General Chairman: H. B. TOLEFSON

SESSION I – EXPERIENCE

Chairman: HAROLD N. MURROW, NASA Langley Research Center

1. A Summary of AFCRL Passive-Sphere Development Efforts and Experience 1
JOHN B. WRIGHT, Air Force Cambridge Research Laboratories

2. The Importance of Environmental Testing Including Experience With the Arcas-Robin System 39
SAMMIE D. JOPLIN, NASA Langley Research Center

3. Recent Passive Density Sensor Effort at the Naval Ordnance Laboratory 55
GEORGE J. SLOAN, U.S. Naval Ordnance Laboratory

4. Operational Experience With Passive Falling Spheres on the AFETR 65
O. H. DANIEL, Pan American World Airways, Inc.

5. Capability of NOL Ballistics Ranges for Obtaining Sphere Drag Coefficient Data 69
W. CARSON LYONS, Jr., U.S. Naval Ordnance Laboratory

SESSION II – TECHNIQUES

Chairman: JOHN B. WRIGHT, Air Force Cambridge Research Laboratories

6. An Assessment of Sphere Drag Coefficient Data 93
HELMUT G. HEINRICH and ROBERT A. NOREEN, University of Minnesota

7. High-Altitude Robin Data-Reduction Program 111
JAMES LUERS and NICHOLAS A. ENGLER, University of Dayton

8. Adequacy of the Passive Inflated Falling Sphere Technique 145
K. D. McWATTERS and J. W. PETERSON, University of Michigan

9. A Capability Model for Passive Spheres at High Altitudes 165
FORREST L. STAFFANSON and R. GARY PHIBBS, University of Utah

10. Requirements for Tracking Radar for Falling Spheres 175
JOHN L. HAIN and WILLIAM E. BROCKMAN,
Booz, Allen Applied Research, Inc.

11. The Tone Range/Telemetry Interferometer Tracking System for Support of Sounding Rocket Payloads 187
JOHN I. HUDGINS and JAMES R. LEASE,
NASA Goddard Space Flight Center

SESSION III – DATA

Chairman: FORREST L. STAFFANSON, University of Utah

12. Some Properties of Data From Falling Sphere Soundings 227
R. S. QUIROZ, Weather Bureau, ESSA

13. Data From Falling Sphere Experiments Including Comparison Tests Between Different Systems 257
LAWRENCE B. SMITH, Sandia Laboratories

14. Results From Several Experiments at White Sands Missile Range Aimed at Assessment of Falling-Sphere Density Data 271
ROBERT OLSEN, White Sands Missile Range

15. Meteorological Data From Falling Sphere Technique Compared With Data From Other Sounding Methods 293
WENDELL S. SMITH, NASA Goddard Space Flight Center

List of Attendees 301

A SUMMARY OF AFCRL PASSIVE-SPHERE DEVELOPMENT EFFORTS AND EXPERIENCE

By John B. Wright

Air Force Cambridge Research Laboratories

SUMMARY

A passive falling sphere, ROBIN, has been developed by the Air Force for atmospheric soundings between 100 and 30 km. The rocket vehicles and simple sphere have been developed to permit a relatively low cost per sounding. The radar space - time data are reduced to meteorological parameters in a digital computer thereby providing nearly real time information.

The sphere is a superpressure balloon fabricated from thin plastic (Mylar) and inflated by vaporization of isopentane. Certain problems in sphere hardware reliability have been solved while others remain. Collapse of the spherical balloon 5 - 15 km above the design altitude of 30 km persists. In order to calculate atmospheric density (temperature and pressure), a precise knowledge of the drag coefficient of a sphere over a wide range of flow conditions is required. The wind tunnel measurements currently being used with this system have areas that produce atmospheric data that either do not compare well with other sensors or have peculiar excursions.

With further attention to these problem areas, the ROBIN has the capability of providing the most economical synoptic soundings of all candidate systems except perhaps indirect sensing techniques which are in their infancy.

INTRODUCTION

Early concepts on the use of a rocket-launched, ground-tracked, passive falling sphere (refs. 1, 2, and 3) led to an active development program by the Air Force Cambridge Research Laboratories starting in the late 1950's. The Vertical Sounding Techniques Branch of the Aerospace Instrumentation Laboratory has the responsibility of developing systems to be used for routine synoptic measurements of atmospheric parameters above-ground levels by the meteorological services of the Air Force. In addition to the usual requirements of any measuring

system, the concept of operational use adds the additional requirements of ease in field operations and data reduction as well as minimized cost and production adaptability. The small inflatable spherical balloon is in itself a low-cost item and because of its light weight and collapsibility can be carried aloft in a minimum cost and easily launched vehicle. Balanced against the low expendable costs is the need for a high precision radar and a sizeable digital computer such as the 7090.

For simplicity, the AFCRL passive falling-sphere system (fig. 1) has been given the name of ROBIN, denoting ROcket Balloon INstrument. This report is intended to present a broad picture of the history of ROBIN, describe the various vehicle systems, indicate problem areas, and provide references for further study. It would be impossible to present in a single report all of the detailed efforts, but other papers to be presented at this symposium by several of the Air Force ROBIN associates and contractors will cover, in more depth, various aspects of the total system.

SYMBOLS

D	drag force, newtons
m	mass, kilograms
a	acceleration, meters/second^2
ρ	atmospheric density, kilograms/meters^3
V	velocity, meters/second
C_D	drag coefficient, $D/.5\ \rho\ V^2A$
A	cross-sectional area, meters^2
M	Mach Number
R	Reynolds Number
h	altitude, kilometers
V_B	volume of ROBIN balloon, meters^3
d	diameter of ROBIN balloon, meters

X, Y, Z	rectangular Cartesian coordinates, meters
Z_o	release altitude
$\dot{X}, \dot{Y}, \dot{Z}$	velocities, relative to origin of these coordinates meters/second
$\ddot{X}, \ddot{Y}, \ddot{Z}$	accelerations, relative to origin of these coordinates, meters/second^2
W_X, W_Y	wind components, meters/second
W_Z	component of local horizontal wind along the Z axis, meters/second
W_{EW}, W_{NS}	local horizontal wind components, meters/second
W	total wind, meters/second (converted to knots in computer output)
Φ	wind azimuth, degrees
g_s	gravity acceleration at earth surface, meters/second^2
r	local radius of earth, kilometers
P	atmospheric pressure, newtons/meter^2 (converted to millibars in computer output)
T	atmospheric temperature, degrees Kelvin
R^*	universal gas constant, 8.31432×10^3 Joules $(°K)^{-1}$ $(\text{kilogram - mol})^{-1}$
M_o	molecular weight of air, kilograms $(\text{kilogram - mol})^{-1}$

CONCEPTS

A falling body may be utilized for atmospheric density measurements provided there is full knowledge of its aerodynamic characteristics. A spherical shape has an advantage in that its principal aerodynamic force is drag (if no rotation occurs) and that it presents an equal area in all directions. A very simplified equation for a falling body is:

$$D = ma = 1/2 \ \rho V^2 C_D A \tag{1}$$

In order to obtain the atmospheric density, all other terms must be known or measured. The acceleration may be obtained directly by means of a

builtin accelerometer and the velocity integrated as is done with several systems to be described in other papers. In addition to its high instrument cost such a system is inherently heavy and therefore has a fast fall rate.

Another technique is to measure space - time positions of the falling sphere by means of a precision ground - based radar, differentiate this space history to obtain velocities, and then differentiate the velocity history to obtain accelerations. The ROBIN utilizes this technique. Because of its light weight - area ratio, it is also sensitive to the force created by the horizontal wind.

APPROACH

The program of developing an operational ROBIN was begun in 1958. Major areas in the effort that were broken out were the vehicle, the ROBIN sphere and its hardware, the drag coefficient and other aerodynamic considerations, and the data reduction technique.

Various contractors were utilized in these major areas of efforts as shown in Table 1. In the course of time different vehicles were utilized and certain problems appeared requiring continuing contractual efforts during the 1960's.

ELEMENTS OF THE ROBIN SYSTEM

Vehicles

When the ROBIN effort began, the ARCAS meteorological rocket development phase was just underway and appeared to be the logical vehicle for the falling sphere as an operational sounding system. Rocketsondes were being developed for the ARCAS but at that time the completion of a fully acceptable system had not occurred. Thus, the ROBIN was a parallel and alternate payload development for the ARCAS rocket.

The ARCAS (fig. 2) is an 11.5-cm-diameter end-burning solid-propellant rocket motor capable of attaining an altitude of 70 km. With the ROBIN payload, it has been standardized as Probe, Meteorological PWN-7A and can be procured through Ogden Air Materiel Area at Hill Air Force Base, Utah. The description of this system is given under the ROBIN section.

In 1962, an even older small rocket system, the LOKI - Dart (fig. 2) was being upgraded in performance and reliability by use of the JUDI motor. In a limited type of effort, experiments were made to incorporate the ROBIN in this flight vehicle (ref. 4). After determining the level of the temperature within the dart, which drag separates from the motor at a low altitude (1 km) and a high Mach Number (3 - 4), successful flights were performed in 1964. At that time the LOKI - Dart was not being developed fully as a rocketsonde system, so further work using this vehicle was dropped in the interest of economy obtained in a one - vehicle approach. Recent standardization of the LOKI - Dart (PWN-8B) rocketsonde system and its substitution for the ARCAS, however, would make this a more economical system at a savings of at least 50%. Both of the above systems attain an altitude of approximately 65 km when fired from sea level.

In the mid - 1960's, requirements for density and winds to 100 km and the standard use and acceptance of rocketsonde winds and temperature (density) data to 65 km dictated the obvious effort to develop a method to sound the atmosphere between 65 and 100 km. A Navy - Air Force in - house effort brought together the two - stage SIDEWINDER - ARCAS - ROBIN system which flew reasonably well after some shop modifications including the drilling of extra bolt holes in the fins of some live ARCAS motors. Two drawbacks of this system, inability to meet National Range Safety igniter requirements and too low an altitude (115 km) for ROBIN density measurements to begin at 100 km, caused a change over to the SPARROW - HV ARCAS. The Navy, at the Pacific Missile Range, had developed the system for their various payloads to attain altitudes of 170 km. The system was acceptable from a safety standpoint, and the HV ARCAS was sufficiently strengthened to be compatible with the higher loads imposed as a second stage. Thus, as indicated in figure 2 much of the ROBIN effort was keyed to the ARCAS or boosted ARCAS vehicles.

Knowing the advantages (low cost, less wind sensitivity, and less dispersion) of the LOKI - Dart over the ARCAS in the 65 km regime, in late 1967 the Air Force proceeded to fund the development of a 140 km dart vehicle (ref. 5). The VIPER - Dart - ROBIN (figs. 2 and 3) system evolved over the past two years and appears to be a most attractive vehicle. The projected production cost of $2500 (plus radar tracking aid if desired) is approximately 50% of the cost of a SPARROW - HV ARCAS system. Less dispersion of the dart occurs and less horizontal range is required because of the short burn time (3 seconds) and resulting high velocity at low altitudes preventing as much gravity turning as experienced by slow burning systems.

While the dart part of the system has these favorable ballistic characteristics, the booster (LOKI or VIPER) tends to "float" in an unstable

manner immediately after burnout and dart separation. Thus, it becomes difficult to provide assured impact points which are, because of low-altitude separation, generally around the launch area. While the 2.7-kg empty LOKI motor might be acceptable at most ranges, the 19.5-kg empty VIPER was felt to be more hazardous. Accordingly, a post-burnout stable VIPER motor was developed by means of a drag cone or nozzle extension beyond the 6.5-in. diameter. The result is a cleaner dart separation condition and an increase in VIPER motor apogee from 5 km to 17 km. The higher apogee does result in more time in the air for wind drift effects, but for a 95% winter wind condition, all of which is assumed to be a head wind, the impact is theoretically further downrange than in the unstable case.

The high velocity of the dart at low altitudes requires protection of payload from aerodynamic heating. Unlike the ablative coating used on current LOKI - Dart systems, the dart on the VIPER system is designed to insulate the payload from the dart wall temperature by means of an air gap. The nearly finalized dart is shown in figure 3.

ROBIN Sphere and Hardware

The early work in the ROBIN efforts for use in the ARCAS rocket nosecone consisted of theoretical studies, chamber tests, radar reflectivity flights on balloons, and some flight tests. Consideration of sphere materials, fabrication techniques, minimized mass-area ratios, folding and packing techniques, reflectivity requirements, optimum inflation chemicals, techniques of chemical encapsulation and controlled delivery within the balloon, and methods of ejection from the rocket nosecone were some of the many aspects investigated. Early chamber tests indicated that a successful system had been evolved so that in late 1960 some 200 ARCAS ROBIN systems were fabricated for feasibility testing.

The ROBIN sphere (fig. 1) which was developed at this time and which, with a few exceptions, has been the configuration flown in various vehicles to the present time is one meter in diameter. It is fabricated from 1/2-mil clear mylar using 20 gores with butt joints and 1/2-in. heat-pressure sensitive mylar tape. Internally, a 6-point corner reflector fabricated from 1/4-mil metallized mylar is suspended from the balloon skin by means of lightweight springs. Its Government nomenclature is Balloon, Radar Target, Meteorological, ML-568/AM, and the design is covered by Specification MIL-B-27373A, the latest updating being 20 January 1965. (This specification covers the ARCAS configuration which differs from that used in the dart types only in the inflation capsule and packaging procedures.) A lightweight aluminum capsule within the balloon (fig. 4, lower) contains liquid isopentane. At ejection the cover is pushed off the capsule by a small mylar pillow expanding

in the low pressure. Isopentane vaporization is controlled by two orifices in the capsule body to prevent explosive inflation found in chamber tests when the inflating chemical was not controlled. The capsule is free to move within the balloon. Packaging of this payload in the ARCAS nosecone includes several sheets of plastic. The first piece of plastic sheet placed forward in the nosecone cavity is rolled up with enough entrapped air to force the system out when the sealed nose cover is pulled by a one - meter long cable at apogee ejection. A 1 - 1/2 meter square plastic pillow ejects first and inflates to provide some protection from a "dirty" pyrotechnic separation charge, prevalent in early ARCAS, which ejected sparks for a brief interval as the nose cone was pushed off and its cover removed.

The aforementioned ARCAS-ROBINs were flown in 1961 - 1962 at Eglin Air Force Base, Holloman Air Force Base, and Wallops Island. It was eventually recognized, but not before standardization took place and additional quantities had been ordered for operational use, that the reliability of the ROBIN to inflate into a rigid sphere deteriorated as the time between fabrication and flight increased. In addition, collapse of the "good" balloon, which was designed for 30 mb pressure or approximately an altitude of 30 km, occurred at an average altitude of nearly 40 km. Many chamber tests indicated a 30-km collapse was possible but not consistently so.

Efforts to eliminate these problems continued in the mid - 60's (Table 1). Due to the need for higher altitude data, the efforts were directed toward the boosted ARCAS configurations. These latter nosecones, incidentally, require different ballasting than for the ARCAS alone due to aerodynamic stability changes at the higher Mach Numbers attained. These efforts were characterized by lack of continuity due to funding variations, vehicle problems, and contractual difficulties including a contractor who went out of business during a contract thereby losing a year in the process of officially transferring the contract to a successor.

It was felt that damage to the balloon by hot sparks in the separation event noticed in some chamber tests caused at least the early deflation problems. Therefore, some work was done on improving protection during the ejection sequence. A longer cable (5 to 20 meters), with and without a canister containing the balloon, was tested in chambers without significant improvements. In this period, the rocket separation charge was improved and post - explosive particles were minimized.

In addition to mechanical protection, the aforementioned canister as well as some reduced packing volume nosecones were tried in the belief that entrapped air in the balloon had a detrimental effect. Since

mylar is microscopically porous, low density packing and long storage could allow gradual leakage of air into the balloon resulting in catastrophic inflation at altitude. In addition, a few empty capsules with no balloon inflation in some tests indicated that isopentane from a leaking capsule could enter the balloon and then leak out through the balloon skin.

The capsule for the ARCAS-ROBIN is perhaps its weakest element. The strip of neoprene under the cap aged to a sticky condition and, coupled with an easily deformable cap, caused capsule malfunction. A few experiments with other capsule ideas associated with other inflatants such as a glass vial were not attractive. An externally mounted bottle for helium injection followed by release after the filling sequence proved to be a larger and more sophisticated problem than anticipated or funded. Certain other inflatants with a few showing mixed improvements were utilized. Ammonia and ammonia water improved the superpressure characteristics over a larger altitude range. However, the complexity of encapsulating ammonia and its solvent effect on metallized mylar were negative factors.

Details on ARCAS - ROBIN theoretical studies and experiments on inflatants, capsules, packing, etc. may be found in final reports on the contracts indicated in Table 1. Some of these reports are in limited and unofficial supply. The net improvements on the original ARCAS configuration were small. Because the basic ARCAS technique does not provide a simple and positive way of controlling the capsule function and because a boosted dart vehicle appeared to offer various advantages, a few ROBIN configurations were designed and tested in 1963 utilizing the LOKI - Dart. At the end of the short program, several successful flights were made (ref. 4). In 1967, this design was incorporated into the VIPER - Dart with encouraging results (ref. 5).

The long cylindrical dart requires that the one - meter sphere be folded differently and more densely packed. Hence, entrapped air or inwardly leaking air is minimized. The payload is held in long half - cylinder staves within the dart body (fig. 3). The separation sequences consist of a pyrotechnic charge in the dart tail exerting pressure on a piston which pushes the staves and payload forward breaking shear pins in the nose ogive. As the staves exit the forward end of the dart, they are free to fall apart and allow the ROBIN payload to deploy. The motion of the piston is utilized for capsule activation, an additional bonus in the use of a dart system.

The dart capsule (fig. 4, Upper), longer and more slender than the ARCAS capsule, is positioned at the aft end of the dart with only one thickness of balloon material between it and the padded piston. A slide - fit cap on the end of the completely sealed capsule body contains a sharp "hypodermic" needle positioned so that first motion of the piston

pushes the cap further on the body and punctures the end of the body. The cap is held on by friction from a piece of rubber and the isopentane flows out through the needle. This capsule, being a completely sealed metal body before activation, is less likely to have leakage or aging problems.

A corner reflector was used early in the general ROBIN development due to its high radar reflectivity ($\sim 25\ m^2$), thought necessary should a lesser tracking radar (e.g., SCR 584, Mod 2) be utilized. Subsequent analysis of ROBIN data obtained by these radars indicated unacceptable meteorological data accuracies. Since FPS-16 or more precise radars are available at most missile ranges and since it was found that metallized one - meter spheres can be tracked by these radars, the use of a corner reflector is not obligatory. It was retained in most of the AFCRL development flights (and Air Weather Service operational flights) however, for several reasons. The radar AGC display or recording shows a W - form of perturbation indicating a corner passage as the ROBIN slowly rotates. At collapse of the balloon and internal reflector, this signal characteristic drastically changes thus providing a simple method of determining the end point of atmospheric thermodynamic data. This method of locating the collapse altitude has correlated well with other methods that are mentioned under "Data Reduction".

An additional advantage of providing a stronger target for any tracking radar is to approach the optimum signal-to-noise ratio in order to attain the minimum target position errors.

Aerodynamic Drag

As indicated by equation (1) the drag coefficient of a falling sphere must be known in order to evaluate atmospheric density (or for some applications vice versa). The descending ROBIN, weighing 110 to 120 grams, falls from 130 - 140 km to 30 km over a wide range of flow conditions, including transitional, slip flow, and continuum flow (fig. 5). Because of error considerations, computations during part of the acceleration portion of the flight are not attempted. Hence, most of the useful part of the high-altitude flight is from a Mach Number of 3.0 downward and a Reynolds Number of 10^2 upward.

During the early development of the ARCAS - ROBIN, however, where the balloon fell from 65 km, only subsonic flow, principally in the continuum flow regime, is experienced. At that time, little information was available on subsonic compressibility effects on drag coefficients of a sphere at Reynolds Number of 5×10^2 to 10^4. Neither was it possible to find many test facilities capable of performing tests at these conditions. A small wind tunnel at the University of Minnesota,

under the direction of Dr. Helmut G. Heinrich, was located and tests made (Table I) as a subcontract under one of the G. T. Schjeldahl hardware contracts. Instrumentation difficulties led to some repeated tests as well as extension of the range of tests into supersonic conditions when the higher altitude systems were begun. These again were made as a subcontractor under the Litton hardware contract (ref. 6) and reported in reference 7. The drag coefficients reported therein have been used in the "March 1965 ROBIN Computer Program" from that date through the present.

Figure 6 illustrates the range of vertical acceleration experienced by the falling sphere released at an altitude of 139 km. Indicated along the curve are the Mach and Reynolds Numbers experienced during flight. Other release altitudes will result in different acceleration levels at these Mach and Reynolds Numbers. Thus it is felt that drag coefficients obtained in static wind tunnel tests, particularly for the high Mach Number - low Reynolds Number conditions, do not represent the accelerated flow condition. Ballistic range data would be more representative if a range of acceleration conditions could be matched to the aerodynamic parameters.

There have been some recent tests made in a ballistic range at subsonic velocities at the Air Force Arnold Engineering Development Center for Sandia Corporation. These newer drag coefficients in the incompressible case ($M < 0.3$) agree better with classical experiments although even this statement seems to be somewhat in disagreement depending on exactly which reproduction of classic data is utilized. Figure 7, upper section, shows the drag coefficients as measured by Heinrich and used in the "March 1965 Program". These drag coefficients were derived from plots and cross plots of the experimental wind tunnel data which consisted of many duplicated test points. However, interpolation through a Mach 1.0 between test points at $M = 0.9$ and $M = 1.2$ required some subjective reasoning. Hence, this area is subject to greater uncertainties than other sections of the table. Figure 7, lower section, is a composite made up of the aforementioned subsonic ballistic range data and the Heinrich supersonic wind tunnel data. This experimental combination of drag coefficients has been used recently and shows in some cases improved agreement between ROBIN and rocketsonde densities at the 50-km level (see Meteorological Data).

Because proper sphere drag is a prime necessity in the system, it is felt that this parameter should be isolated and made the subject of a basic and major aerodynamic program. The Air Force Arnold Engineering Development Center recently indicated not only their capability of duplicating these aerodynamic flow conditions but their scientific interest in the problem and the availability of their personnel and facilities for these purposes.

An Air Force plan to fund AEDC in a substantial amount for a two year program beginning in FY70 was not approved. Several techniques and facilities would have been used with the hope of analyzing the whole problem and duplicating the correct flow conditions by different techniques.

Data Reduction

The tasks outlined at the beginning of the ROBIN effort in this category were simply stated as: given the radar space - time coordinate history of a falling sphere, determine (1) the technique of obtaining atmospheric wind, density, temperature, and pressure utilizing modern digital computers, (2) the errors associated with these parameters, and (3) the potential of using a graphical or desk type of reduction. The third task was quickly resolved as a solution capable of producing only gross numbers much to the disappointment of meteorological personnel.

The other two tasks, not independent of each other, have and are still requiring considerable time and effort. One aspect of the philosophy adopted in the data reduction area was to establish a computer program using equations, smoothing techniques, drag coefficients, formats, etc., which would represent the best knowledge and information at a given time and to leave it untouched. In this fashion, all ROBIN flights would be reduced in the same manner and subject to the same errors or uncertainties. When several reasons accumulated such as new smoothing intervals or drag coefficients, then a new program was introduced into the field.

Thus references 8 and 9 define the first field programs used until reference 10 introduced the "March 1965 ROBIN Computer Program". This program is in use today at most of the U.S. missile test ranges although a few minor details have been changed or added.

In general the development of the ROBIN computer program has required considerable effort in the classic task of eliminating "noise" from the raw data without removing real detail and conversely not introducing "noise" by inadvertent mathematical operations.

Without any discussion of the background and decisions leading up to the adoption of the current program, an abbreviated description of its operation will describe its highlights (ref. 11). The simple equation presented earlier in this paper is considerably amplified since (1) the sphere is moving in three - dimensional space with winds present, (2) buoyancy, apparent mass and a moving reference point on earth must be considered, and (3) there are "noise" and bias errors in the radar coordinates. In general, the raw radar data are smoothed in order to

obtain sphere velocities and accelerations followed by the use of equations of motion, hydrostatic and gas law relationships to obtain the atmospheric parameters in the one - pass digital computer program.

Following sphere deployment, usually at apogee, the horizontal and vertical velocities are obtained first by the least squares fitting of straight lines to 31 one - half-second space points and assigning the slope as the velocity at the midpoint. The horizontal and vertical accelerations are determined by the least squares fitting of straight lines to 7 one-second velocity points and assigning the slope as the acceleration at the midpoint. Sufficient points are dropped and added to obtain velocities and accelerations every one second immediately preceeding the balance of computations described below. In addition the values of density and W_Z from the previously computed (higher altitude) point are brought in as first approximations.

Figure 8 is a simplified flow chart showing the meteorological parameter computations. W_X and W_Y are computed, then W_Z is computed,and a convergence check of W_Z is made. If a 1% convergence value is not obtained, the small loop indicated is traversed using the computed W_Z. When convergence is indicated, the value of V (the balloon velocity with respect to the air) is computed; then using the drag coefficient from the previous higher point as an approximation, the first calculation of density is made. The hydrostatic equation is then used to calculate pressure and the gas law to calculate temperature. Because Mach and Reynolds Numbers serve to define the aerodynamic flow conditions of the sphere and, hence, its drag coefficient, these numbers are calculated using the velocity, density, and temperature. A drag coefficient table is entered and a drag coefficient obtained. A check of density probably indicates no convergence with the previous higher altitude density and a loop back to the start of the chart is indicated. Calculated values, rather than previous point values, are used in progressing down the chart again and at the density step, the drag coefficient previously obtained from the table is used. When density convergence with the previous computed density is indicated, the final values of density, pressure, temperature, and wind parameters are printed out for this particular altitude. It should be noted that the balloon horizontal displacement per unit time, X or Y, is not taken to be the wind velocity as with most wind sensors in current use. Instead, the equations indicated are used wherein the terms after the minus signs represent the lag of the balloon in responding to wind changes.

Figure 9 is a flow chart similar to figure 8, but depicting the operations required at the first or highest altitude point where the main thermodynamic program commences. It can be seen that a temperature estimate is required which is carried through and printed in the output format for only this point. In addition, the pressure here is calculated

by the use of the gas law. For missile launch sites such as Patrick Air Force Base, Eglin Air Force Base, and Point Mugu, the initial temperature guess is based on a 30°N latitude average summer - winter atmosphere (ref. 12). The program at present does not begin until acceleration reaches - g/3 in order that the magnitude of various terms is sufficient to prevent excessive errors. Hence, the ROBIN sphere must be ejected at an altitude well above the altitude at which measurements are desired. In the case of the VIPER - Dart - ROBIN, for example, a flight having a 128-km ejection altitude provided data from 91 km downward.

With the collapse of the balloon from a rigid spherical shape to a nondescript shape, the thermodynamic parameters may no longer be deduced, although the winds may be calculated by using somewhat simplified equations. The determination of ROBIN balloon collapse is made within the computer program by a "lambda check" in which parameters of balloon motion, which in turn may be associated with density lapse rate, are calculated internally throughout the fall. When the limits of the lambda terms are exceeded, the following type of line is printed:

Lambda = <0.00005 or >0.0002 Balloon has collapsed.

The program then optionally continues its complete computations or shifts to a calculation of wind terms only.

Another method of determining balloon collapse, most applicable for quick field use, is to time the sphere through fixed altitude layers. Table II, based on many successful flights, shows the time corridor for a rigid, 115 - 120-gram, 1-meter-diameter ROBIN to fall through 3-km-altitude layers after ejection well above 73 km altitude. A collapsed sphere requires a longer time to fall than indicated in Table II.

A third method of determining sphere quality involves the observation of the strength of radar signal return, the character of the return in which the corner - reflector pattern in a rigid sphere may be seen, and the level of the range and angle error signals.

Error analyses of the current ROBIN system were made during the development of the "March 65" data reduction program. However, these were done while only ARCAS - ROBIN data were available and hence the errors shown apply only to data from 70 km downward. Table III indicates the RMS errors for the various parameters when a precision radar (AN/FPS-16) is utilized for tracking a rigid sphere at 0.1 second to 0.5 second sampling rate. In addition, at the start of the computations, where the initial temperature estimate might be in error by 10%, a corresponding 2.5% density error would occur which would decrease very

rapidly with decreases in altitude. If a radar of lesser accuracy, such as the AN/MPS-19 radar, is used (standard angle errors of approximately 1.5 mils instead of 0.1 mils), errors occur of the magnitudes shown in Table IV.

Reference 13 presents a technique for error estimation which was used to approximate the errors associated with using the "March 65" computer program at higher than program design altitudes. Table V indicates the degradation experienced in applying this program above 70 km.

Obviously the use of the "March 65" computer program with ROBIN flights in the 100-km to 70-km region is undesirable. During the past year, efforts have been directed to improving and optimizing the program for reduction of data for a complete sounding from 100 km to 30 km. Another paper at this symposium will describe the types of changes that will be made to minimize the errors and describe the program which will be introduced into the field within the next few months. It is planned to modify some of the drag coefficients, in the new program, as previously discussed knowing that future changes may again be needed if a significant aerodynamic program were initiated. The new program will be distributed to those NASA, Army, Navy, and Air Force agencies currently in possession of the "March 65" computer program.

METEOROLOGICAL DATA

More complete coverage of the ROBIN and examples of measured data may be found in references 5, 8, 10, 14, 15, and 16. Reduced data from approximately 300 research and development flights as well as several hundred operational flights by the Air Force 6th Weather Wing have been forwarded to the Air Force Climatic Center and the U.S. Meteorological Rocket Network for storage and dissemination. Research and development flights with the VIPER - Dart - ROBIN system have supported most of the recent SATURN - APOLLO launches.

Figures 10 through 15 present examples of meteorological data obtained during the VIPER - Dart development. Figure 16 shows the complete density profile from the surface to 90 km provided by rawinsonde, rocketsonde, and ROBIN for the APOLLO 11 flight. Figure 17 indicates the effect of using the previously mentioned experimental drag coefficient table. The resulting density profile agrees more closely with the rocketsonde density in the 40 - 60 km levels. However, the temperature profile departs further from the rocketsonde temperature over this altitude range.

CONCLUSIONS AND RECOMMENDATIONS

The intent in this section is to summarize the AFCRL view of the ROBIN falling - sphere system as well as point out problem areas and suggest the direction of further study, development, or test. The comments are given also as recommendations should the general program suggested in the NASA study under Contract NASI - 7911 be implemented in the coming years. Not all of the following remarks have been fully discussed in the body of this report due to varying degrees of complexity beyond the scope of this summary paper. By perusal of the various references listed as well as by means of a round table discussion with others present here, these points can be more fully analyzed.

1. The feasibility of measuring atmospheric winds, density, temperature, and pressure from 100 km to 30 km by means of a passive radar - tracked falling sphere has been established. Subjective analysis indicates reasonable values of the measured parameters.

2. Error analyses made to date for data gathered between 65 and 30 km indicate errors of 3 to 0.5 m/sec in wind magnitude, 3% in density, 10 to 4% in temperature and 6 to 3% in pressure.

3. In spite of these quoted figures, comparison with rocket-sondes flown within one hour sometimes indicated differences in the order of 20% in density while at times better agreement is found.

4. A data reduction computer program developed satisfactorily for the 65 - 30 km range of altitudes after further analysis, which will be presented at this Symposium, seems to show that the degree and thickness of the smoothing interval is critical as the altitude, and hence, fall velocity, becomes sufficiently large. To some degree, the character of the wind profile needs to be known in order to minimize the error in the wind.

5. It is possible that an optimum density program may not provide an optimum temperature output and vice versa.

6. Consideration of errors and the computation procedure indicates that a constant percent error in the drag coefficient or density is required if one wishes to minimize temperature error.

7. The above two statements indicate the need to more rigidly define the exact parameters to be measured in a synoptic meteorological network. Density is probably the principle parameter desired by the aero-space community although some meteorologists may prefer temperatures for their analyses of the atmosphere.

8. Vertical winds are assigned as a zero - value in the computations. Various experimenters indicate this is not the case and have published values which are significant only at the lowest altitudes where the sphere velocity is small.

9. Some analyses with a few 65-km ROBIN flights were made by assuming that the small perturbations in density were caused by vertical winds. The maximum vertical winds detected by this method were $\pm$ 5 m/sec (but more typically, $\pm$ 3 m/sec) with wavelengths in the order to 2 km. A 3-m/sec error in vertical sphere velocity represents a 6 - 1/2% error in vertical velocity or 13% density error at 40 km. This reduces to less than a 2% density error at 75 km.

10. To some extent the above two statements might lead to consideration of the tradeoffs in using either (a) a single system for winds and density from 100 km down to nearly 30 km or (b) two systems or a compound system for separation of measurements into optimum altitude levels. A rocketsonde might be ejected at 60 km or two spheres of differing mass area ratios might be utilized from a two-stage dart.

11. In a similar vein, it was found that the measurement of winds above 70 km with the ROBIN, as will be reported in another paper here, requires special attention. It is possible that chaff or a slower falling target than the ROBIN will be required to sense horizontal winds to the accuracy desired.

12. The requirements for horizontal winds needs to be more precisely defined before further effort be expended in developing a final system. Not only does the accuracy in wind magnitude need defining, but the wavelengths of wind perturbations that must be sensed should be indicated as an aid in establishing design goals in hardware and computer techniques.

13. The input from the tracking radar scientific community has been tedious and only by a gradual item by item approach have certain, but possibly not all, of the radar characteristics been investigated. On one program it was found that the servo bandwidths were better set at a different position for minimal target position error than recommended to the technicians by their official training instructions. Other as yet unknown peculiarities should be isolated and an expert assigned to any overall new development.

14. Analysis of error recordings indicated that FPS-16 radars at Eglin, at least when tracking the standard 65-km ROBIN, has RMS errors of less than $\pm$ 0.2 mil in elevation and azimuth angles, not unlike their

handbook values. From other programs it is known that individual FPS-16 radars vary appreciably in their noise characteristics and the quotation of a single error figure for one type of radar is misleading. A decrease in signal-to-noise ratio whether caused by a weaker target, greater slant range, more background noise, or an "untuned" radar can increase the tracking error.

15. Enhancement of radar return without use of a corner reflector is desirable for simplification in fabrication and packaging.

16. If a new radar concept is pursued as suggested in the recent aforementioned NASA conceptual study report for a 1980 rocket system, its design approach should include not only the minimization of tracking error but also the shaping of its "noise" character to optimize data reduction techniques.

17. Drag coefficient values used in ROBIN soundings are uncertain as judged at least by (a) rocketsonde data in the lower altitude portions and (b) by data peculiarities in the transonic region around 75 km.

18. Drag coefficients for the most part obtained by static wind tunnel tests are used in the ROBIN and other falling sphere systems. Vertical accelerations during the measurement phase descending from 100 km pass from negative values through zero to as much as + 3 g's at 80 km and then decrease to insignificant values at 30 km. Similarly, lateral accelerations are present. Static drag coefficients do not, to varying degrees, represent proper values under accelerated flow conditions. Hence, some attempt should be made in the future work to utilize ballistic ranges where Mach and Reynolds Numbers and acceleration levels may be simulated.

19. Consideration of apparent mass indicates this term is negligible above 20 km and it is felt does not adequately attack the accelerated flow condition.

20. The state of knowledge of the aerodynamic parameters accuracies is perhaps the weakest point in the ROBIN system. If a world meteorological rocket network of a scale initimated in the aforementioned study were pursued and implemented, a world standard atmosphere would most assuredly follow from the large amount of data gathered. To have this standard based on questionable sphere drag coefficients would be folly indeed. Hence, it is strongly recommended by this author that a significant program be established and managed by a Government aeronautical agency for this very basic research problem for application to either current or future falling - sphere systems.

21. The feasibility of using the ROBIN in several types of rockets, subject to accelerations of over 100 g's, has been demonstrated. The vehicle would seem to be the least of all problems in the system. Some further reduction in cost over the already reasonably priced VIPER - Dart might be attained by further efforts along the line of the Super LOKI motor in a new dart configuration or possibly other vehicles under development (Canada - Army, Astrobee, etc.). Gun probe personnel have indicated a nearly hopeless hardware task with this approach and it is assumed that this is a final conclusion.

22. The ROBIN hardware development has demonstrated that thin plastic spheres can be ejected at high altitudes and inflated by means of vaporization of various liquids. In-depth studies and tests some years ago indicated for example that sublining solids were too slow in action for this application. There may be today newer chemicals, solids, or liquids, that might offer promise leading to simplification of encapsulation and release of the chemical and reduce further the mass-area ratio of the sphere.

23. Evaluations of the internal sphere gas temperature for hardware considerations as well as the skin temperature for aerodynamic considerations have been attempted but without assurance by the theorists that their methods are rigorous.

24. A significant reduction in the sphere's mass - area ratio would of course reduce the range of aerodynamic flow conditions and possibly improve sensing ability through simplification of the required measured parameters. Reference 1 indicates that in a wind shear of .02/sec , a 5 m/sec wind error would result if the fall velocity were 45 m/sec and the horizontal acceleration terms were completely ignored. While such a velocity is unattainable at high altitudes, it indicates a limit in simplification.

25. Consideration of better ejection and deployment techniques is suggested wherein lower dynamic loads would be imposed thereby allowing light gauge (and weight) materials. Attempts to use 1/4 and 1/3 mil with ARCAS - ROBIN indicated a decrease in reliability.

26. Similarly, newer materials should be considered with improved strength and weight characteristics. While perhaps heavier than desirable, a scrim - plastic combination might permit simple and relatively uncontrolled pressurization techniques. In addition, a larger superpressure than the 30-mb design in the ROBIN would assure spherical conditions down to less than 30 km.

27. While there is disagreement with other experimenters concerning this matter, the usual collapse altitude of the ROBIN at 40 km

rather than 30 km is felt to be another as yet unresolved problem. Temperature balance is felt to be a part of the problem. The University of Michigan uses metallized spheres and publishes density data to 30 km. However, Air Force experiments with metallized spheres has shown little correlation with collapse altitudes. Quantity of inflatant and temperature - pressure characteristics need refinement particularly if new chemicals are considered.

28. It was hoped that a report could be made here on the successful deployment of a ram - air inflated sphere from a rocket. Two were attempted; one was not tracked and the other track indicated the descent of a heavy object. The idea, originally conceived and demonstrated at sea level by the AFCRL Starute contractor, Goodyear Aerospace Corporation, is worthy of further pursuit. The elimination of chemicals, capsules, etc. should simplify the total hardware picture.

29. Consideration of body shapes other than a sphere, possibly using the ram - air inflation principle, might be attractive due to potentially larger and less varying drag coefficients during their fall. The remaining aerodynamic characteristics (C_m , C_L) would possibly lead to other design problems which would have to be solved for all flow conditions.

30. Before the final framework of aerodynamic test requirements are established for a sphere (or other body), all hardware improvements should at least be checked and verified.

31. If a flexible development program is possible, there are payoffs in intermixing flights of spheres of various sizes and weights with laboratory or wind tunnel tests. For example, a peculiar hook in the current drag coefficient table was found after the reduction of flight data using early wind tunnel data indicated a hook existed in the density profile. More detailed wind tunnel tests uncovered a peculiar drag coefficient variation thereby smoothing the calculated density profile.

32. Comparative flight tests between spheres of various masses and sizes and with other sensors during day and night can be productive in evaluation of errors and consistency. Only a small amount of this comparison testing has been accomplished. Comparisons of ROBIN densities with rocketsonde densities have in general shown inconsistent disagreements.

33. In summation, it is believed that FPS-16 radars, available at missile ranges in this country, contribute less to the total density error in falling-sphere data than the uncertainties in the drag coefficients now utilized. Additional efforts with sphere hardware are also required to improve reliability and low-altitude performance.

REFERENCES

1. Lally, V.E., and Leviton, R., Accuracy of Wind Determination from the Track of a Falling Object, Air Force Surveys in Geophysics No. 93, (ASTIA No. AD 46858) Geophysics Research Directorate AFCRC, Mar. 1958

2. Peterson, J.W., Schulte, H.F., and Schaefer, E.J., A Simplified Falling - Sphere Method for Upper-Air Density, AFCRL-TR-59-263, University of Michigan Research Institute, May 1959.

3. Leviton, R., and Wright, J.B., Accuracy of Density from the ROBIN Falling Sphere, AFCRL, GRD Research Note No. 73, (ASTIA No. AD 274213), Dec. 1961

4. Watson, C.W., JUDI - ROBIN Balloon Dart Sounding Vehicle, AFCRL Report No. 64-471, (ASTIA No. AD 607074), Rocket Power, Inc., May 1964

5. Bollermann, B., and Walker, R.L., Design, Development and Flight Test of the VIPER Dart ROBIN Meteorological Rocket System, AFCRL Report No. 68-0418 (ASTIA No. AD 675608), Space Data Corporation, Jun. 1968

6. Smalley, J.H., and Flink, L.R., Modification of the ROBIN Meteorological Balloon, Vol 1, Design and Test, AFCRL Report No. 65-734, (ASTIA No. AD 629774), Applied Science Division, Litton Systems, Inc., Sept. 1965

7. Heinrich, H.G., Haak, E.L., and Niccum, R.J., Modification of the ROBIN Meteorological Balloon, Vol. II, Drag Evaluations, AFCRL Report No. 65-734 II, (ASTIA No. AD 629775), University of Minnesota, Sept. 1965

8. Engler, N.A., Development of Methods to Determine Winds, Density, Pressure and Temperature from the ROBIN Falling Balloon, (ASTIA No. AD 630200), University of Dayton Research Institute, (Contract No. AF 19(604)-7450), Oct. 1962

9. Brockman, W.E., Computer Programs in Fortran and Balgol for Determining Winds, Density, Pressure, and Temperature from the ROBIN Falling Balloon, University of Dayton Research Institute, (Contract No. AF 19(604)-7450), Jan. 1963

10. Engler, N.A., Development of Methods to Determine Winds, Density, Pressure, and Temperature from the ROBIN Falling Balloon, University of Dayton Research Institute Final Report, Contract No. AF 19(604)-7450, AFCRL Report No. 65-448, May 1965

11. Wright, J.B., and Leviton, R., The ROBIN Falling Sphere, COSPAR Technical Manual, Falling Sphere Method for Upper Air Density, Temperature and Wind, Feb. 1967

12. Court, A., Kantor, A. J., Cole, A. E., Supplemental Atmospheres, Research Note, AFCRL 62-899, Sept. 1962

13. Luers, J.K., Estimation of Errors in Density and Temperature Measured by the High Altitude ROBIN Sphere, Proceedings of the Third National Conference on Aerospace Meteorology, May 1968

14. Engler, N.A., and Wright, J.B., Wind Sensing Capability of the ROBIN, AFCRL Report No. 62-273 (II), AFSG No. 140, Proceedings of the National Symposium on Winds for Aerospace Vehicle Design, Vol II, Mar. 1962

15. Lenhard, R.W., Jr., and Wright, J.B., Mesospheric Winds from 23 Successive Hourly Soundings, AFCRL Research Report No. 63-836 (ASTIA No. AD 417441), Jul. 1963

16. Engler, N.A., High Altitude ROBIN Flights, AFCRL Report No. 67-0433, (ASTIA No. AD 675810), University of Dayton Research Institute, May 1967

TABLE I - HISTORY OF AFCRL ROBIN CONTRACTUAL EFFORTS

Year	Drag Coefficients	ARCAS-type Hardware	Dart-type Hardware	Data, Programs, etc.	Year
1958					1958
1959		G.T.Schjeldahl Co. Contract AF19(604)-4569			1959
1960	U. of Minnesota Contract AF19(604)-6653	G.T.Schjeldahl Co. Contract AF19(604)-6653			1960
1961	U. of Minnesota Contract AF19(604)-8034	G.T.Schjeldahl Co. Contract AF19(604)8034			1961
1962			Rocket Power, Inc. Contract AF19(628)-1624	U. of Dayton Research Institute Contract AF19(604)-7450 Ref. 8, 9, 10	1962
1963			Rocket Power, Inc. Contract AF19(628)-2805 Ref. 4		1963
1964	U. of Minnesota Contract AF 19(628)-2945 Ref. 7	(General Mills) Litton Systems Contract AF19(628)-2945 Ref. 6			1964
1965				U. of Dayton Research Institute Contract AF19(628)-4796 Ref. 16	1965
1966		(G.C.A., Viron) G.T.Schjeldahl Co. Contract AF19(628)-5538	Space Data Corp. Contract AF19(628)-5911 Ref. 5		1966
1967					1967
1968			Space Data Corp. Contract F19628-68-C-0393	U. of Dayton Research Institute Contract F19628-67-C-0102 Ref. 17	1968
1969					1969

TABLE II

ROBIN DESCENT TIMES

Altitude Layer From, km	Altitude Layer To, km	Time Seconds	Altitude Layer From, Feet	Altitude Layer To, Feet
73.2	70.1	12 - 15	240,000	230,000
70.1	67.1	13 - 16	230,000	220,000
67.1	64.0	14 - 17	220,000	210,000
64.0	61.0	16 - 19	210,000	200,000
61.0	57.9	19 - 24	200,000	190,000
57.9	54.9	23 - 28	190,000	180,000
54.9	51.8	29 - 32	180,000	170,000
51.8	48.8	35 - 40	170,000	160,000
48.8	45.7	43 - 49	160,000	150,000
45.7	42.7	53 - 60	150,000	140,000
42.7	39.6	65 - 75	140,000	130,000
39.6	36.6	Approx. 89	130,000	120,000
36.6	33.5	Approx. 113	120,000	110 000
33.5	30.5	Approx. 145	110,000	100,000

TABLE III

RMS ERRORS FOR ROBIN DATA USING THE AN/FPS-16 RADAR AND THE "MARCH 65" DATA REDUCTION PROGRAM

Meteorological Parameter	Altitude Bands 70 - 60, km	60 - 50, km	50 - 30, km
Altitude, km	± 10	± 10	± 10
Magnitude of wind vector, m/sec	± 3	± 1.5	± 0.5
Density, %	± 3	± 3	± 3
Pressure, %	± 6	± 3	± 3
Temperature, %	± 10	± 3	± 4

TABLE IV

RMS ERRORS FOR ROBIN DATA USING THE AN/MPS-19 RADAR AND THE "MARCH 65" DATA REDUCTION PROGRAM

Meteorological Parameter	Altitude Bands		
	70 - 60 km	60 - 50 km	50 - 30 km
Altitude, km	± 50	± 50	± 50
Magnitude of wind vector, m/sec	∓ 15	∓ 10	∓ 5
Density, %	∓ 6	∓ 6	∓ 10
Pressure, %	∓ 10	∓ 8	∓ 10
Temperature, %	∓ 12	∓ 8	∓ 10

TABLE V

APPROXIMATE ERRORS FOR ROBIN USING THE AN/FPS-16 RADAR AND THE "MARCH 65" DATA REDUCTION PROGRAM

Meteorological Parameter	Altitude		
	90 km	80 km	70 km
Wind			
RMS Noise Error, m/sec	20	5	4
Bias Error, m/sec	3	3	2
Sinusoidal Wind Field Bias Error, % of Amplitude Measured			
4 km Sinusoidal Wind	1	5	20
10 km Sinusoidal Wind	16	40	80
Density			
Random Error, %	5	3	4
Bias Error, %	14	2	0

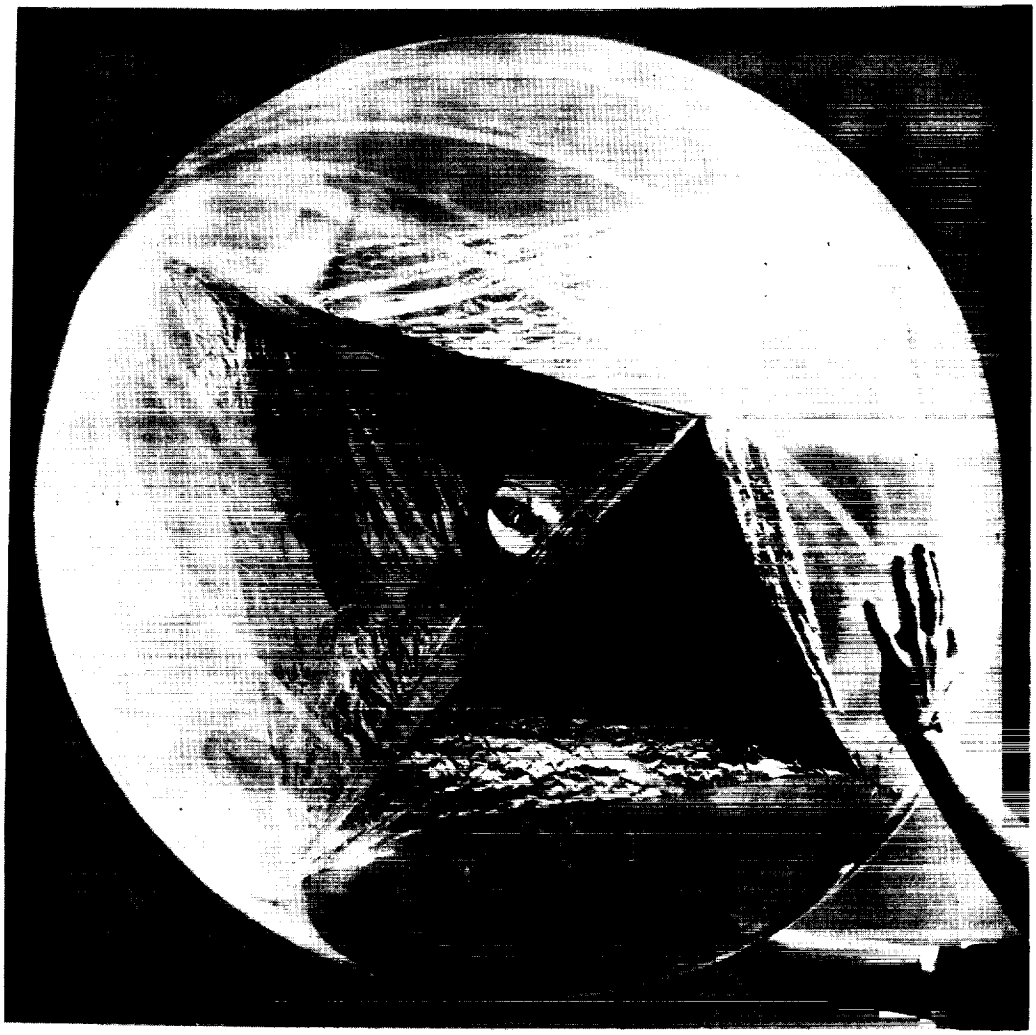

Figure 1.- ROBIN (ML-568/AM) spherical balloon.

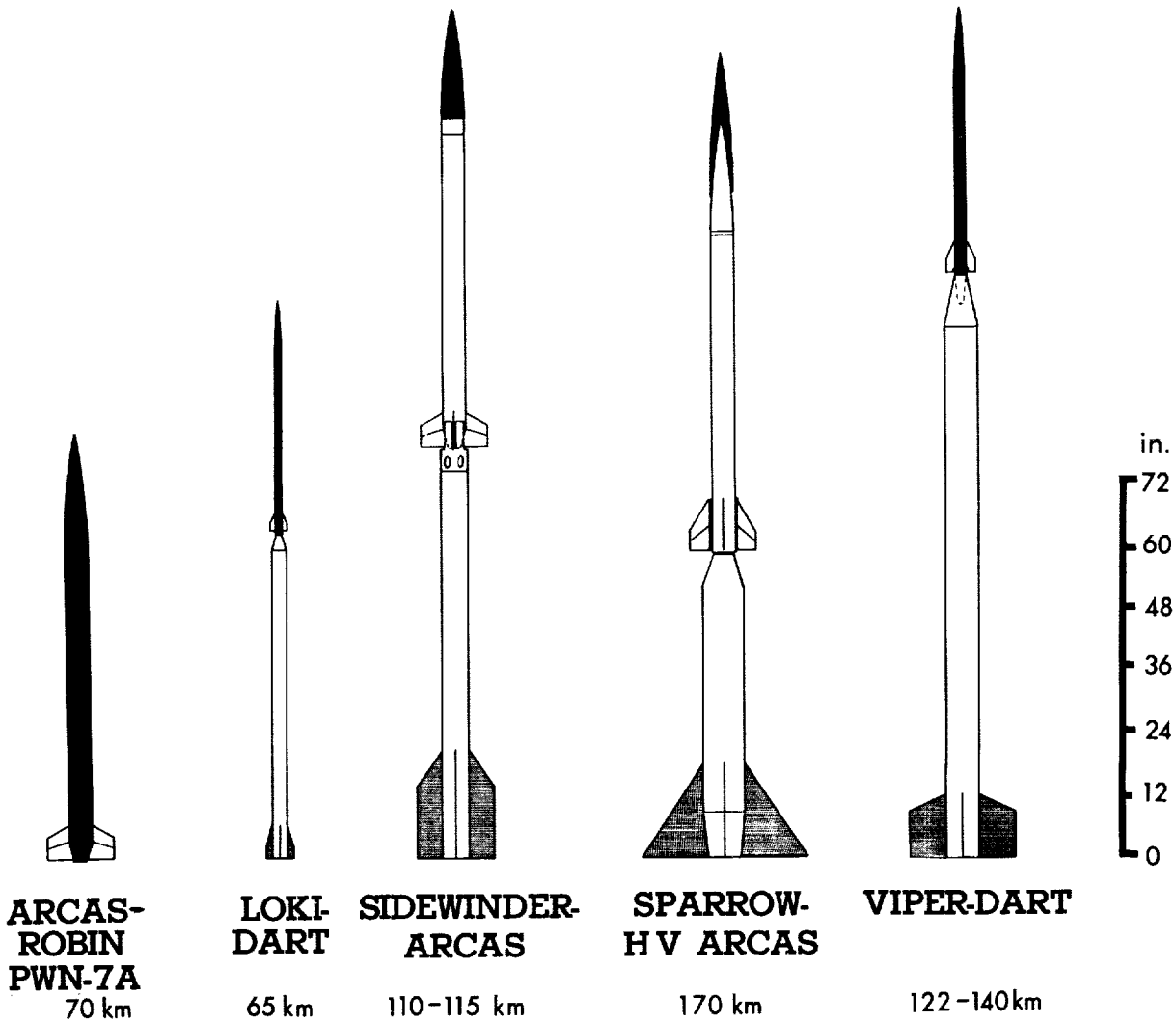

Figure 2.- Meteorological rockets utilizing ROBIN.

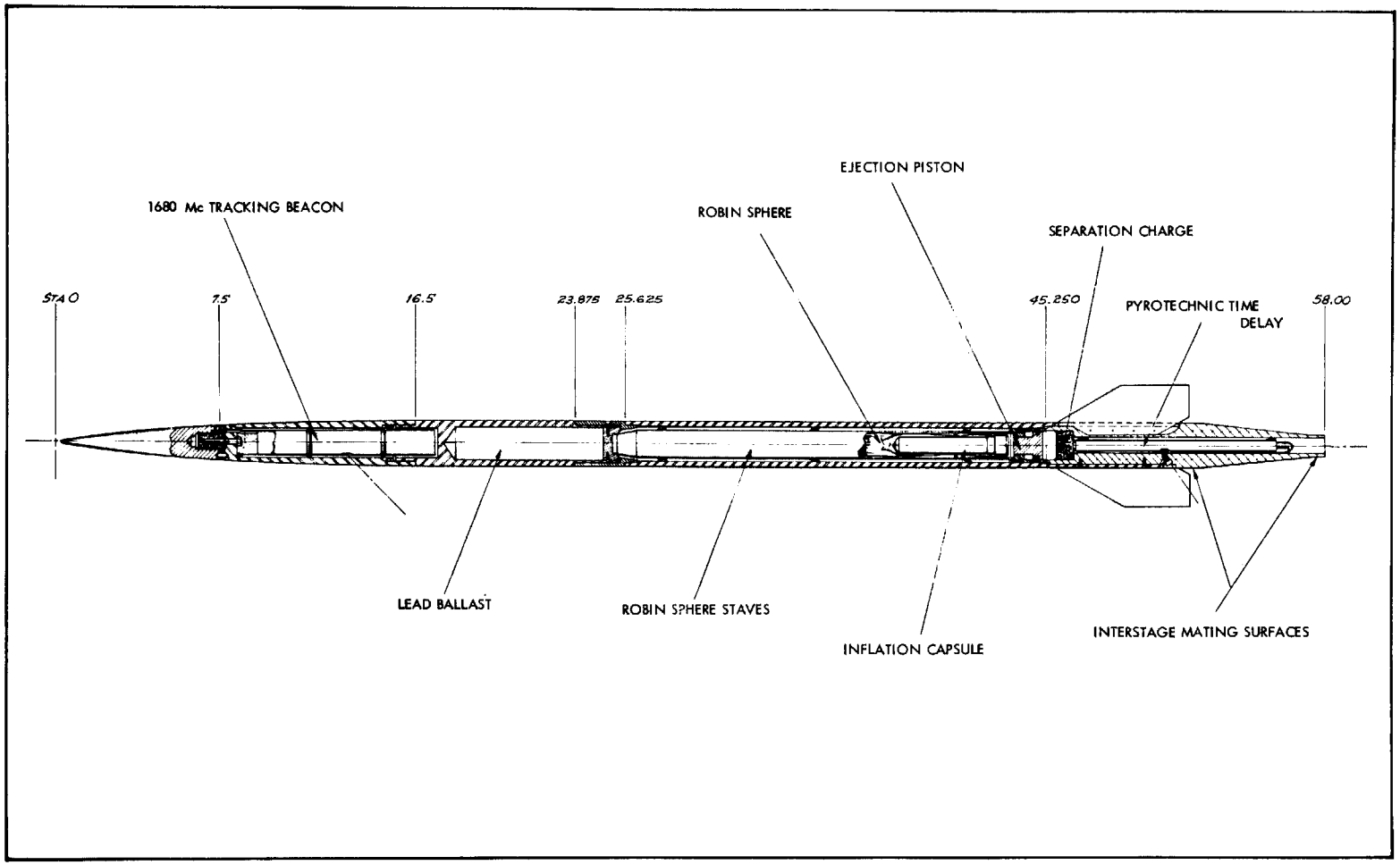

Figure 3.- VIPER-Dart-ROBIN cross section.

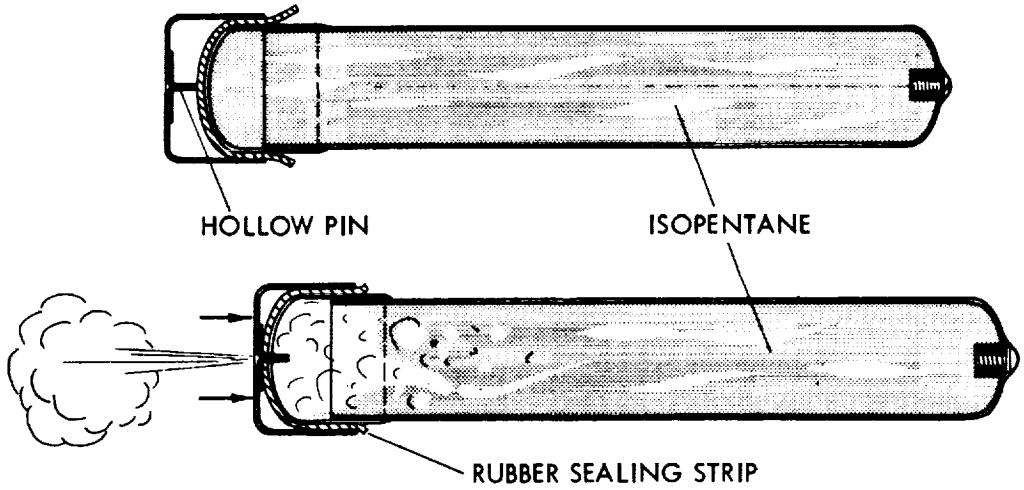

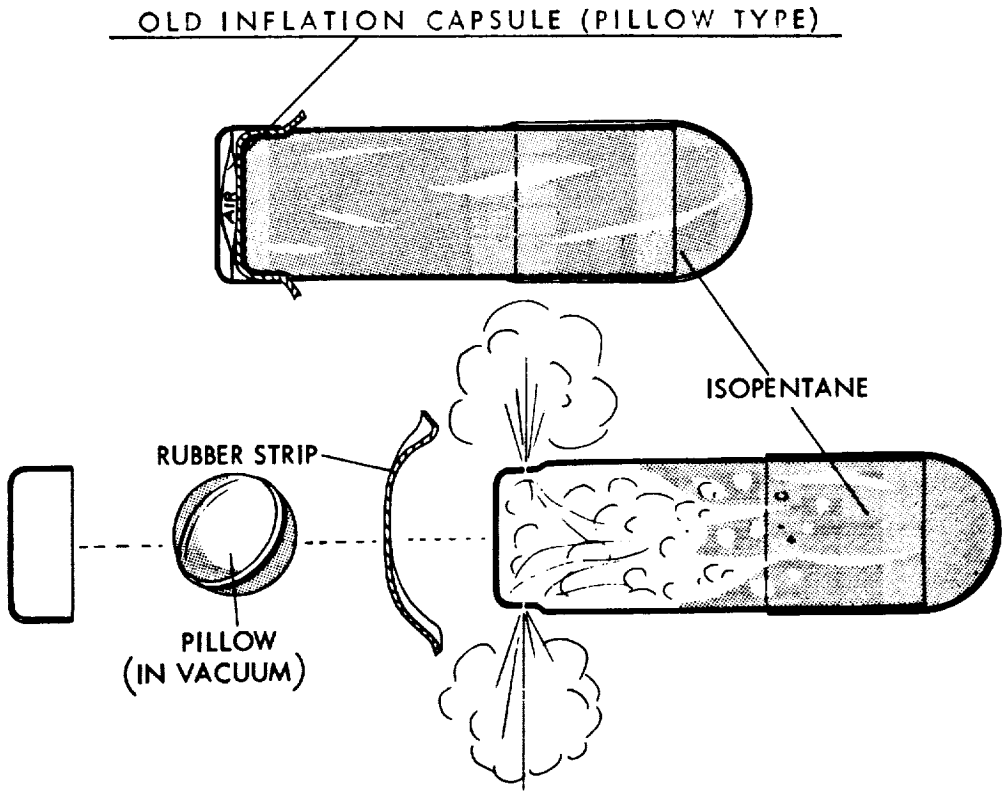

Figure 4.- Isopentane inflation capsules.

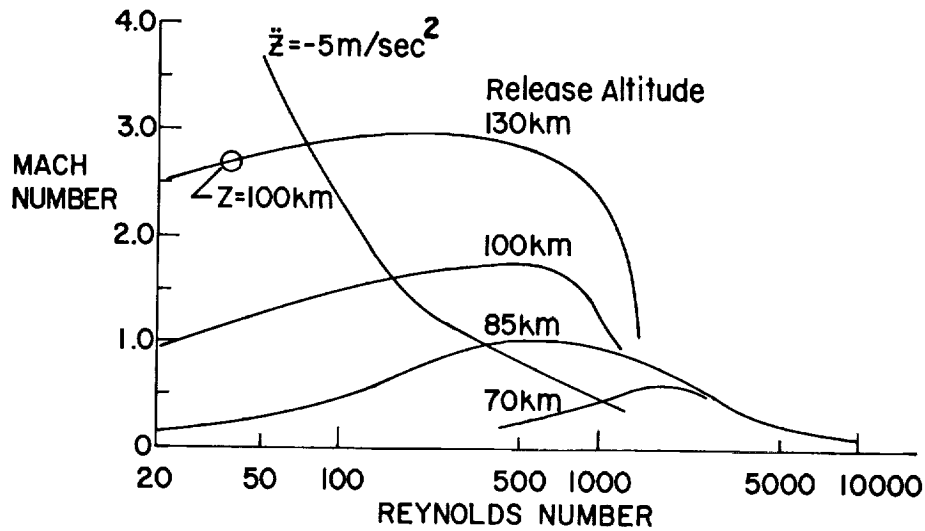

Figure 5.- ROBIN falling-sphere aerodynamic flow conditions.

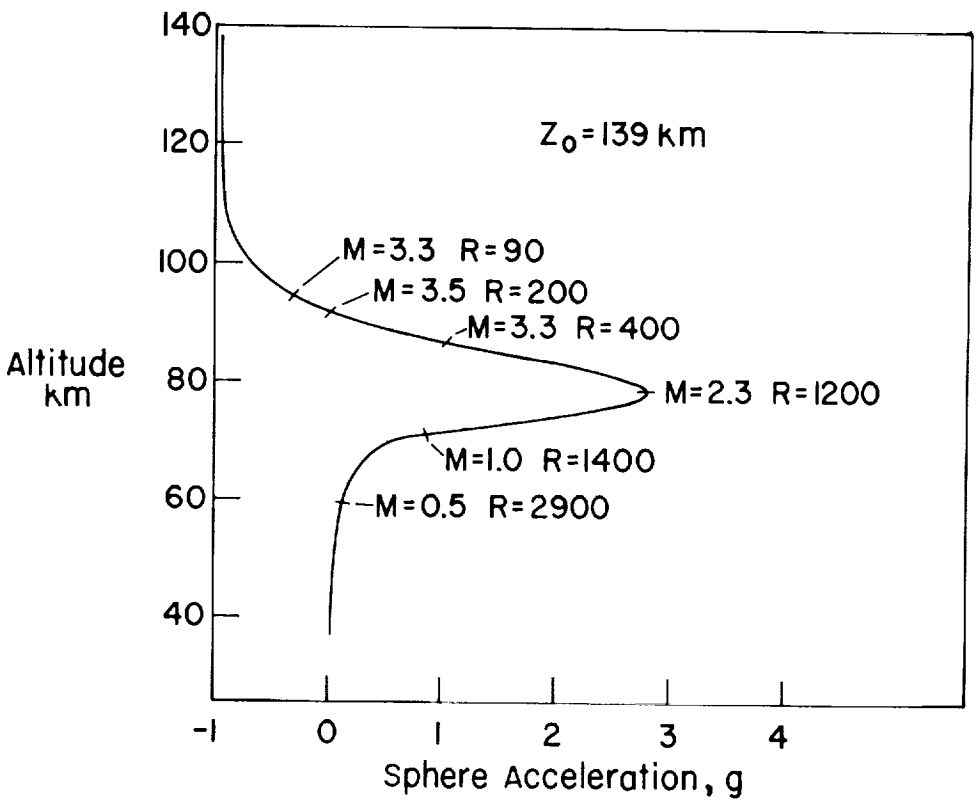

Figure 6.- ROBIN flight profile.

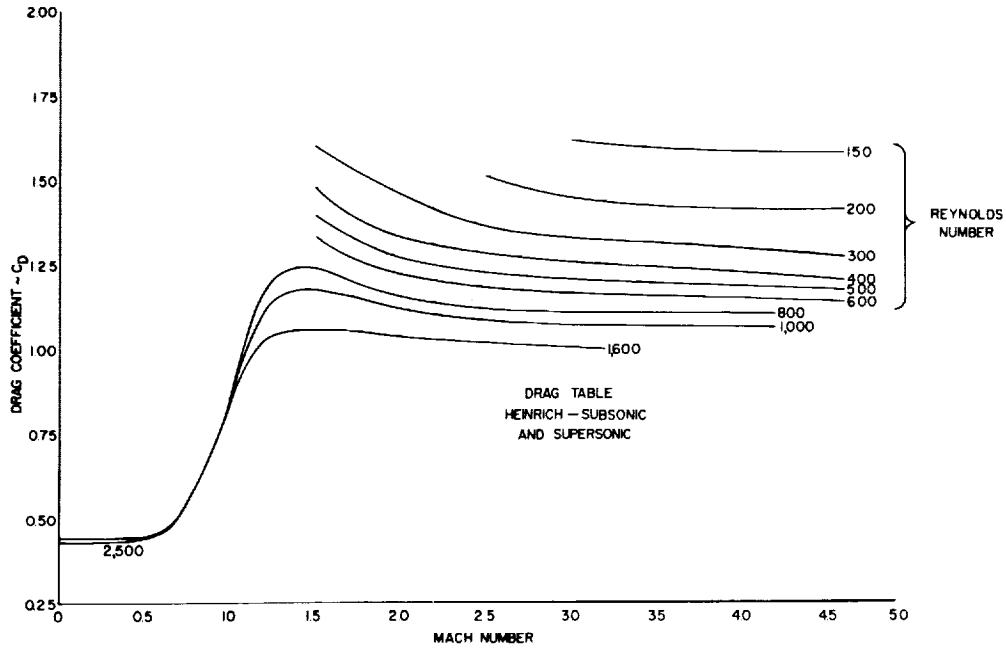

(a) Utilized in "March 65" Computer Program.

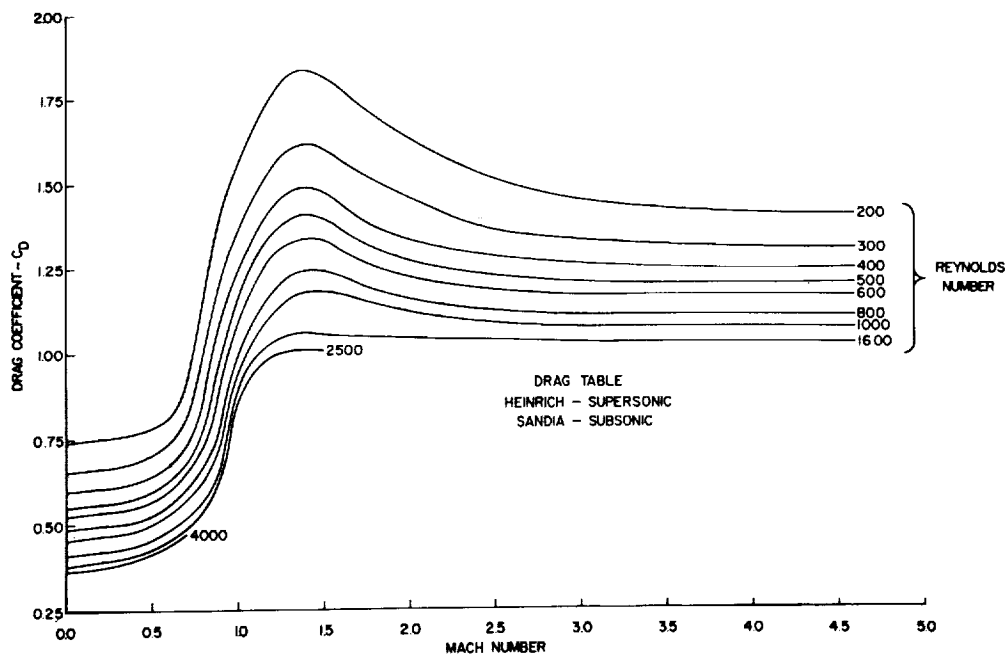

(b) Experimental.

Figure 7.- Drag coefficients of a sphere.

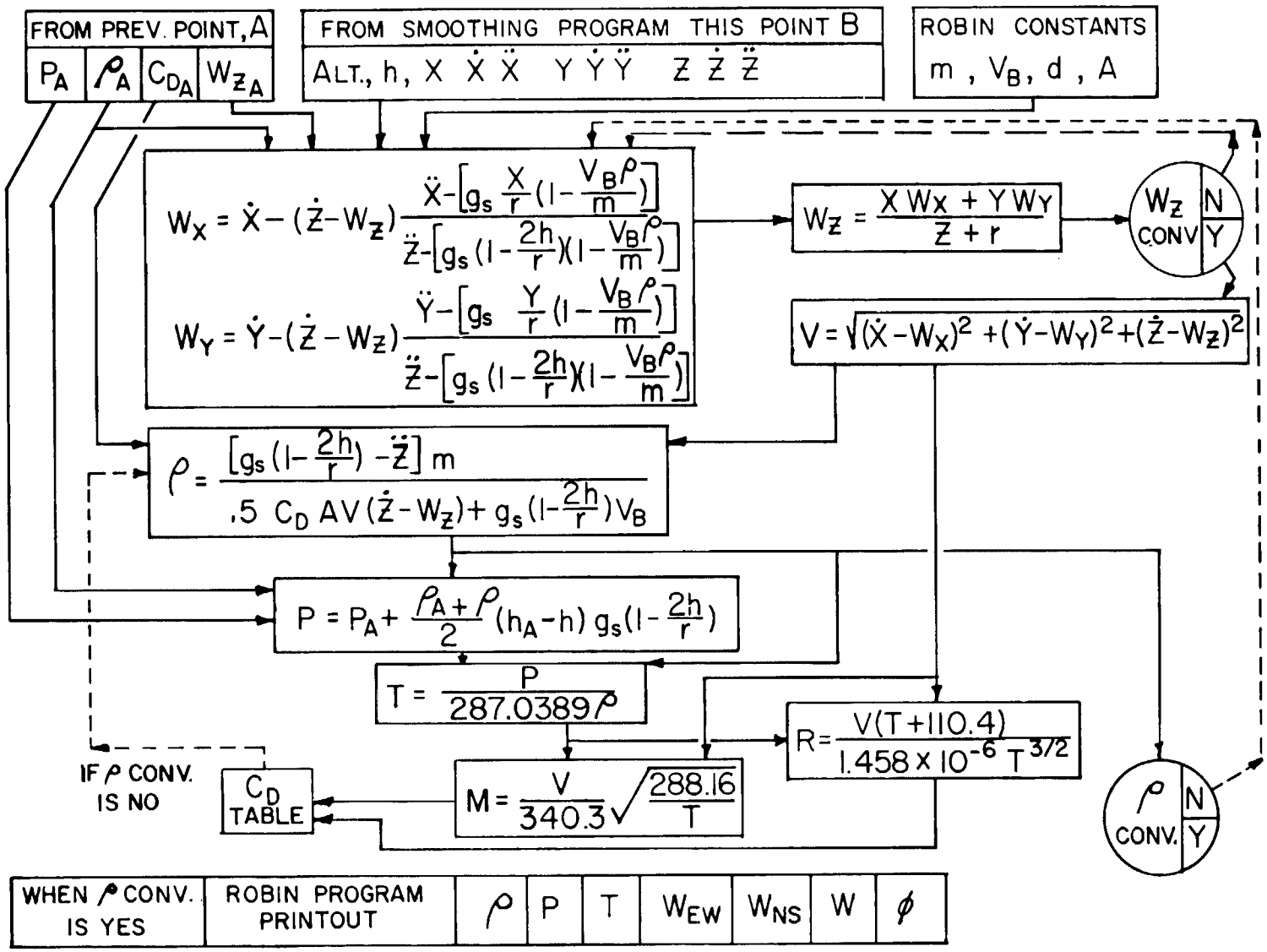

Figure 8.- ROBIN computer program, typical point.

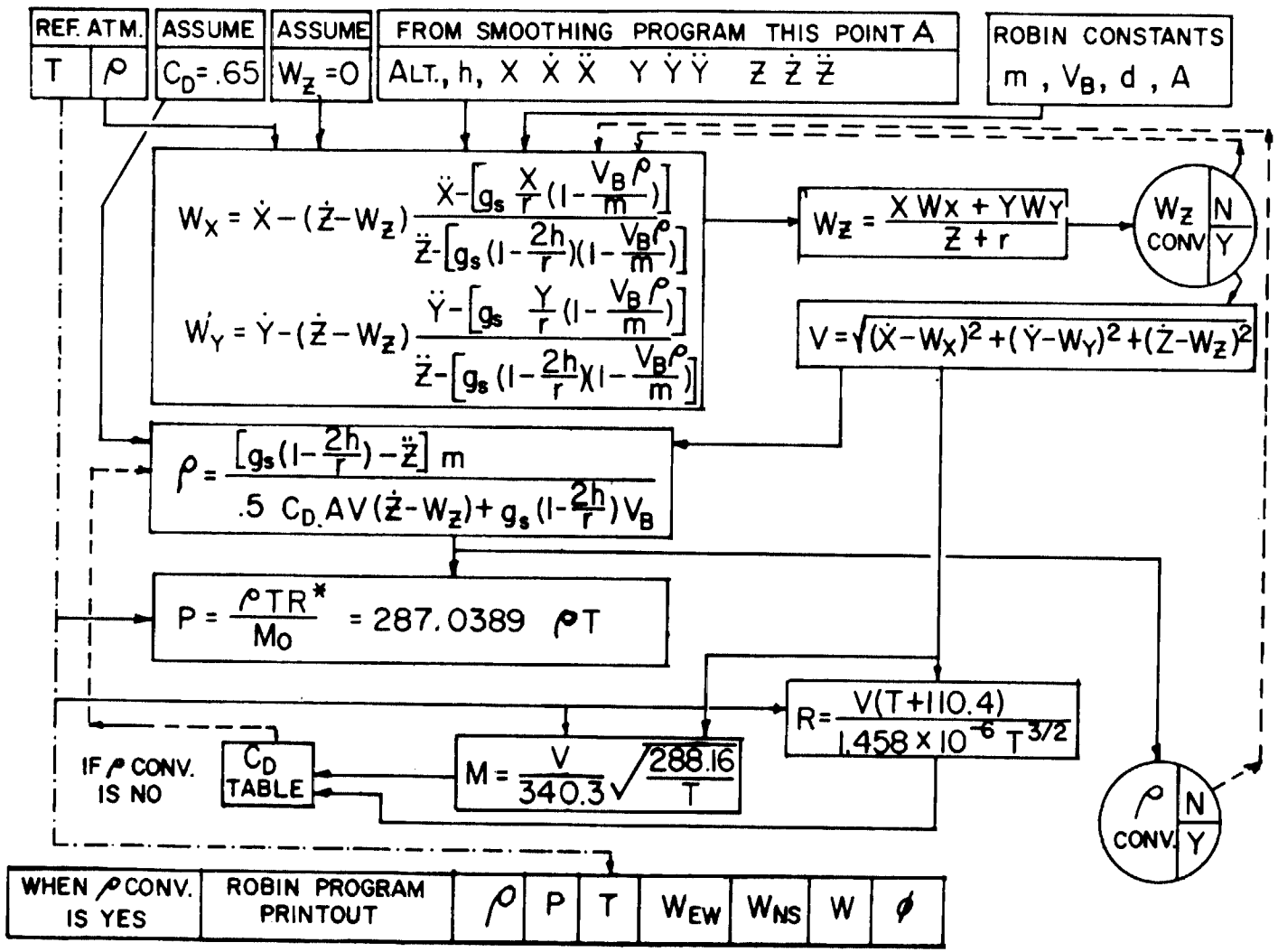

Figure 9.- ROBIN computer program, first point.

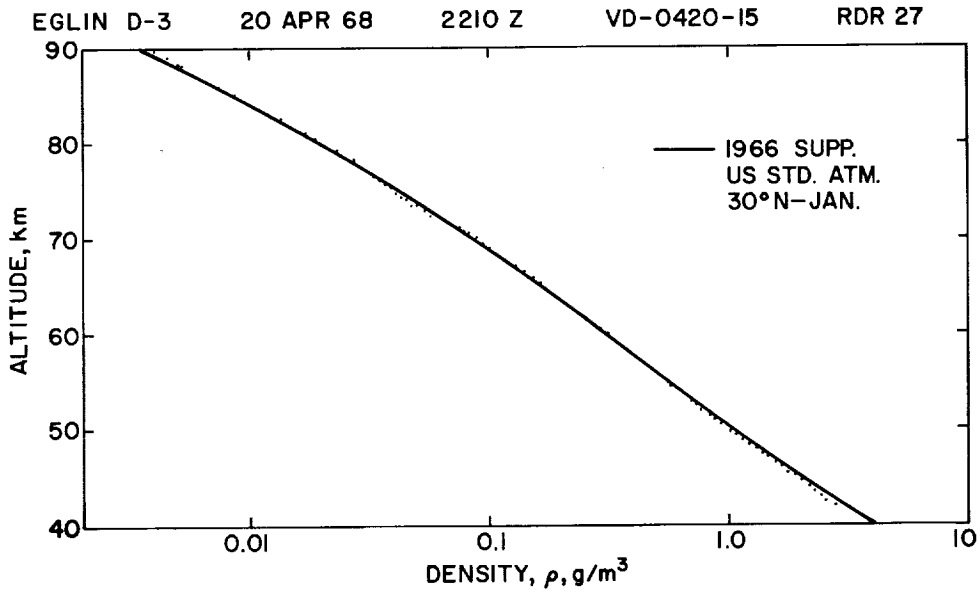

Figure 10.- Density profile from a ROBIN flight.

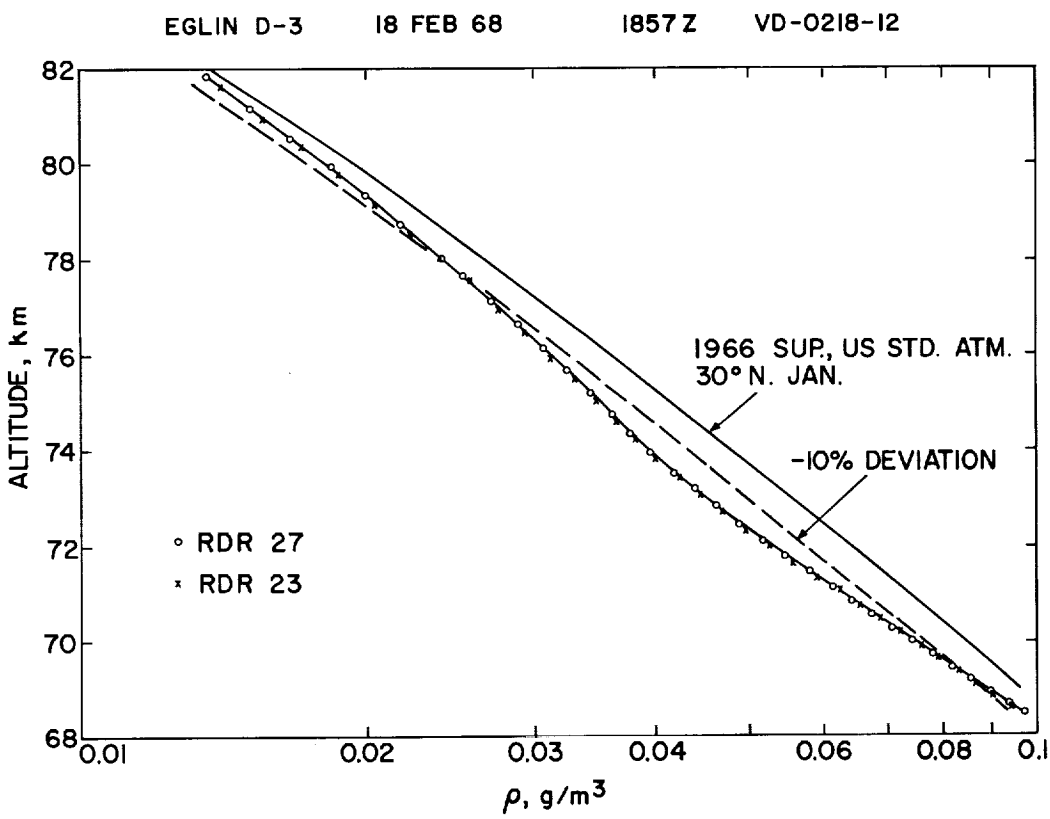

Figure 11.- Section of a density profile from a ROBIN flight.

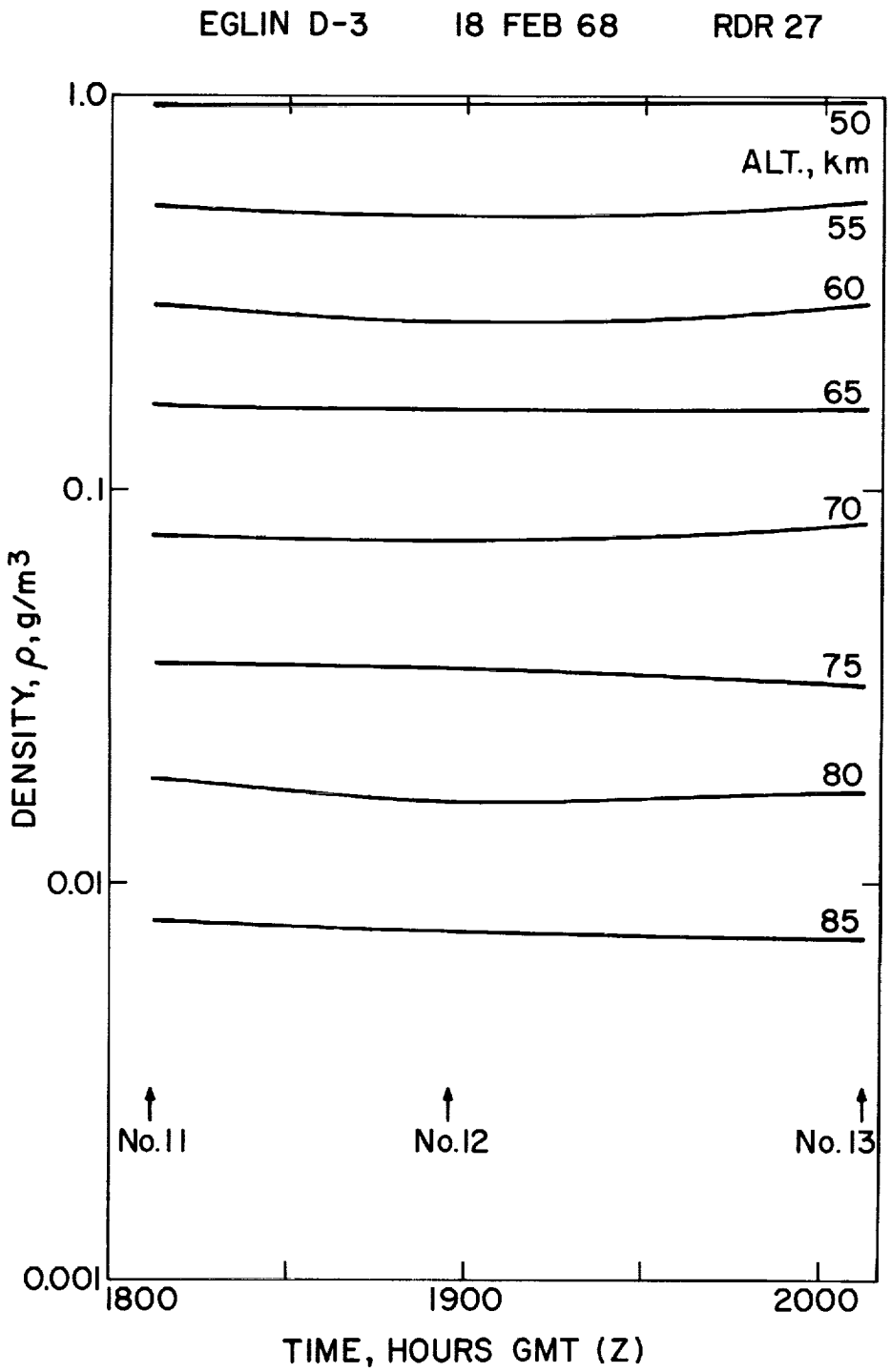

Figure 12.- Constant level densities from three ROBIN flights.

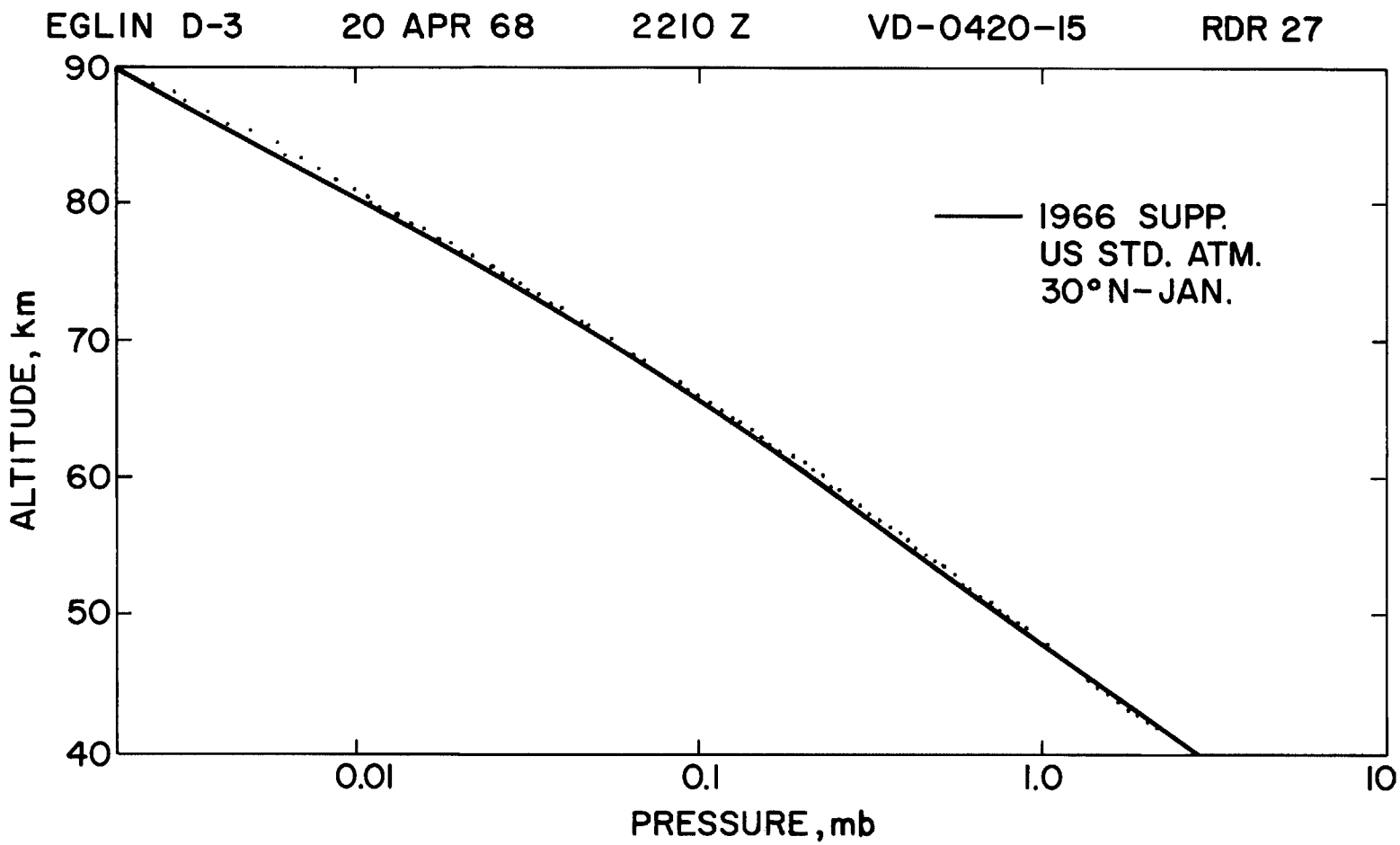

Figure 13.- Pressure profile from a ROBIN flight.

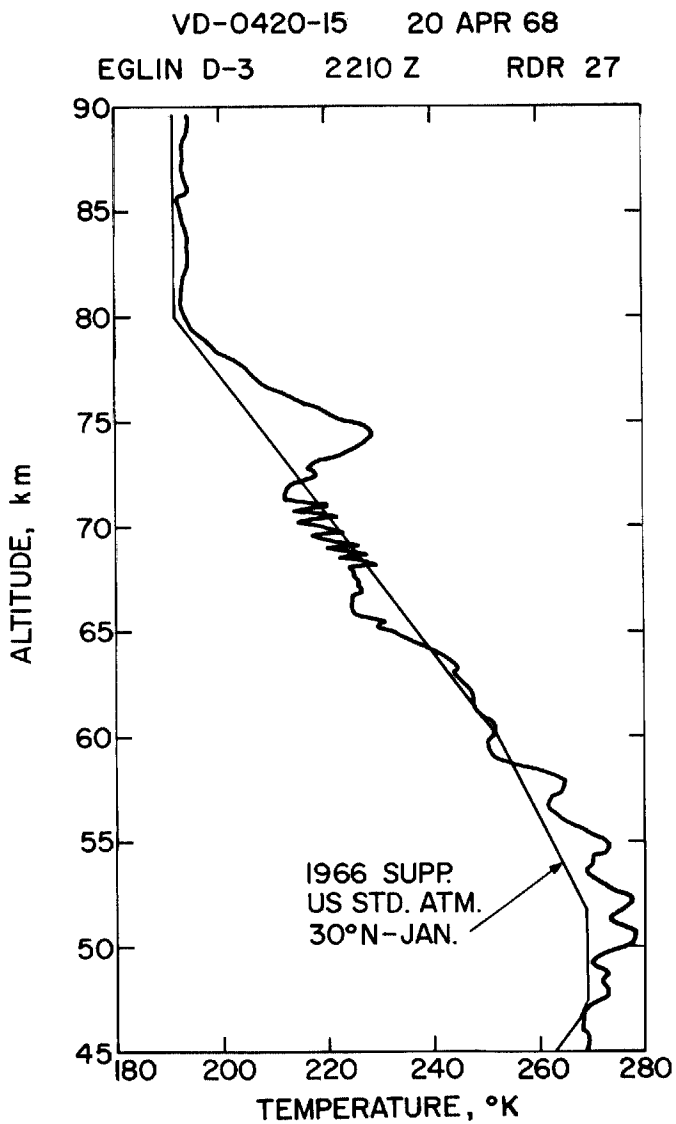

Figure 14.- Temperature profile from a ROBIN flight.

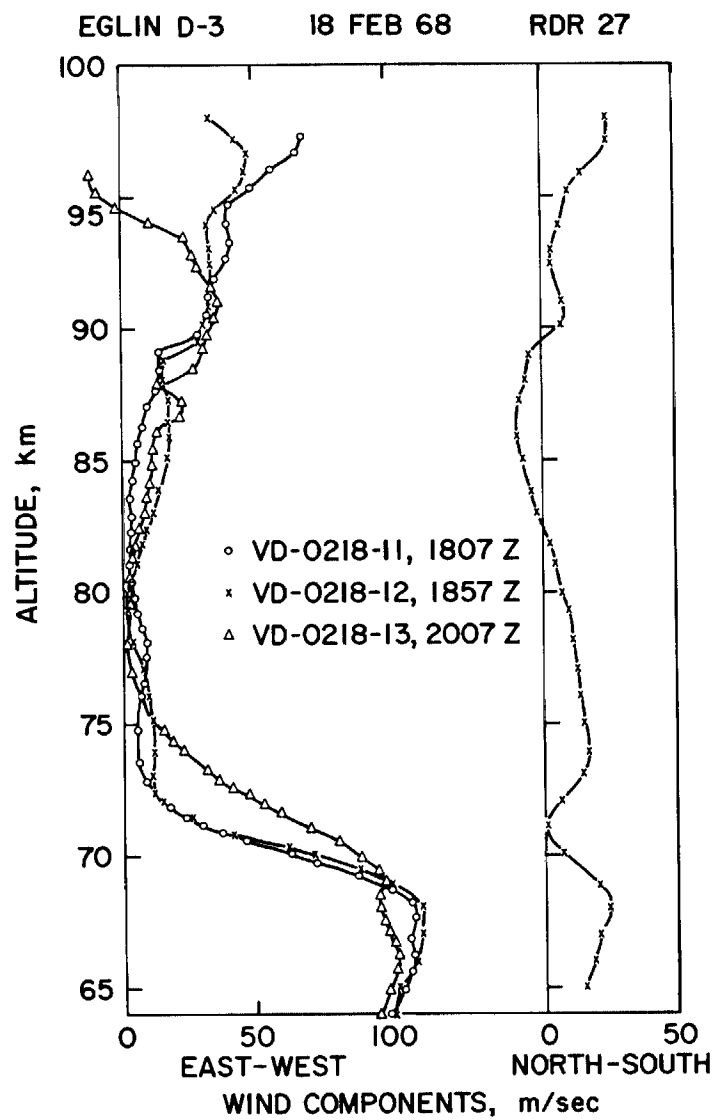

Figure 15.- Wind components from three ROBIN flights.

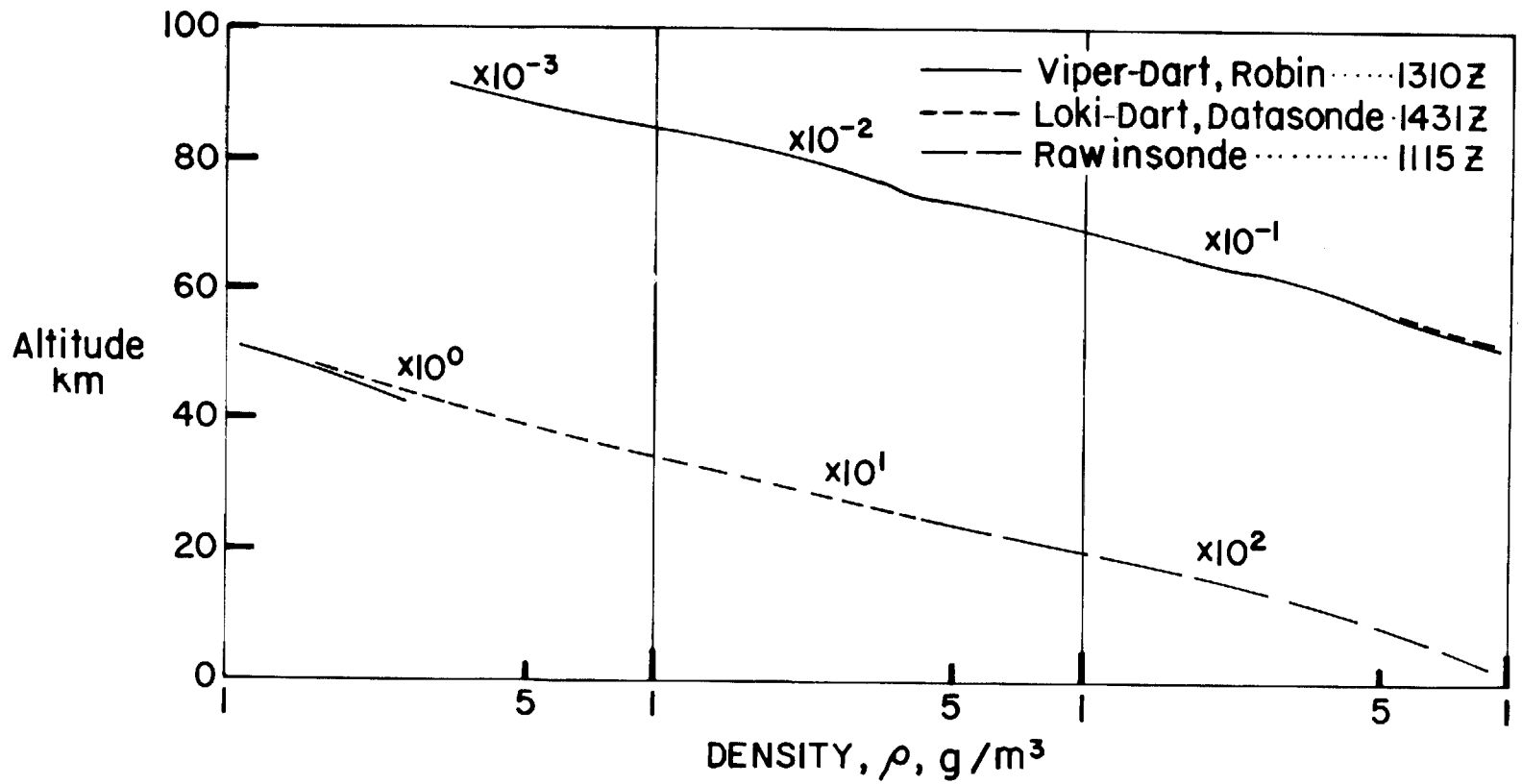

Figure 16.- Density profile, Apollo 11 launch support, ETR, Cape Kennedy, Fla., 14 July 1969.

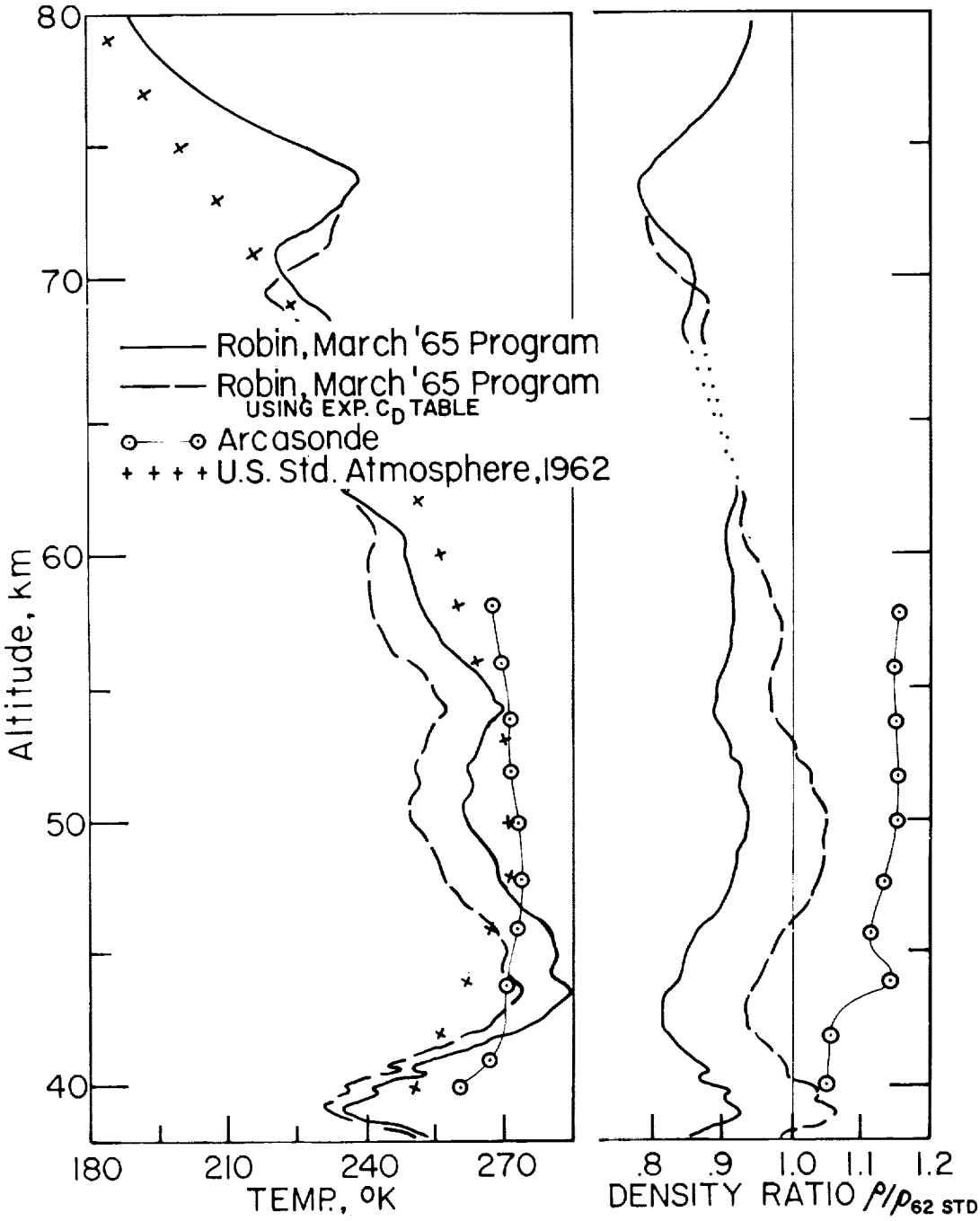

Figure 17.- Effect of using experimental drag coefficients on measured density and temperature, ETR, Cape Kennedy, Fla., 20 Dec. 1968.

THE IMPORTANCE OF ENVIRONMENTAL TESTING INCLUDING EXPERIENCE WITH THE ARCAS-ROBIN SYSTEM

By Sammie D. Joplin

NASA Langley Research Center

2

INTRODUCTION

The testing of flight spececraft under simulated space conditions is used to confirm the analyses and assumptions of spacecraft design. This general approach has wide acceptance. The problem is to select a test program within the allocation of funds and the availability of facilities and manpower and to answer the following questions:

(1) What types of tests will be conducted on the complete system and subsystems?

(2) What method will be used to simulate the space environment?

(3) What test levels will be used?

The emphasis of this paper is on the selection of an environmental test plan that will result in the development of a reliable system for obtaining atmospheric measurements. First, the availability of facilities and their capability of providing a simulated environment for a falling-sphere system will be considered; then, the types of tests and test levels that have resulted in the development of successful flight systems. Finally, some techniques that can be used to simulate the environment of an inflatable falling sphere will be considered.

FACILITIES

The facilities at the Langley Research Center that can be used in an environmental test program for inflatable falling spheres are in the following categories:

First are the thermal vacuum and vacuum facilities. By utilizing one or more of the 16 facilities in this category, a system can be tested at the pressure altitude of its flight environment. Several of these facilities are capable of producing more than one condition. For example, a system could be operated under the pressure altitude, temperature range, and solar radiation that it experiences during flight. Another facility is capable of subjecting a system to the combined effect of a pressure altitude, a range of temperatures, and vibrations. Many of the facilities allow for the installation of special equipment to obtain a special condition on a system. For example, in a test that will be discussed subsequently, an airlock was installed inside one of the vacuum facilities to maintain the system being tested at sea-level pressure during the hours that are required to pump the facility to the test condition.

The next category, vibration and shaker facilities, also includes the equipment needed to perform acceleration tests. These facilities are used to provide the environment that a system would experience due to ground handling, rocket flight, and separation of the spacecraft from the rocket motor.

The balancing equipment and spin tables are used to subject the system to the spin rate provided by rocket flight, to balance the spacecraft, and to subject the system to a steady-state acceleration.

Solar simulation equipment is available and can be used with several of the vacuum facilities to obtain a combined effect.

There are numerous pieces of equipment in the fatigue and load testing category for use in testing the structural integrity of a system.

The descriptions here have been brief, but there appear to be sufficient facilities available to allow for the design of an experimental test program that will give confidence that an inflatable-falling-sphere system will survive the rocket launch and operate in its environment. A detailed listing of the environmental test equipment at the Langley Research Center and their characteristics is available in reference 1.

TYPES OF TESTS AND TEST LEVELS

With the facilities available, attention can now be directed to the following question: What types of tests and test levels should be incorporated in an environmental test plan? The appendix outlines a general test plan that is desirable in the development of a flight system and the types of tests and activities within the elements of the test plan. Obviously, each system must be considered individually with variations made in the test plan and selection of the types of tests based on the following criteria:

(1) Mission criticality

(2) Level of design uncertainty

(3) Level of environmental uncertainty

(4) Resources available

One approach to the testing level that has resulted in a high rate of success is documented in reference 2. The engineering test model (ETM) systems and/or prototype systems are tested at stress levels up to $1\frac{1}{2}$ times the expected environments of launch or space. The flight systems are tested under the expected environments of launch or space.

SIMULATION TECHNIQUES

The final question to be considered is how to simulate the environment for an inflatable falling sphere. There is no single answer to this question. However, some examples are available from a limited test program conducted at the Langley Research Center during 1964 on the Arcas-Robin system. These examples were functional tests in a simulated environment designed to aid in identifying the failure modes of an Arcas-Robin system.

The Arcas-Robin system is a 1-meter-diameter, 1/2-mil Mylar inflatable sphere designed to be carried to release altitude by a small rocket motor. The Robin sphere used in this test program had an internal corner reflector for radar tracking. The four basic functions that must take place in order for the system to function properly are illustrated in figure 1. First, the separation charge must fire and give the nose cone an increase in velocity. The next function is the removal of the nose-cone aft bulkhead by a lanyard that is permanently attached to the rocket motor. Removal of the bulkhead allows the next function, egress of the inflatable sphere from the nose cone, to occur. Finally, the sphere inflation capsule must function to inflate the sphere. Each basic function also has a series of subfunctions upon which it is dependent. These functions will be considered in more detail after a description of the three series of tests conducted on the Arcas-Robin system.

The first and second series of tests were conducted in a 5-foot-diameter, 10-foot-long thermal vacuum facility. The capabilities of this facility are as follows:

(1) A pressure of 1×10^{-6} torr (or a pressure altitude of approximately 650 000 feet)

(2) A temperature range of -320° F to 600° F

(3) A solar simulator which is a 15-kW carbon arc light

The tests in this facility consisted of mechanically removing the bulkhead from the Arcas nose cone. This procedure allowed the Robin sphere to egress and inflate. The test environment provided was a pressure of 64×10^{-3} torr and a solar simulator. The pressure utilized for these tests, 64×10^{-3} torr, can be achieved in 30 to 45 minutes. Two glass side ports and a 5-foot-diameter glass door permitted high-speed photographic coverage of the tests, as well as visual inspection of the inflated sphere. After sphere deployment, the pressure in this vacuum chamber was increased to 8.3 torr over the average time that the sphere experiences this pressure change in flight.

The results of the first series of tests are presented in table I. All six spheres ruptured during inflation.

Experience gained during the development of the Echo satellite indicated that the most likely cause of failure was an excessive rate of inflation caused by residual air trapped in the Robin sphere during packing. This cause of failure was easily eliminated by restricting the packing volume from 40 cubic inches to 22 cubic inches, and another series of tests was conducted on this modified system to evaluate the inflation system. Figure 2(a) is an illustration of the complete assembly of the standard sphere as used in the first series of tests, figure 2(b) shows the modified assembly, and figure 3 illustrates the modified deployment sequence.

The results of the second series of tests are presented in table II. The inflation capsule was omitted from tests 1 and 2 in order to evaluate the effect of residual air on inflation. All four tests were successful.

The third series of tests was conducted in the 60-foot vacuum sphere. This facility provided the space necessary to separate the nose cone from a dummy rocket motor during free fall by using the flight-separation device and to deploy and inflate the sphere before it contacted the walls of the test facility. An airlock was designed and installed in the facility to keep the Arcas-Robin system at sea-level pressure during the hours required to reach the test condition. The airlock was also designed to simulate the real-time altitude change of the Arcas-Robin system during the rocket flight. These tests were designed to obtain additional information on the reliability of the inflation system of the Robin sphere. (See fig. 4.) They also provided information about the relative position of the rocket motor, the nose cone, and the inflating sphere during separation. The results of the six tests conducted in this series are shown in table III. An analysis of the failures showed that the inflation capsule failed to function properly. In one test (3), all systems functioned properly.

An analysis of failure mode and effects has been prepared on the Arcas-Robin system in order to identify the single-point failures that are critical to mission success, to list the possible failures and the effects, and to aid in eliminating similar problem areas in future inflatable-sphere systems. The portion of that analysis identifying the failure modes of the Robin sphere is summarized in table IV. In this table it should be noted that the inflation system of the Robin sphere has five components, and each component has a serious malfunction associated with its operation. A malfunction of any one of these components could result in the failure of the Robin sphere to obtain useful data. The situation is complicated further because all the malfunctions support each other. This type of analysis should be performed on future inflatable falling-sphere systems to minimize malfunctions and to avoid placing an unreliable system into general use.

CONCLUDING REMARKS

The tests described here are only indications of what can be done with existing facilities to simulate the environment of a falling-sphere system. The justification for expenditure of resources in performing environmental tests is that insufficient design data are available to predict that the system will operate satisfactorily in its environment. The use of available facilities to conduct a well-planned environmental testing program can, for the most part, limit failures in the system to failures during environmental tests where instrumentation and high-speed photography in a controlled environment can be used to provide the data needed to identify the cause of failure. This method will give the designer the information needed to provide a reliable system for obtaining meteorological measurements.

APPENDIX

TEST PLAN

Flow Chart: Engineering Test Model (ETM), Prototype, Flight, and Flight Spare

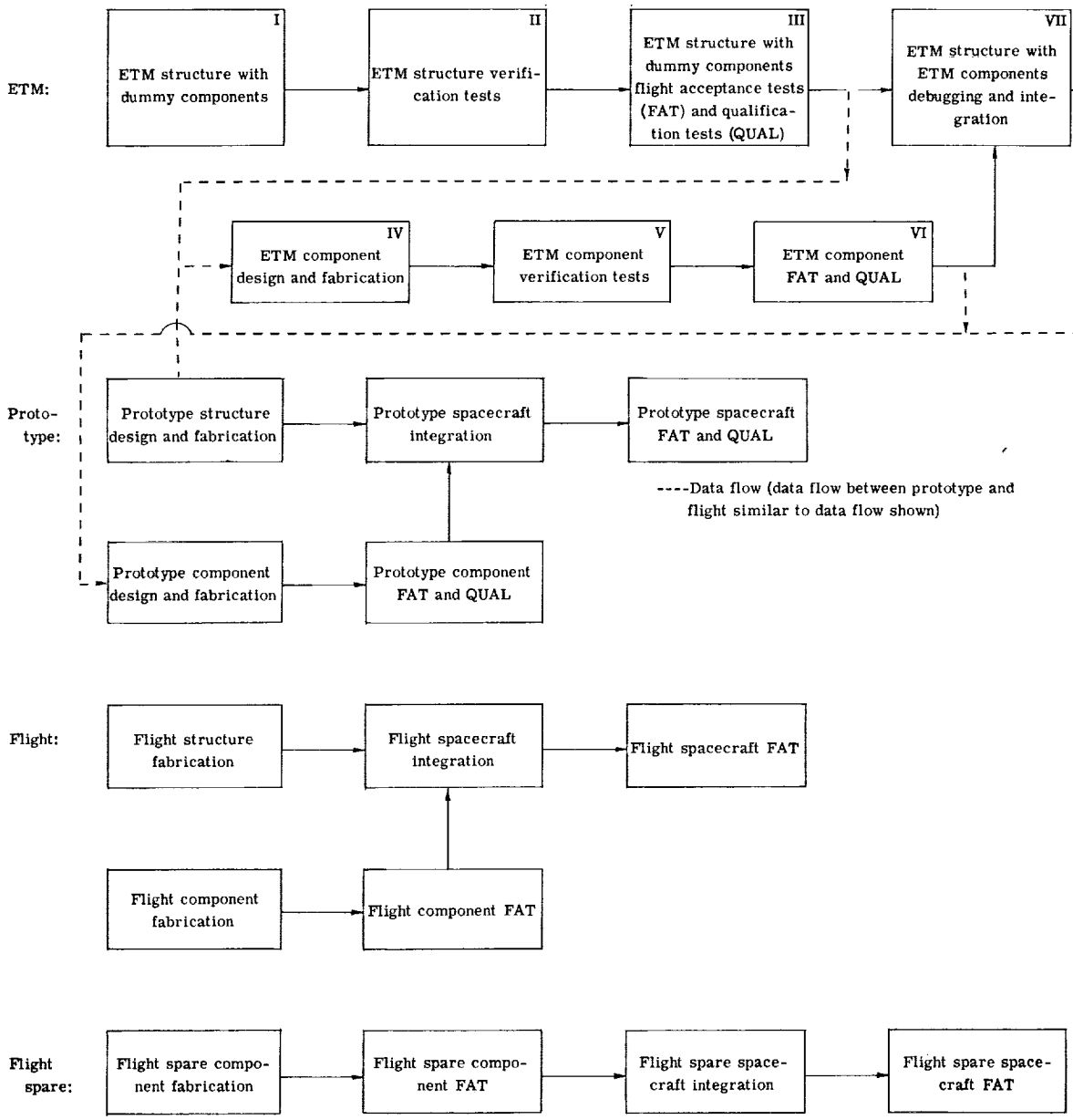

Tests and Activities Within Elements of the Test Plan

I. ETM structure With Dummy Components
   A. Integration of structural members
   B. Integration of dummy components (fit check, interference check, alinement, etc.)

II. ETM Structural Verification Tests
   A. Vibration survey for structural design verification (resonance survey)
   B. Structural integrity (bending, compression, etc.)

III. ETM Structure With Dummy Component Flight Acceptance Tests (FAT) and Qualification Tests (QUAL)
   A. Vibration, shock, and acceleration tests
      1. Qualifies structural design
      2. Develop transmissibilities for ETM component design considerations

IV. ETM Component Design and Fabrication
   A. Apply data from III

V. ETM Component Verification Tests (Subsystem)
   A. Verifies and/or improves design concepts or intent
   B. Examples of tests
      1. Antenna pattern
      2. Pyrotechnic
      3. Despin
      4. Panel or boom deployment
      5. Spinup
      6. EMI (electromagnetic interference)

VI. ETM Component Flight Acceptance Tests and Qualification Tests
   A. Vibration, shock, acceleration, decompression, and thermal vacuum (FAT followed by QUAL)

VII. ETM Structure With ETM Components Integration, Debug, and Verification
   A. Physical electrical and mechanical capabilities and interfaces verified and resolved
   B. Operational compatibilities between components and between subsystems determined
   C. Compatibility of spacecraft and checkout equipment evaluated
   D. Subsystem and spacecraft response to command signals evaluated
   E. Refer to item V for test examples plus
      1. Alinement tests
      2. Heat-shield fit and ejection
      3. Physical parameters (weight center of gravity balance, moment of inertia)

NOTE: Similar activities take place with the prototype, flight, and flight spares.

REFERENCES

1. Clevenson, Sherman A.; and MacConochie, Ian O.: Characteristics of Environmental Test Equipment at the Langley Research Center. NASA TM X-1129, 1965.
2. New, John C.; and Timmins, A. R.: Effectiveness of Environment-Simulation Testing for Spacecraft. NASA TN D-4009, 1967.

TABLE I.- STANDARD DEPLOYMENT

[First test series; 5-foot-diameter, 10-foot-long thermal vacuum facility]

Test	Test pressure, torr	Sphere description	Inflation system	Remarks
1	64×10^{-3}	Standard 1-meter-diameter sphere	Std. aluminum capsule with 35 cc of iso-pentane	Sphere burst immediately with a tear developing from pole to pole
2	64×10^{-3}	Standard 1-meter-diameter sphere	Std. aluminum capsule with 35 cc of iso-pentane	2-inch-long tear in sphere. Inflated to full size but collapsed after $1\frac{1}{2}$ minutes
3	64×10^{-3}	Standard 1-meter-diameter sphere	Std. aluminum capsule with 35 cc of iso-pentane	3-inch-long tears in sphere. Inflated to full size but collapsed in less than 1 minute
4	64×10^{-3}	Standard 1-meter-diameter sphere	Std. aluminum capsule with air	Sphere inflated to full size by residual air. Sealed inflation capsule, no iso-pentane inside, broke through sphere wall
5	64×10^{-3}	Standard 1-meter-diameter sphere	Std. aluminum capsule with 35 cc of iso-pentane	Sphere burst immediately with a tear developing from pole to pole
6	64×10^{-3}	Standard 1-meter-diameter sphere	Std. aluminum capsule with 35 cc of iso-pentane	Sphere burst immediately with a tear developing from pole to pole

TABLE II.- MODIFIED DEPLOYMENT

[Second test series; 5-foot-diameter, 10-foot-long thermal vacuum facility]

Test	Test pressure, torr	Sphere description	Inflation system	Remarks
1	64×10^{-3}	Standard 1-meter-diameter sphere	Air trapped in sphere during folding	Sphere inflated to 1/4 size with residual air
2	64×10^{-3}	Standard 1-meter-diameter sphere	Air trapped in sphere during folding	Sphere inflated to 1/4 size with residual air
3	64×10^{-3}	Standard 1-meter-diameter sphere	Std. aluminum capsule with 35 cc of iso-pentane	Sphere inflated to full size in approximately 1/4 sec and maintained a stressed skin to a pressure of 8.3 torr
4	64×10^{-3}	Standard 1-meter-diameter sphere	Std. aluminum capsule with 35 cc of iso-pentane	Sphere inflated to full size in approximately 1/4 sec and maintained a stressed skin to a pressure of 8.3 torr

TABLE III.- MODIFIED DEPLOYMENT

[Third test series; 60-foot vacuum sphere]

Test	Test pressure, torr	Sphere description	Inflation system	Remarks
1	8.9×10^{-3}	Standard 1-meter-diameter sphere	Std. aluminum capsule with 35 cc of isopentane	Sphere did not inflate immediately because isopentane-capsule cap did not come off. Cap remained on capsule, but isopentane leaked into sphere over a 10-minute period and inflated it.
2	8.9×10^{-3}	Standard 1-meter-diameter sphere	Std. aluminum capsule with 35 cc of isopentane	Sphere did not inflate immediately because isopentane-capsule cap did not come off. Cap remained on capsule, but isopentane leaked into sphere over a 5-minute period and inflated it.
3	8.9×10^{-3}	Standard 1-meter-diameter sphere	Std. aluminum capsule with 35 cc of isopentane	This sphere inflated to full size immediately. Isopentane capsule functioned correctly. Sphere remained inflated to a pressure of 8.3 torr.
4	8.9×10^{-3}	Standard 1-meter-diameter sphere	Std. aluminum capsule with 35 cc of isopentane	Sphere did not inflate immediately. Cap came off inflation capsule after $1\frac{1}{2}$ minutes and sphere inflated to full size. Sphere remained inflated to a pressure of 8.3 torr. Steel lanyard between booster and nose cone broke in pulling bulkhead from nose cone.
5	8.9×10^{-3}	Standard 1-meter-diameter sphere	Std. aluminum capsule with 35 cc of isopentane	Deployment of the sphere was good, but the sphere fall rate was retarded by the snapback of the lanyard system. The dummy rocket motor overtook and hit the sphere. The cap did not come off the inflation capsule immediately, but inflation did occur in approximately $2\frac{1}{2}$ minutes. The sphere remained inflated to a pressure of 8.3 torr.
6	8.9×10^{-3}	Standard 1-meter-diameter sphere	Std. aluminum capsule with 35 cc of isopentane	Steel lanyard assembly broke at the dummy rocket motor. The sphere egressed from the nose cone, but the cap stayed on the inflation capsule, and the sphere did not inflate.

TABLE IV.- SUMMARY ANALYSIS OF FAILURE MODE AND EFFECTS FOR ROBIN SPHERE

Component	Function	Malfunction	Cause	Effect	Remarks
Mylar skin of Robin sphere	Contain inflation media and keep spherical shape	Leak	1. Pin holes due to handling or manufacturing. 2. Burn holes from separation charge. 3. Too rapid inflation causing structural damage. 4. Puncture from contacting the rocket motor or separating parts. 5. Sphere inflates out of nose cone contacting the metal rim of the nose cone.	Sphere failure or loss of data accuracy	Several instances were noted for the first three causes of failure. In approximately 1/3 of the tests the steel lanyard that removes the nose-cone bulkhead broke away from the rocket motor; in one of these instances the lanyard contacted the sphere causing a 1-inch long puncture. In the case of cause 5, the extent and cause of damage have not been determined.
Inflation-capsule container	Contain inflation media	Leak	Damage or assembly.	Sphere rupture	No incidents during these tests.
	Meter flow	1. No flow or slow flow 2. Flow too rapid	Freeze. Orifice size.	1. Partial inflation 2. Sphere rupture	Freezing noted in tests. No incidents of orifice problem.
Inflation media	Pressurize sphere	Insufficient pressure	Freeze or quantity too small.	Partial inflation	Freezing noted in tests. No incidents of quantity problem.
Inflation-capsule cap	Hold seal	1. Premature release 2. Stuck	Tolerance or damage.	1. Sphere rupture 2. No inflation	Tolerance noted to contribute to cap sticking.
Inflation-capsule pillow	Force cap off	1. Premature operation	Vacuum used during packing.	1. Sphere rupture	No incidents of premature operation.
		2. Insufficient force	Stroke too short. Not enough air. Leak in pillow.	2. No inflation	Insufficient force considered prime cause of inflation-capsule failure.
Inflation-capsule rubber gasket	Seal orifice	1. Leak	Improper assembly.	1. Sphere	No incidents of leaks.
		2. Orifice sealed with cap off	Rubber extruded into orifice. Rubber adheres to container.	2. No inflation	Extruding into orifice and adhering to container contribute to capsule failure.

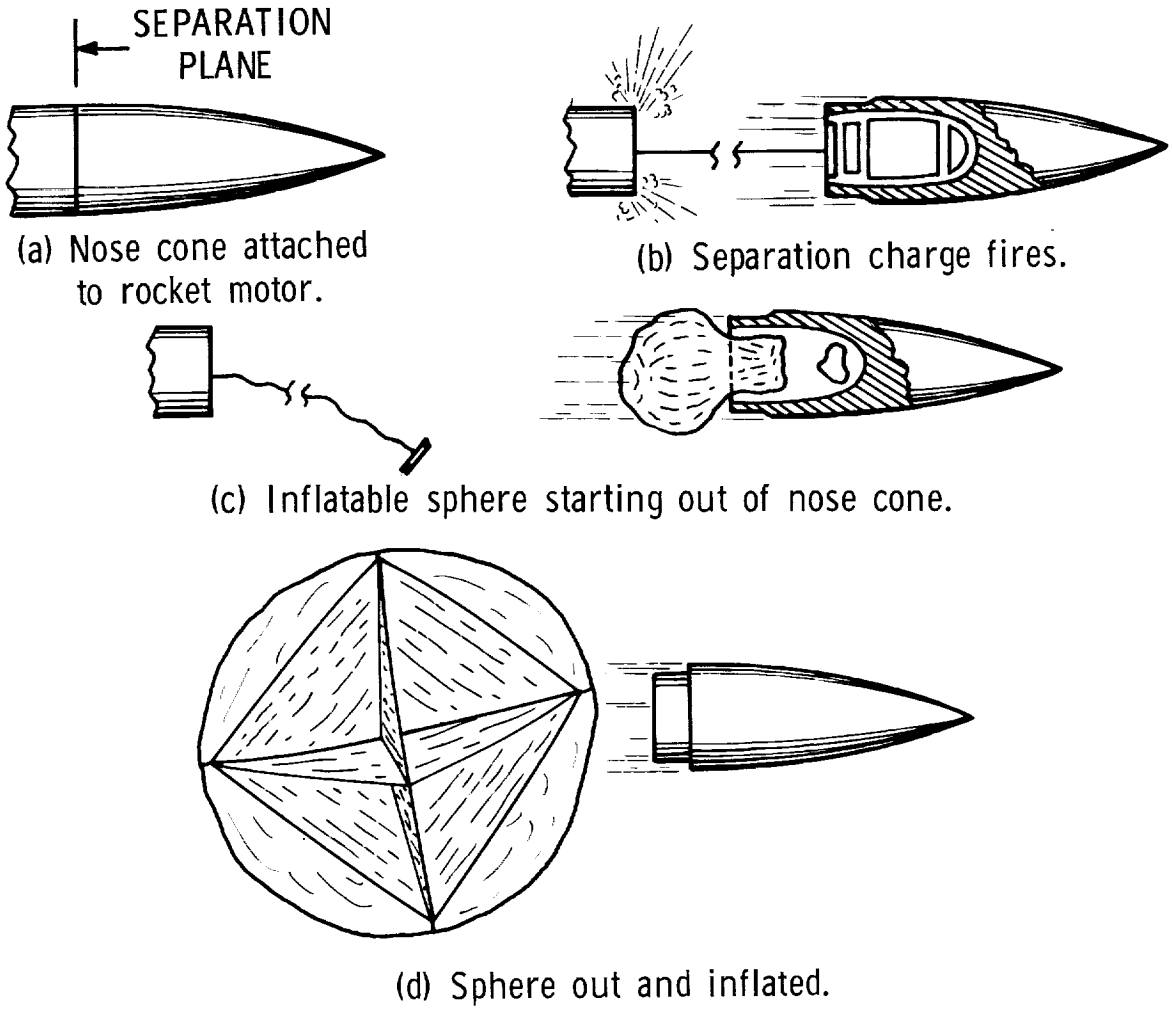

(a) Nose cone attached to rocket motor.

(b) Separation charge fires.

(c) Inflatable sphere starting out of nose cone.

(d) Sphere out and inflated.

Figure 1.- Sketch of standard Arcas-Robin deployment sequence.

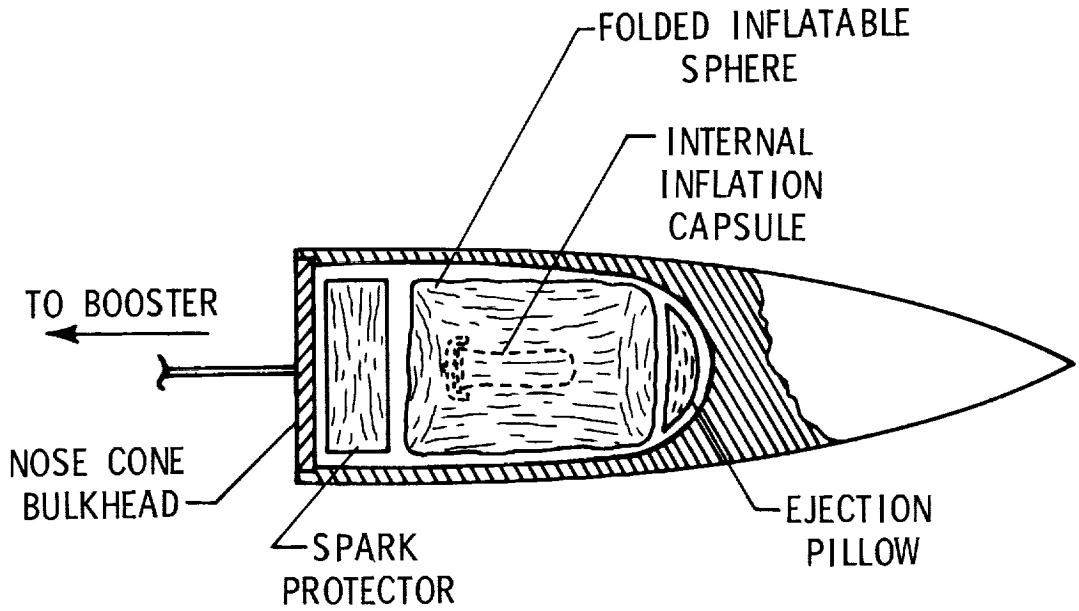

(a) Standard system.

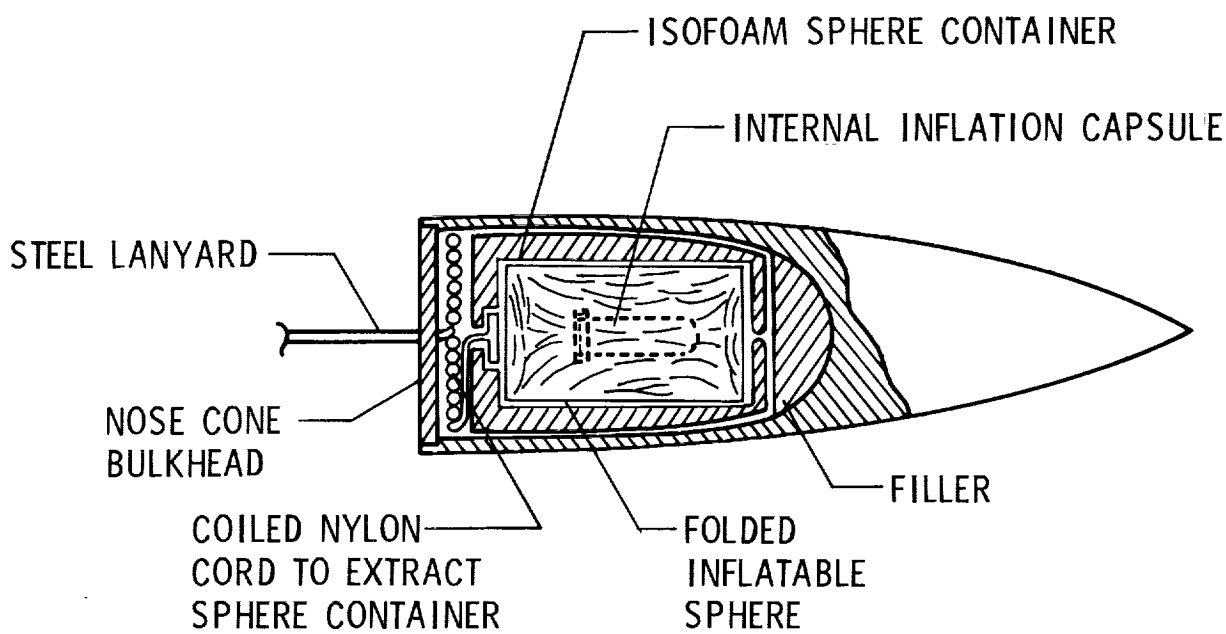

(b) Modified system.

Figure 2.- Standard and modified Arcas-Robin payload assembly.

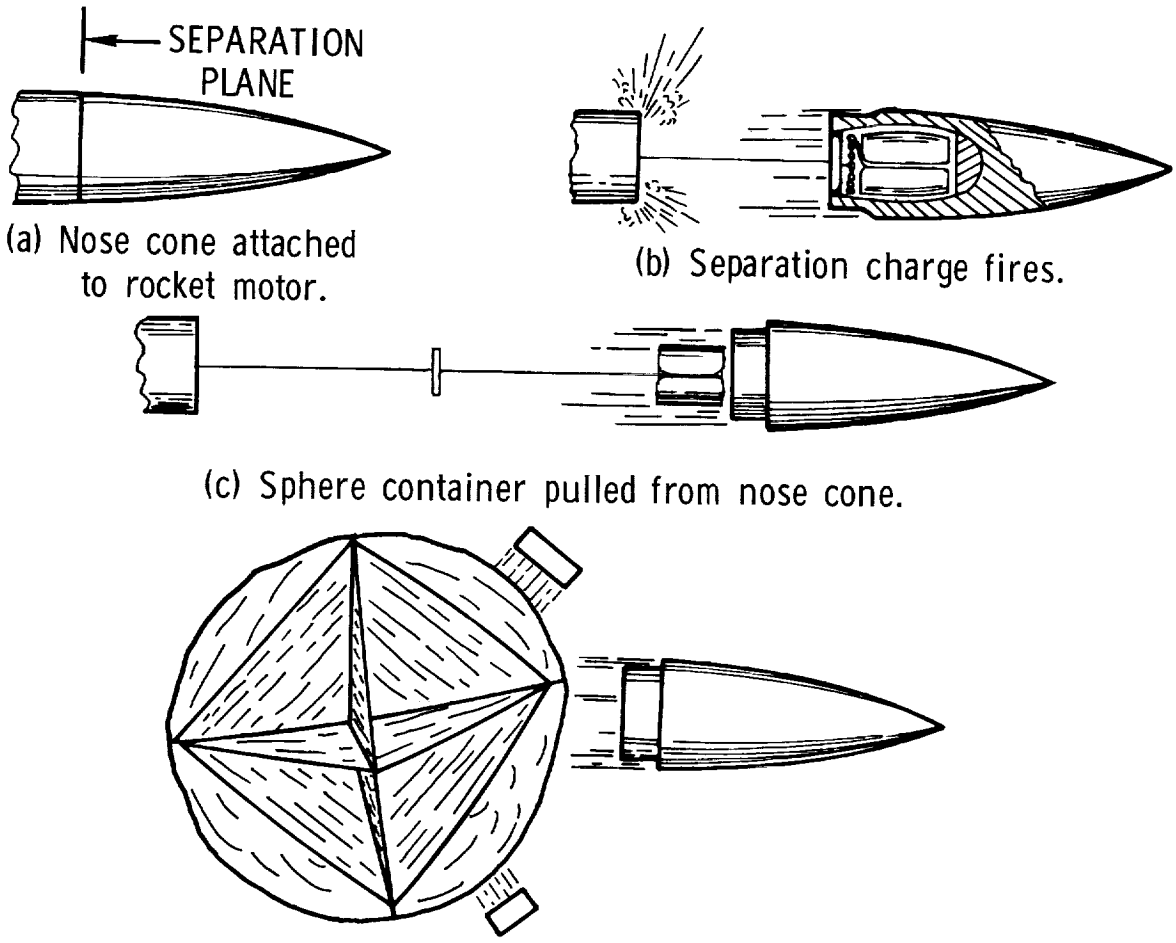

(a) Nose cone attached to rocket motor.

(b) Separation charge fires.

(c) Sphere container pulled from nose cone.

(d) Container separates and sphere inflates.

Figure 3.- Modified deployment sequence.

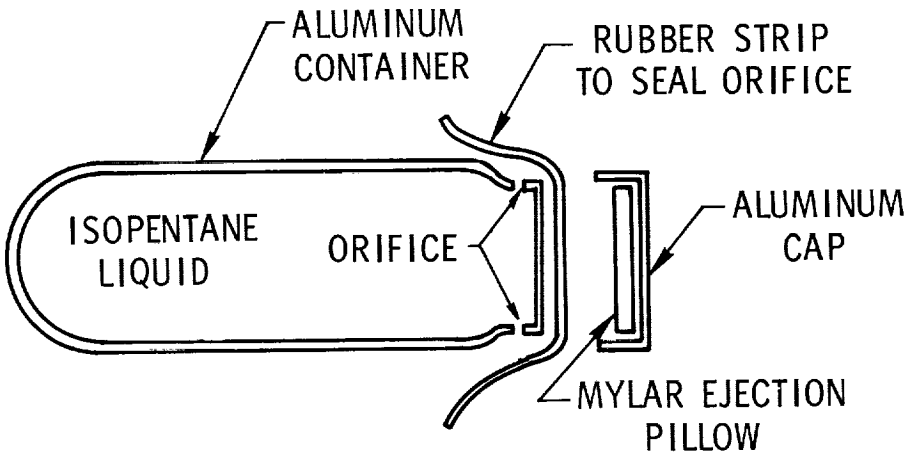

Figure 4.- Sketch of Arcas-Robin inflation capsule.

RECENT PASSIVE DENSITY SENSOR EFFORT AT THE NAVAL ORDNANCE LABORATORY

By George J. Sloan

U.S. Naval Ordnance Laboratory

3

The Naval Ordnance Laboratory has developed an atmospheric sounding system known as HASP, or High Altitude Sounding Projectile, capable of shipboard launching from a five-inch 38-caliber slow-fire gun. In this system, which is based upon the Loki antiaircraft rocket system, a three-inch-diameter booster is used to boost a dart vehicle to a velocity of about 5,000 feet per second in 1.9 seconds, at which time the booster separates, and the dart vehicle coasts to an altitude of 65 to 70 kilometers. For such a system to have good altitude capability, the dart must have a high sectional density. The normal HASP dart is therefore $1\frac{3}{8}$ inches in diameter, 40 inches long, and weighs eight to ten pounds, depending on the payload. The space available in such a dart is a compartment one inch in diameter and 20 inches in length, which is a volume of about 16 cubic inches. Efforts to develop a passive density sensor have been directed toward a system compatible with the small payload volume. It is the purpose of this paper to briefly describe the efforts to develop a useful passive density system for the HASP dart.

The first effort was directed toward use of the Robin sphere in the dart vehicle, but the Robin, as configured for the Arcas nose cone, simply would not fit the small dart compartment. It was necessary to reshape the isopentane capsule and remove the internal corner reflector to package the one-meter sphere in the 16-cubic-inch compartment. This configuration, called a Robinette, was constructed of half-mil metalized mylar for radar reflectivity and weighed 95 to 100 grams, or 20 to 25 grams less than the Robin. Flight tests of this configuration resulted in practically no useful data for several years of experimentation. Environmental tests conducted in the Langley Research Center 60-foot-diameter vacuum sphere in March 1964 revealed several important problems. The isopentane capsule, which incorporates an entrapped-air bag to displace the capsule cover similar to the Arcas Robin capsule, was not reliable. It was also discovered that hot particles from the expulsion charge were burning small holes in the sphere. These hot particles were not experienced in static firings at sea level since there is enough atmospheric oxygen to insure complete combustion within the dart. A reduction in the expulsion charge and a redesign of the charge holder eliminated the burning problem. The use of a sealed isopentane capsule, which is pierced by the force of the expulsion charge, proved to be a much more reliable inflation system.

Problems with sphere inflation with isopentane led to the concurrent development of a system of inflation of small spheres by entrapped air. Spheres of 12 to 16 inches

in diameter were inserted in the dart compartment, folded along the gore seams with the polar caps at the end of the tube-like compartment. Air was introduced at one end with a hand pump to expand the sphere to the maximum volume of the compartment, and then the inflation tube was sealed. Of course, half-mil mylar will leak any super pressure in several hours, but this method tends to maximize the volume of residual air at atmospheric pressure. Two types of construction of spheres were used, namely, construction with longitudinal gores with polar caps and a draped form construction of one-eighth sections of the sphere. In the gore construction, similar to Robin, the half-mil mylar was metalized for reflectivity. In the draped formed construction laminated half-mil material was used with an internal corner reflector.

Evaluation of sphere performance is usually made with the lambda check in the University of Dayton density program. All of the early Robinette flight tests were evaluated, using the Dayton program at LRC, and were rejected as collapsed at ejection. In order to evaluate the system from other than a go or no-go basis, a computer program was written by the NOL Mathematics Department which incorporated a unique feature for performance evaluation. In this program, the theoretical vertical velocity of the descending device is computed and then plotted, using the weight, dimensions, drag coefficient tables, and the 1962 standard atmosphere values of density and temperature. The vertical velocity, as obtained from the radar tape, is also plotted at the same time so a comparison can be made. Figure 1 is an example of a Robinette-type sphere ejected from a Cajun dart vehicle at an altitude of 308,000 feet. The vertical velocity profile is smooth and follows the theoretical curve down to an altitude of about 100,000 feet, at which time it appears to have collapsed. The density derived from these data is plotted as a ratio to the standard atmosphere density, Figure 2. Temperature is plotted on the same plot as the standard atmosphere values for a quick comparison, Figure 3. This is an example of a good flight with a one-meter Robinette in which data were obtained from 270,000 to 100,000 feet.

The performance of the 16-inch-diameter entrapped-air configurations can be evaluated from the velocity profile, Figure 4. Flight number 2990, flown 10 March 1967, is a good example of the 16-inch sphere of a normal longitudinal gore configuration. The fall-rate curve appears to follow the theoretical curve very well at the top end, but departs from it below 160,000 feet. Density data derived from these data were not satisfactory. Data from the 16-inch draped formed sphere, Figure 5, were completely unsatisfactory. This poor performance was probably due to the rough and inaccurate shape of the draped formed sphere. Some improvement could possibly have been made with further development of this construction technique.

In an effort to eliminate some of the problems of the use of inflatable spheres as passive density sensors, a development effort was started to develop a self-erecting

ram-air inflated configuration. As a result of this study, a biconical ram-air inflated balloon evolved, Figure 6. This configuration is comprised of a frustum of a 45° cone with a 28° cone extending the air inlet opening and the attached weight forward of the center of pressure. An octagonal shape of the top was selected, rather than circular, to preclude the generation of one large helical vortex which might generate a coning motion during descent. The aerodynamic characteristics of this device, determined by the University of Minnesota,* are presented in Figure 7 and illustrate why this shape was selected. The moment coefficient curve indicates excellent stability characteristics with no areas of neutral stability. The tangent-force coefficient curve indicates that there is virtually no change in coefficient with angle of attack for the small angles of attack which would be associated with the high degree of stability of the device.

From an aerodynamic standpoint this is an ideal shape; however, construction of such a shape has presented many problems since the shape is not determined entirely by the internal pressure. A construction, using quarter-mil mylar for the conical surfaces and internal supporting ribs with a one-mil roof panel, evolved from environmental testing as the construction which would produce the theoretical shape in free flight. However, free-flight tests showed good fall rate curves, but not with the same drag coefficient values as determined by the University of Minnesota. There was good agreement in performance among units manufactured at the same time, but poor agreement between manufacturing lots. Figure 8 illustrates this discrepancy between the theoretical fall rate and the actual performance. In an effort to improve this condition the configuration was changed to one without sharp corners, a shape that could be determined by the internal pressure. Such a shape is shown in figure 9. The performance of this configuration has been very satisfactory, as illustrated in Figure 10. However, the drag coefficients used for the theoretical fall rate are only estimated. Once a sufficient number of flight tests have been completed to establish reliability and reproducibility of this configuration, the actual drag coefficients will be determined.

Temperature-sensing instrumentation is also undergoing further development with the HASP system. Instrumentation currently under evaluation has a total weight of less than six ounces. It is the ultimate objective to combine the density sensor and instrumentation to derive density from fall rate and measure the temperature. The fall-rate curve in Figure 10 is such a combination. With the lightweight instrumentation the fall rate is approximately half of that of a Robin sphere, which should provide a more sensitive wind and density sensor than the Robin in the upper atmosphere, i.e., above 40 kilometers.

---

*U.S. Air Force Contract No. F33615-67-C-1010.

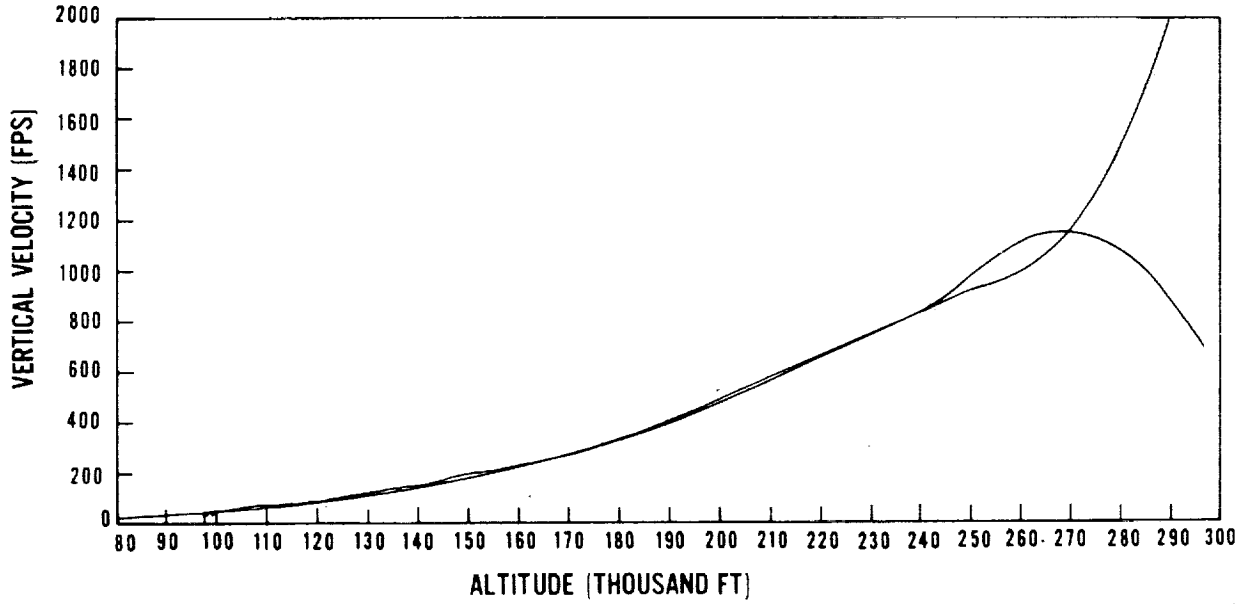

Figure 1.- Experimental and theoretical vertical velocities of 1-meter Robinette sphere (model 2290) ejected from a Cajun dart vehicle at an altitude of 308,000 feet, 5 May 1966.

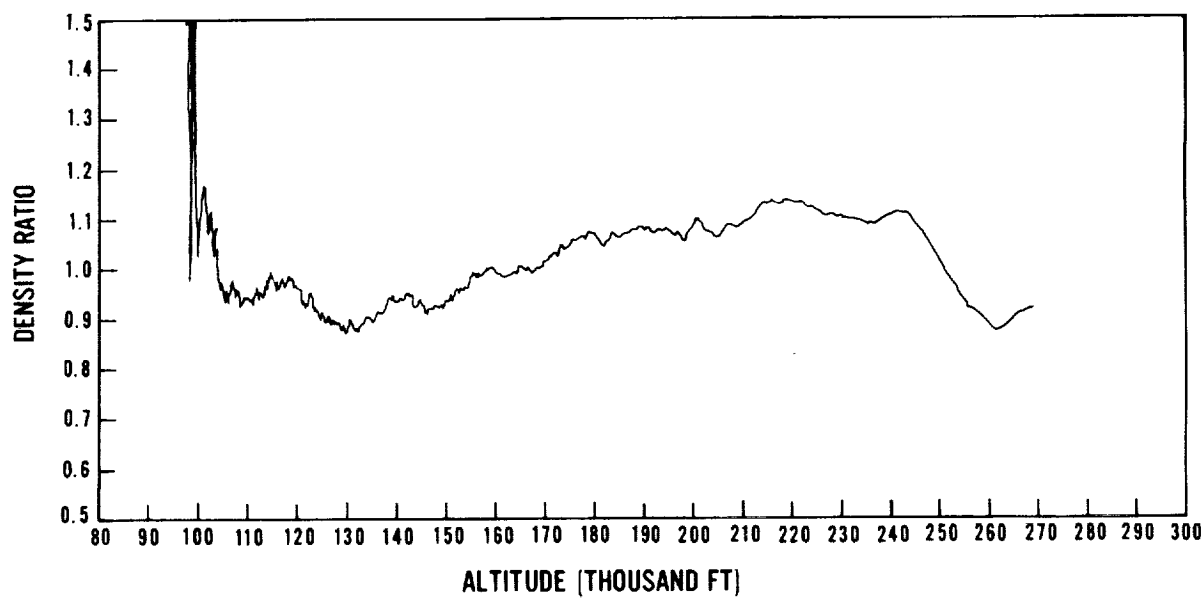

Figure 2.- Ratio of density derived from data of figure 1 to standard-atmosphere density.

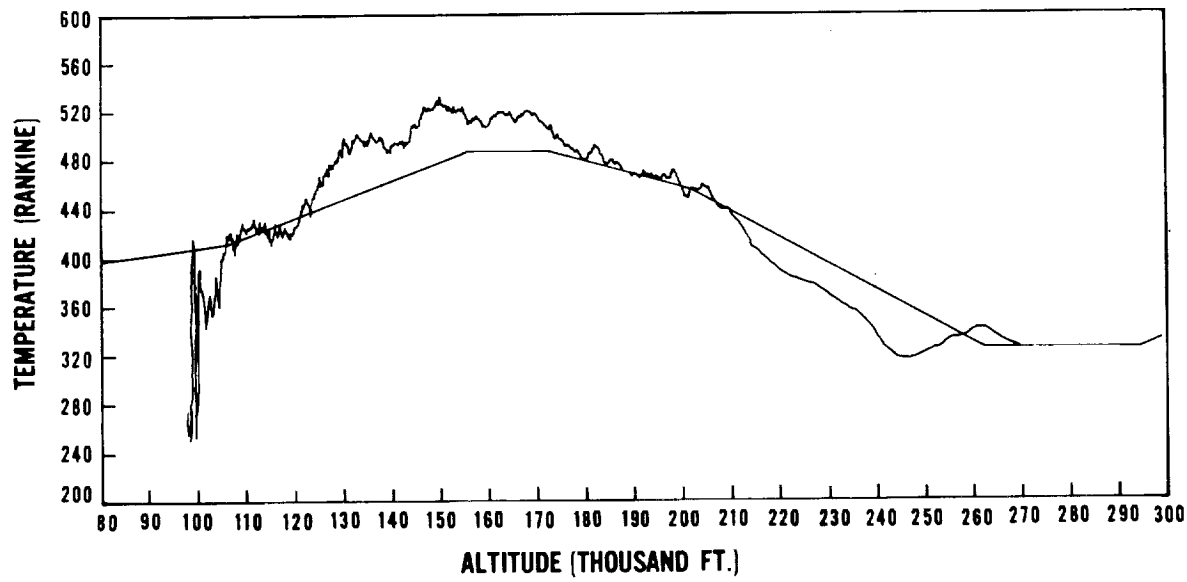

Figure 3.- Experimental and standard-atmosphere temperatures for flight test of figure 1.

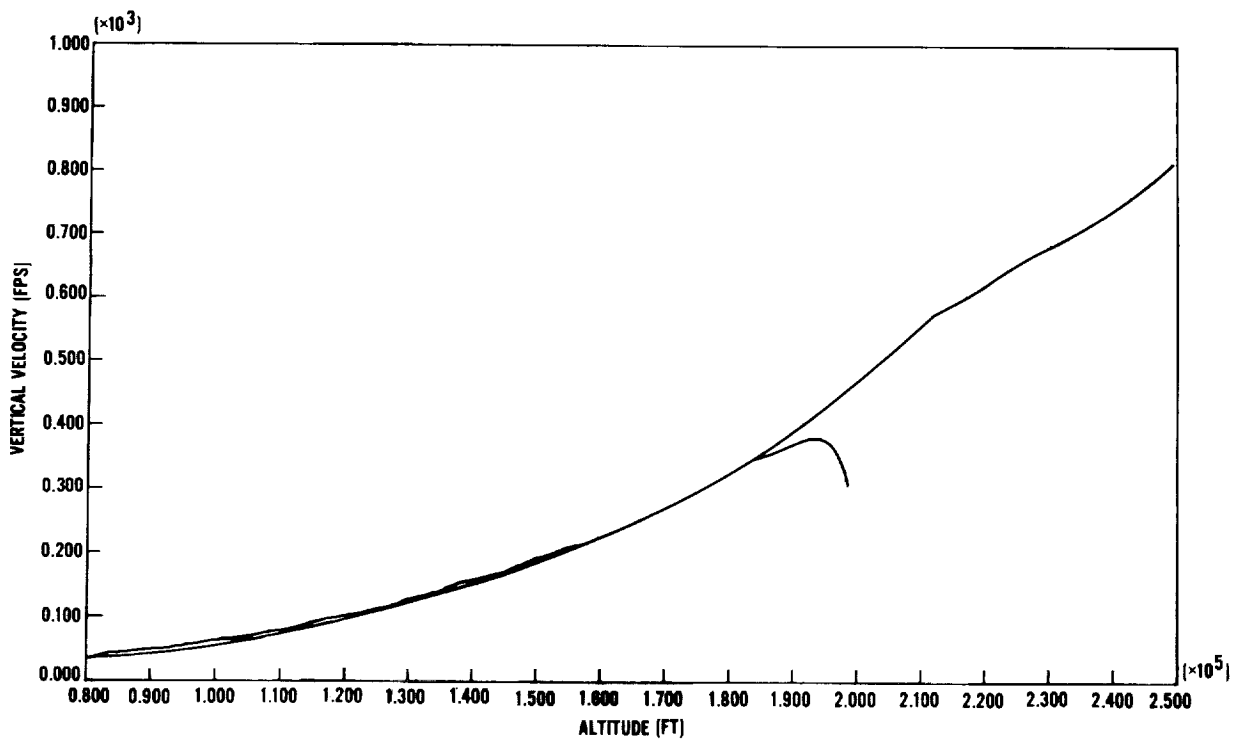

Figure 4.- Experimental and theoretical vertical velocities of 16-inch entrapped-air sphere with longitudinal gores and mass of 16.9 grams (model 2990), 10 March 1967.

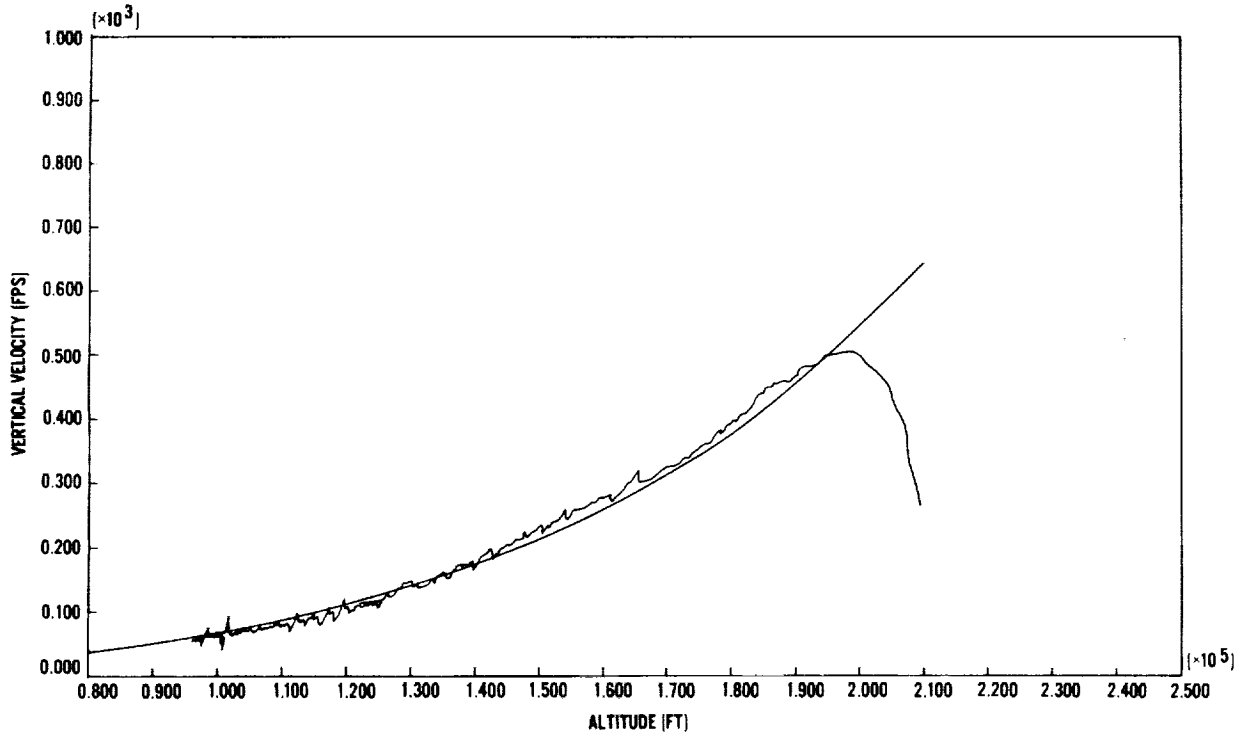

Figure 5.- Experimental and theoretical vertical velocities of 16-inch entrapped-air sphere of draped formed construction with mass of 0.0495 pound (model 2127).

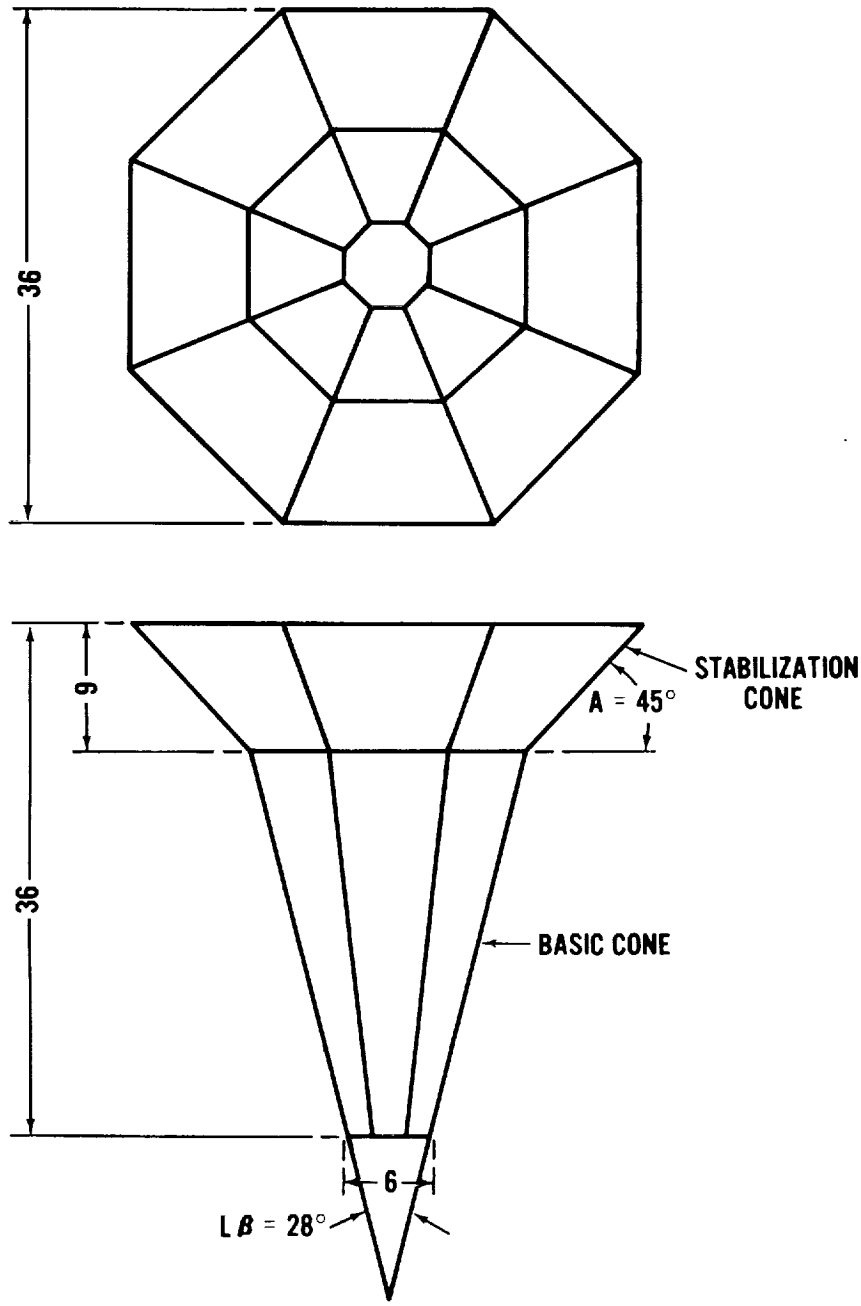

Figure 6.- Self-erecting biconical ram-air-inflated balloon.

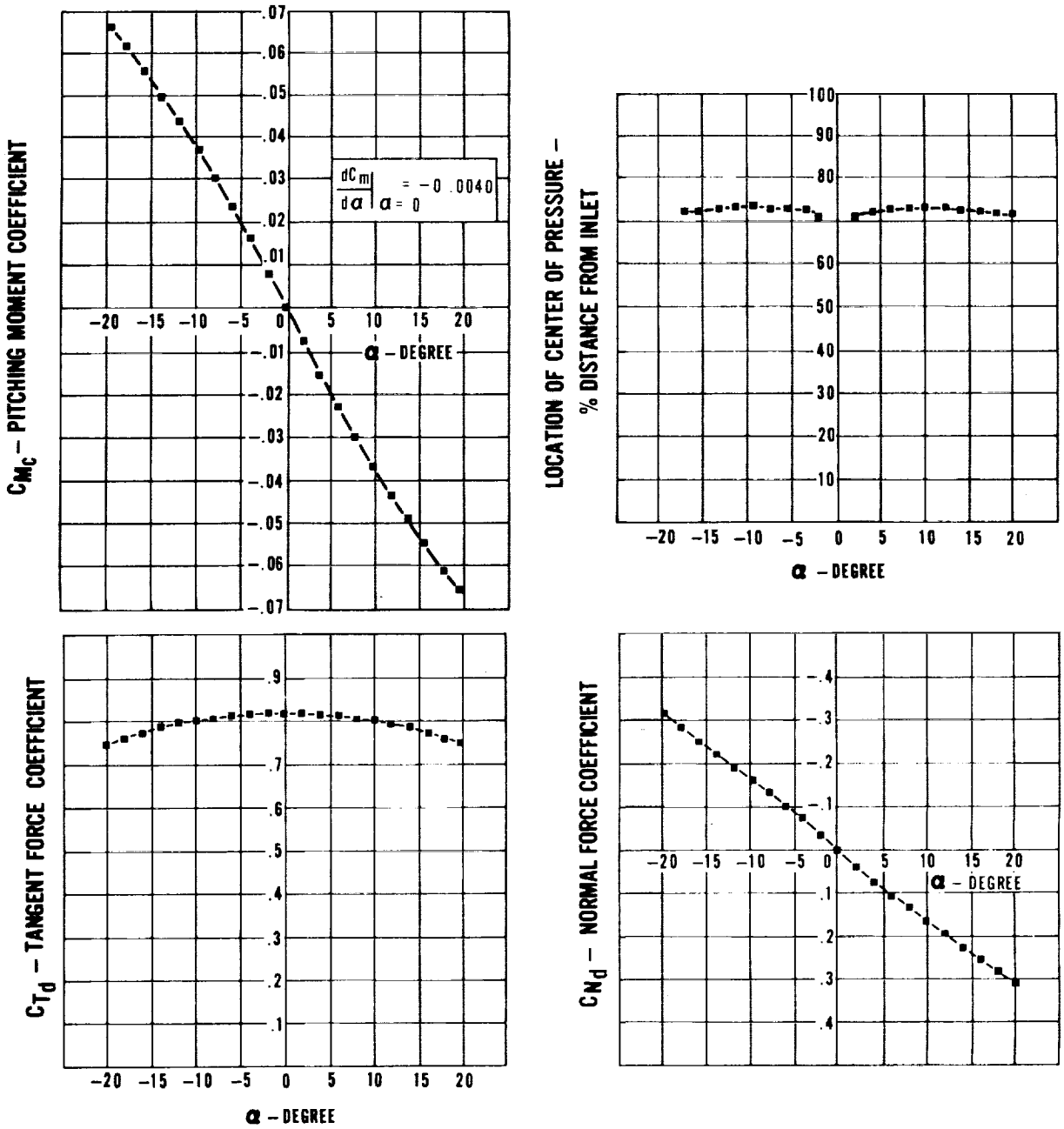

Figure 7.- Aerodynamic characteristics of configuration of figure 6.

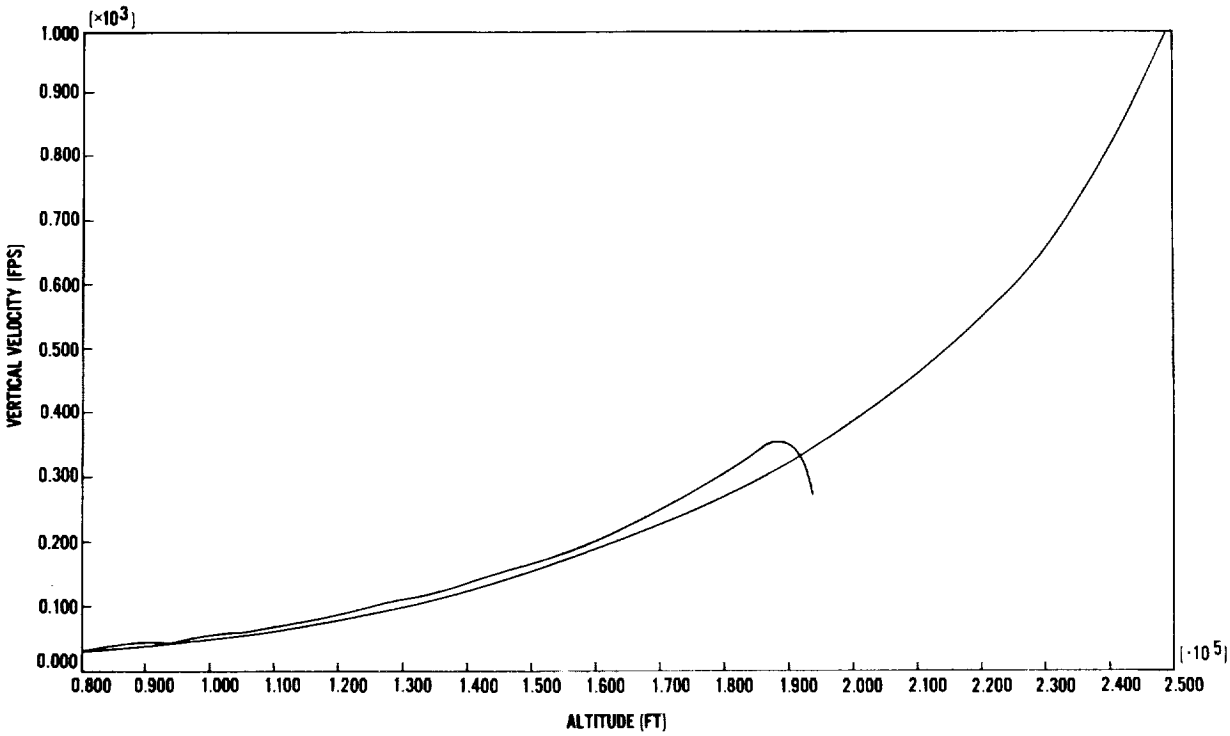

Figure 8.- Experimental and theoretical vertical velocities of configuration of figure 6 with mass of 0.23105 pound (model 3296).

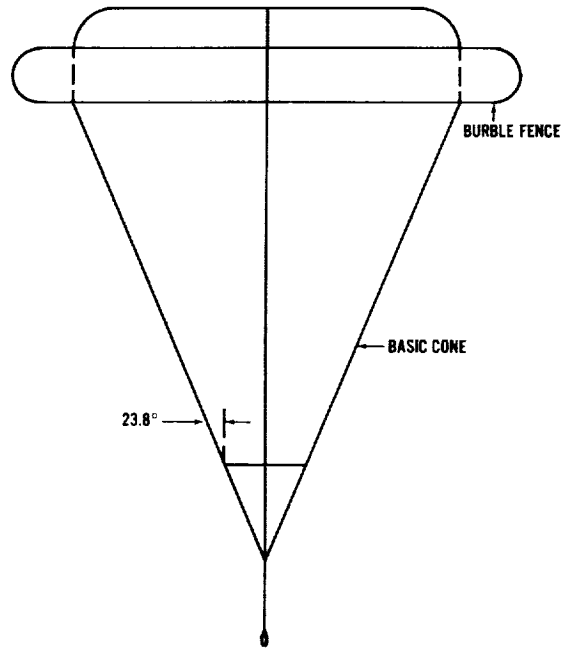

Figure 9.- Revised version of configuration of figure 6.

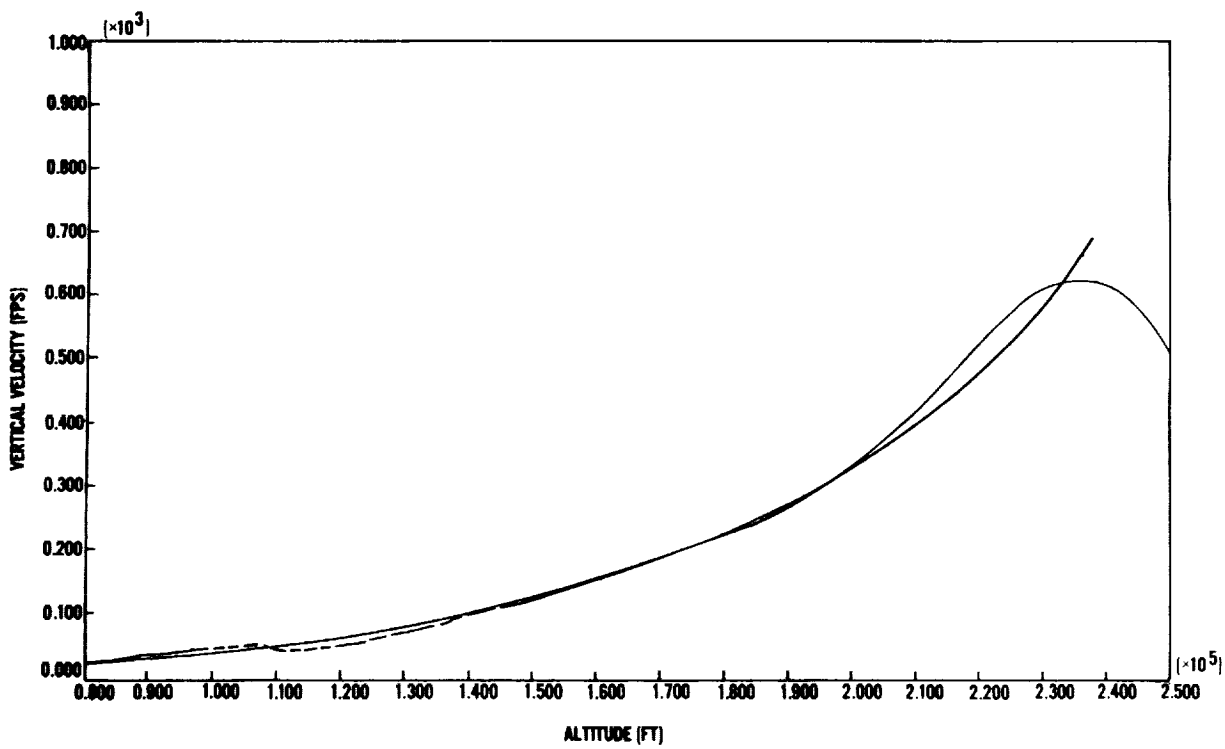

Figure 10.- Experimental and theoretical vertical velocities of configuration of figure 9 (model 4180), 2 May 1969.

OPERATIONAL EXPERIENCE WITH PASSIVE FALLING SPHERES ON THE AFETR*

By O. H. Daniel

Pan American World Airways, Inc.
Aerospace Services Division
Patrick AFB, Fla.

The use of small rockets to measure meteorological parameters above the altitude limits of the balloon rawinsonde systems began on the Air Force Eastern Test Range (AFETR) in 1957. The Range at that time was known as the Atlantic Missile Range and the first meteorological rockets used were of the Loki II type with radar-reflective-chaff payloads. The Army Ballistic Missile Agency at Huntsville, Alabama, the range user, conducted their own launch operations during the early part of their program. The high-altitude data were needed at that time to assess the environmental conditions affecting the R & D testing of the Jupiter and Redstone rocket systems.

In 1959, the Air Force Cambridge Research Laboratories (AFCRL) implemented a development program to try and improve the performance of the Loki II meteorological rocket. Their version of this system was called the Overrange Wind Logging system (OWL) and also used a radar-reflective-chaff payload. Data for altitudes as high as 250 000 ft were required in 1959 and 1960 for programs such as testing of the Atlas and Titan missile systems. This was somewhat above the altitude capability of the Loki II system when launched from sea level. The effort to improve the performance of the system was not significantly successful and therefore was discontinued after a short flight-test series.

During the same period the Office of Naval Research was engaged in a development effort to develop the meteorological rocket system which became known as the Arcas. This development effort was also supported by the Air Force and Army. The Air Force Cambridge Research Laboratories developed the inflatable falling-sphere payload (Robin) for use with the Arcas rocket, while at approximately the same time, the Army was developing various configurations of parachute-borne sonde payloads, also for use with the Arcas.

The first flight tests of the Arcas/Robin system were conducted on the AFETR in 1959. This series consisted of 25 systems, 13 of which properly deployed the Robin sphere at or near apogee. The average apogee altitude reached by these 13 systems was over 200 000 ft. A number of the remaining 12 systems ejected the sphere successfully,

*Activities reported upon in this paper were performed under contract to the Air Force Eastern Test Range, Air Force Systems Command.

although various malfunctions occurred with the payload, such as rupture and partial inflation. During the period 1960 through 1961 the Arcas rocket system was used interspersed with Loki II chaff systems. The payloads used with the Arcas at that time were mainly Delta, Gamma, and AN/DMQ-6 sondes developed by the Army and furnished to the AFETR to support the early Meteorological Rocket Network (MRN) effort. Concurrently, other series of flight tests of the Arcas/Robin system were conducted at Eglin AFB, Holloman AFB, and NASA Wallops Station.

To provide some idea of the Arcas/Robin performance of the system during the 1960-61 period, the 104 systems launched at Eglin AFB produced usable density data in 40 cases. The average apogee altitude of the 104 systems launched was 226 000 feet. Of the systems which produced usable density data, the average layer thickness of the density data was 69 000 feet. The average lower altitude limit of the density data for the 40 successful systems was 142 000 feet. The Arcas/Robins launched at Holloman and Wallops Station resulted in somewhat lower performance for the Robin sphere than that obtained at Eglin AFB during this period.

Beginning in late 1961, a number of Arcas/Robin systems were procured by the Air Force and made available for both missile test support and MRN activities. Fifty-six of these systems were launched in 1962 of which 45 produced usable density data. In 1963, 72 systems were launched, 48 of which produced usable density data. Thirty-four systems were launched on the AFETR in 1964, 31 of which were completely successful. The average apogee altitude for these three years of operation with the Arcas/Robin system was approximately 212 000 feet. The average lower limit for the usable density data obtained was about 145 000 feet. In 1965, 101 Arcas/Robins were launched, 89 of which produced usable density data for an 88-percent success rate. The average apogee altitude reached by these 101 launches was 210 000 feet, and the lower limit for the usable density data still averaged near 145 000 feet.

During the period 1962 through 1965, the Arcas/Robin systems were used primarily for MRN support. Several of the missile test programs on the Range during that period had stringent requirements for wind, density, temperature, and pressure data from the surface to about 250 000 feet. The Arcas/Robin system was performing well and producing what appeared to be good density and wind data in the region of from 145 000 to 200 000 feet. However, a severe gap in the density data existed between the upper limit of the rawinsonde observations at about 105 000 feet and the average Robin balloon collapse altitude near 145 000 feet. The acquisition of density and temperature data in the intervening 40 000-foot layer was significantly more important than the acquisition of the data to altitudes above 200 000 feet. This is because of the obviously greater effects of the atmosphere on missile system performance at the lower altitudes.

From the early days of the development of the Robin sphere payload for the Arcas rocket, there were several reservations in the minds of meteorologists at the AFETR regarding the reliability of the density data being obtained. These reservations stemmed from our experience with numerous chaff payload launches, which on many occasions seemed to indicate the presence of significant vertical components to the high-altitude wind field. This, in our opinion at that time, caused uncertainties in the mean layer densities computed from the Robin data. We suspected other uncertainties in the data caused by the questionable reliability of drag information available at that time for use in the data-reduction routine. Several times during the development of the Robin data-reduction process, changes in drag data were made as a result of additional data analyses and study. This had the effect of changing density values previously computed by several percentage points and, in one case, by a range of from 10 to 15 percent.

Some of the AFETR test programs required temperature data for use in evaluation of heat-transfer processes in the development testing of ablative materials and reentry vehicles. A particular program having important needs for density and temperature data in the critical region from 100 000 to 200 000 feet was the aerothermodynamic structural systems environmental test (ASSET) program. Since these data requirements were not being met by the Arcas/Robin system, the launch sites that were activated at Eleuthera, San Salvador, Grand Turk, and Antigua to support this program used the Arcas rockets with sonde-type payloads.

During the mid-1960's, a sonde payload was developed for the Loki II meteorological rocket system. There was also a Robin payload adapted to the Loki system but this was never employed on the AFETR. With the advent of the sonde payload for the low-cost Loki system and its marked advantage over the Robin in the measurement region between 100 000 and 150 000 feet, nearly all test support data since 1965 have been provided on the AFETR by sonde-type payloads with either the Arcas or Loki II rockets. The exception to this has been the use of the Viper-Dart-Robin system to acquire data above 200 000 ft. Some of our MRN requirements have been partially met by the use of Arcas rockets with outdated Robin payloads which were not expected to inflate properly for density determinations but were used only for wind measurements.

The Viper-Dart rocket system with Robin payload became available for use on the ETR in the fall of 1968 in time to support the high-altitude data requirements of the Apollo 7 launch from Cape Kennedy. The Viper systems used on the ETR during the past year have been a combination of developmental flight-test models launched in support of an AFCRL development project and a quantity of preproduction models purchased by the ETR for Apollo launch support.

For the Apollo support, density and wind data to 295 000 feet are required. At the present time, the Viper-Dart vehicle with a Robin payload is the only near-operational

system capable of supplying these data to this altitude. Of 20 similarly configured Viper-Dart systems with Robin payloads, 12 produced the required wind and density data to 295 000 feet. The average apogee altitude achieved by these 12 systems was 430 000 feet, and the average lower limit of usable density data was about 170 000 feet. The average thickness of the layer through which density data were obtained was therefore 125 000 ft. Wind data were generally usable beginning at about 20 000 feet above the altitude for the usable density data, and of course, the wind data were obtained well below the minimum altitude for the density data by continuing to track the partially collapsed sphere.

Of the eight systems which failed to produce the required data, three failed because of no inflation of the sphere; one, because of a motor malfunction; one, because of no payload separation; and three, because of late radar acquisition of the payload.

We plan to continue the use of the Viper-Dart system with the standard Robin payload during the immediate future to obtain density and wind data above the altitude of the Loki-Dartsonde system. By using Rawinsonde, Loki-Dartsonde and Viper-Dart-Robin systems, complete profiles of winds and densities are obtained to approximately 295 000 feet, with additional parameters such as temperature and pressure being obtained from the surface to the top of the Loki-Dartsonde profile at about 200 000 feet.

The data from the three different observations, Rawinsonde, Dartsonde, and Robin, display remarkable agreement in the overlap regions. One area presently causing some difficulty is in the transonic-fall-rate region of the high-altitude Robin system where some unusual oscillation in the density profile is evident. Recent investigations of this problem by AFCRL and the University of Dayton Research Institute have resulted in the experimental use of some revised drag data which, in most cases, seems to improve the consistency of the computed density in the area of concern. The fall rate of the Robin sphere when deployed at above 400 000 feet with the Viper-Dart rocket system is transonic at approximately 233 000 feet. The layer of questionable density data usually extends over several thousand feet on either side of this point, though predominantly on the subsonic side. In general, density data computed throughout the altitudes where the sphere is falling supersonically appear quite consistent, which seems to suggest somewhat more reliable data than those obtained in the subsonic-fall-rate region.

CAPABILITY OF NOL BALLISTICS RANGES FOR OBTAINING SPHERE DRAG COEFFICIENT DATA

By W. Carson Lyons, Jr.

U. S. Naval Ordnance Laboratory, White Oak

SUMMARY

Descriptions of three ballistics range facilities at the Naval Ordnance Laboratory are presented. The Mach number-Reynolds number capability for each facility is shown for the case of obtaining drag coefficients of spheres. It is shown that these three facilities can cover most of the Mach number-Reynolds number field between Mach numbers of 0.1 and 22 and between Reynolds numbers of 10^1 and 10^7. A discussion of various sources of errors involved in measuring sphere drag coefficients in a ballistics range and of estimates of the magnitude of the errors is presented.

5

INTRODUCTION

The well-equipped, modern, ballistics range represents a unique facility for determining the aerodynamic drag and stability characteristics of projectiles in free flight. These projectiles can be intricate models of full-scale vehicles, full-scale armament projectiles, or a very simple aerodynamic shape, such as a sphere. Part of the uniqueness of this type of facility is the wide range of test conditions that can be achieved for the simulation of various flight environments. Of the various measurements that can be made in a ballistics range, the drag coefficient is determined with the highest degree of accuracy.

Although there are many ballistics ranges in operation in the United States, the three aerodynamic-aerophysics ranges at the Naval Ordnance Laboratory form a good representation of ballistics range capabilities. Therefore, no attempt will be made to present a survey of ballistics ranges and their capabilities in general. Most of the discussion of measurements of drag coefficients will apply to any model configuration, although, where it is necessary to be more specific, only the determination of the drag of spheres will be considered.

SYMBOLS

a	speed of sound or semimajor axis of an ellipse
A	reference area
b	semiminor axis of an ellipse
c	constant in linear drag coefficient relation; Eq. (8)
C_D	drag coefficient
C_{p_M}	maximum pressure coefficient
f	constant in linear drag coefficient relation; Eq. (8)
g	acceleration of gravity
m	mass of projectile
M	Mach number
Re	Reynolds number
Re_d	Reynolds number based on sphere diameter
t	time
V	velocity
W	weight of projectile
Y	vertical distance in the ballistics range measured from range centerline
Z	longitudinal distance in the ballistics range
β	ballistic parameter (W/C_DA)
ρ	gas density
σ	standard deviation

Subscripts:

m	indicates midrange conditions
o	indicates initial conditions
∞	indicates free-stream conditions

DESCRIPTION OF FACILITIES

There are three ballistics ranges currently being operated at the Naval Ordnance Laboratory suitable for making either drag or drag and stability measurements. They vary from a small, 5-inch-diameter, 300-foot-long facility referred to as the Aerophysics Range to the largest of NOL's range facilities, which is 10 feet in diameter and 1000 feet long, referred to as the 1000-foot Hyperballistics Range. The third facility, an intermediate size facility, is called the Pressurized Ballistics Range. A description of each of these three facilities, their instrumentation, and their testing capabilities will be presented.

1000-Foot Hyperballistics Range (HBR)

This facility consists of a 10-foot-diameter, 1000-foot-long steel tube. Models are launched into this testing chamber using a two-stage, light gas gun. An artist's drawing of the launcher and a portion of the steel tube and supporting structure is shown in figure 1. The ambient pressure of the air within the 1000-foot-long test chamber can be varied from one atmosphere down to approximately 0.5 torr. The temperature of the air in the tube is maintained at approximately 65°F. Although most tests are conducted in air, a nitrogen atmosphere can be substituted for tests that require pressures of only 200 torr or less.

Instrumentation for conducting drag and stability tests currently includes 37 dual-plane spark shadowgraph stations covering a testing length of 870 feet. Figure 2 is a photograph of the inside of the 10-foot-diameter tube showing some of these stations. Each station consists of two barium-titanate spark light sources, two cameras, two 4-foot-diameter spherical reflectors, and a model detection system. A schematic drawing of one of these stations is shown in figure 3. It is seen from this drawing that, although the range tube is 10 feet in diameter, the usable cross section is approximately a 22-inch-diameter circle in the center of the tube. The model detection system with which each of the 37 shadowgraph stations is equipped detects the model and activates the spark light source when the model is in the field of view of the station. This system has sufficient sensitivity to detect spheres as small as 3/16 inch flying in this facility.

The model launcher used with this facility is a two-stage, light gas gun currently having a 2-inch, smooth-bore launch tube, 80 feet long. A 4-inch-inside-diameter launch tube is also available for this gun. Hydrogen is used as the working gas to launch the models. Slender conical models have been launched at velocities in excess of 25,000 ft/sec. Spheres can be launched at even higher velocities.

The first 80 feet of the 1000-foot test chamber are separated from the remainder of the range by a bulkhead having a 13-inch-diameter hole on the range centerline. This 13-inch hole is further restricted to 3 inches for most tests. This section of the range is referred to as the blast tank and is used to catch the hydrogen following the model out of the gun barrel. The sabot used in launching the model is stripped from the model and impacts in this section. Three short-duration X-ray stations are mounted in this section to monitor the separation of the sabot from the model and to determine the structural integrity of the model after undergoing the high-acceleration phase of launching. The stations are located 6.5, 16.5 and 26.5 feet from the gun muzzle.

Pressurized Ballistics Range (PBR)

The Pressurized Ballistics Range utilizes a steel tube, 300 feet long and 3 feet in diameter, as a test chamber. A variety of guns can be mounted at one end of this tube for launching models. The pressure of the test gas within this facility can be adjusted from five atmospheres to approximately two torr. Except for a 20-foot-long special instrumentation section, the temperature of the gas in this range is maintained at 74°F. In the 20-foot-long special instrumentation section, the temperature can be varied from -280° to +1000°F. Tests in gases other than air can readily be conducted in this facility (ref. 1). A gas chromatograph and a mass spectrometer are available for monitoring the constituents of the test gas at five locations along the tube.

Twenty-seven dual-plane shadowgraph stations are used to determine the trajectory of a model flying in the range. The stations cover a usable testing length of 188 feet. These stations are directly illuminated shadowgraphs. A short-duration spark light source on one side of the range tube directly illuminates a vertical, 14x17-inch glass photographic plate. Light from this single light source is reflected off a flat-faced mirror at the top of the tube to illuminate a horizontal photographic plate located at the bottom of the tube. This results in a set of pictures of the model in orthogonal planes at each of the 27 stations. A sketch of one of these stations is shown in figure 4. Each station is equipped with a model detection and triggering system.

For velocities up to approximately 5000 ft/sec, several different size powder-driven guns are available for model launching. Velocities greater than 5000 ft/sec require the use of a two-stage, light gas gun. This gun can launch models at velocities up to approximately 22,000 ft/sec and has a 1.3-inch-inside-diameter launch tube.

This facility is equipped with a blast tank in which the sabot is stripped from the model and in which most of the driving gases are retained. Two X-ray stations in the blast tank monitor the separation of the sabot from the model shortly after they emerge from the gun muzzle.

Aerophysics Range (APR)

The Aerophysics Range consists of a 5-inch-diameter test chamber, 350 feet long. Models are launched down this tube using a two-stage, light gas gun. The pressure of the test gas in this facility can be controlled from one atmosphere down to 0.2 torr. The test gas is also maintained at room temperature. A photograph of this facility is shown in figure 5. Because of the small volume of this test chamber, various test gases can conveniently be used.

The instrumentation in this facility for measuring drag coefficients consists of four single-plane, high-resolution, rotating-mirror camera stations and associated detection and triggering units.

Velocities up to 23,000 ft/sec are achieved with a two-stage, light gas gun having a smooth-bore barrel 0.375 inch in diameter.

The initial 18 feet of the range tube form the blast tank for this facility. As described for the other two facilities, the sabot is removed from the model and captured in this chamber.

TEST CONDITIONS

The drag coefficient of a sphere has been discussed thoroughly by many authors and investigators (for example, refs. 2, 3, and 4). The purpose of this current discussion will be to reiterate the pertinent similarity parameters for different flow regimes that must be duplicated when performing scaled experiments in ground-based test facilities.

Flow regimes can be specified as indicated by Tsien (ref. 5) by ratios of the Mach number to Reynolds number functions. These flow regimes are illustrated in figure 6. The continuum flow regime is represented by the two regions defined by $M/\sqrt{Re} \leq 0.1$. The ordinary gas dynamic regime is a continuum flow regime where it is assumed that "no slip" (zero fluid velocity) occurs at a body surface, while, in the slip flow regime, the flow is considered continuum but a finite velocity is assumed to exist at a body surface. For values of $M/Re \geq 10$ (this is representative

of large Knudsen numbers), the flow is considered in the free molecular regime. Between the slip flow continuum regime and the free molecular regime, there is a transitional region.

Within these flow regimes sphere velocities can be subsonic, supersonic, or in the transonic region. It can be shown, in general, that to duplicate the drag coefficient of a sphere, it is sufficient to duplicate the Mach number and the Reynolds number. In rarefied gas flow regimes, the Knudsen number is a significant parameter. However, the Knudsen number can be expressed approximately as a Mach number-Reynolds number function.

Figure 7 is a plot of the drag coefficient for a sphere as a function of Mach number, for continuum flow. The two branches of the curve in the subsonic region reflect the difference in the drag coefficient for a subcritical and a supercritical Reynolds number. The curves in figure 7 were compiled from information in reference 2.

One current use of accurate measurements of drag coefficients of spheres is in the determination of the atmospheric density at various altitudes from descending sphere experiments. In these experiments spheres are launched to high altitudes, released, and allowed to fall. The trajectory of the sphere is then determined, usually by radar tracking. Since the trajectory of the sphere is uniquely a function of the atmospheric density and the ballistic parameter (W/C_DA) of the sphere, accurate measurements of the drag coefficient, weight, and size of the sphere, along with the trajectory information, allow the density to be determined. To illustrate Mach numbers and corresponding Reynolds numbers for a typical free-fall balloon trajectory, calculations have been performed for three different size-weight combination balloons. For all three cases trajectories were calculated by assuming that the spheres started falling with zero velocity from an altitude of 300,000 feet. During actual tests two of the balloon systems are carried to their release altitude using a Nike-Cajun sounding rocket. The one-meter balloon is part of the Robin system. The Mach number-Reynolds number trajectory resulting from these calculations is presented in figure 8. Although the maximum Mach number attained during the flight of any of these three example spheres does not exceed 3, nor the Reynolds number exceed 1×10^6, tests in a ballistics range can be conducted at much higher Mach numbers and slightly higher Reynolds numbers.

From the discussion on drag coefficients it was shown that, except for a few certain flow regimes, both the Mach number and the Reynolds number must be duplicated when performing scaled-model tests to determine the drag coefficient for spheres. It is, therefore, appropriate to show the Mach number-Reynolds number field which can be covered by the three ballistics range

facilities described earlier. The Mach number that can be attained in a ballistics range is only a function of the flight velocity of the projectile. The temperature of the test gas, and hence the speed of sound in the test gas, is essentially a fixed value. For air at room temperature, the speed of sound is approximately 1140 ft/sec. Hence, $M_\infty = V_\infty/1140$, where V_∞ is expressed in feet per second. The pressure of the air in a ballistics range can be set at any desired value, commensurate with the pumping capability and structural strength of the test chamber, and is independent from the flight Mach number. Since the temperature is essentially a fixed value, the Reynolds number can be expressed for room temperature air as

$$Re_d = 0.57\ P_\infty M_\infty\ d \times 10^6 \tag{1}$$

where P_∞ is expressed in atmospheres and the sphere diameter, d, in inches. The maximum-diameter sphere that can be launched at various Mach numbers in the Hyperballistics Range and the Pressurized Ballistics Range is shown in figure 9. These sphere diameters were used in computing the maximum Reynolds numbers that can be achieved.

The maximum and minimum Mach number-Reynolds number envelope for the supersonic and hypersonic regime that can be achieved in the three ballistics range facilities is shown in figure 10. Only the boundary of the envelope unique to each particular facility is shown. A large region of overlap among all three facilities exists in the center portion of the envelope. This envelope is based on the use of the two-stage, light gas guns available for use in each of the three facilities.

The upper boundary of the envelope is dictated by the maximum velocity that can be achieved reliably with the gas gun model launchers. The Hyperballistics Range can achieve a Mach number of 22, while the other two ranges can achieve a Mach number of 20.

The maximum Reynolds numbers for Mach numbers of 20 or less (see the right-hand boundary of the envelope) are achieved in the Pressurized Ballistics Range. Even though larger spheres can be launched in the Hyperballistics Range, larger Reynolds numbers can be obtained in the Pressurized Ballistics Range, since it can be operated at a pressure of five atmospheres, five times greater than the HBR. The smallest Reynolds numbers for Mach numbers between approximately 2 and 20 are obtained in the Aerophysics Range. These Reynolds numbers are based on sphere diameters of 400 microns and range pressures of 0.2 torr. Tests using spheres this small can only be conducted in this facility, since it is the only facility that has a model detection and triggering system for the instrumentation sensitive enough to detect a sphere only 400 microns in diameter.

The minimum Mach number forming the lower boundary of the envelope, shown in figure 10, is a result of the usable cross section of each of the three facilities involved. The usable cross section for the HBR is approximately a 22-inch circle in the center of the 10-foot-diameter tube formed by the field of view of the instrumentation. This can be seen in figure 3. Steel baffle plates having a 13-inch square opening in the center separate each instrument station in the PBR. These openings restrict the usable cross section in this facility. The 5-inch diameter of the Aerophysics Range tube represents the usable cross section of this facility. For supersonic and hypersonic testing, the gas guns are used. The centerlines of the launch tube of these guns are aligned to coincide with the centerline of the range tube. If the launch velocity of a projectile is too low, the projectile will drop out of the usable cross section of the range before traveling a sufficient length downrange to allow a drag coefficient measurement to be made. The minimum Mach number has been calculated from the relation

$$M_{min} = \frac{2\beta}{a_\infty \rho_\infty} \sqrt{\frac{g}{2Y}} \left(e^{\frac{\rho_\infty Z}{2\beta}} - 1 \right) \tag{2}$$

In this relation Y is the allowable vertical drop. This is 11 inches, 6.5 inches, and 2.5 inches for the HBR, PBR, and APR, respectively. The value of Z used was 300 feet, 236 feet, and 300 feet for the HBR, PBR, and APR, respectively. Minimum Mach numbers were calculated only for the maximum and minimum Reynolds numbers for each of the three facilities. Straight lines were then used to connect these points to form the lower boundary of the envelope in figure 10.

For low supersonic and subsonic testing, only the Pressurized Ballistics Range can be used presently. In addition to the gas gun, smaller powder-driven guns are available for use in this facility. The centerline of the barrel of these powder-driven guns can be elevated at various angles with respect to the centerline of the range tube. This allows, with the gun set at the proper elevation angle, the full 13-inch usable cross section of the PBR to be used, rather than just half of it as is the case with the gas gun. Further, the location of the powder gun when mounted in the PBR puts the muzzle 13 feet from the first usable shadowgraph station. The first usable station in this case is station number 4, which limits the total number of instrumentation stations to 24. Using standard projectile ballistic equations (see, for instance, ref. 6), trajectories of a 2-inch-diameter sphere have been calculated for initial Mach numbers from 0.1 to 0.6 and a range pressure of 5 atmospheres. These calculations were performed for the gun aligned at an

elevation angle that allows almost complete use of the usable 13-inch-square cross section of the PBR. These trajectories have been plotted in figure 11. For $M_\infty = 0.1$, a flight of approximately 36 feet of instrumented length can be achieved. This will allow the sphere to be observed at five stations. For $M_\infty = 0.2$, the sphere can be observed by 12 stations. For initial Mach numbers of 0.6 or greater, a 2-inch sphere flying in air at a pressure of 5 atmospheres will travel the full length of the range. The calculations represent the highest Reynolds numbers that can be achieved at these subsonic Mach numbers. To investigate the lowest Reynolds numbers that can be achieved at these subsonic Mach numbers, additional calculations were performed for a sphere having a 3/16-inch diameter and a range pressure of 2 torr. These calculations indicated slightly more favorable conditions. A small increase in testing length was realized.

A Mach number-Reynolds number field for Mach numbers less than 2 that can be achieved in the Pressurized Ballistics Range is shown in figure 12. It can be seen by comparing figures 8, 10, and 12 that the Mach number and Reynolds number can both be duplicated in one of the three ballistics range facilities for a significant portion of a typical trajectory for a falling balloon. Specifically, data at Mach numbers below approximately 0.1 cannot be obtained at any Reynolds number.

Further, data cannot be obtained at any Mach number for Reynolds numbers less than approximately 3×10^1. Data can be obtained for all other Mach number and Reynolds number combinations up to Mach number 20 and Reynolds numbers of 1×10^7.

DATA REDUCTION AND ESTIMATES OF ERRORS

The method used to obtain values for the drag coefficient from ballistics range tests consists of fitting measured time-distance points to an algebraic relation. This relation is obtained from the longitudinal equation of motion for a projectile flying in the ballistics range given as

$$-C_D\left(\frac{1}{2}\rho_\infty V^2\right)A = m\,\frac{dV_\infty}{dt} \tag{3}$$

Assuming a constant drag coefficient, this equation can be solved to give

$$Z-Z_m = Z_o + \frac{2\beta}{\rho_\infty}\ln\left[1 + \frac{\rho_\infty}{2\beta}V_\infty(t-t_m)\right] \tag{4}$$

where

$$\beta = W/C_D A$$

and Z_m and t_m are the values of the distance and time for the station nearest midrange. This equation is approximated by using the first three terms of the series expansion for the logarithmic function, and the resulting equation

$$Z-Z_m = Z_o+V_\infty\left(t-t_m\right)-\frac{\rho_\infty}{2\beta}\frac{V_\infty^2}{2}\left(t-t_m\right)^2+\left(\frac{\rho_\infty}{2\beta}\right)^2\frac{V_\infty^3}{3}\left(t-t_m\right)^3 \tag{5}$$

is fitted by the method of least mean squares to the time-distance data. The drag coefficient and the velocity at the station nearest midrange are computed from the constants of Eq. (5). This, of course, requires that the mass of the model and the density of the test gas be measured prior to launching the model.

Using the shadowgraph stations in the ballistics ranges, the position of models can be determined to within ±0.002 foot and time to 2×10^{-7} seconds. The weight of a model, up to 1000 grams, is determined prior to launching, using NBS class S weights, and is considered to be accurate to within ±0.1 milligram. The diameter of a sphere is measured prior to launching to an accuracy of ±0.0001 inch.

The error in measuring the range pressure is less than 0.2 percent at pressure as low as 0.2 torr. The percent error is, of course, less as the range pressure being measured increases. The maximum leak rate at the lowest pressure in any of the ballistics ranges is 0.08 torr per minute. Normally the pumps are turned off approximately 30 seconds prior to launching the model. For tests conducted at very low pressures, where the leak rate might be significant, pumping can be maintained throughout launching.

The temperature of the test gas in the ballistics ranges is measured at three locations. As previously mentioned, the temperature is approximately 74°F and is measured to within ±0.1°F.

Some analyses have been performed to illustrate the magnitude of the error in C_D due to various effects. One effect considered is sphere distortion, where the body for which it is assumed a drag coefficient is being measured has been distorted into a nonspherical shape. Another effect considered is the use of a constant C_D data reduction method for reducing data from variable C_D trajectories. Finally, the effect of inaccuracies in distance measurements and number of available data stations will be discussed.

For high-velocity testing ($M_\infty > 15$) the spheres undergo very high accelerations during the launching phase of the test. It is conceivable that, under this high-inertial loading, a sphere of certain materials which do not possess sufficiently high strength might become distorted. Estimates have been made to determine the error induced in the drag coefficient resulting from distortion of the sphere. During launching it is assumed that it could become flattened. To represent the resulting body of revolution, an ellipse has been rotated about one of its axes to form an axisymmetric body. Using modified Newtonian impact theory, the drag coefficient of such a body is given as

$$C_{D_B} = \frac{C_{p_M}(b/a)^2}{(b/a)^2-1}\left[1 - \frac{1}{(b/a)^2-1}\ln(b/a)^2\right] \tag{6}$$

The percent error induced by flattening a sphere is defined as

$$\%\Delta C_D = \frac{C_{D_B} - C_{D_S}}{C_{D_S}} \times 100 \tag{7}$$

where C_{D_S} is the drag coefficient of a sphere given by Newtonian impact theory as $C_{D_S} = C_{p_M}/2$. The results of these calculations are shown in figure 13. It is seen from figure 13 that the curve is nearly linear. The error in drag coefficient for 1 percent flattening is approximately 0.6 percent. The curve has been plotted for two cases: The upper portion of the curve is for the case of the minor axis of the ellipse aligned with the velocity vector, while the lower portion of the curve is for the major axis aligned with the velocity vector.

As was illustrated in the section on drag coefficients, there is a large change in C_D with variation in Mach number in the transonic region ($0.6 \le M \le 1.75$). In the relations used for reducing the time-distance data to drag coefficients, it was assumed that the drag coefficient remained constant during a flight in the range. This assumption is certainly valid in the subsonic and hypersonic continuum flow region. However, in the transonic region this assumption is not valid, and significant changes in the drag coefficient can occur if the velocity decrement during a flight is too large. In practice, the drag coefficient derived from a test in the ballistics range is associated with the midrange Mach number, since there is always some change in velocity during a flight. To investigate the error in the drag coefficient resulting from a ballistics range test, Eq. (3) was solved for the case of C_D, varying linearly with velocity

(or Mach number for a constant range temperature), and expressed as

$$C_D = c + fV \tag{8}$$

The solution of Eq. (3) is

$$Z = -\frac{2m}{\rho_\infty cA} \ln\frac{V}{V_o}\left(\frac{f + c/V_o}{f\ V/V_o + c/V_o}\right) \tag{9}$$

The solution of Eq. (3) for the case of a constant drag coefficient ($c = C_D$; $f = 0$) is

$$Z = -\frac{2\beta}{\rho_\infty} \ln\frac{V}{V_o} \tag{10}$$

Equating Eqs. (9) and (10) and solving for C_D results in a relation for an average value of C_D computed from a variable C_D trajectory. This equation is given as

$$C_{D_A} = \frac{c \ln\frac{V}{V_o}}{\ln\frac{V}{V_o}\left(\frac{f + c/V_o}{f\ V/V_o + c/V_o}\right)} \tag{11}$$

Notice that the average C_D is only a function of the initial velocity and the final-to-initial velocity ratio. As is the practice in ballistics-range data reduction, this C_D is associated with the Mach number which occurs at the midrange value of Z. Referring to Eq. (8), an exact value of C_D is

$$C_{D_E} = c + fV_m \tag{12}$$

A percent error in C_D due to using a constant C_D data reduction method to reduce data obtained from a variable C_D trajectory can be defined as

$$\%\Delta C_D = \frac{C_{D_E} - C_{D_A}}{C_{D_E}} \times 100 \tag{13}$$

Values of $\%\Delta C_D$ will be a function only of the initial velocity and the final-to-initial velocity ratio, which can be expressed as a percent velocity decrement. Calculations were performed for initial velocities from 794 to 1475 ft/sec and for percent velocity decrements from 0 to 38 percent. It was found that the value of the initial velocity has a negligible effect on the results. The percent error in C_D is shown as a function of the percent velocity decrement in figure 14. It is seen that a 10 percent velocity decrement results in only 0.1 percent error in C_D. Although it is recognized that this is an idealized calculation, it does serve as a guide when performing tests in a ballistics range in the transonic flow regime where there are large variations in C_D with Mach number. The results also indicate that, except for extremely large velocity changes, a negligibly small error is incurred in the C_D measurement.

A digital computer program was utilized to illustrate the effect of measuring accuracy, number of stations, and station spacing in the NOL ranges on the accuracy of measured drag coefficients. An "exact" time-distance trajectory was calculated using the standard ballistic trajectory equations for a projectile previously mentioned. It was then assumed that the times were exact, but some error was incurred at each measuring station, which alters the value of Z. It was assumed that the maximum error or alteration in Z is ±0.002 foot. At each value of Z to be perturbed, the computer chose at random an integral number between 1 and 10. If this number was even, the perturbation in Z was positive, while if the number was odd, the perturbation was negative. The magnitude of the perturbation was determined as follows: A Gaussian distribution curve was used in which the peak of the curve is taken as zero along the ordinate to a value of 1 at the origin of the ordinate. Along the abscissa the peak of the curve corresponds to zero while the 3σ point corresponds to 1. Again using the computer, a random number was selected between 0 and 1. This number was located along the abscissa which then specified a number between 0 and 1 along the ordinate corresponding to the Gaussian curve being used. This number obtained along the ordinate was multiplied by the maximum possible error of 0.002 foot. The result was the magnitude of the perturbation applied to the value of Z being considered. Eq. (5) was then fitted to these new values of Z and their corresponding values of time. This allowed a value of C_D to be determined for measurements considered obtained from a prescribed number of stations, with a given distribution, and with a normal distribution of error. For any set of conditions, this process was performed ten times. The resulting drag coefficient from each of the ten runs was compared to the original or "exact" value of C_D used in performing the trajectory calculations. A

standard deviation is defined as

$$\sigma = \sqrt{\frac{\sum_{i=0}^{10} \left[C_D(\text{exact}) - C_D(\text{calculated})_i \right]^2}{10}} \tag{14}$$

A percent error in the drag coefficient is given by

$$\%\Delta C_D = \frac{2\sigma}{C_D(\text{calculated})} \tag{15}$$

Using 2σ in determining the percent error means that 95 percent of the tests conducted will have percent errors equal to or less than the value given by Eq. (15). Using this analysis, selected Mach number-Reynolds number conditions were investigated. Since the error incurred for any particular condition is a function of the deceleration of the projectile, for each Mach number-Reynolds number condition several different combinations of sphere diameter and range pressures were used. Calculations were made for both copper and lexan spheres, giving a large difference in the material density and, hence, their trajectory. This allowed a selection of the near minimum error to be made corresponding to the optimum amount of deceleration.

The results of this investigation are shown in figure 15. It is seen that the error in the drag coefficient is equal to or less than 1.1 percent for Reynolds numbers greater than 1×10^4 at all Mach numbers considered. Errors are larger at subsonic Mach numbers and low Reynolds numbers due to the lack of sufficient velocity decrement in the flight trajectory. Accurate measurements at low Reynolds numbers can be made in the APR. This results from the small-size sphere that can be tested in this facility, allowing sufficient deceleration to occur during a flight. A study similar to that just discussed on the number and location of measuring stations was presented in reference 7.

CONCLUSIONS

Ballistics ranges allow extremely accurate drag coefficients of spheres to be measured over a wide variation in Mach numbers and Reynolds numbers. To obtain the maximum accuracy at a specified Reynolds number, care should be exercised in selecting the size of the sphere, the material for sphere fabrication, and the pressure of the test gas. These three parameters should be selected to obtain the optimum amount of deceleration during a flight. Accurate measurements can be made in the transonic region

if the velocity decrement is maintained at 10 percent or less. Spheres should be fabricated from materials with sufficiently high strength to eliminate the possibility of distortion during the high-acceleration launch phase of a test.

REFERENCES

1. Krumins, M. V.: Drag and Stability of Various Mars Entry Configurations. 19th Congress of the International Astronautical Fed, IAF Paper RE 138, Oct. 1968.

2. Hoerner, S. F.: Fluid-Dynamic Drag. Published by author, 148 Busteed Dr., Midland Park, N. J., 1958.

3. Schlichting, H.: Boundary Layer Theory. McGraw-Hill Book Co., Inc., 1955.

4. Shapiro, A. H.: The Dynamics and Thermodynamics of Compressible Fluid Flow.
   Vol. I. Ronald Press Co., c.1953.
   Vol. II. Ronald Press Co., c.1954.

5. Tsien, H. S.: Superaerodynamics, Mechanics of Rarefied Gases. Jour. Aeronautical Sci., vol. 13, no. 12, Dec. 1946.

6. Synge, J. L., and Griffith, B. A.: Principles of Mechanics. McGraw-Hill Book Co., Inc., c.1942.

7. Karpov, B. G.: The Accuracy of Drag Measurements as a Function of Number and Distribution of Timing Stations. BRL Rept. No. 658, Feb. 1948.

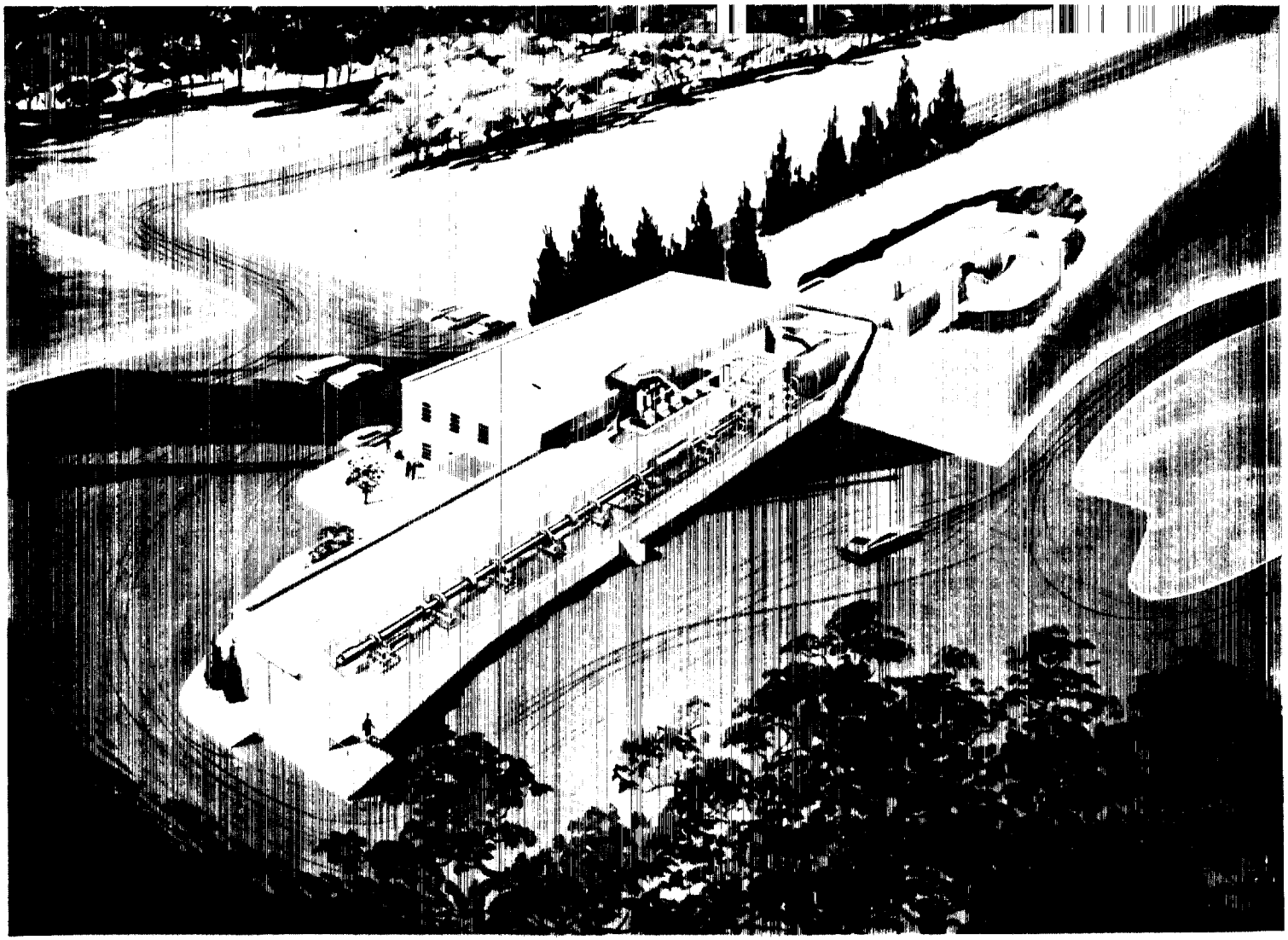

Figure 1.- NOL 1000-foot Hyperballistics Range.

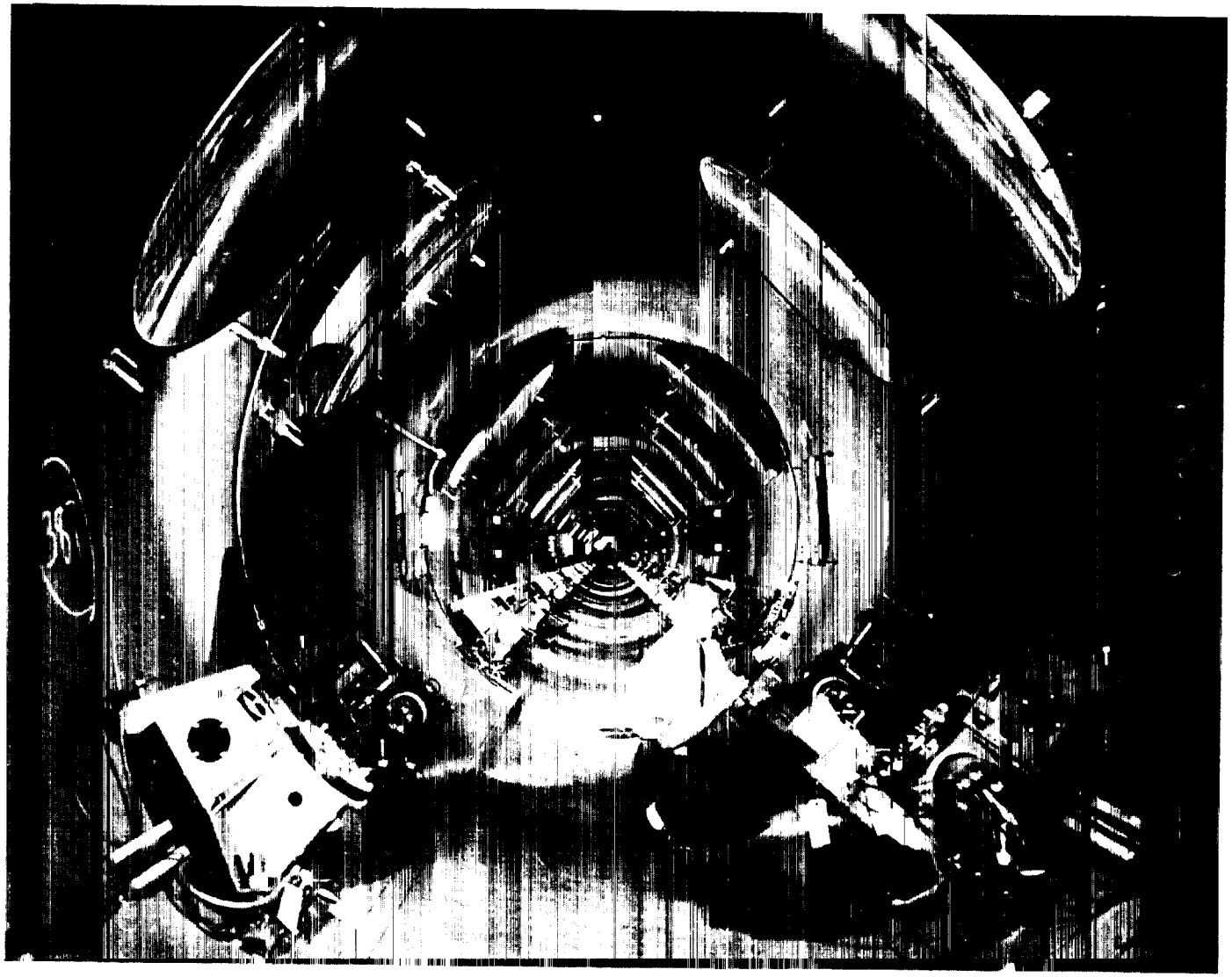

Figure 2.- Inside NOL 1000-foot Hyperballistics Range.

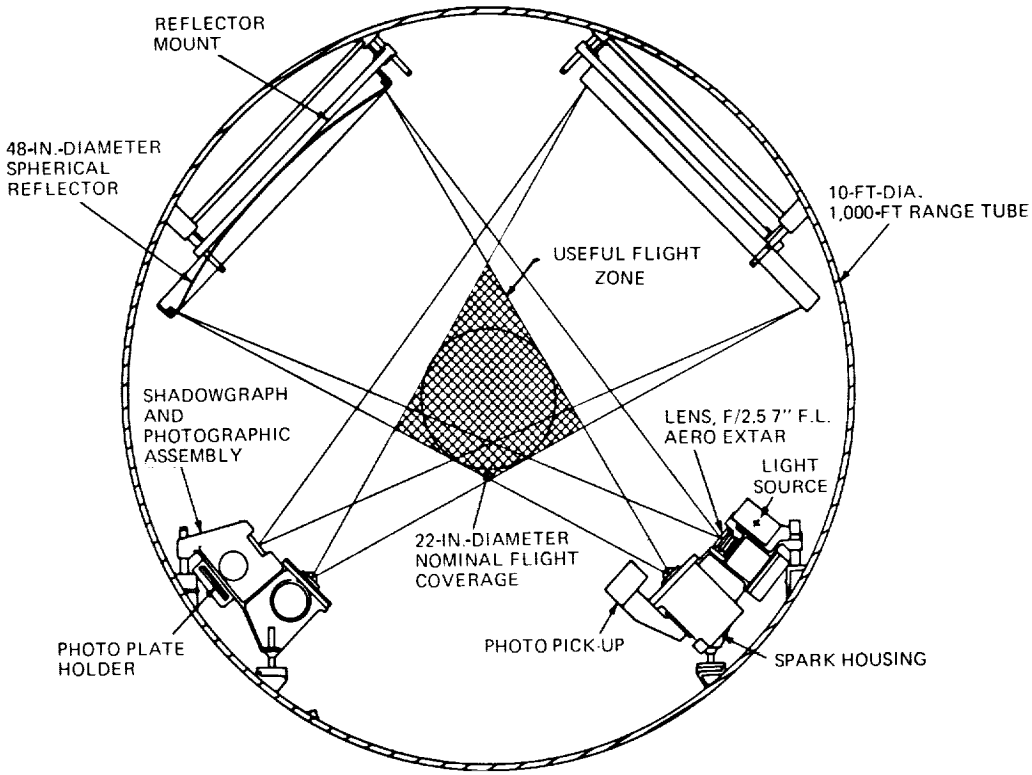

Figure 3.- Schematic drawing of spark shadowgraph station in NOL 1000-foot Hyperballistics Range.

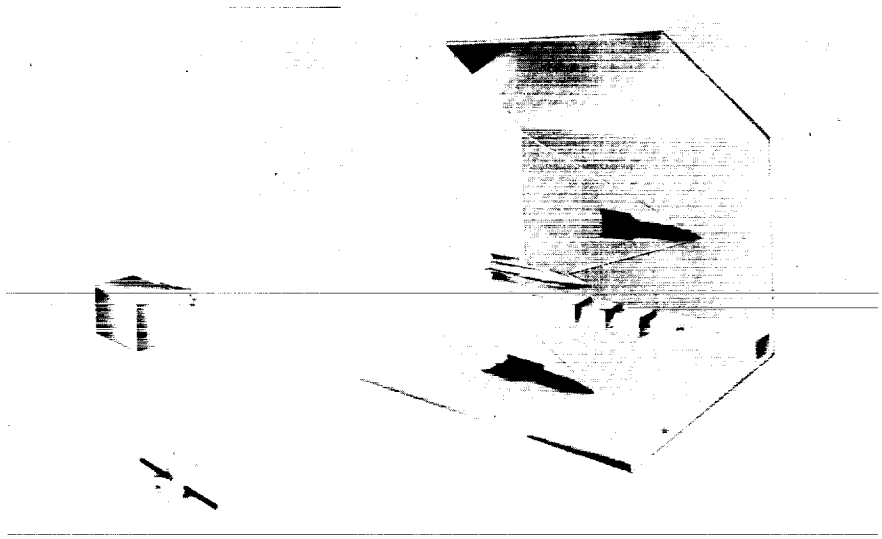

Figure 4.- Schematic drawing of shadowgraph station in NOL Pressurized Ballistics Range.

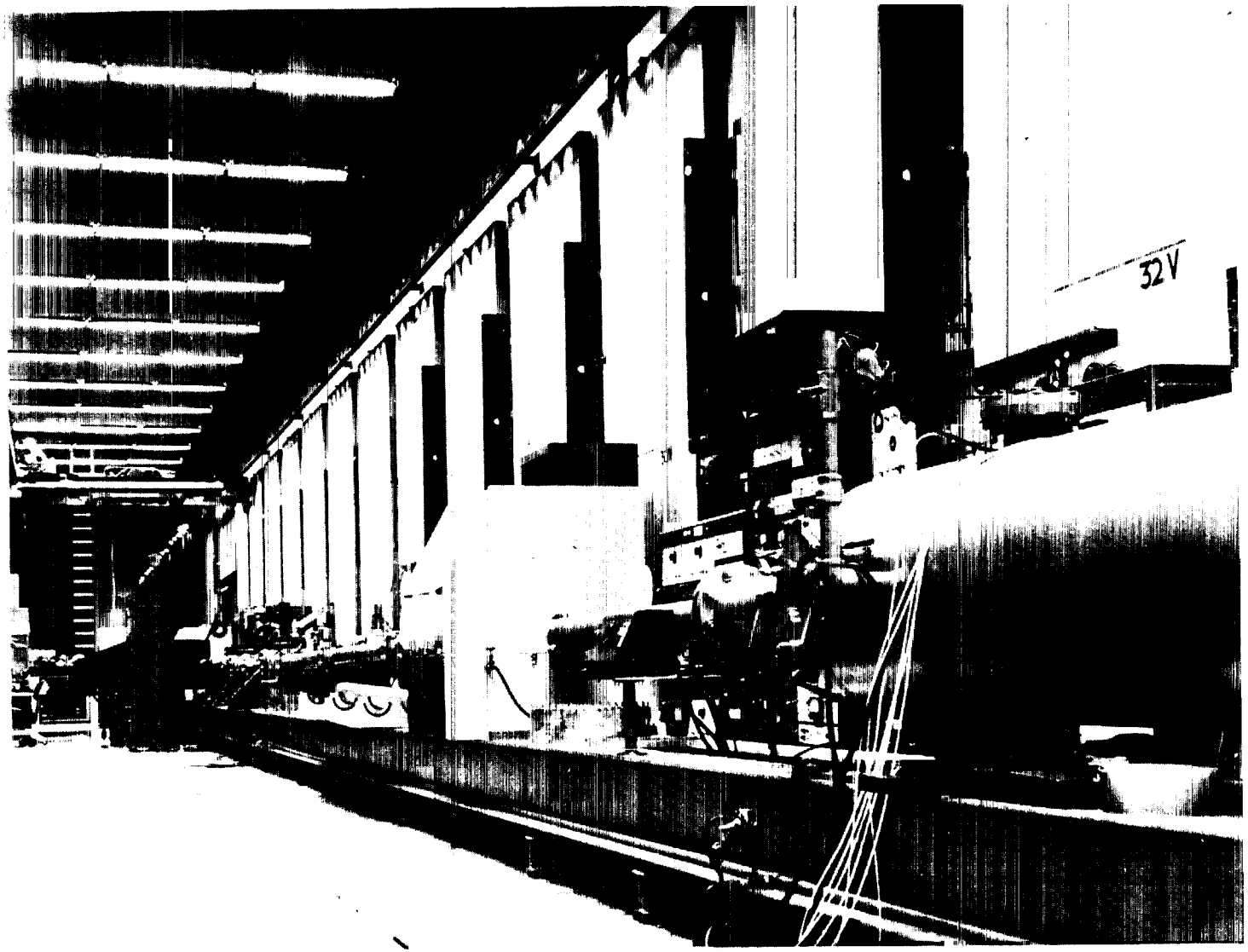

Figure 5.- NOL Aerophysics Range.

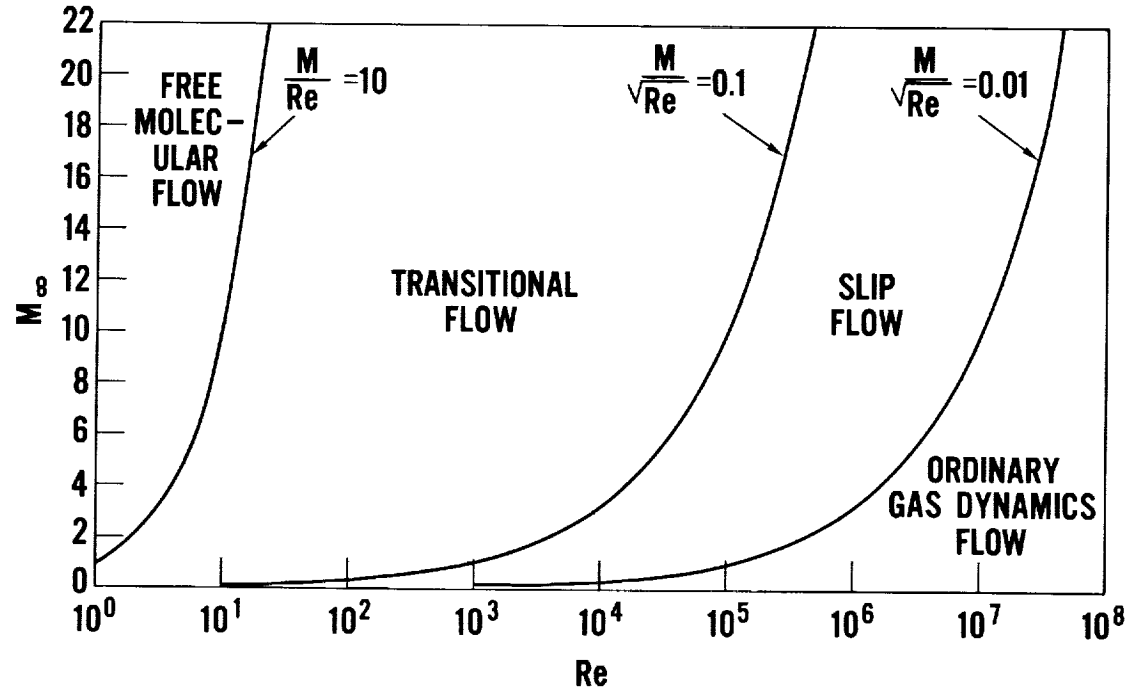

Figure 6.- Flow regimes.

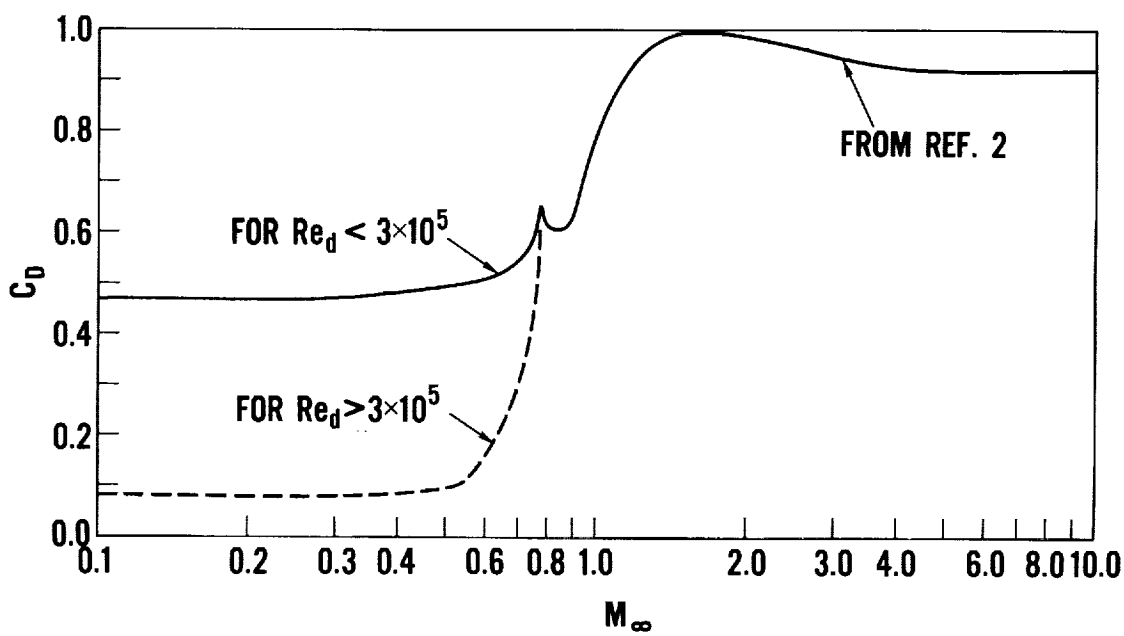

Figure 7.- Drag coefficient for sphere in continuum flow.

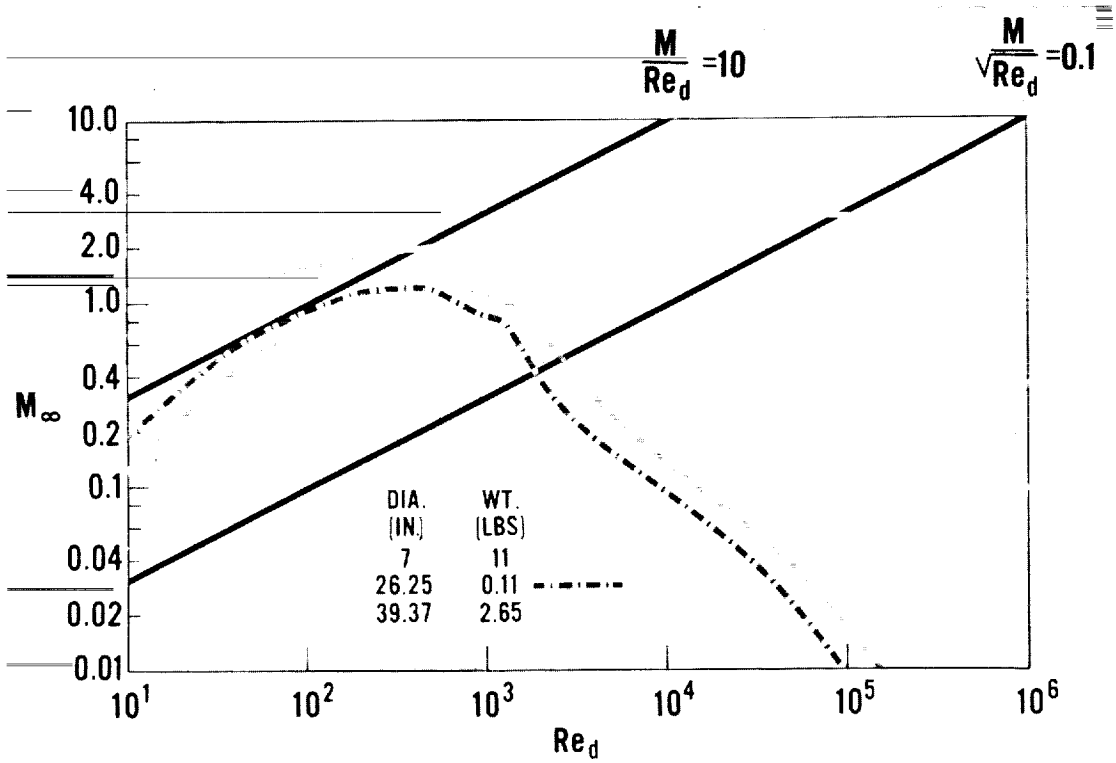

Figure 8.- Trajectory of free-falling spheres.

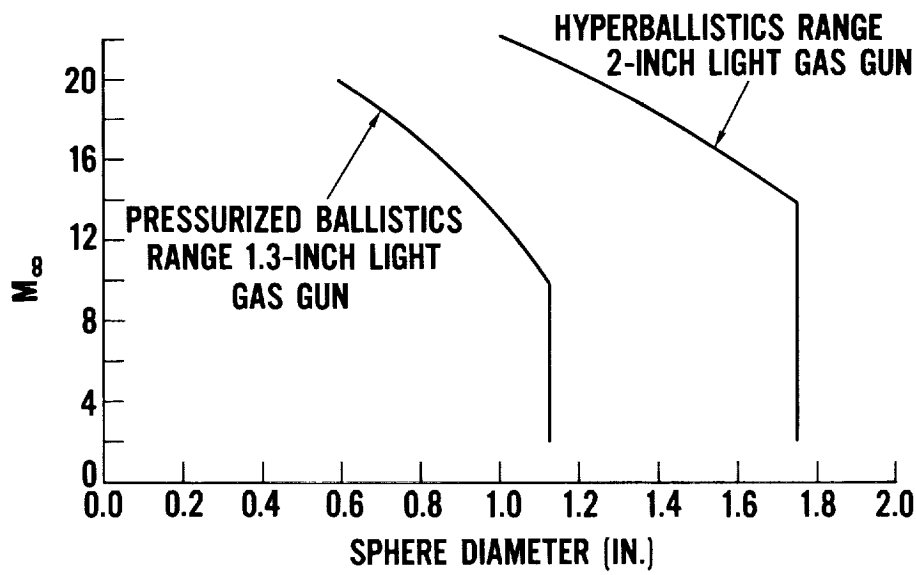

Figure 9.- Maximum diameter of spheres that can be launched from light gas guns in Hyperballistics Range and Pressurized Ballistics Range.

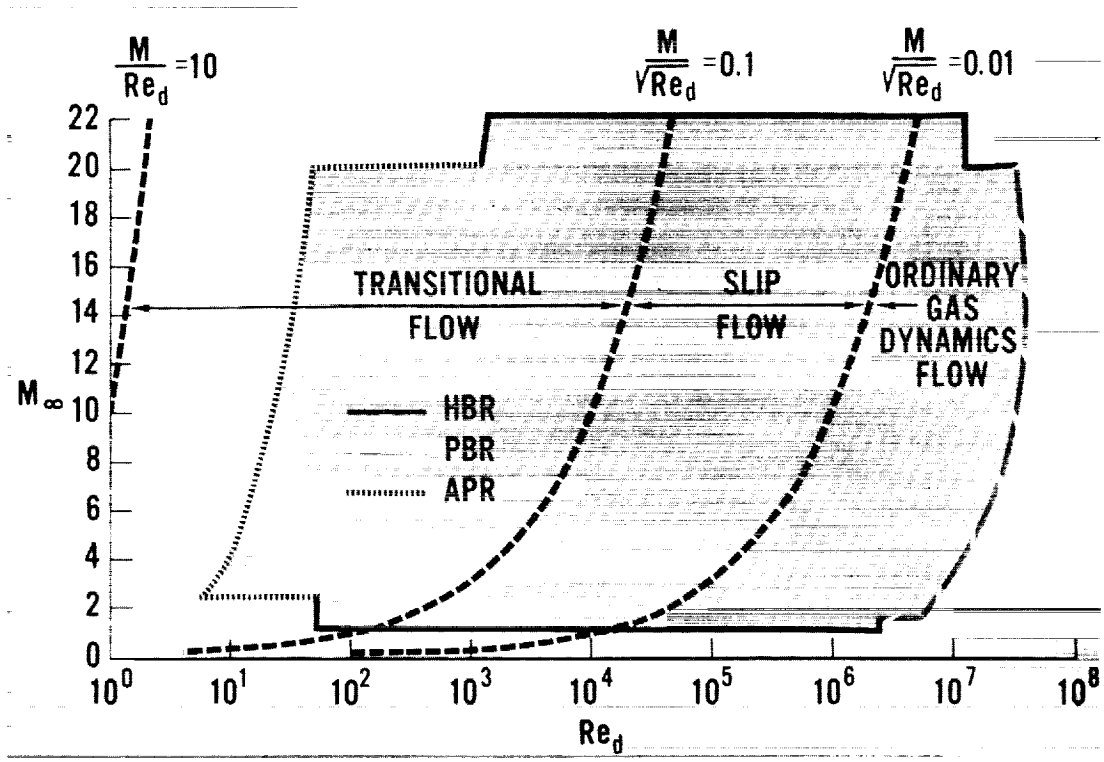

Figure 10.- Mach number-Reynolds number capability of NOL ballistics ranges for spheres in supersonic and hypersonic flight.

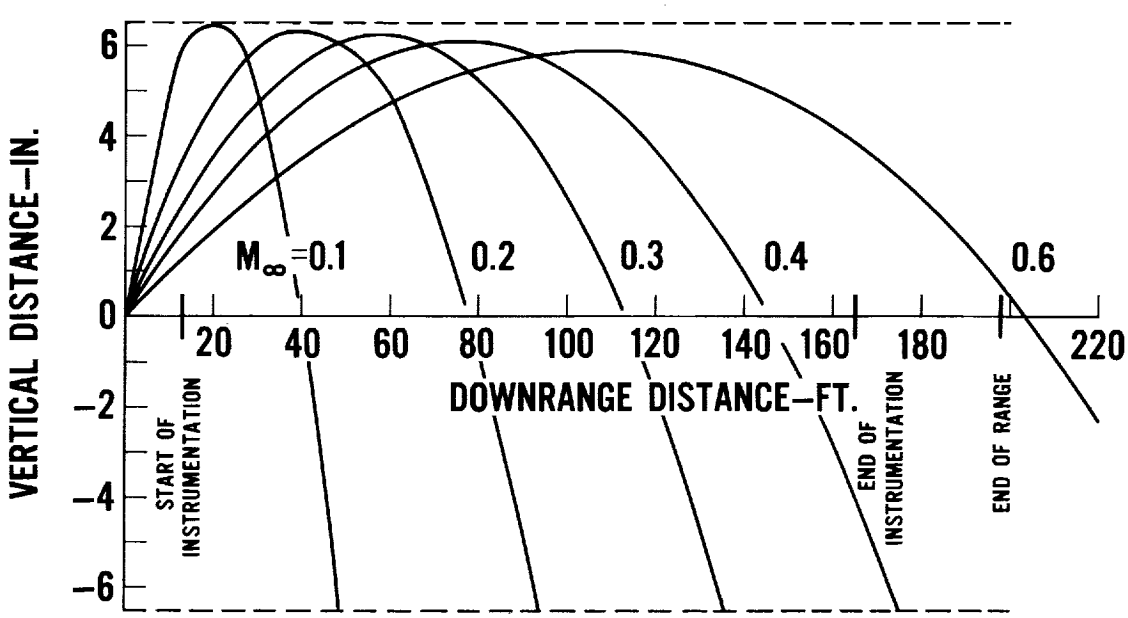

Figure 11.- Sphere trajectories in NOL Pressurized Ballistics Range.

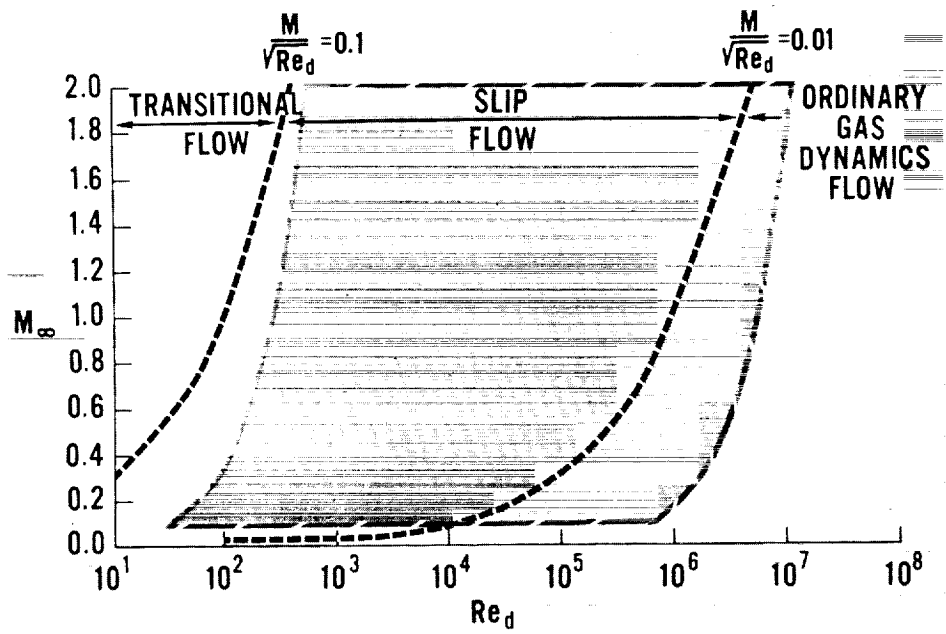

Figure 12.- Mach number-Reynolds number capability of NOL Pressurized Ballistics Range for spheres in subsonic and supersonic flight.

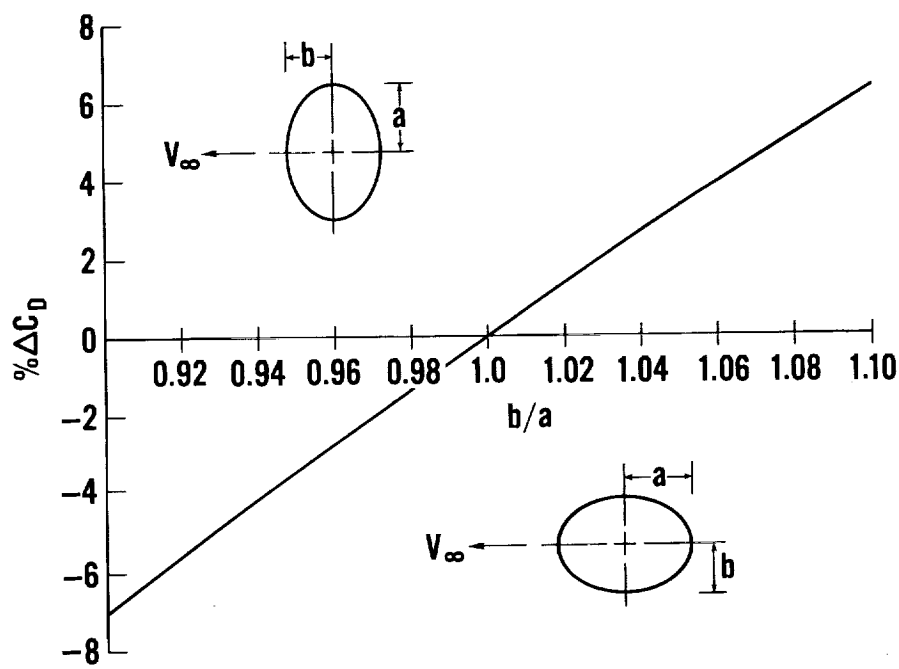

Figure 13.- Error in sphere drag coefficient due to distortion.

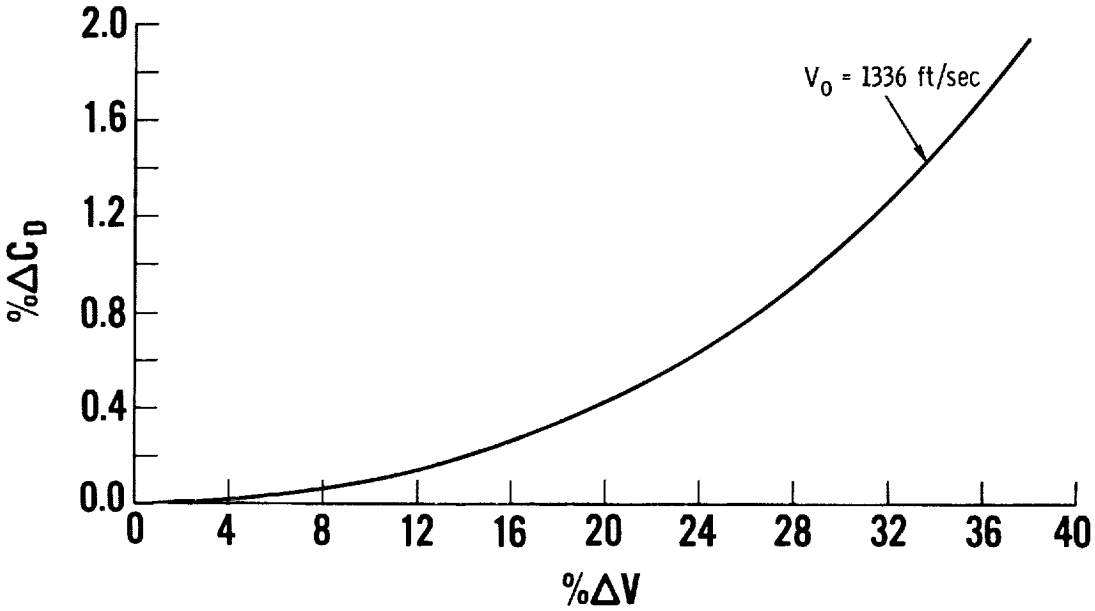

Figure 14.- Error in sphere drag coefficient due to constant C_D.

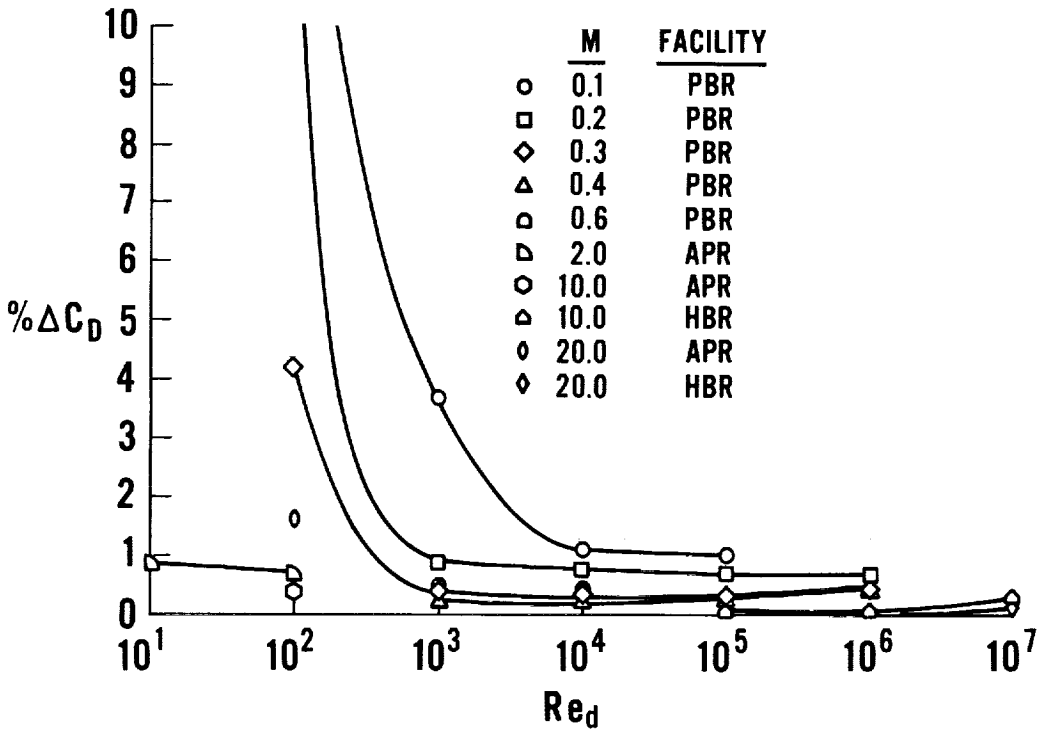

Figure 15.- Error in sphere drag coefficient due to error in distance, number, and distribution of measurements.

AN ASSESSMENT OF SPHERE DRAG COEFFICIENT DATA

By Helmut G. Heinrich and Robert A. Noreen

University of Minnesota

INTRODUCTION

In order to reliably determine atmospheric conditions from the descent velocity of a sphere, the drag coefficient of the sphere as it falls through the air must be known to a high degree of accuracy. This paper covers wind tunnel studies which established drag coefficients from 360,000 ft. altitude down for a one meter sphere with a given weight, when ejected from a rocket at an altitude of 450,000 ft. The wind tunnel test conditions were adjusted for simultaneous duplication of the Mach and Reynolds Numbers as they occur during the descent of the sphere in a standard atmosphere. The range of the test conditions was wide enough to cover the expected atmospheric deviations.

TEST FACILITIES

The drag coefficient of a perfect sphere moving through air is a function of the Mach and Reynolds Numbers and under certain conditions also of the Knudson Number which is, however, a combination of Mach and Reynolds Numbers. These relationships require that meaningful drag measurements must be made with simultaneous duplication of the respective Mach and Reynolds Numbers. In standard atmospheric pressure wind tunnels, this condition is usually difficult to fulfill. Therefore, the University of Minnesota used for the required measurements a subsonic and a supersonic variable density wind tunnel, because the density variation provides the third parameter necessary to establish the required Mach-Reynolds and Knudson Number simulation.

The low density subsonic wind tunnel is of the closed horizontal return type, Fig. 1 (Ref. 1), with a mechanical vacuum pump used to evacuate the circuit and a centrifugal compressor to move the air around the circuit. Continuous operation at Mach Numbers from nearly 0 up to approximately 0.9 can be obtained by using various nozzles and a throttling valve. Wind tunnel operating

pressures range from 200 torr down to approximately 0.2 torr, depending upon the flow Mach Number. The nozzles exhaust into an open jet test section and have outlet diameters varying from 12 in. for lowest Mach Numbers to 3 in. for highest Mach Numbers.

The low density supersonic wind tunnel, Fig. 2 (Ref. 2), has a standard "blow down" configuration, operating between a 5000 psig high pressure source and a 10 millitorr vacuum reservoir. For these tests the supersonic wind tunnel was equipped with five axisymmetric nozzles for operation at Mach Numbers of 1.2, 1.5, 2.0, 2.5, and 3.2 at static pressures in the order of 1 torr. All five nozzles have a core flow region 4 in. in diameter at their design operating pressures and exhaust into an open jet test section. For the pressures of interest in the sphere drag tests, the 33,500 cu. ft. vacuum reservoir could sustain nearly constant pressures for run times of a minute or longer.

MODELS

The sphere models used in both test sequences were 0.50 in. Teflon spheres with diameter tolerances of 0.002 in. and sphericity of 0.001. Teflon was selected because its surface roughness characteristics approximate those of an inflated spherical Mylar balloon.

MEASUREMENTS

The primary measurements made during the tests were flow pressures and the drag forces of the spheres. Naturally the size of the models and flow temperature were also measured, but these measurements presented little or no difficulty and could be made with sufficient accuracy to be neglected in an error analysis.

The pressure measurements in the required range from 20 torr to 10 millitorr presented the most difficulties and created the largest portion of the total error. For both the subsonic and supersonic tests measuring two pressures enabled determing the flow conditions. In the subsonic tests, total pressure and the difference between total and static pressure were measured, while in the supersonic tests, total pressure and static pressure were determined. These measurements were made using Bourdon tube, strain-gaged diaphragm, and thermocouple gages, all having different ranges, accuracies, and reliabilities (Refs. 1 and 2). Total pressures were detected with a total probe rake located in a near stagnation region, and static pressures were obtained from static pressure taps in the nozzle wall near the exit.

Drag forces were measured using the force balance shown in Fig. 3. A drag force acting on the sphere twists the torsion member causing the core of a linear variable differential transformer to deflect within the coil, thus producing a measurable change in coil current. Two permanent magnets placed near a copper "paddle", also attached to the torsion member, produced sufficient eddy currents to damp any oscillation of the balance system. The balance was calibrated by hanging weights on the damping support strut and relating the moment produced by the weight to a force on the sphere by the ratios of lengths to the moment center. Changing torsion members allowed selecting nearly any required sensitivity of the force balance. Repeated calibrations indicated that the balance performed quite well and was more accurate than the electrical read-out equipment used to measure the coil currents.

For each data point two types of drag measurements were made, one with the sphere mounted on its sting support, and another one of the support alone with the sphere rigidly mounted slightly ahead of the support (Fig. 4). Subtracting the support drag from the total drag yielded the drag of the sphere. The drag of the support was, of course, considerably smaller than that of the sphere.

RESULTS

The results from the supersonic and subsonic tests are shown in Figs. 5 and 6, respectively, as plots of drag coefficient vs Reynolds Number with Mach Number as a parameter. One notices that the higher speed subsonic data is somewhat scattered and that there are a few questionable points among the supersonic results. In view of this uncertainty, the data was replotted in Figs. 7a and 7b as C_D vs Mach Number with Reynolds Number as parameter. The critical review of both types of presentations provides guide lines for the data interpretation and for the establishment of the final conclusion. In this view, the data in the previous figures was carefully analyzed by members of the staff of the University of Minnesota and USAF Cambridge Research Laboratories. The results of this joint effort are the curves shown in Figs. 8 and 9 which are considered to be the final results of this study. The two dashed curves in Fig. 8 show the spread of data obtained at Mach Numbers between 2 and 4 in wind tunnel tests by Ashkenas who performed wind tunnel tests with spheres mounted on thin wires (Ref. 3).

The agreement between the different supersonic data can only be termed approximate at best, and even though Ashkenas (Ref. 3) presents no error estimate, there is no principal reason that accurate results could not be obtained with his methods.

Figure 9 includes several data points from tests conducted with moving spheres in a ballistic range (Ref. 4). The agreement between these data is again approximate, and not within the estimated error range of either set of measurements. However, it is not known if drag measurements taken from a sphere which is decelerating to various degrees as it travels along the ballistic range can be compared to steady state measurements. In a flow field that changes with time, the flow pattern may be quite different from the one under steady state conditions at the same Mach and Reynolds Numbers. The kinetic energy in that flow field varies definitely, and apparent mass effects may have to be accounted for. Therefore, it is at this time not known if these effects involved in the ballistic tests are or are not significant, but it is a possible explanation for the difference between results obtained under steady state and non-steady conditions.

ERRORS

References 1 and 2 give extended analyses of the random and instrument errors encountered in the measurements performed at the University of Minnesota. The analysis follows the standard concept of expressing the error in drag coefficient as a total differential considering all the terms measured to obtain the drag coefficient. The results of this analysis predict errors from 1% to 5% for the subsonic measurements, and from 2% to 28% for the supersonic measurements; these numbers represent the maximum possible errors due to random or instrument errors, and the possible error for a particular point is a function of the Mach and Reynolds Number at that point. For both the subsonic and supersonic data, the highest errors occur at the lowest Reynolds Numbers of the range, and in both cases, the highest possible error is due to the pressure error term.

CONCLUSIONS

Sphere drag coefficients have been measured over the range of Mach and Reynolds Numbers encountered by a falling sphere density sensor. An error analysis of the data shows that generally the data should be accurate to within about 5%; agreement with other measurements is within about 10% and results from actual tests show that the data is at worst very reasonable and at best highly accurate. Of course, since the drag coefficient data is one basic part of a measuring system where greater and greater accuracy is needed, the drag coefficients must be critically checked for possible inaccuracy and improvement. Reviewing the measurements from this aspect, several possible areas for improvement arise.

1. Pressure Measurement

Since the measurements were conducted fairly significant improvements in pressure measuring instrumentation and techniques have been made. Realizing that the highest errors in the data presented above were no doubt caused by pressure errors, it seems probable that at least in some ranges significant improvements could be made in the accuracy of the coefficients.

2. Sphere Temperature

Recent publications have shown that sphere temperature does have an influence on drag coefficients in this low density flow regime (Ref. 5). Although this effect is not large and the model spheres should have been at a temperature very near wall temperature, the sphere temperature was not measured. If temperature differences existed, this may have caused some unknown error.

3. Sphere Surface Roughness

Only one type of sphere was used in the tests at the University of Minnesota, hence the effects of roughness were not determined experimentally. It is possible that at least part of the deviation from measurements at other institutions is due to different surface roughness of the models.

SUMMARY

It appears that the drag of the sphere is known reasonably well with an accuracy usually expected from aerodynamic measurements. Yet an over-all improvement of the accuracy of the pressure sensing system offers greater certainty in the process of data acquisition and probably a significant improvement of the accuracy of the drag coefficients.

A new effort to measure the sphere drag under well simulated steady state flow conditions with the best instrumentation and facilities available appears to be justified and desirable.

ADDENDUM

During the discussion following this and other presented papers, questions were raised about the origin of the $M \leqq 0.39$ sphere drag coefficient data between Reynolds Numbers of 1,600 and 25,000 presented in Ref. 1. The uncertainties center around Fig. 19 of Ref. 1, added here as Fig. 10, which shows the results of measurements by the University of Minnesota. All of the data in Fig. 10, except the $M \leqq 0.39$ data, has been superseded by the data shown in Fig. 9 (Ref. 2), which were obtained from tests conducted with better instrumentation at a later date. The drag coefficients shown in Fig. 10 and identified as belonging to Mach Number $\leqq 0.39$ have not been changed because newer test cases with improved instrumentation did not show significant deviations from the earlier established data.

The $M \leqq 0.39$ curve is based on seven series of measurements at various Mach Numbers between Reynolds Numbers of 1.5×10^3 to 3×10^4. This is also stated in Ref. 1. Detailed results of these measurements are shown in Fig. 11. The data points presented in Fig. 11 were not shown in Fig. 19 of Ref. 1 in order to avoid overcrowding the presentation.

Figure 10 shows an additional curve representing drag coefficients in the incompressible flow regime for Reynolds Numbers less than 10^3. This information is taken from Fig. 10 in Chapter III of Hoerner's "Fluid-Dynamic Drag," as well as a graphical transposition can be made. Admittedly, Fig. 19, Ref. 1, can easily be misunderstood to the extent that the entire curve representing the sphere drag coefficients in the incompressible range is credited to Hoerner. This is, however, not true and the right-hand segment represents the average values shown in Fig. 11. Merely the left-hand portion is from Hoerner.

Comparing the University of Minnesota curve $M \leqq 0.39$, one finds as minimum drag coefficient $C_D = 0.427$ for Reynolds Numbers between 3.5 and 4.0×10^3. Trying to extract the minimum C_D value from Hoerner's curve one finds for the same Reynolds Number range $C_D = 0.407$ with a possible reading inaccuracy of ± 0.025. This fact led to the remark in Ref. 1 that the University of Minnesota measured data agree well with Hoerner's curve covering this Reynolds Number range.

Furthermore, it will be noticed that Fig. 11 also contains data points taken from numerical values of Ref. 6, which is one publication listed in Hoerner. Figure 12 is a photographic reproduction of Fig. 26, Ref. 6.

This figure is particularly interesting since it shows different drag coefficients for the same Reynolds Numbers obtained by a different experimental technique, namely dropping steel spheres in water.

Figure 13 which is reproduced from Ref. 7, Fig. 178, is also included and shows the variation of drag coefficients measured in the same institution under the supervision of the same individuals but in different wind tunnels. Of course, it must be considered that Fig. 13 shows the drag coefficients in the

critical subsonic range, and the degree of wind-tunnel turbulence is in this region particularly influential.

Summarizing then all matters of accuracy, it is the opinion of these authors that the accuracy of the drag coefficients measured at the University of Minnesota is about as good as can be expected from wind-tunnel experiments at that time. Repeating these measurements and utilizing instrumentation improved over that available in 1960 to 1962 may provide somewhat different results, but the deviations cannot be large. Furthermore, different measuring techniques such as measuring the descent speed of spheres in water or their deceleration in a ballistic range may again produce slightly different numerical values.

REFERENCES

1. Heinrich, Helmut G.; Niccum, Ronald J.; and Haak, Eugene L.: The Drag Coefficient of a Sphere Corresponding to a "One Meter ROBIN Sphere" Descending From 260,000 ft Altitude (Reynolds Nos 789 to 23,448, Mach Nos 0.056 to 0.90). Research and Development of ROBIN Meteorological Rocket Balloon, Vol. II, Contract No. AF 19(604)-8034, Univ. of Minnesota, May 1963. (Available from DDC as AD 480309.)

2. Heinrich, H. G.; Niccum, R. J.; Haak, E. L.; Jamison, L. R.; and George, R. L.: Modification of the Robin Meteorological Balloon. Vol. II - Drag Evaluations. AFCRL-65-734(II), U.S. Air Force, Sept. 30, 1965. (Available from DDC as AD 629775.)

3. Ashkenas, H. I.: Sphere Drag at Low Reynolds Numbers and Supersonic Speeds. Res. Summary No. 36-12, Vol. I (Contract No. NAS 7-100), Jet Propulsion Lab., California Inst. Technol., Jan. 2, 1962, pp. 93-95.

4. Lawrence, W. R.: Free-Flight Range Measurements of Sphere Drag at Low Reynolds Numbers and Low Mach Numbers. AEDC-TR-67-218, U.S. Air Force, Nov. 1967. (Available from DDC as AD 660545.)

5. Ashkenas, Harry: Low-Density Sphere Drag With Equilibrium and Nonequilibrium Wall Temperature. Rarefied Gas Dynamics, Vol. II, J. A. Laurmann, ed., Academic Press, 1963, pp. 278-290.

6. Ergebnisse der Aerodynamischen Versuchsanstalt zu Goettingen. II. Lieferung, Verlag von R. Oldenbourg, 1923, pp. 28-30.

7. Ergebnisse der Aerodynamischen Versuchsanstalt zu Goettingen. IV. Lieferung, Verlag von R. Oldenbourg, 1932, pp. 106-108.

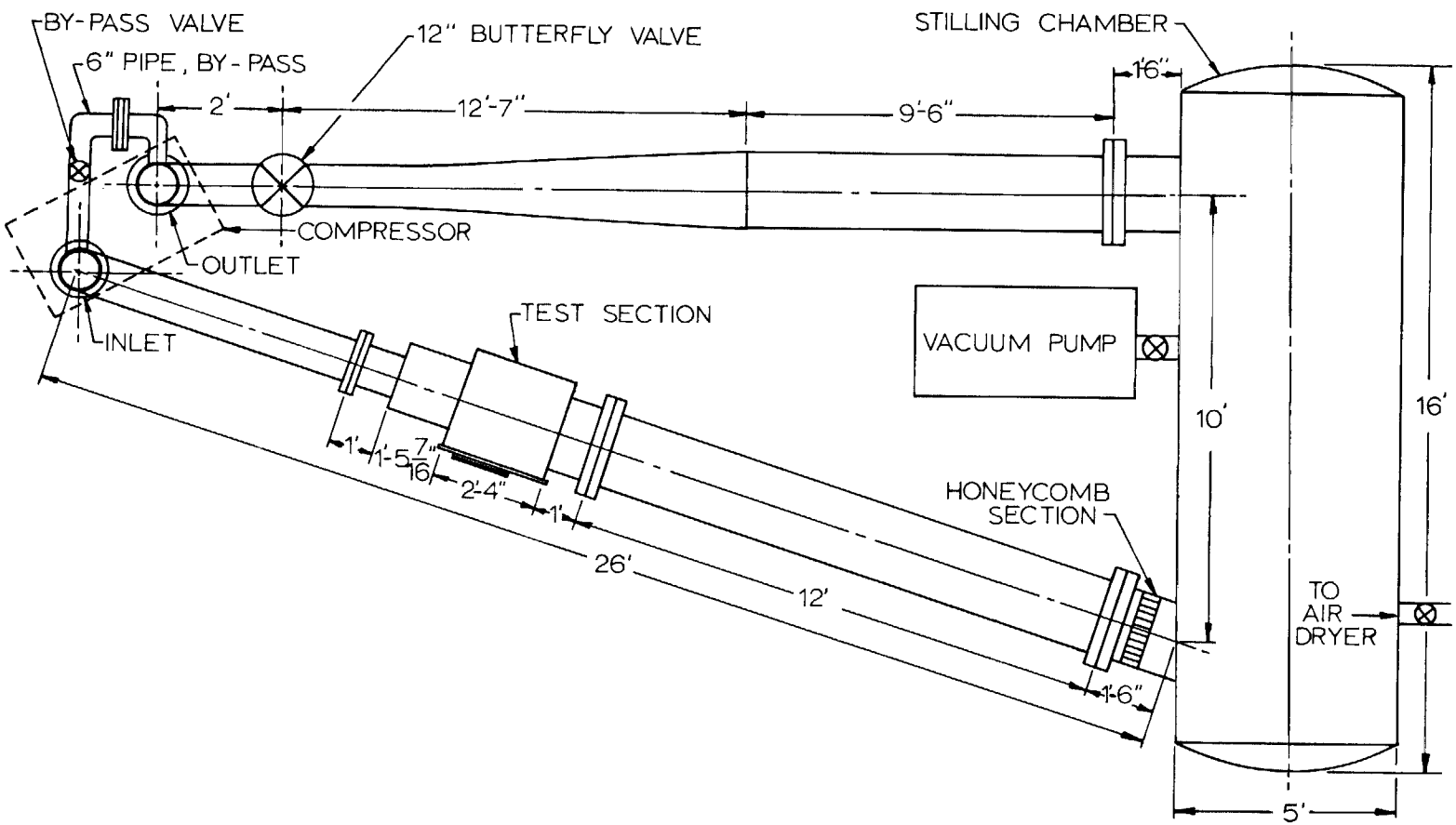

Figure 1.- Low density wind tunnel layout.

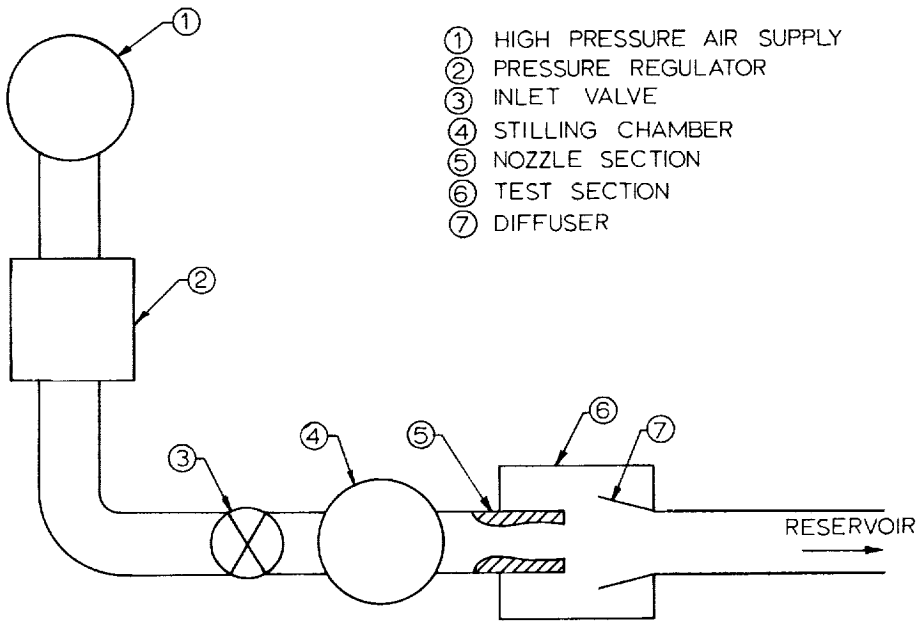

Figure 2.- Schematic representation of the low density supersonic wind tunnel.

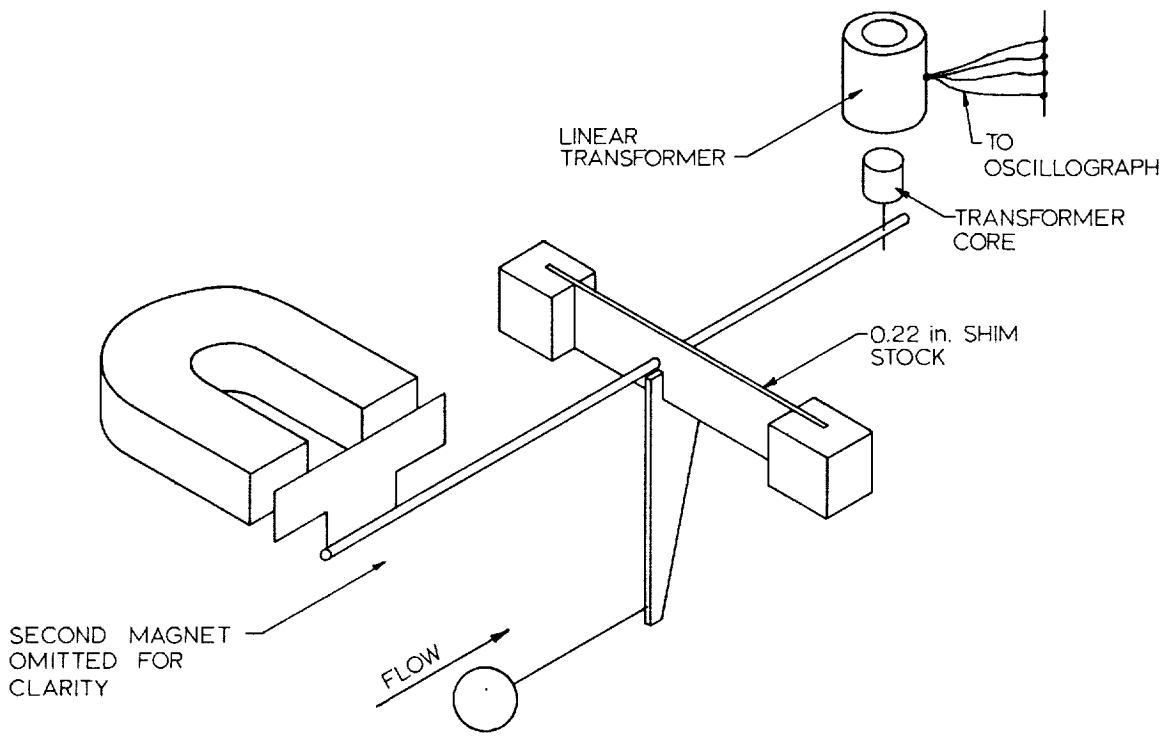

Figure 3.- Schematic of drag balance used in low density supersonic wind tunnel.

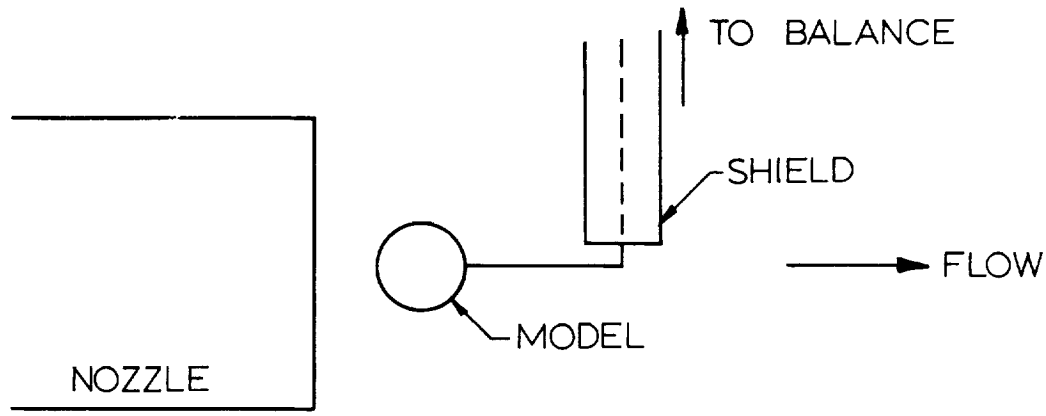

(a) Total force arrangement.

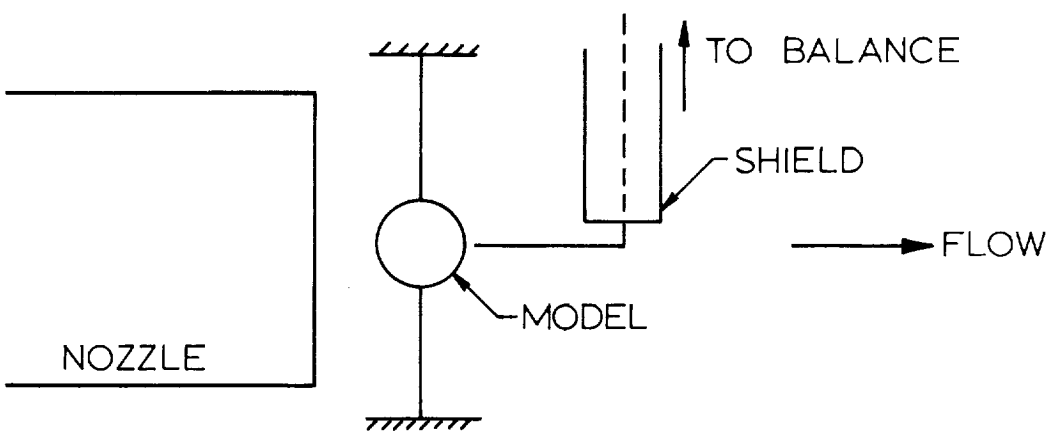

(b) Tare force arrangement.

Figure 4.- Schematic representation of suspension arrangement for force measurements.

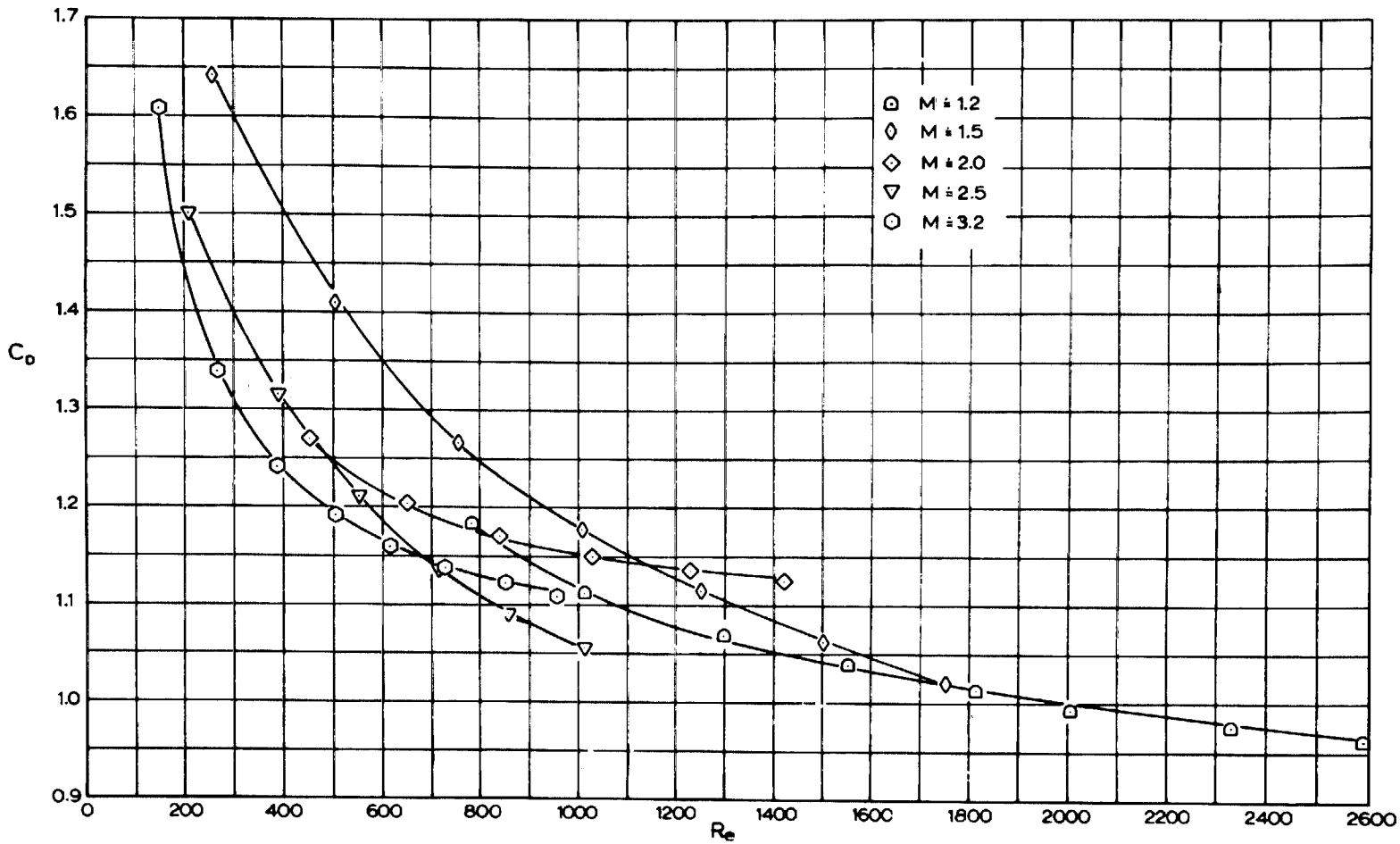

Figure 5.- Drag coefficient of a sphere in supersonic flow as a function of the free-stream Reynolds number.

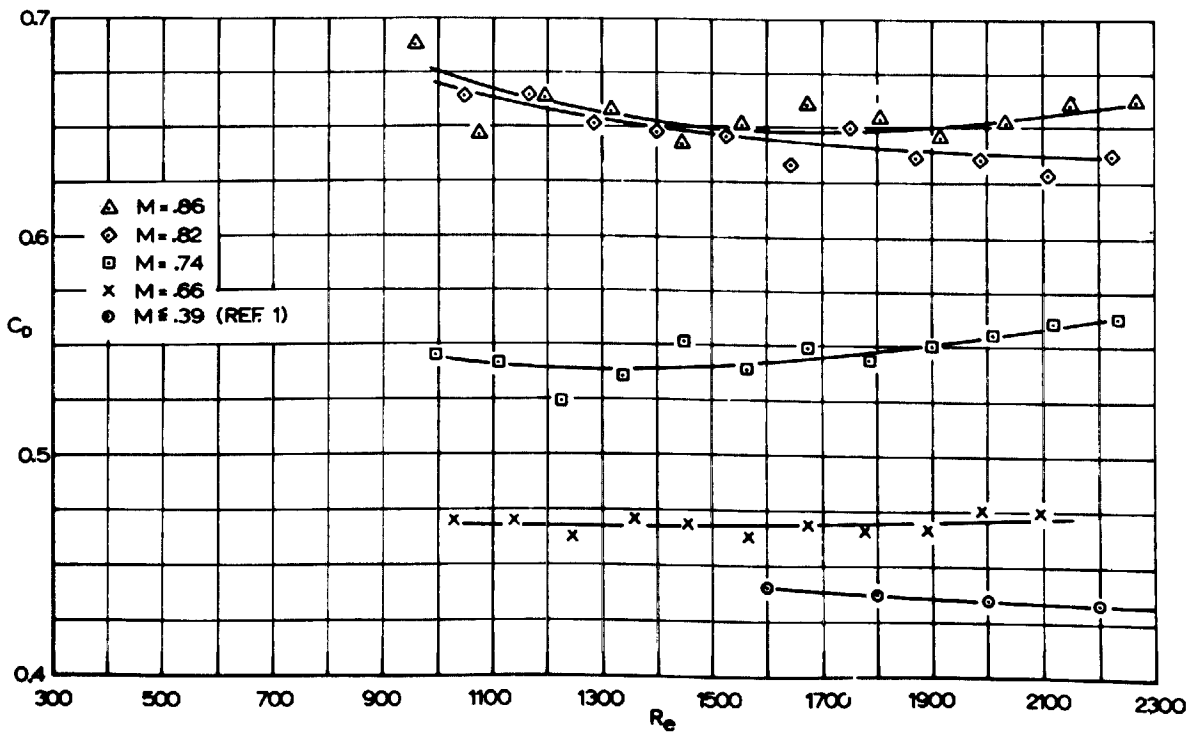

Figure 6.- Drag coefficient of a sphere in subsonic flow as a function of the free-stream Reynolds number.

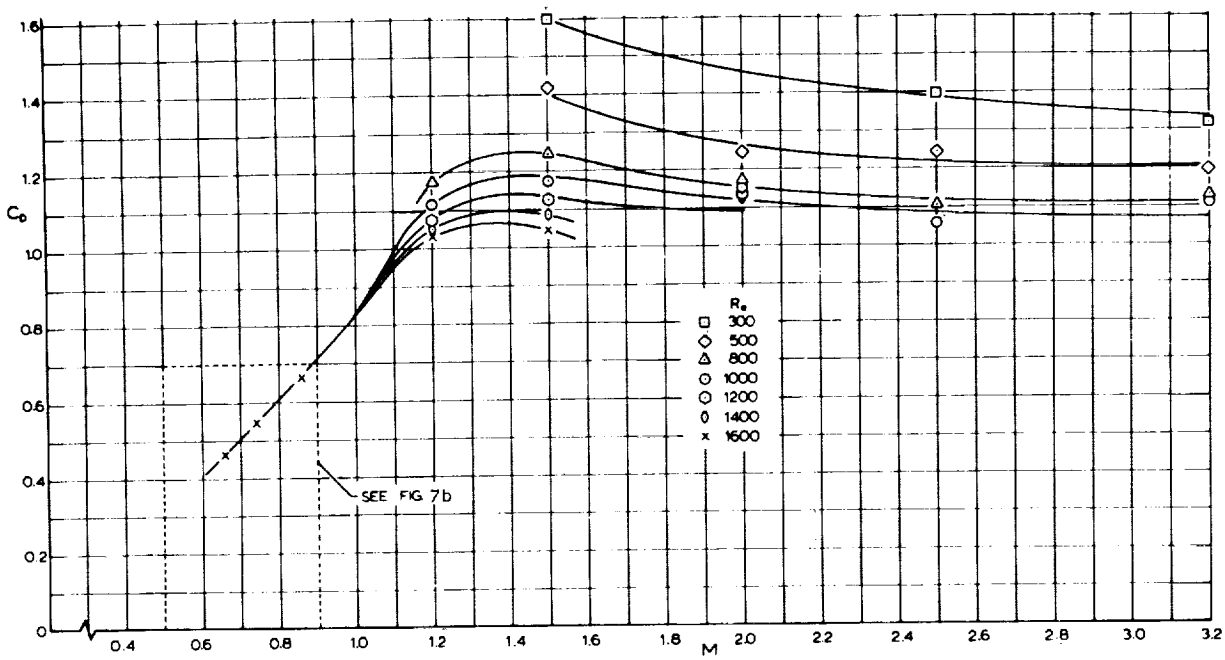

(a) $0.66 \leqq M \leqq 3.2$.

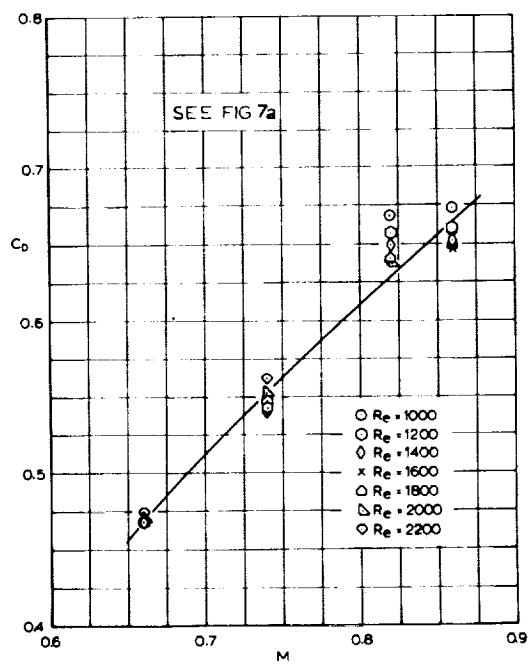

(b) $0.66 \leqq M \leqq 0.86$.

Figure 7.- Drag coefficient of a sphere as a function of the free-stream Mach number with Reynolds number as a parameter.

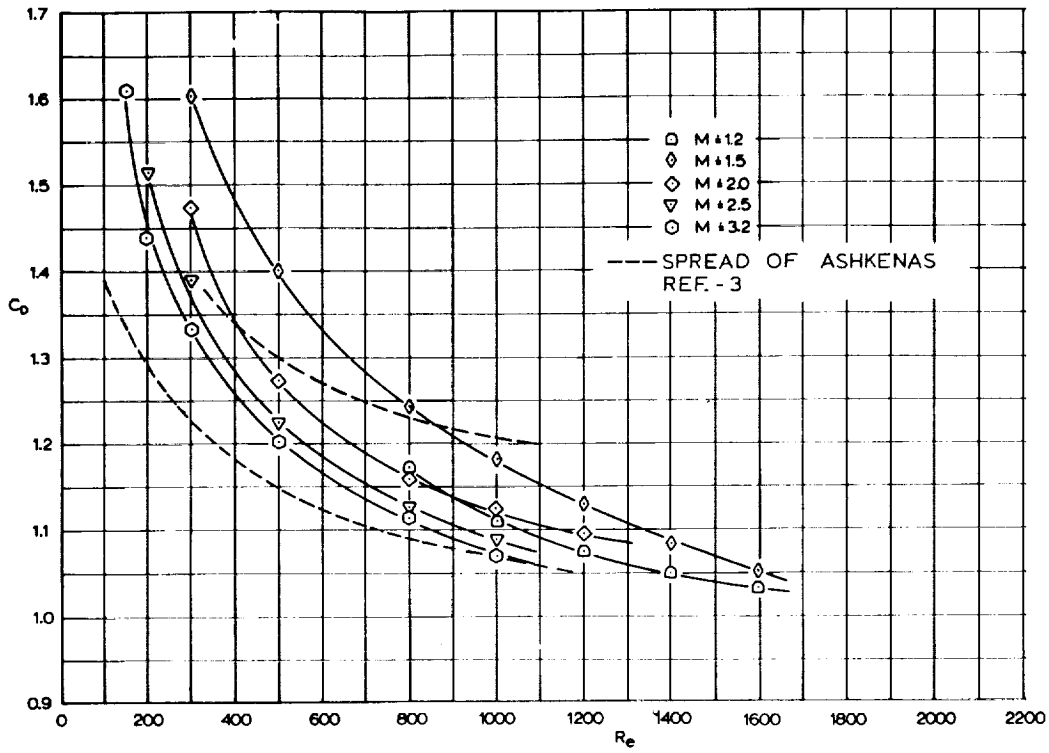

Figure 8.- Drag coefficient of a sphere in supersonic flow as a function of the free-stream Reynolds number.

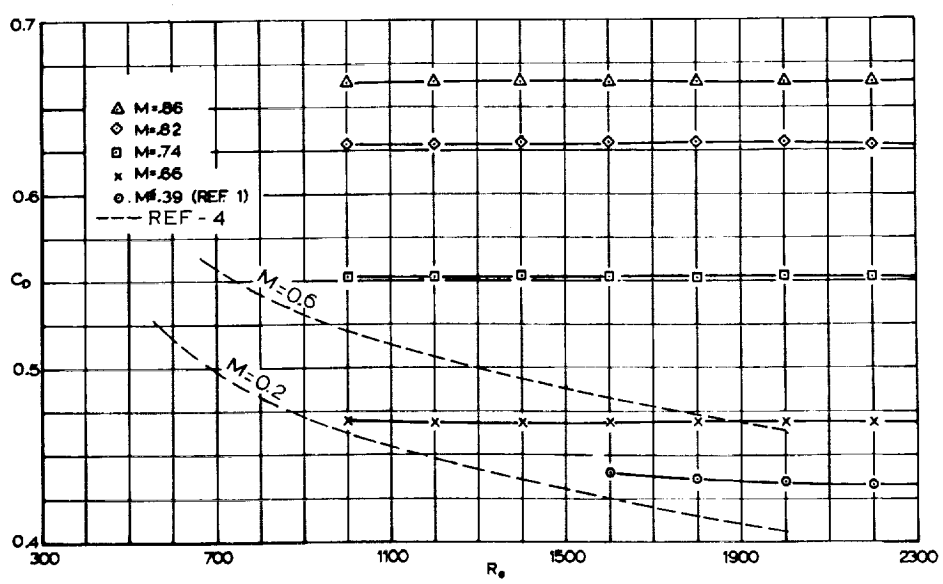

Figure 9.- Drag coefficient of a sphere in subsonic flow as a function of the free-stream Reynolds number.

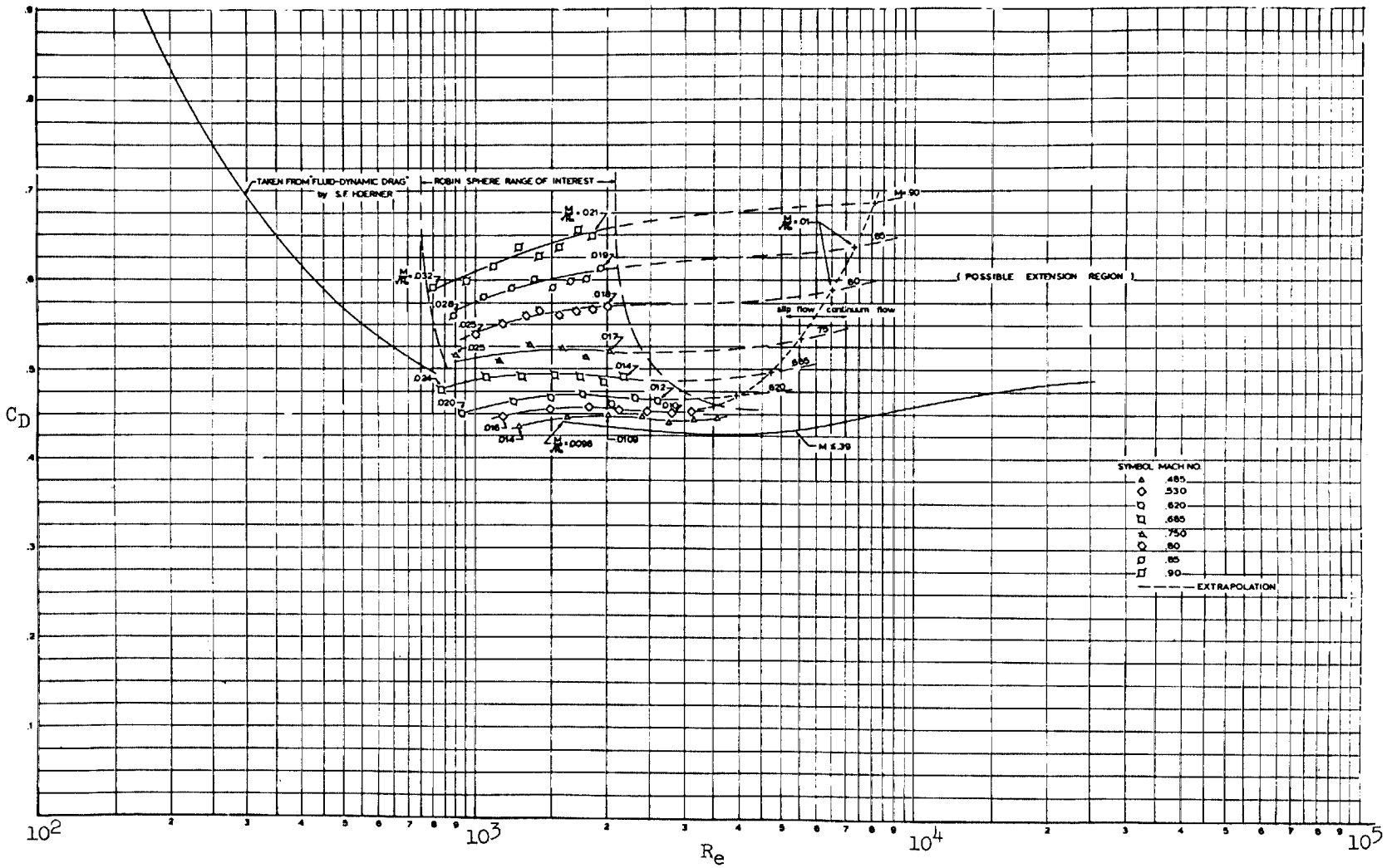

Figure 10.- Drag coefficients of a sphere at various Reynolds Numbers in subsonic flow (taken from Ref. 1, Fig. 19).

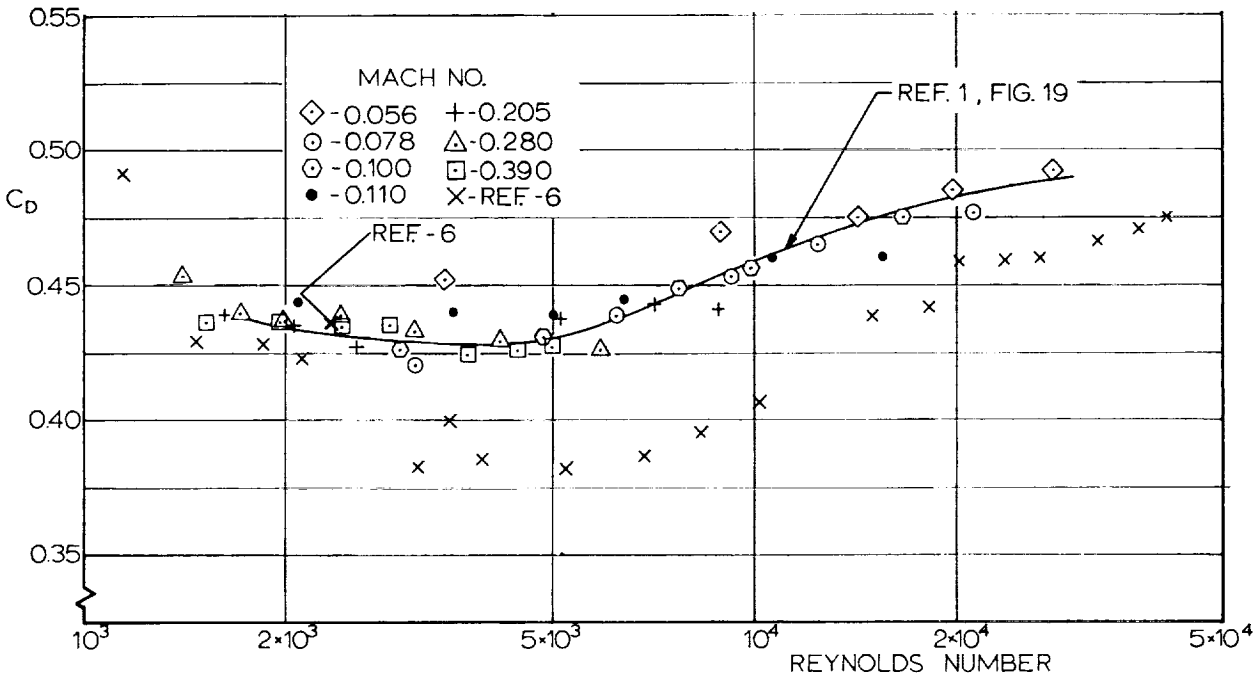

Figure 11.- Low subsonic drag coefficients measured at University of Minnesota compared with data taken from Ref. 6.

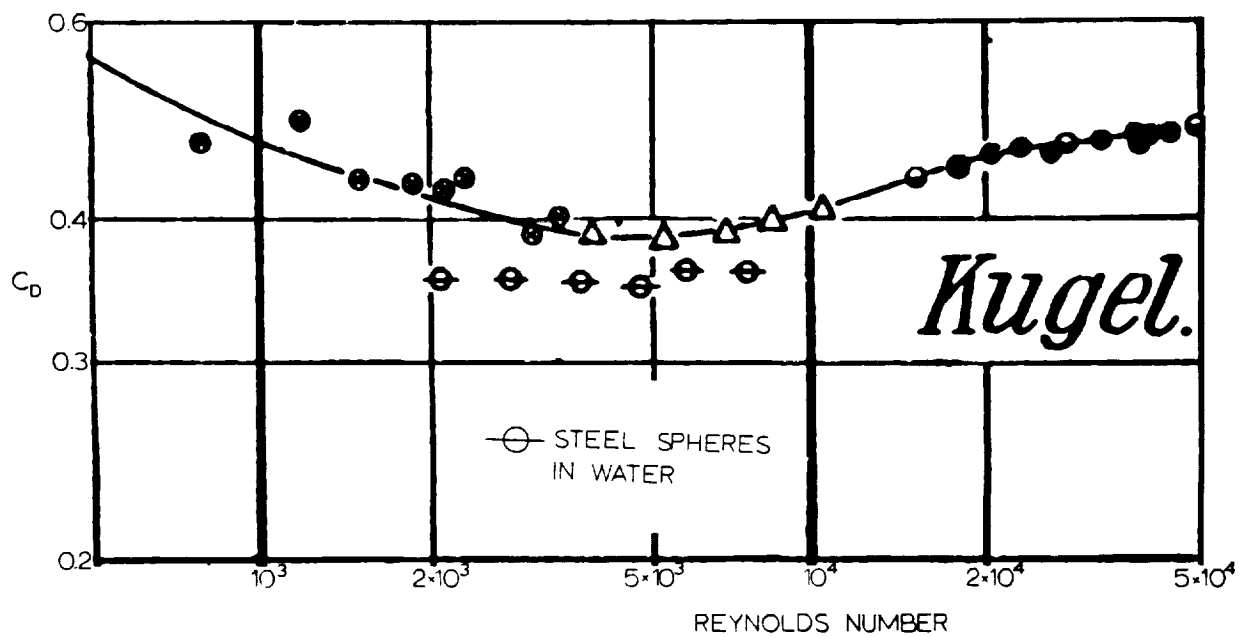

Figure 12.- Drag coefficients of a sphere in subsonic flow at Reynolds Number between 10^3 to 5×10^4. (Reproduced from Ref. 6.)

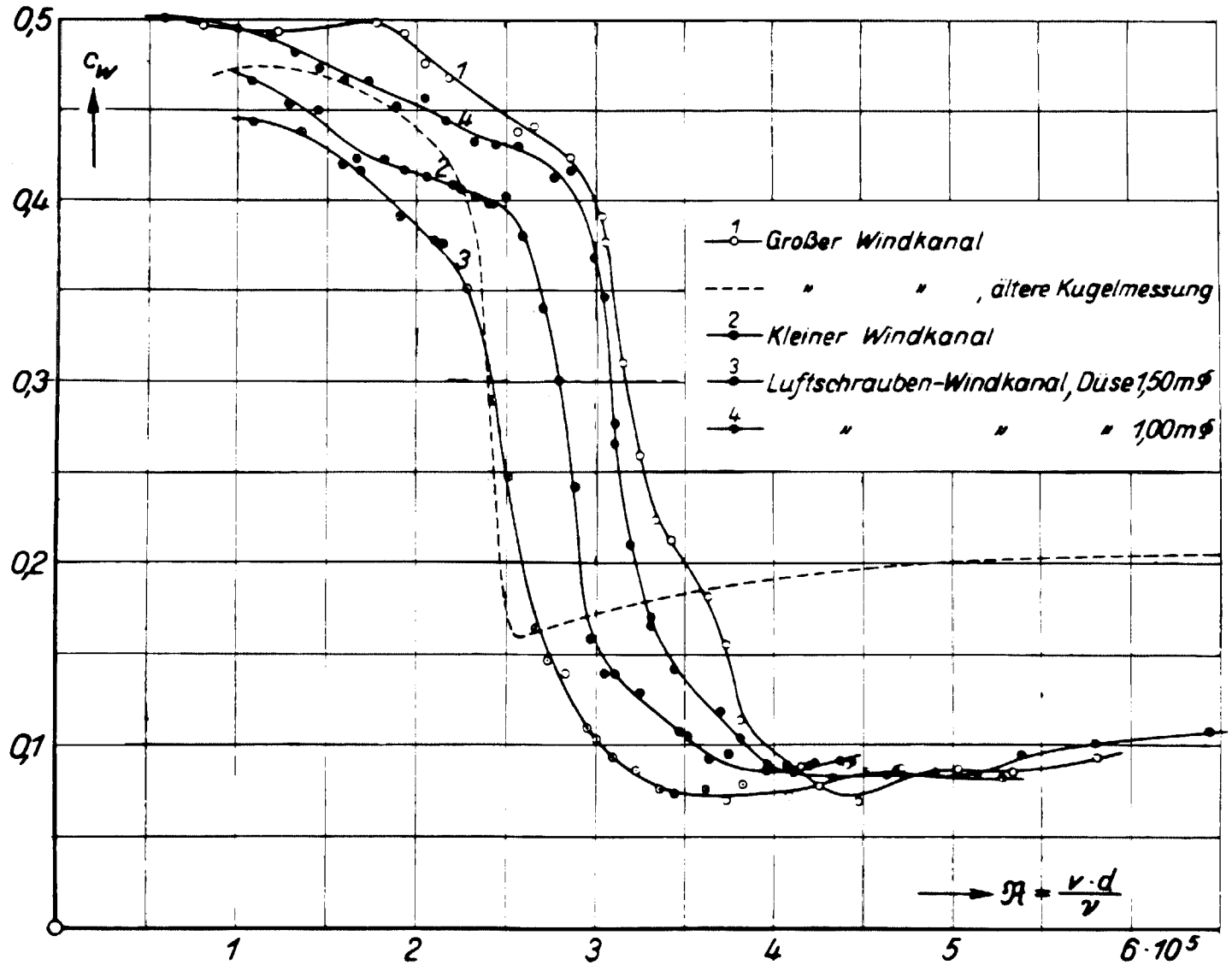

Figure 13.- Drag coefficients of a sphere in subsonic flow in the critical range measured in different windtunnels. (Reproduced from Ref. 7.)

HIGH-ALTITUDE ROBIN DATA-REDUCTION PROGRAM

By James Luers and Nicholas A. Engler

University of Dayton Research Institute
Dayton, Ohio

SUMMARY

The problem of computing winds and thermodynamic data utilizing the space-time coordinates of a falling sphere becomes complex when the apogeee of the sphere is over 100 km. This paper describes the methodology used in constructing the computer program.

ROBIN/ARCAS SYSTEM

The ROBIN/Arcas system consists of a ROBIN balloon, an Arcas rocket motor, and an AN/FPS-16 tracking radar. The ROBIN sphere is made of $\frac{1}{2}$- mil Mylar inflatable to a diameter of 1 meter containing an internally supported corner reflector. Packaged in a collapsed condition within the nose-cone of a meteorological rocket, it is ejected at the apogee of the rocket and inflated to a super pressure of approximately 10 millibars by vaporization of a liquid such as isopentane. Thus inflated, the ROBIN sphere is tracked from apogee to approximately 30 km altitude by an AN/FPS-16 high-precision tracking radar. The Arcas rocket motor is a 4.5-inch-diameter solid-propellant end-burning rocket capable of carrying the sphere payload to an altitude of 75 km. The FPS-16 tracking radar generates spherical space-time coordinates at digitized increments of 1/10 second. From the space-time coordinates, the meteorological parameters of density, wind, temperature, and pressure are deduced. A discussion of the ROBIN/Arcas system, with some of its advantages and shortcomings, is contained in reference 1.

Early results from the ROBIN/Arcas system whetted man's appetite to extend the passive sphere experiment to altitudes beyond the reach of the Arcas motor. To achieve this dream the Air Force Cambridge Research Laboratories (AFCRL) has experimented with a variety of boosted rocket motors. The most successful of these is the Viper-Dart rocket motor. The Viper-Dart rocket is capable of carrying the ROBIN payload to an apogee of 125 to 140 km. It was anticipated that the extended balloon apogee of 125 km would enable density and perhaps wind measurements to be extended to 100 km.

The data-reduction program designed by Engler (ref. 1) to reduce the data from ROBIN/Arcas flights produced accurate density and wind measurements below an altitude of 70 km. The high-altitude ROBIN/Viper-Dart system, however, produces balloon

velocities and accelerations much larger than the ROBIN/Arcas system. For this reason the smoothing techniques used in the 1965 ROBIN/Arcas program are not optimum for use with the ROBIN/Viper-Dart system. It has been shown by Engler (ref. 2) that the standard ROBIN/Arcas data-reduction program is not satisfactory for use with high-altitude flights. Accepting the recommendations of Mr. Engler, AFCRL has requested the University of Dayton Research Institute (UDRI) to develop a new ROBIN data-reduction program which would result in optimum density and wind measurement for high-altitude rocket launches as well as the standard Arcas rocket. It is the purpose of this paper to discuss the new data-reduction program, to explain the rationale and methodology used to design the program, and to discuss the errors in the winds and thermodynamic data that result from the use of this program.

PROGRAM SPECIFICATIONS

The preliminary specifications for the program consisted of the following items: (a) the program should be optimum for measuring density and wind in the 70 to 100 km region of the atmosphere assuming a balloon apogee of 125 km, (b) the program should also give accurate and reliable density measurements from 30 to 70 km, (c) even though the data-reduction technique need not be optimum for balloon apogees other than 125 km, other balloon apogees between 75 and 140 km should not result in a serious degradation of the meteorological parameters, (d) temperature and pressure accuracies should be commensurate with density accuracy, and (e) the program should accurately determine the altitude of balloon collapse so that density calculations can be terminated.

DENSITY AND WIND MEASUREMENTS

To obtain density, the drag force that the atmosphere exerts upon the sphere must be measured. In the altitude region from 70 to 100 km, the vertical velocities and accelerations are much larger than the horizontal velocities and accelerations. For this reason the drag acceleration is primarily in the vertical direction. Accurate density calculations are thus largely a result of the accuracy to which vertical velocities and accelerations can be measured.

Horizontal winds influence the sphere's trajectory by inducing horizontal excursions in its path in three-dimensional space. These horizontal excursions are used to reconstruct the wind profile. Thus, for measuring wind, the horizontal velocity and acceleration components must be determined accurately.

Since densities depend primarily on vertical measurements and winds depend primarily on horizontal measurements, it is possible to construct a data-reduction scheme which will optimize both wind and density measurements. The data-reduction scheme used to reduce Viper-Dart flights is so designed.

DENSITY

Density is computed by the following equation:

$$\rho = \frac{m\left(g - \ddot{z} - C_Z\right)}{\frac{1}{2}C_D A v\left(\dot{z} - W_Z\right) + V_B g} \tag{1}$$

The symbols are defined in the appendix. The computed density error is a result of the errors present in the parameters on the right side of equation (1). A negligible contribution to the error in density is made by V_B, C_Z, g, m, and A. The remaining variables which make a significant contribution to density error are C_D, $\dot{z}$, $\ddot{z}$, W_Z, and v.

DENSITY ERROR EQUATIONS

For the purpose of deriving an error equation for density, the density equation (eq. (1)) can be simplified to

$$\rho = \frac{m(g - \ddot{z})}{\frac{1}{2}C_D A\left(\dot{z} - W_Z\right)^2} \tag{2}$$

where v has been set equal to $\left(\dot{z} - W_Z\right)$ and both buoyancy and Coriolis force have been neglected.

Considering the error in density to be a function of the errors in C_D, W_Z, $\dot{z}$, and $\ddot{z}$ only and assuming further that the errors in the radar coordinates are independent and normally distributed with mean zero and variance σ, the error equation for the percent error in density is given by

$$\left[\frac{\sigma_\rho}{\rho}\right]^2 = \left[\frac{\sigma_{C_D}}{C_D}\right]^2 + \left[\frac{2\sigma_{W_Z}}{\dot{z} - W_Z}\right]^2 + \left[\frac{\sigma_{\ddot{z}}}{\ddot{z} - g}\right]^2 + \left[\frac{2\sigma_{\dot{z}}}{\dot{z} - W_Z}\right]^2 + \left[\frac{\dot{z}^2\left(\ddot{z} + \Delta\ddot{z} - g\right) - \left(\dot{z} - \Delta\dot{z}\right)^2\left(\ddot{z} - g\right)}{\left(\ddot{z} - g\right)\left(\dot{z} + \Delta\dot{z}\right)^2}\right]^2 \tag{3}$$

The object of the computer program as mentioned earlier is to minimize equation (3) in the altitude region from 70 to 100 km. Equation (3) cannot be minimized by minimizing each of the terms on the right-hand side of the equation because the last three terms are

interrelated. The first two terms, however, are independent and thus allow for individual minimization.

ERROR IN DRAG COEFFICIENT

There is no commonly accepted drag table in use today with known accuracy. Of the drag tables being used, disagreements as high as 15% to 20% exist in certain areas (ref. 3). As seen in figure 1, disagreement exists not only between the values of C_D for various drag tables (refs. 4 to 6) but also in the slope of the curves. The drag tables used in previous ROBIN programs designed by UDRI rely primarily on the work of Dr. Helmut Heinrich and others (ref. 5). The accuracy of this table is uncertain especially in areas where interpolation of the drag coefficient is necessary such as from Mach 0.7 to Mach 1.0. In an effort to evaluate the most recent drag table to appear in the literature (ref. 4), UDRI reinvestigated the drag-coefficient values of references 5 and 4. The table which appears as figure 2 is basically the work of reference 5 in the supersonic region and of reference 4 in the subsonic region. The impressive aspect of this drag table is the similar shapes of the C_D curves given as a function of Mach and Reynolds number even though the drag table was the result of two independent researchers using two different techniques for calculating drag. However, even though this drag table shows smooth consistent drag curves, it is impossible to quote specific accuracies of the drag table because of the conflicting results obtained by the other experimenters and because of the interpolated section of the table. The stated accuracies by the experimenters are as follows:

Goin and Lawrence: approximately 2%

Heinrich et al. (supersonic): maximum possible error ranges from ±2.3% to ±27.9%; however, actual errors are usually not the possible maximum

Since the accuracy of the drag table cannot be determined precisely, it is impossible to give an exact RMS error value for the percent error in density when reducing a high-altitude balloon flight. It is, however, possible to determine the error in density that results from the other terms of equation (3). Improvements and verifications of drag results will enable one at some future time to accurately state the true percent error in density.

VERTICAL WIND ERROR

The density error variance resulting from vertical winds is given by the expression $\left[\frac{2\sigma_{W_z}}{\dot{z} - W_z}\right]^2$. To a falling sphere, a vertical wind looks identical to a change in density.

As a result, a data-reduction program cannot distinguish density perturbations from vertical-wind oscillations. In order to compute densities, an assumption must be made either concerning vertical winds or concerning density perturbations in the atmosphere.

Assumption A: $W_z = 0$

Assuming no vertical motions in the atmosphere, equation (1) can be solved by substituting $W_z = 0$ on the right-hand side of equation (1) and evaluating all other terms by conventional means. Under this assumption, any vertical winds present in the atmosphere will appear as density oscillations. The relationship between vertical winds and density perturbations is exhibited in figure 3 for an escape altitude of 125 km. Care must be used in interpreting figure 3, however, because of the smoothing effect produced in the program. An example will clarify this point. If a sinusoidal vertical wind varying with altitude with amplitude of 5 m/sec is present at 60 km, then this vertical wind would be damped by the smoothing and appear in the printout as something smaller, approximately 2 m/sec amplitude. Since the program attributed the vertical motion to density perturbations, the result of an actual 5 m/sec vertical wind would, using figure 3, appear as a 2.4% density perturbation. To effectively determine what vertical wind could have caused a density perturbation in reduced data in addition to figure 3 one must know the reduction in magnitude of the vertical wind resulting from the smoothing technique applied, i.e., the frequency response of the program's smoothing filter to a sinusoidal vertical-wind oscillation.

Assumption B: $\rho = \rho_0 e^{\alpha z}$

If density is assumed to follow some mean path then perturbations from this path can be attributed to vertical winds. Since density varies exponentially with altitude, a mean exponential path is appropriate. Using this assumption, vertical winds can be computed by the equation

$$W_z = \frac{\ddot{z}_{th} - \ddot{z}_{emp}}{2K\dot{z}\rho_0 e^{\alpha z}} \tag{4}$$

A description of the variables in this equation and its application is given in reference 1.

Since, to the best of our knowledge, meteorologists accept density perturbations at least as much as they accept vertical winds, assumption A has been and will be used in this program.

NOISE AND BIAS ERROR TERMS

The remaining terms in the density error equation are given by

$$\left[\frac{2\sigma_{\dot{z}}}{\dot{z} - W_z}\right]^2 + \left[\frac{\sigma_{\ddot{z}}}{\ddot{z} - g}\right]^2 + \left[\frac{\dot{z}^2(\ddot{z} + \Delta\ddot{z} - g) - (\dot{z} - \Delta\dot{z})^2(\ddot{z} - g)}{(\ddot{z} - g)(\dot{z} + \Delta\dot{z})^2}\right]^2 \tag{5}$$

The first two terms of equation (5) are the result of the noise present in the radar coordinates (noise error). The third term is the error in density resulting when the smoothing function does not adequately represent the true path of the sphere. In this case, a bias error will result in density since the smoothing function will not fit the real perturbation in the path.

NOISE ERROR TERMS

The noise errors in vertical velocity $(\sigma_{\dot{z}})$ and acceleration $(\sigma_{\ddot{z}})$ depend upon

The noise present in the radar coordinates (σ_z)
The type of smoothing technique used
The number of data points (N) used in the smoothing process
The time spacing between consecutive data points (Δt)

For an FPS-16 radar, σ_z varies between 10 and 15 meters depending upon slant range and Δt is generally fixed at 0.1 second.

ESTIMATION OF NOISE ERROR

There are two methods of evaluating the noise error terms:

(a) Consider an actual flight of a passive sphere tracked by two identical FPS-16 radars. For an N and a smoothing function, density can be calculated for each of the two radar tracks. By calculating the RMS difference between the densities measured by the two radars, the noise error terms can be determined. Since the same bias error will appear in the density computations from each of the two radar tracks, differencing the densities determines only the noise error terms.

(b) The noise error terms can also be calculated by formulas which directly relate $\sigma_{\dot{z}}$ and $\sigma_{\ddot{z}}$ to N, Δt, σ_z, and the smoothing function. The formulas for polynomial[1] smoothing functions of degrees one and two are given in the following equations:

---

[1]Polynomials were chosen as the proper class of smoothing functions. This decision was based on previous work showing the polynomial yielding less noise error than other functions.

Noise Error Equations

Velocity:

Linear fit $$\sigma^2_{\dot{x}_1} = \frac{12}{N(N^2 - 1)} \frac{\sigma^2_x}{\Delta t^2}$$

Cubic fit $$\sigma^2_{\dot{x}_3} = \left[\frac{12}{N(N^2 - 1)} + \frac{7(3N^2 - 7)^2(N - 4)!}{(N + 3)!}\right] \frac{\sigma^2_x}{\Delta t^2}$$

Quadratic fit Same as linear fit $\sigma^2_{\dot{x}_2} = \sigma^2_{\dot{x}_1}$

Acceleration:

Linear-linear fit $$\sigma^2_{\ddot{x}_{11}} = \frac{12}{M(M^2 - 1)} \frac{\sigma^2_{\dot{x}_1}}{\Delta t_1^2}$$

Cubic-linear fit $$\sigma^2_{\ddot{x}_{31}} = \frac{12}{M(M^2 - 1)} \frac{\sigma^2_{\dot{x}_3}}{\Delta t_1^2}$$

Cubic-cubic fit $$\sigma^2_{\ddot{x}_{33}} = \left[\frac{12}{M(M^2 - 1)} + \frac{7(3M^2 - 7)^2(M - 4)!}{(M + 3)!}\right] \frac{\sigma^2_{\dot{x}_3}}{\Delta t_1^2}$$

Linear-cubic fit $$\sigma^2_{\ddot{x}_{13}} = \left[\frac{12}{M(M^2 - 1)} + \frac{7(3M^2 - 7)^2(M - 4)!}{(M + 3)!}\right] \frac{\sigma^2_{\dot{x}_1}}{\Delta t_1^2}$$

Quadratic (second derivative) $$\sigma^2_{\ddot{x}_2} = \left[\frac{720}{N^5 - 5N^3 + 4N}\right] \frac{\sigma^2_x}{\Delta t^4} \qquad (6)$$

(Linear polynomial smoothing is defined as fitting a linear polynomial over N data points and assigning the slope of the fit to be the velocity at the midpoint $\frac{N+1}{2}$ of the interval. Linear-linear smoothing to obtain acceleration is described as fitting N position points to a polynomial to obtain velocities and obtain acceleration from velocities in a like manner. A cubic-linear fit is described as fitting N position points to a cubic polynomial taking the slope at the midpoint as the velocity and fitting M of these velocities by a linear polynomial to obtain acceleration; similarly, for cubic-cubic and linear-cubic

smoothing techniques. Quadratic smoothing is defined as fitting a second-degree polynominal to position points and evaluating the first and second derivatives of the polynomial, at the midpoint, as the velocity and acceleration, respectively.) The validity of these formulas has been established by comparisons to RMS errors obtained by method (a).

BIAS ERROR TERMS

The bias errors in velocity and acceleration ($\Delta\dot{z}, \Delta\ddot{z}$) depend upon

- The type of smoothing technique used
- The number of data points (N) used in the smoothing process
- The time spacing between consecutive data points (Δt)
- The true position field, which itself is a function of the balloon apogee

ESTIMATION OF BIAS ERRORS

For a given apogee, bias errors can be determined by following the flow chart of figure 4. Given a drag table and balloon apogee, by assuming the sphere fell in the 1962 Standard Atmosphere, the equations of motion can be integrated to obtain the theoretical path of the sphere. The vertical position z, velocity $\dot{z}$, and acceleration $\ddot{z}$ are determined by the theoretical trajectory. One now treats the z position as a function of time as though it were the radar coordinates and applies the smoothing routine using N data points and the degree polynomial P. The smoothed z, $\dot{z}$, and $\ddot{z}$ coordinates differ from the theoretical z, $\dot{z}$, and $\ddot{z}$ coordinates only because of the bias error resulting from the smoothing technique. (No noise has been introduced into the data.) The smoothed coordinates are then substituted into the equations of motion using the same drag table, and density is computed. The only difference between this computed density and the original input density, that is, the 1962 Standard Atmosphere density, is due to the bias error induced by the smoothing function. The percent bias error in density is then plotted as the ratio of the computed density to the standard density.

DETERMINATION OF OPTIMUM SMOOTHING TECHNIQUE

The choice of the optimum polynomial and interval for use in the high-altitude program was derived by using the above techniques. Initially, an escape altitude of 125 km was chosen. For each type double smoothing (linear-linear, cubic-linear, linear-cubic, cubic-cubic) the total error in density, defined as the square root of the sum of the noise and bias errors squared, was computed for all possible combinations of N and M. The

noise error was calculated by method (b) (the formulas as given in equations (6)) using $\Delta t = 1/2$ second and σ_Z equals 15 meters. The bias error was computed as described in figure 4. Figures 5, 6, and 7 are plots showing the percent bias error (the deviation of the density ratio from 1) and the 1σ confidence bands of the noise error about the bias. None of the combinations of the degree polynomials and smoothing intervals met the design requirements of 5% density accuracy at 100 km. A compromise was necessary to either reduce the altitude requirements, say to 95 km, maintaining the 5% design accuracy requirements or slackening the accuracy requirements to say 9% while maintaining the 100 km altitude range. The former choice was made. Careful analysis of total error plots for all combinations of degree polynomial and N and M resulted in the choice of the 19-21 linear-cubic combination as optimum.

Total error plots were generated in the same fashion using a quadratic polynomial fit and its first and second derivatives for velocity and acceleration. The best smoothing interval for using a quadratic was determined to be 31 data points (fig. 7). In comparing the optimum quadratic and the optimum linear-cubic smoothing techniques, it is easily seen that the 19-21 linear-cubic produced significantly better results in the altitude region from 70 to 100 km. The probable explanation for this is as follows. By fitting two different functions, one to get velocity and the other to get acceleration, it is possible to partially compensate for, say, a positive bias in density due to a velocity error by using a different degree polynomial or different interval to generate accelerations which will produce a negative density bias. This advantage is not present when using a single function for smoothing.

OPTIMUM FITTING FUNCTIONS TO ACQUIRE DENSITIES

After careful consideration of the results of all the above analysis it was decided that the 19-21 linear-cubic smoothing was the optimum fitting function to acquire densities.

SUMMARY OF DENSITY ERRORS USING OPTIMUM REDUCTION

The total percent error in density resulting from a computation using the high-altitude ROBIN program with optimum smoothing cannot be precisely determined because of the unknown accuracy of the drag table and the occurrence of unknown vertical winds. However, the other contributing terms to density errors have been accurately determined using the optimum smoothing interval. They are less than 1% bias error from 30 to 70 km with a noise error of 3% and a bias error from 3% to 5% from 70 to 95 km with a noise error less than 3%.

WINDS

The equation used for computing wind with the falling sphere method is given as

$$W_x = \dot{x} - \frac{(\dot{z} - W_z)\left(\ddot{x} + C_x - g_x - \frac{g_x V_B \rho}{m}\right)}{\ddot{z} + C_z - g_z - \frac{g_z V_B \rho}{m}} \tag{7}$$

The variables in equation (7) which may contribute significantly to wind errors are the horizontal and vertical components of velocity and acceleration.

WIND ERROR EQUATIONS

Having retained only those variables which significantly influence the error in a computed wind, the wind equation simplifies to

$$W_x = \dot{x} - \frac{\ddot{x}\dot{z}}{\ddot{z} - g} \tag{8}$$

The first order of approximation to an error in W_x resulting from the errors in the parameters is given by the following equation:

$$dW_x = d\dot{x} - \frac{\dot{z}}{\ddot{z} - g} d\ddot{x} - \frac{\ddot{x}}{\ddot{z} - g} d\dot{z} + \frac{\ddot{x}\dot{z}}{(\ddot{z} - g)^2} d\ddot{z} \tag{9}$$

If the differential error components are considered as noise error with normal distribution, then by taking the variance of equation (9) the noise error in a wind calculation is given as

$$\sigma^2_{W_x} = \sigma^2_{\dot{x}} + \left[\frac{\dot{z}}{\ddot{z} - g}\right]^2 \sigma^2_{\ddot{x}} + \left[\frac{\ddot{x}}{\ddot{z} - g}\right]^2 \sigma^2_{\dot{z}} + \left[\frac{\ddot{x}\dot{z}}{(\ddot{z} - g)^2}\right]^2 \sigma^2_{\ddot{z}} \tag{10}$$

where $\sigma_{\dot{x}}$, $\sigma_{\ddot{x}}$, $\sigma_{\dot{z}}$, and $\sigma_{\ddot{z}}$ are the noise errors in velocity and acceleration due to the noise in the radar data. To determine the bias of a wind measurement resulting from the bias (oversmoothed) velocity and acceleration measurements, equation (9) is again applied. Considering the component differentials as bias error, the square of the bias wind error is given as

$$\Delta^2 W_x = \left[\Delta\dot{x} - \frac{\dot{z}}{\ddot{z} - g} \Delta\ddot{x} - \frac{\ddot{x}}{\ddot{z} - g} \Delta\dot{z} + \frac{\ddot{x}\dot{z}}{(\ddot{z} - g)^2} \Delta\ddot{z}\right]^2 \tag{11}$$

where the Δx, etc., refers to the bias error in the x velocity component. The total wind error $\left(\sigma_{W_{x_{total}}}\right)$ is defined as the square root of the sum of the noise errror variance plus the bias square error and is given as

$$\sigma^2_{W_{x_{total}}} = \sigma^2_{W_x} + \Delta^2 W_x \tag{12}$$

The problem simply stated is to determine the type smoothing (degree) and smoothing intervals which minimize equation (12). As in the case of the density smoothing the noise error will decrease as the smoothing interval increases, and the bias error increases as the smoothing interval increases so that a minimum does exist for equation (12).

MINIMIZATION OF TOTAL WIND ERROR

The calculation of noise error for the wind computation uses equations (6). However, the calculation of the bias error cannot use figure 4 because, with such a variety of wind profiles in nature, choosing one profile to be representative would not be realistic. Besides it was felt that the use of the following bias equations would be more precise:

Bias Error Equations

$$\left.\begin{array}{ll}
\multicolumn{2}{l}{\text{Position assumed 4th degree over } N \text{ data points, i.e.,}} \\
\multicolumn{2}{r}{x = A_0 + A_1 t + A_2 t^2 + A_3 t^3 + A_4 t^4} \\
\multicolumn{2}{l}{\text{Velocity assumed cubic over } M \text{ data points, i.e.,}} \\
\multicolumn{2}{r}{\dot{x} = B_0 + B_1 t + B_2 t^2 + B_3 t^3} \\
\text{Velocity:} & \\
\quad \text{Linear fit} & \Delta\dot{x}_1 = \dfrac{A_3 \Delta t^2 \left(3N^2 - 7\right)}{20} \\
\quad \text{Cubic fit} & \Delta\dot{x}_3 = 0 \\
\text{Acceleration:} & \\
\quad \text{Linear-linear} & \Delta\ddot{x}_{11} = \ddot{x}_{33} - \ddot{x}_{11} \\
\quad \text{Cubic-linear} & \Delta\ddot{x}_{31} = \dfrac{B_3 \Delta t_1^2 \left(3M^2 - 7\right)}{20} \\
\quad \text{Cubic-cubic} & \Delta\ddot{x}_{33} = 0
\end{array}\right\} \tag{13}$$

To use these equations requires a knowledge of the position field of the balloon. This was accomplished by a separate program which utilizes experimental data to compute the coefficients A_3 and A_5. It is beyond the scope of this paper to describe that program.

DETERMINATION OF OPTIMUM SMOOTHING FUNCTIONS

The optimum double smoothing technique is that combination of degree polynomials (cubic-cubic, cubic-linear, linear-linear) and smoothing intervals (N and M) which gives the minimum total wind error. Plots of the total wind error for each type double smoothing and for N-M values of 51-43, 53-11, and 53-25 are presented in figures 8 to 10. These are merely three illustrations of all the possible combinations for feasible values of N and M. After analyzing plots of the types illustrated by figures 8 to 10, it was determined that the 51-43 cubic-cubic smoothing provides optimum wind reduction.

SUMMARY OF WIND ERRORS USING OPTIMUM REDUCTION

With the type smoothing described above, the total wind error remains less than 10 m/sec to altitudes of nearly 100 km. The amount of detail that can be observed at the very high altitudes is, however, limited because of the large altitude layer used in the smoothing. The frequency response curves presented as figure 11 indicate the detail that can be observed. Plotted in this figure is the ratio of the amplitude of a sinusoidal wave after passing through the smoothing filter to the true amplitude of the original. Each curve gives the ratio as a function of wavelength at a specific altitude. For example, at 90 km altitude the amplitude of a 10 km vertical wave would appear to be only 1/5 the amplitude in the reduced data. A 20 km vertical wave would retain 65 percent of its amplitude in the reduced data. As seen from figure 11, for 70 km, wavelengths less than 10 km are largely destroyed so that only a mean wind profile can be ascertained. Below 70 km, wavelengths of 5 km and less will appear in the reduced data.

OPTIMUM PROGRAM DENSITY RESULTS

A series of three Viper-Dart flights were flown at Eglin Air Force Base, Florida, on February 18, 1968, at 18:00, 19:00, and 20:00 zulu. Each flight was tracked by two FPS-16 radars. The flights are identified as Viper-Dart 11, 12, and 13 and the radars as radar 23 and 27. Figure 12 shows the density ratio (compared with the 1962 Standard Atmosphere) for each track of the three flights. For each of the flights, there is excellent agreement between the two FPS-16 radar tracks. The small differences in densities that are observed are commensurate with the noise errors predicted for the 19-21 linear-cubic

smoothing. There are, however, variations in density as observed from flights 1 hour apart, particularly in the altitude region from 62 to 54 km. The cause of these differences is not known. Possible causes are

(a) An actual time fluctuation in density
(b) Special variation in density between the paths of the three spheres
(c) Inaccuracy in the drag table being experienced at different altitudes for the three flights
(d) A change in the vertical motions of the atmosphere

These discrepancies in density, 1 hour apart, are not due to the inability of the radar to accurately track the spheres. Comparison of densities from the two tracks of the same balloon clearly rules this out. Nor are the density discrepancies thought to be a result of balloon collapse or elongation. All balloon collapse checks indicate the balloon is still spherically inflated to at least a 45 km altitude.

OPTIMUM PROGRAM WIND RESULTS

Figures 13 and 14 are plots of the W_x and W_y components for each of the three flights. Both the W_x and W_y components obtained from both tracks of Viper-Dart 11 show nearly identical agreement. Viper-Dart 12 shows good agreement at altitudes below 85 km but only fair agreement above. Viper-Dart 13 gives good agreement only to 84 km. The cause of this decrease in agreement which is beyond what one should anticipate from the total error plots for 51-43 cubic-cubic smoothing (fig. 8) has been investigated and the following results obtained.

The tracks of radar 23 from both Viper-Dart 12 and Viper-Dart 13 flights show large oscillations which did not appear in the tracks of radar 27 from the same flights. Previous experience with FPS-16 tracking data indicates that the oscillations are probably due to a low servo-bandwidth setting. The fact that radar 27 produces a smooth nonoscillating track indicates the oscillations are not real. Further investigation of the effect of the servo on tracking of passive spheres is in order.

SUMMARY OF RESULTS

Essentially there are three ways of determining the accuracy of the density and wind data: equations (6) and (13) and the model simulation outlined in figure 4. The assumptions made in applying equations (6) and (13) and the model given in figure 4 are not precisely met by the data but are exact enough for their purpose, which was to obtain the optimum smoothing technique. The use of double track flights to obtain errors only gives the noise error of the system. The dual tracking wind data shows that the radars need to

be well tuned in order to acquire winds, and that the tracking problem is more critical to winds than to density. Flights close together in time and space should yield system error information provided the time and space separation is small enough to rule out actual changes. One hour apart for density should be small enough to pick up the system errors. Comparison of the curves in figure 12 indicates that there are system errors in density. These system errors can conceivably come from the tracking radar, but they are larger than the equations predict. The system errors are believed to come probably from other elements of the system, sphere shape, or drag table. To strengthen this conclusion, the wind plots (figs. 13 and 14) have to be examined. The accuracy of the wind data does not depend upon the drag table or sphere shape (the last is almost true) but depends rather heavily upon the tracking radar. Figures 13 and 14 show that the wind repeatability is good, which proves that the tracking is good. Therefore, the conclusion is made that the discrepancy in density is not due to radar tracking but to other elements in the system. The dual tracked data agrees well with the noise errors predicted by equation (5) for density and by equation (10) for winds. There is no other proof given here that the predicted bias errors are correct. This proof could come from simultaneous flights of different type sensors.

TEMPERATURE AND PRESSURE

Since the ROBIN is a density and wind sensor, the program optimized these variables. Temperature and pressure errors fall where they may. The results of these parameters for the Viper-Dart flights 11, 12, and 13 are given in figures 15 and 16 without comment.

APPENDIX

SYMBOLS

Units are not given in the symbol list but any consistent set of units may be used in the equations.

A	cross-sectional area of sphere
AMP	amplitude
A_n, B_n	coefficients in bias error equations, $n = 0,1,2,\ldots$ (see eqs. (13))
C_D	drag coefficient
C_x, C_z	Coriolis acceleration in x- and z-direction, respectively
g	gravitational acceleration
g_x, g_z	gravitational acceleration in x- and z-direction, respectively
K	balloon constant
M	number of data points used in acceleration smoothing process
m	mass of sphere
N	number of data points used in velocity smoothing process
t	time
Δt	time spacing between consecutive position data points
Δt_1	time spacing between consecutive volume data points
V_B	volume of balloon
v	relative velocity of balloon, $\left[\left(\dot{x} - W_x\right)^2 + \left(\dot{y} - W_y\right)^2 + \left(\dot{z} - W_z\right)^2\right]^{1/2}$

W_x, W_y	wind velocity in x- and y-direction, respectively
W_z	vertical wind
x,y,z	position coordinates of radar
$\dot{x}$	balloon velocity in x-direction
$\ddot{x}$	balloon acceleration in x-direction
$\dot{y}$	balloon velocity in y-direction
$\dot{z}$	vertical velocity
$\ddot{z}$	vertical acceleration
$\ddot{z}_{th}, \ddot{z}_{emp}$	theoretical and empirical vertical acceleration, respectively
α	density gradient constant
Δq	bias error of parameter q
ρ	density
ρ_0	initial density
σ_q	variance of parameter q

REFERENCES

1. Engler, Nicholas A.: Development of Methods To Determine Winds, Density, Pressure, and Temperature From the ROBIN Falling Balloon. AFCRL-65-448, U.S. Air Force, May 1965. (Available from DDC as AD 630 200.)

2. Engler, Nicholas A.: Report on High Altitude ROBIN Flights, October 1966. AFCRL-67-0433, U.S. Air Force, May 1967. (Available from DDC as AD 657 810.)

3. Luers, J. K.: Estimation of Errors in Density and Temperature Measured by the High Altitude ROBIN Sphere. Proceedings of the Third National Conference on Aerospace Meteorology, Amer. Meteorol. Soc., 1968, pp. 472-477.

4. Goin, Kennith L.; and Lawrence, W. R.: Subsonic Drag of Spheres at Reynolds Numbers From 200 to 10,000. AIAA J. (Tech. Notes), vol. 6, no. 5, May 1968, pp. 961-962.

5. Heinrich, H. G.; Niccum, R. J.; Haak, E. L.; Jamison, L. R.; and George, R. L.: Modification of the Robin Meteorological Balloon. Vol. II – Drag Evaluations. AFCRL-65-734(II), U.S. Air Force, Sept. 30, 1965. (Available from DDC as AD 629 775.)

6. Peterson, J. W.; Hansen, W. H.; McWatters, K. D.; and Bonfanti, G.: Atmospheric Measurements Over Kwajalein Using Falling Spheres. NASA CR-218, 1965.

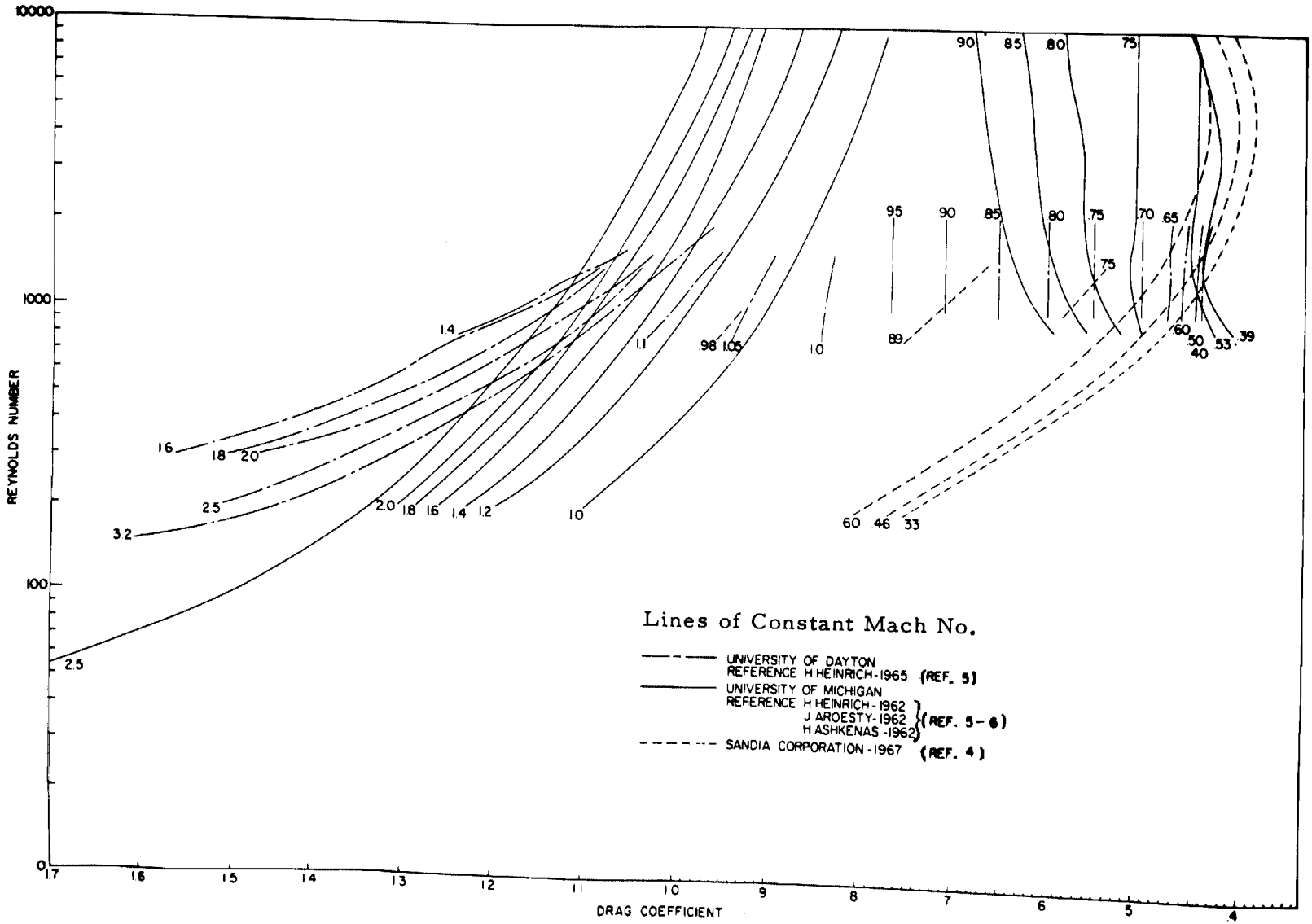

Figure 1.- Drag coefficient as a function of Reynolds number for lines of constant Mach number.

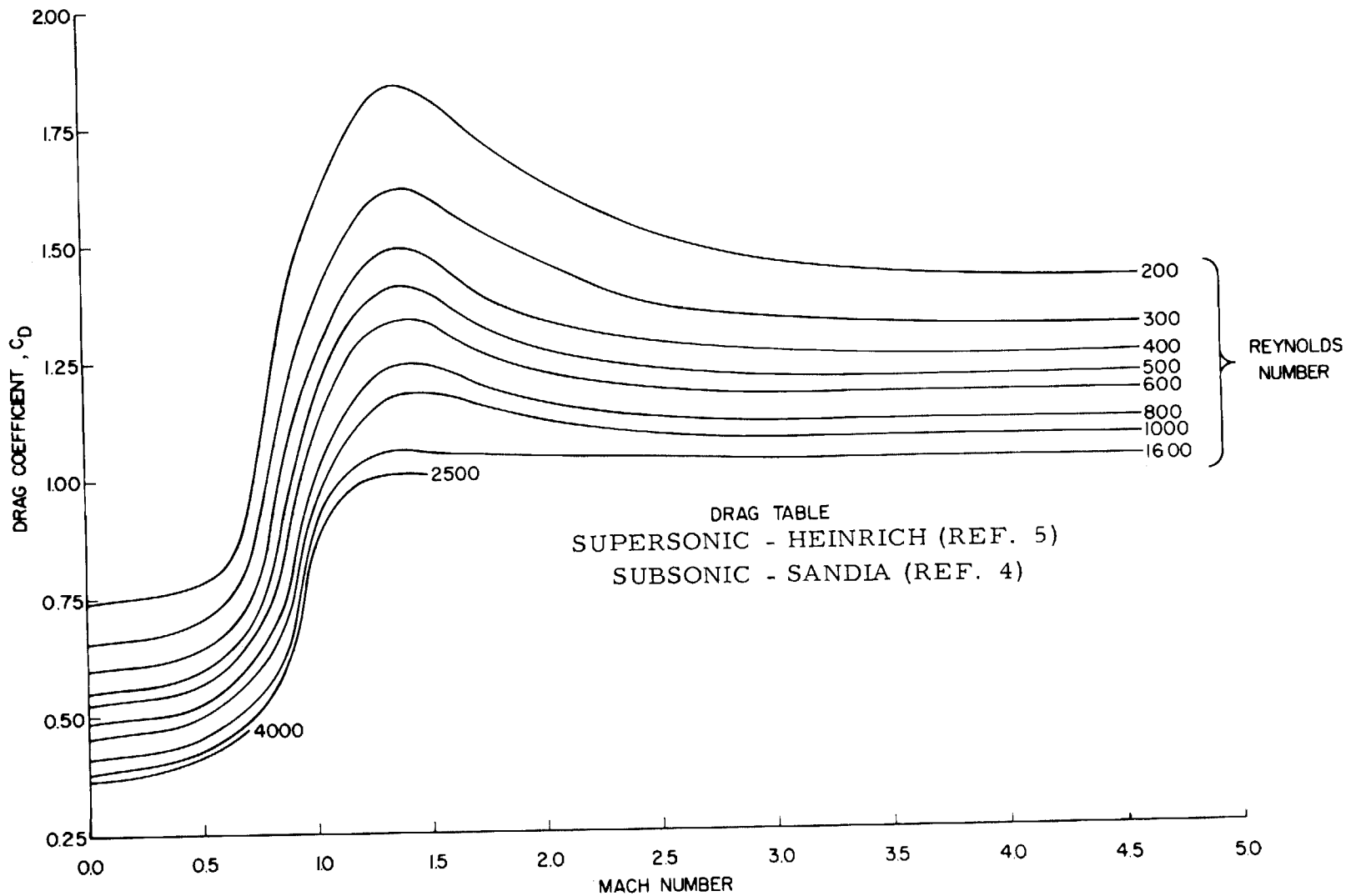

Figure 2.- Drag table derived from Heinrich et al. supersonic data (ref. 5) and Goin and Lawrence subsonic data (ref. 4).

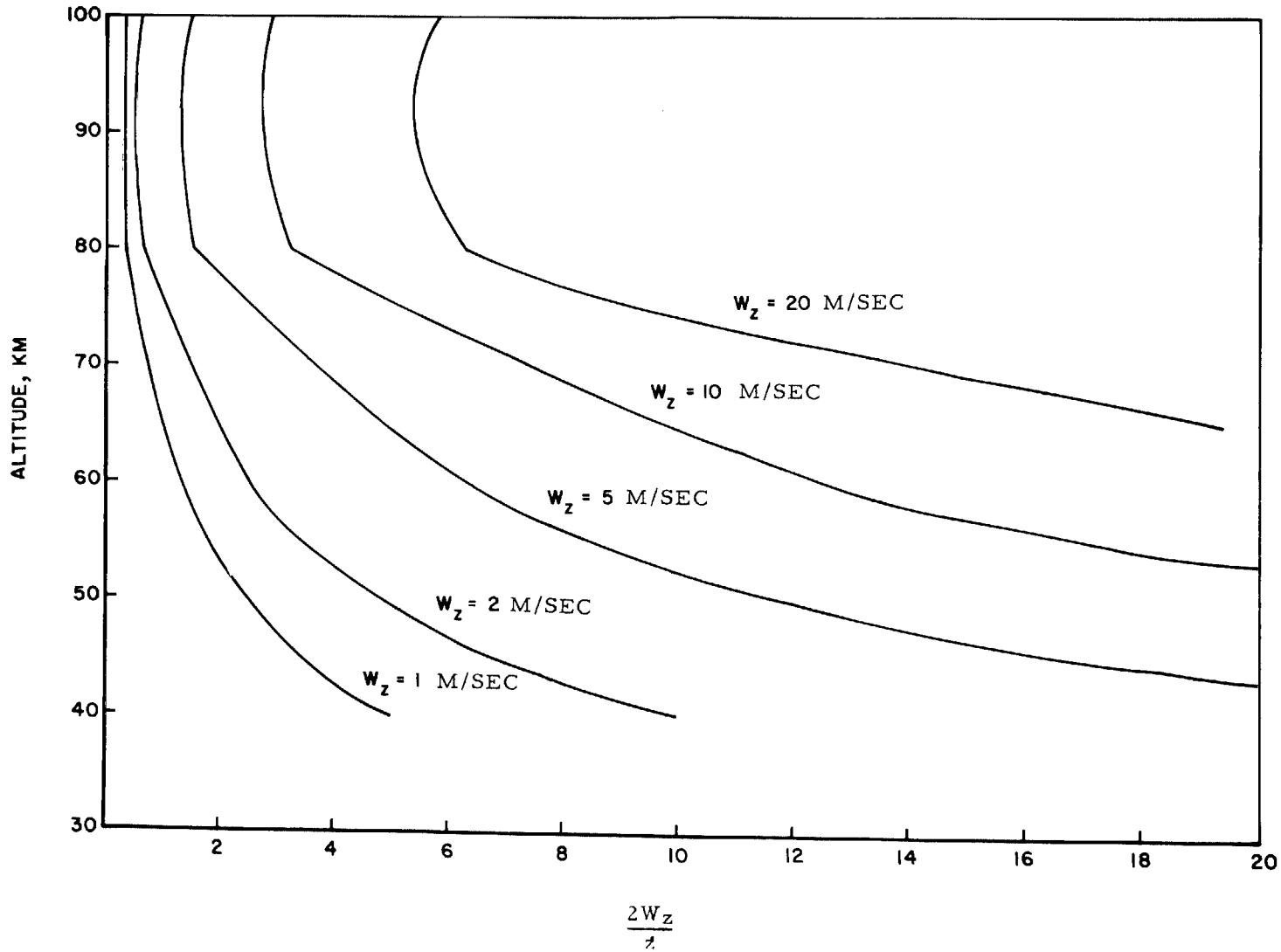

Figure 3.- Density error resulting from vertical winds as a function of altitude. Escape altitude, 125 km.

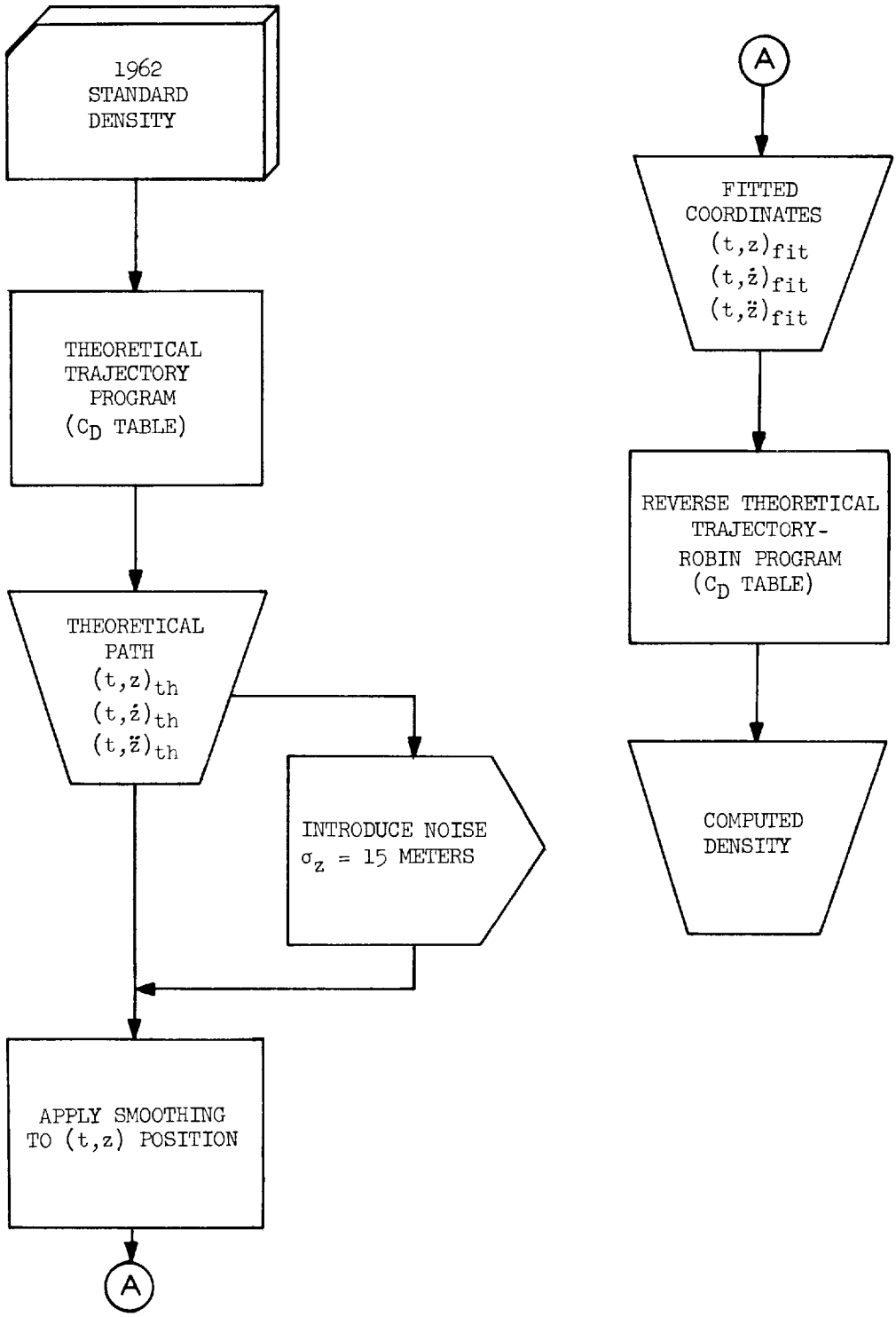

Figure 4.- Flow diagram illustrating procedure used to measure bias error in density.

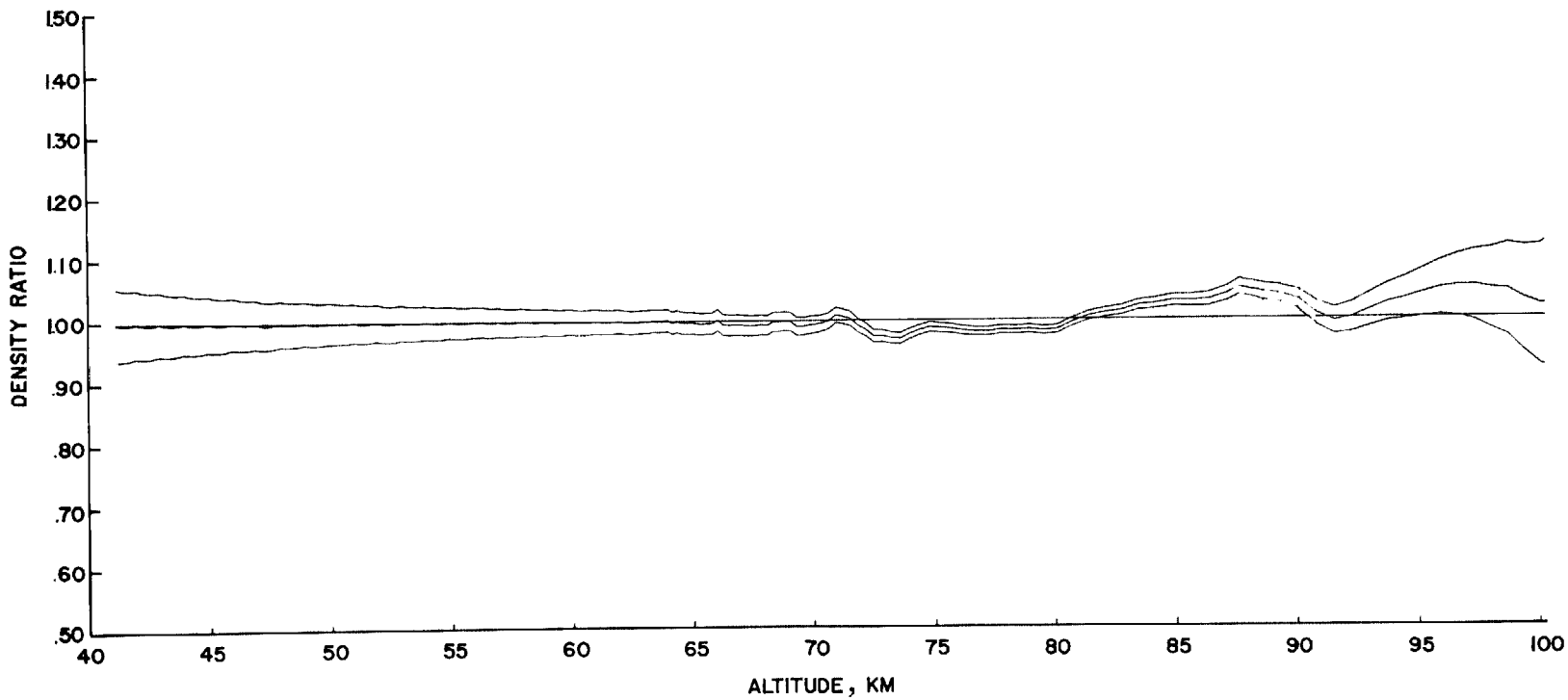

Figure 5.- Ratio of smoothed to standard density (middle curve) using 19-21 linear-cubic smoothing and 1σ noise error about bias.

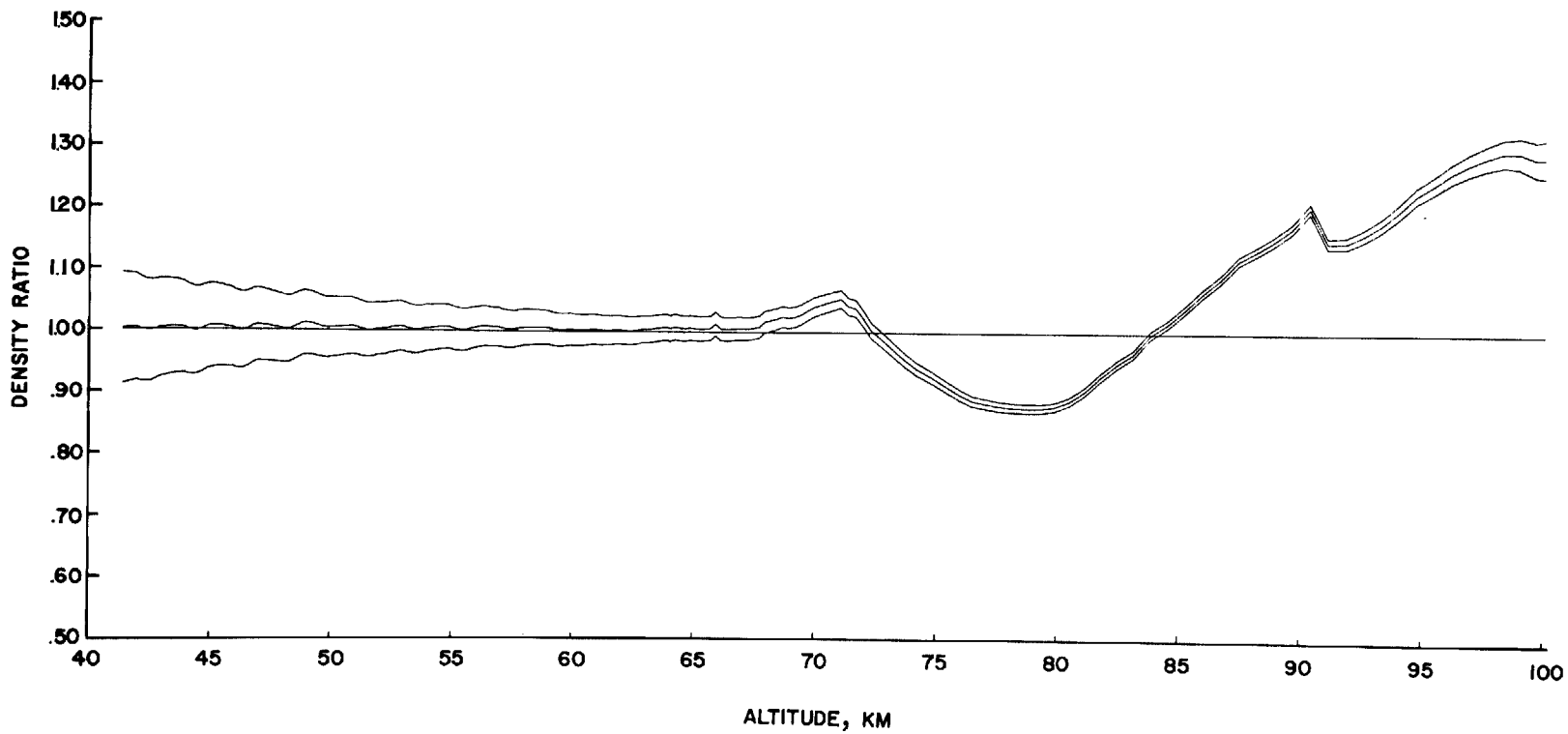

Figure 6.- Ratio of smoothed to standard density (middle curve) using 29-25 cubic-linear smoothing and 1σ noise error about bias.

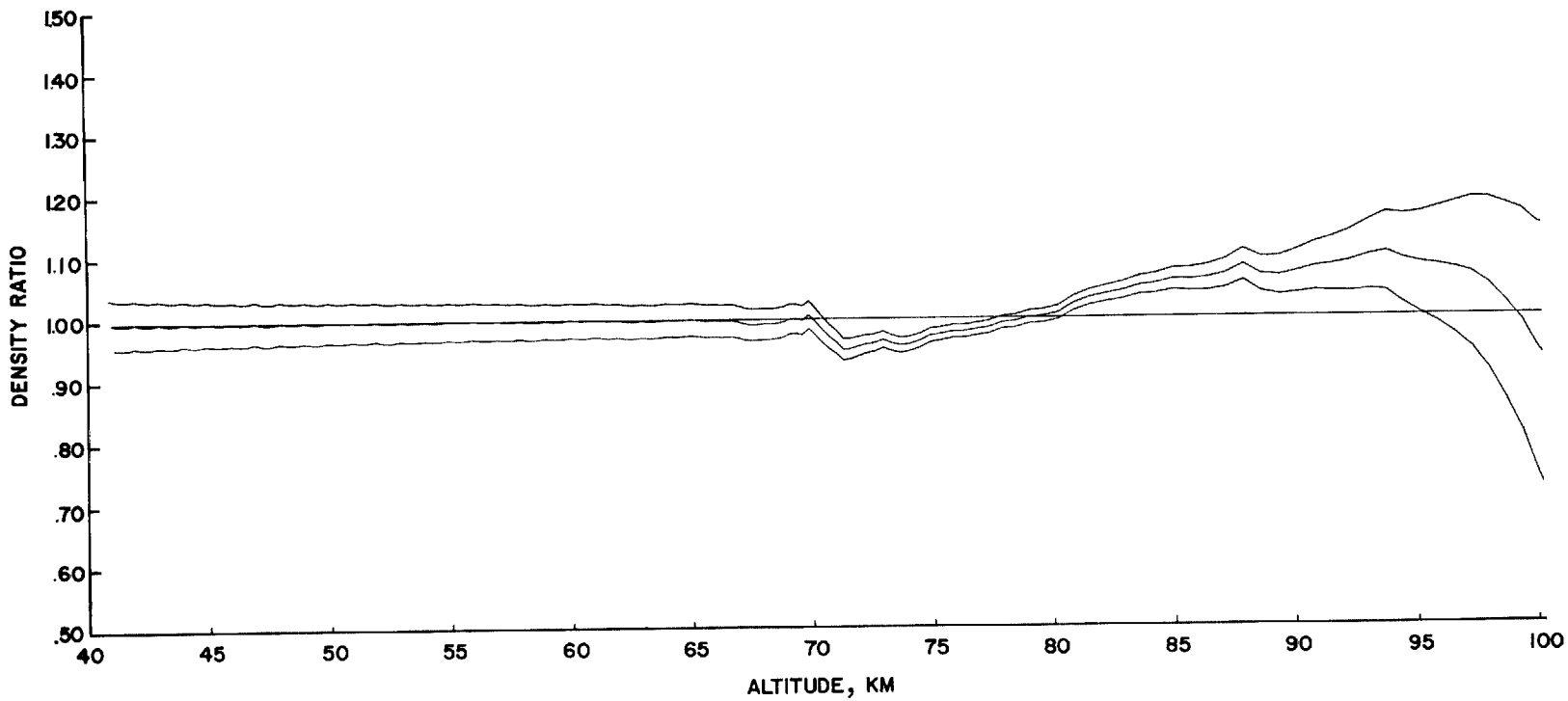

Figure 7.- Ratio of smoothed to standard density (middle curve) using 31 quadratic smoothing and 1σ noise error about bias.

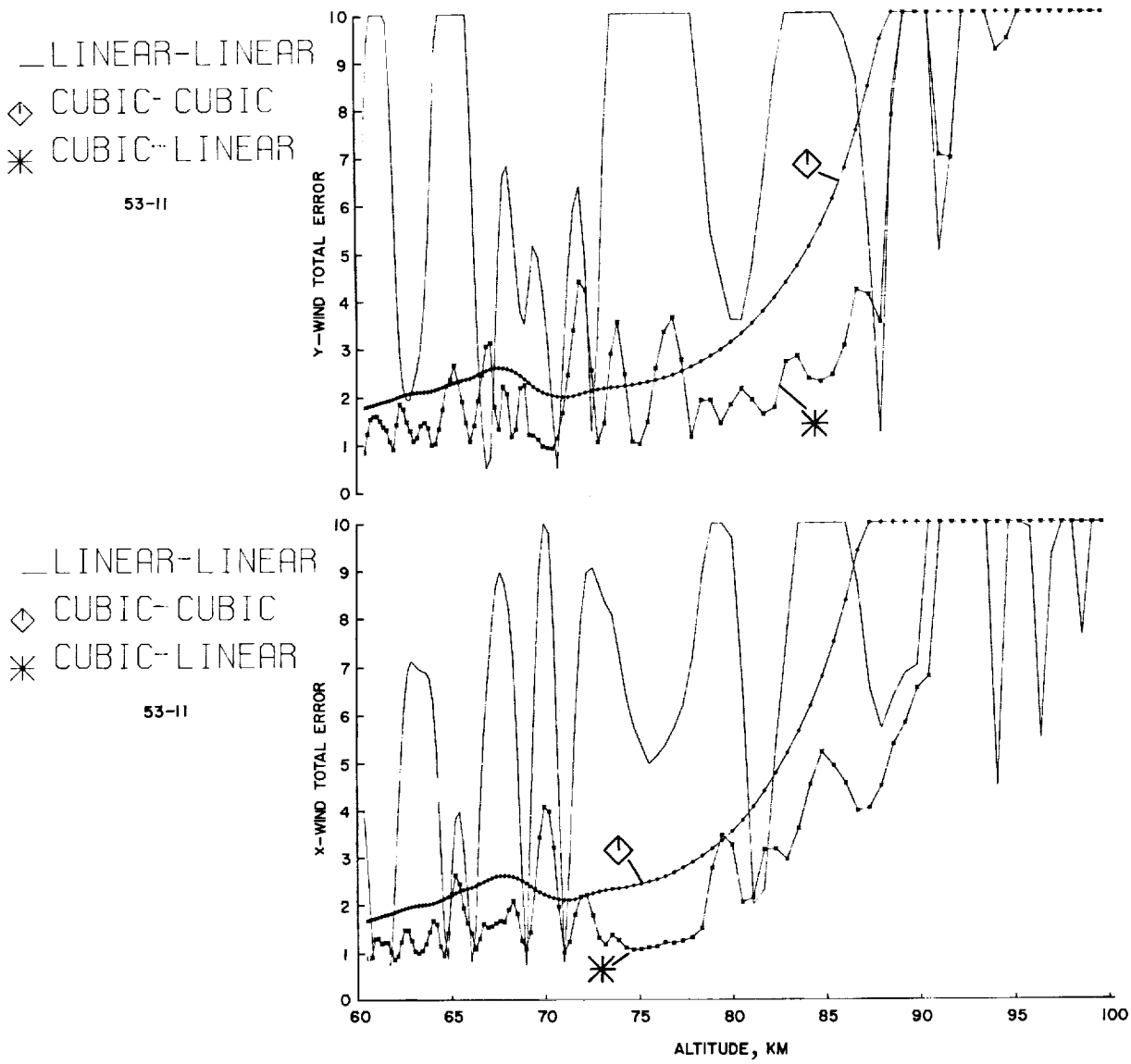

Figure 8.- Total wind error plots for 51-43 cubic-cubic, cubic-linear, and linear-linear smoothing.

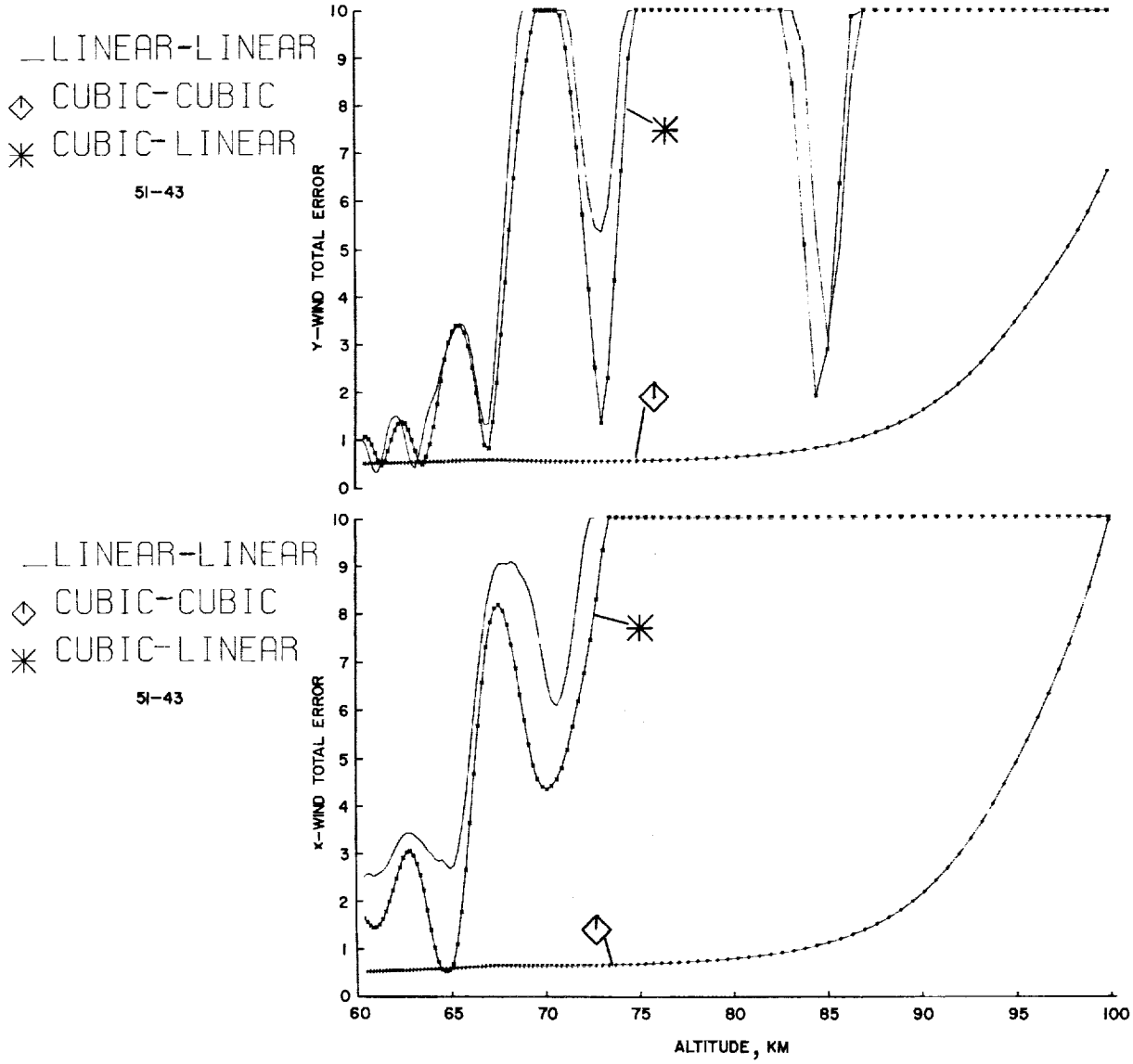

Figure 9.- Total wind error plots for 53-11 cubic-cubic, cubic-linear, and linear-linear smoothing.

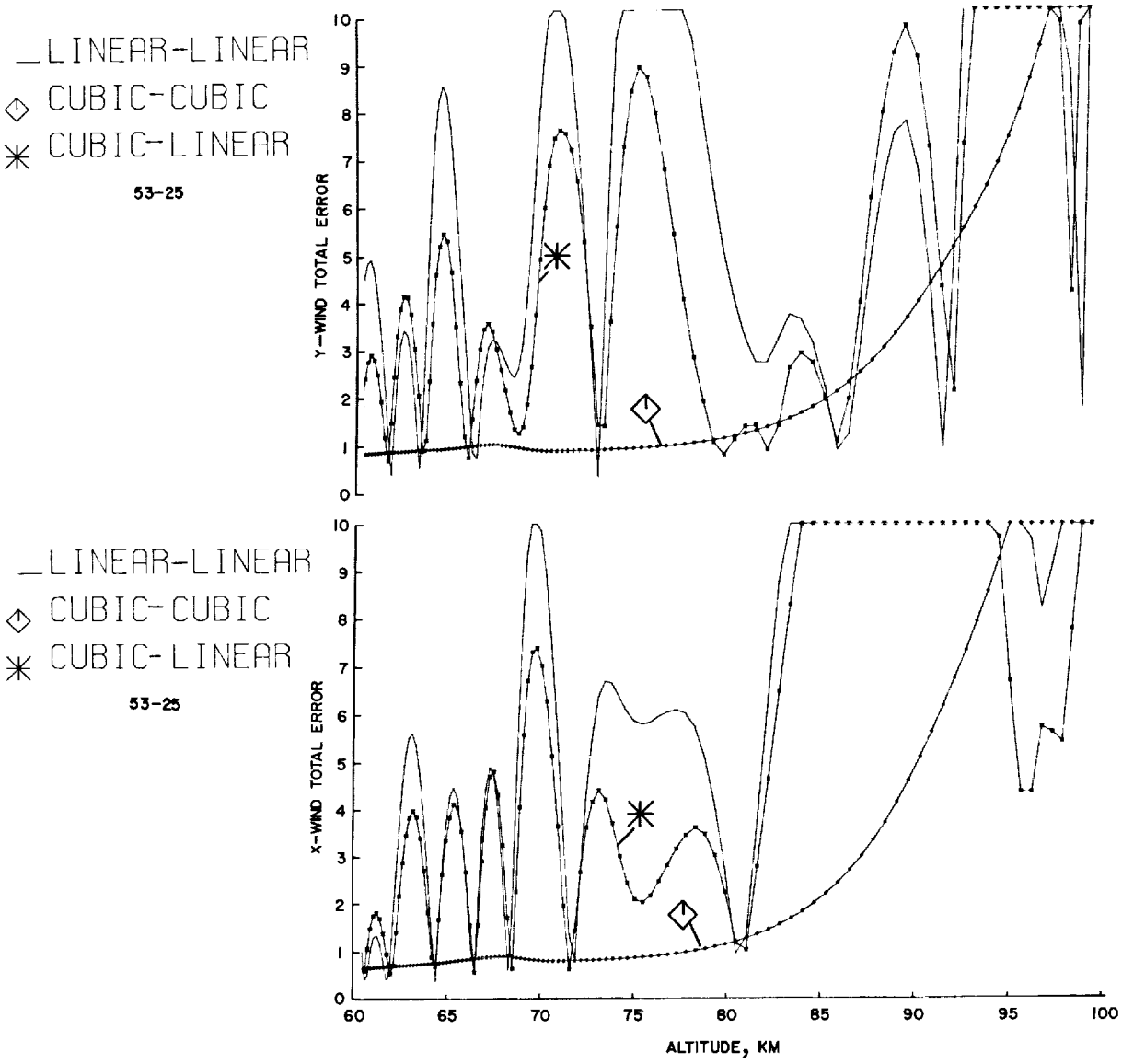

Figure 10.- Total wind error plots for 53-25 cubic-cubic, cubic-linear, and linear-linear smoothing.

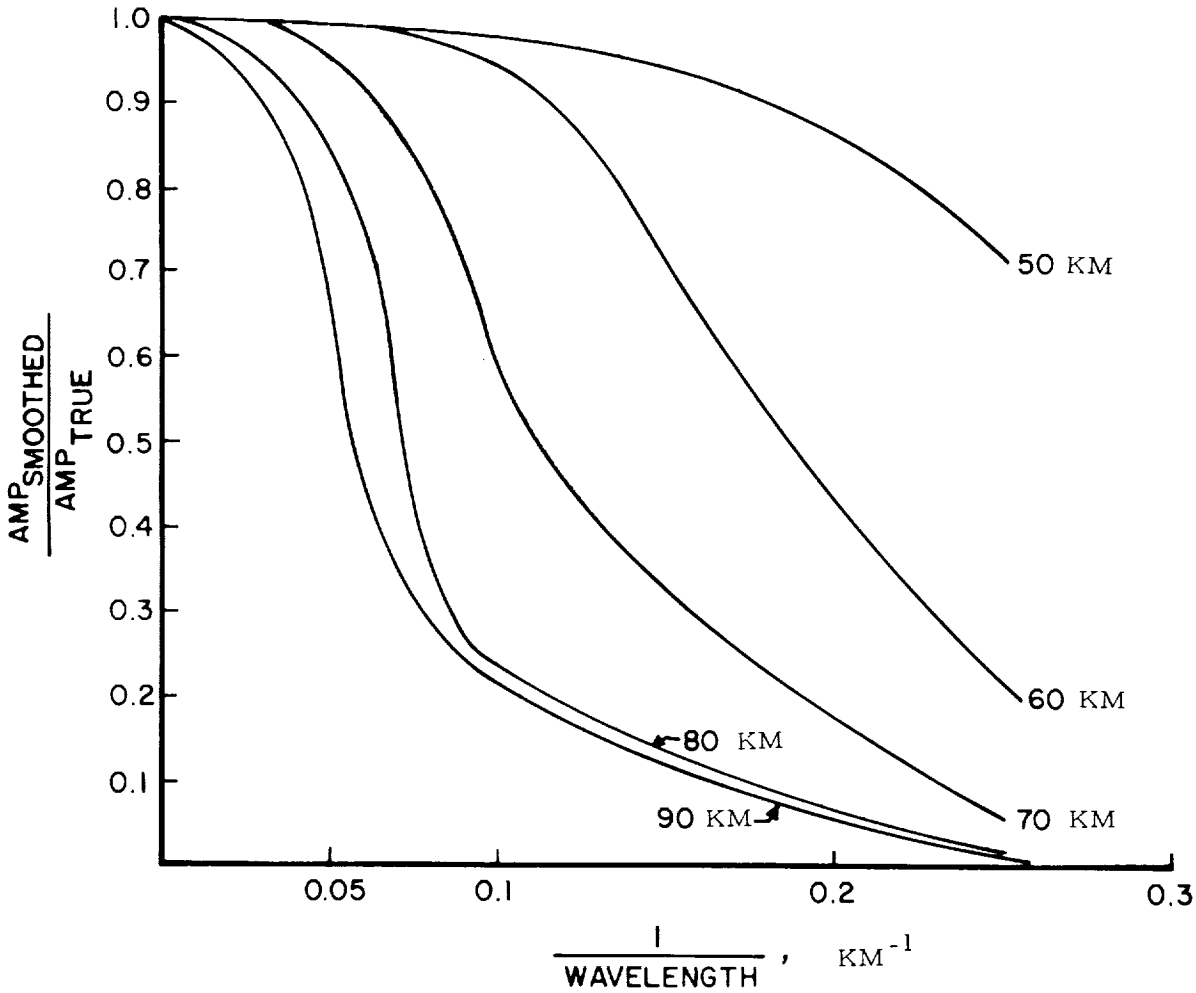

Figure 11.- Ratio of the amplitude of a sinusoidal wave as it would appear in the reduced data to its true amplitude at various altitudes. 51-43 cubic-cubic smoothing; escape altitude, 125 km.

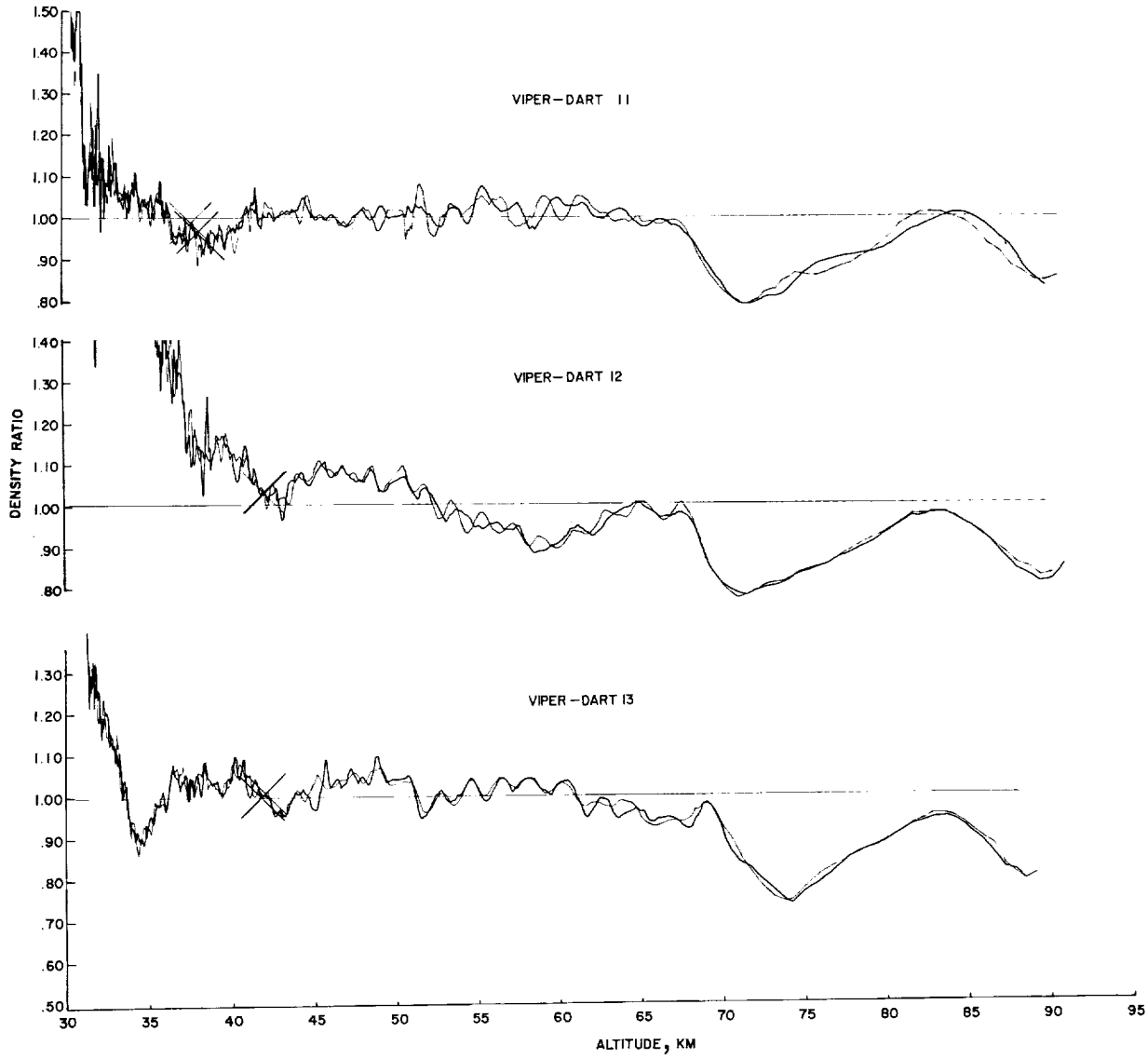

Figure 12.- Ratio of density from Viper-Dart flights 11, 12, and 13 for each radar compared with 1962 Standard Atmosphere density. 19-21 linear-cubic smoothing.

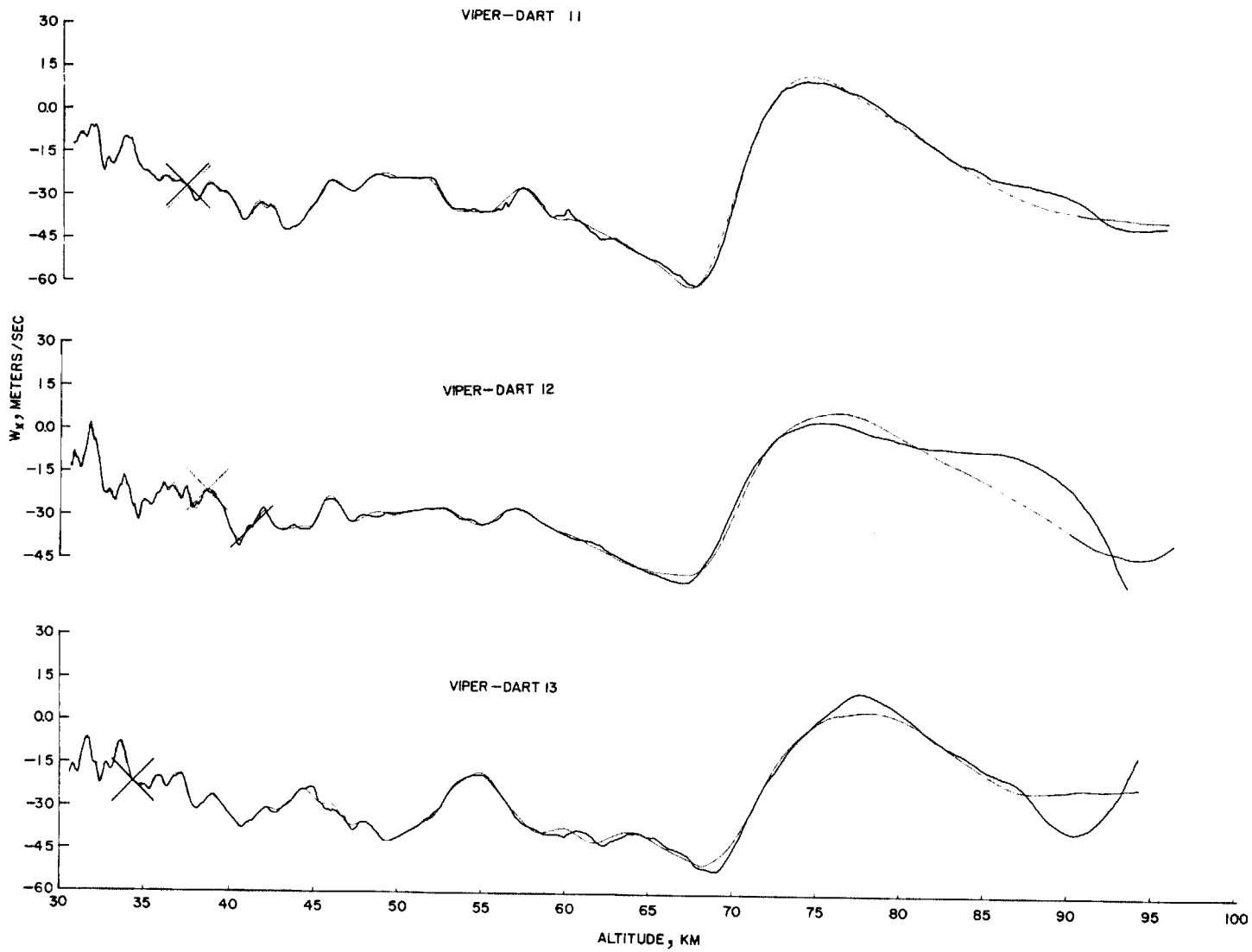

Figure 13.- x-wind component from Viper-Dart flights 11, 12, and 13 for each radar using 51-43 cubic-cubic smoothing.

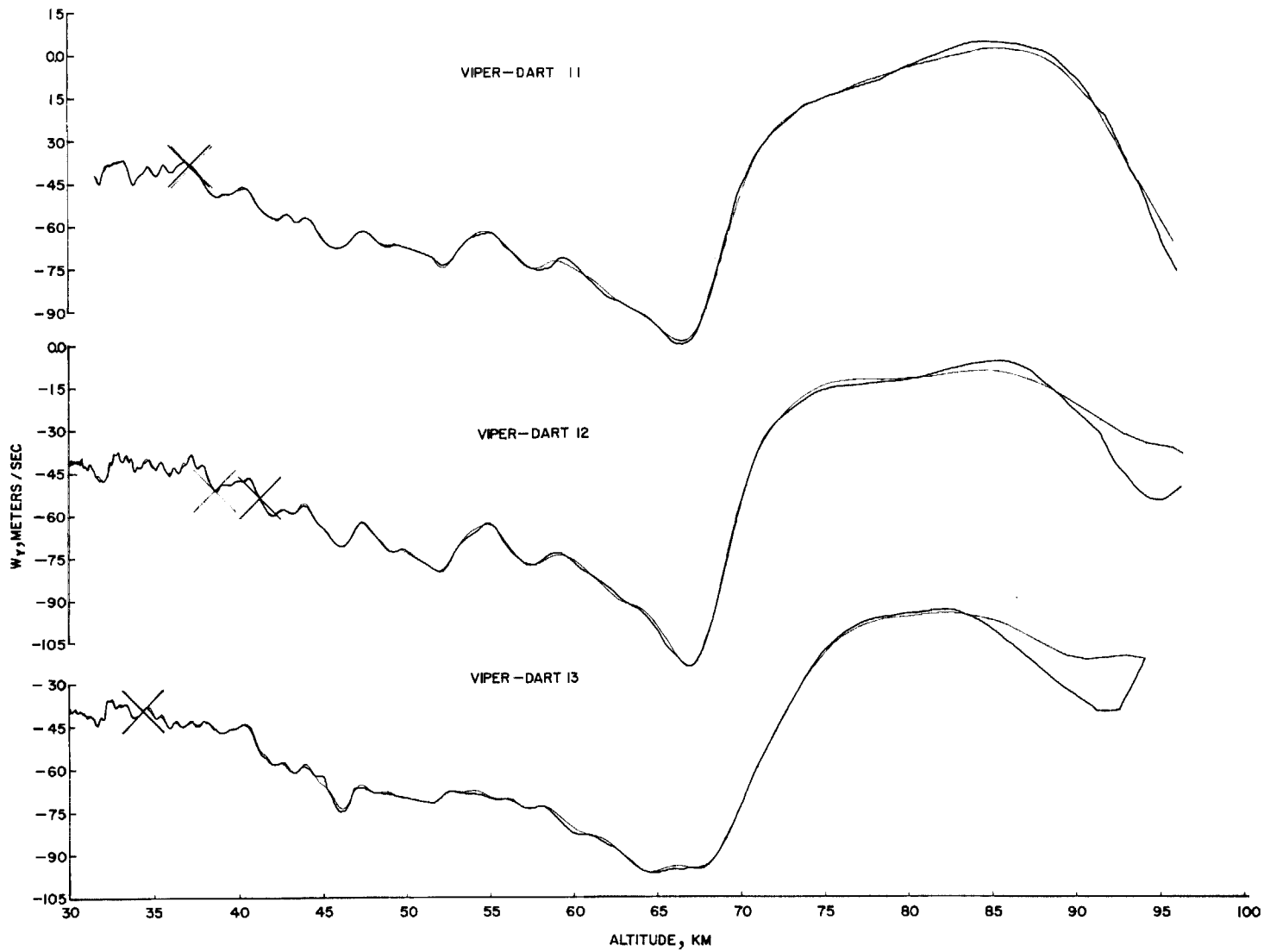

Figure 14.- y-wind component from Viper-Dart flights 11, 12, and 13 for each radar using 51-43 cubic-cubic smoothing.

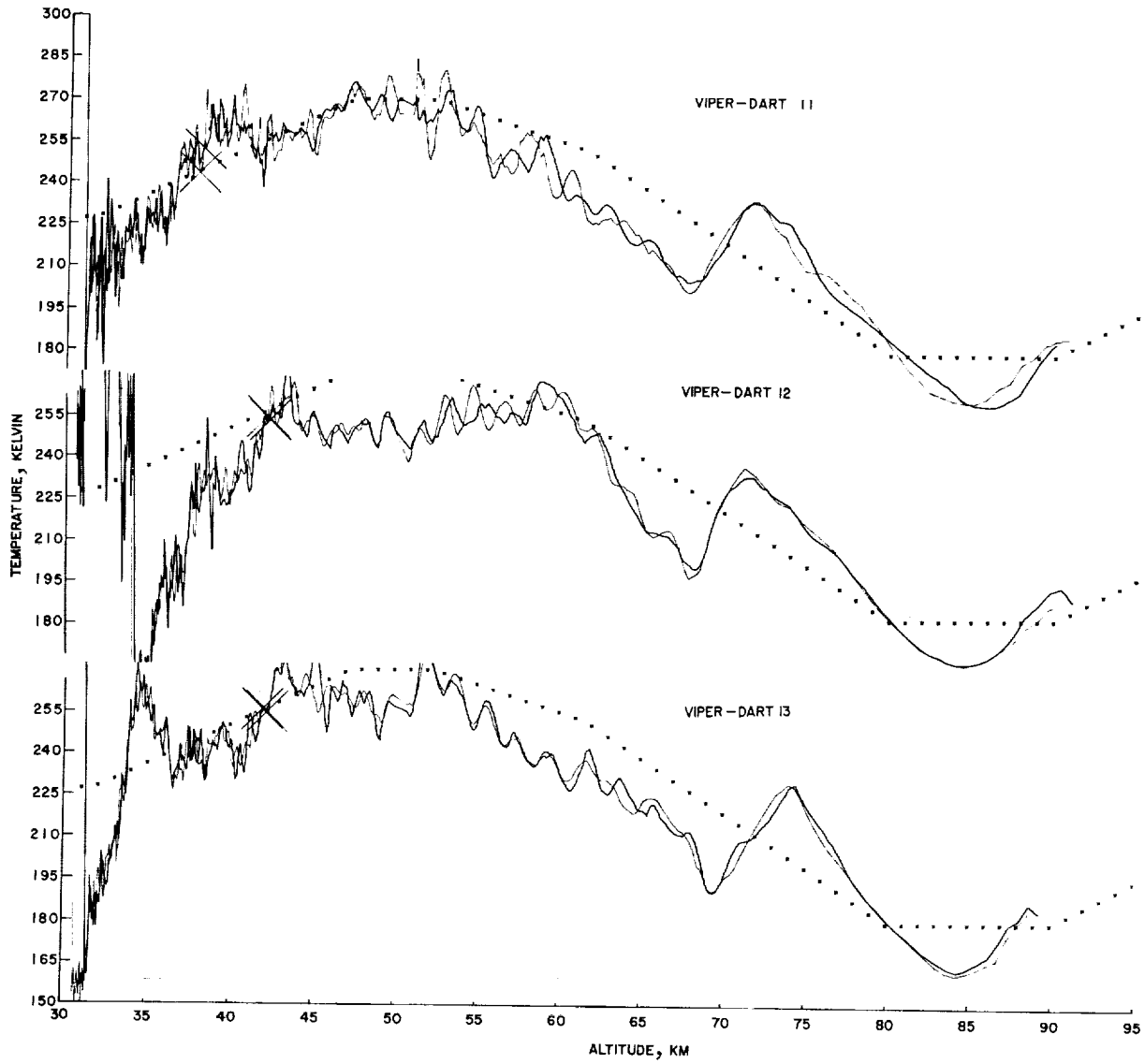

Figure 15.- Temperature from Viper-Dart flights 11, 12, and 13 for each radar compared with 1962 Standard Atmosphere temperature (dotted line) using 19-21 linear-cubic smoothing.

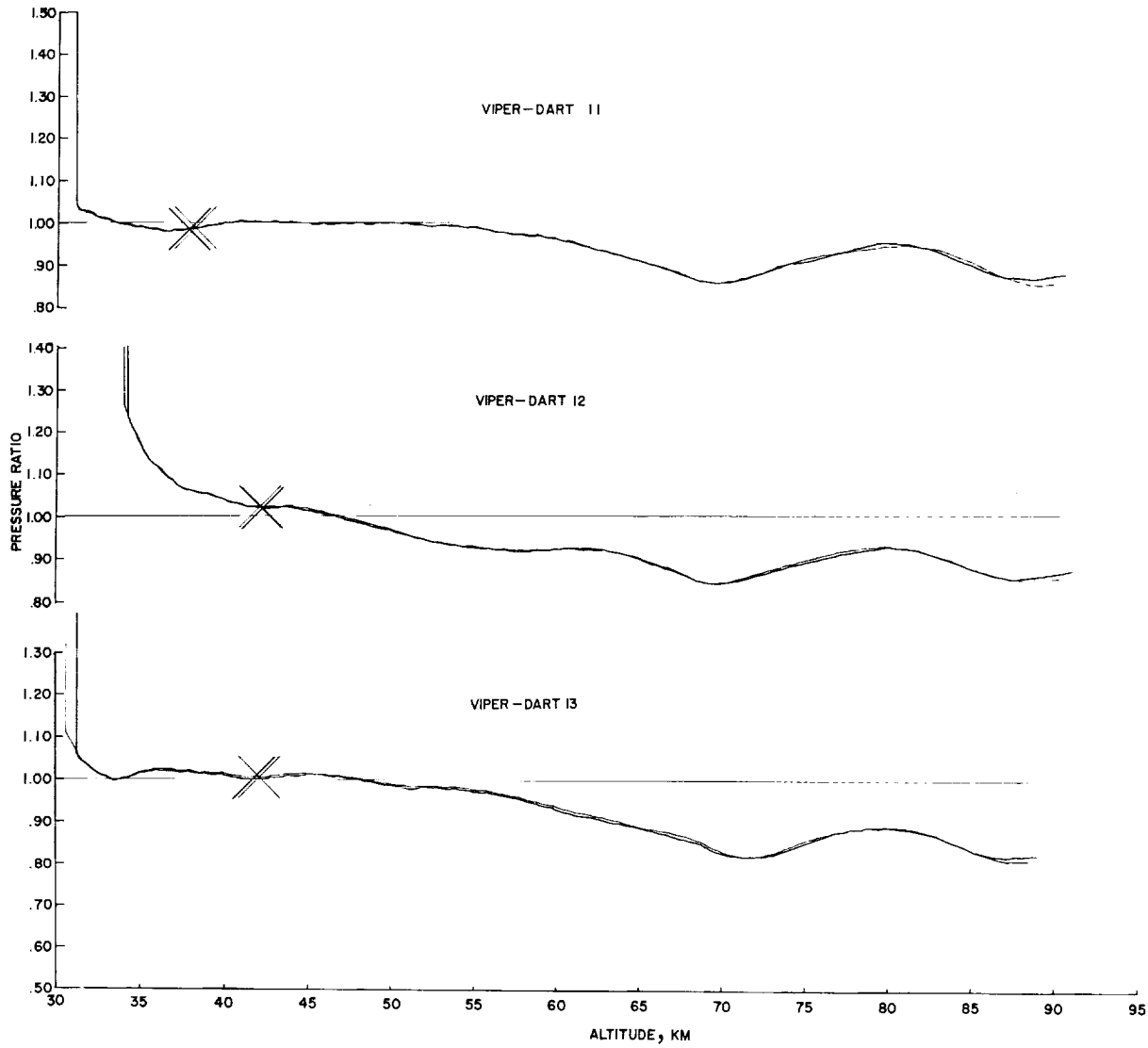

Figure 16.- Ratio of pressure from Viper-Dart flights 11, 12, and 13 for each radar compared with 1962 Standard Atmosphere pressure. 19-21 linear-cubic smoothing.

ADEQUACY OF THE PASSIVE INFLATED FALLING SPHERE TECHNIQUE

K. D. McWatters and J. W. Peterson*

The University of Michigan
High Altitude Engineering Laboratory

SUMMARY/INTRODUCTION

The radar-tracked, inflated, falling sphere is an economical technique for obtaining high-altitude density data at any launch site possessing a high-powered radar. The technique as utilized by many experimenters has provided a large amount of grossly adequate density and temperature data in the stratosphere, mesosphere, and lower thermosphere. In addition, winds are very accurately measured to 70-km altitude.

There are several sources of error inherent in the technique, and a general agreement on their magnitudes has yet to be reached. However, recent experiments and studies have been undertaken specifically to ascertain errors. This paper describes those carried out by The University of Michigan's High Altitude Engineering Laboratory.

In particular the following areas were examined: detection of sphere deflation, consequences of premature deflation, radar tracking errors, drag coefficients, and methods of data reduction.

DETECTING THE MAGNITUDE OF ERRORS

Error Sources

In discussing the detecting of errors we shall limit ourselves to discussion of density which is the primary atmospheric parameter measured. Temperatures derived from the densities are sometimes a key to understanding and in those cases will be mentioned, but errors arising from the inference of a temperature profile from a density profile are not discussed here. Neither are wind errors considered.

8

---

*Present address: Martin Marietta Corp., Orlando, Florida

While it is always impossible to state with certainty that a list of experimental error sources is truly exhaustive, we here make the attempt. Known possible error sources are:

1. Incorrect value of sphere mass

2. Incorrect value of sphere frontal area

3. Incorrect radar position data

4. Incorrect drag coefficient as a function of Mach and Reynolds numbers

5. Incorrect Mach number determination

6. Incorrect Reynolds number determination

7. Vertical wind component

Some of the listed sources could be further broken down. Sphere mass error might be due to a mistake in weighing, or loss of a component after launch: Mylar envelope, metal capsule, or isopentane. Sphere frontal area error might arise from incorrect measurement, asphericity, or collapse (partial or complete). Radar data always exhibit some degree of scatter. Smoothing is required to yield the velocity and acceleration. The smoothing technique therefore influences the amount of error. Drag coefficients are based on experimental data in which scatter is evident. Surface roughness is not accounted for. Peculiar instability in the boundary layer may be the result of rotation or varying attack angle. In some regimes such as the transonic region there are insufficient measurements.

Analyzing an Unusual Sounding

Shortly after noon (1330 EST) on 7 August 1965 a sphere payload was launched at Wallops Island, Virginia. The ratio of the derived downleg densities to the U. S. Standard Atmosphere, 1962, is shown in figure 1. This sounding exhibits a remarkable wave-like structure of three cycles between 30 and 60-km with peak-to-peak amplitudes of 24, 36, and 24%, and wavelength of 10-km. The sounding was sufficiently unusual that the question immediately arose as to whether the result was an atmospheric effect or some error. The remainder of this paper is devoted to discussing the error contributions which will enable a conclusive answer to that question.

ERRORS DETERMINED TO BE NEGLIGIBLE

Discussion

For errors to be called negligible, they must be negligible with respect to other errors or with respect to the desired measurement accuracy, preferably to both. If they are negligible only with respect to other errors, future improvements in other parts of the system might cause them to be important.

Three of the seven error sources are presently negligible because other errors are more important. They must be kept in mind because recent improvements show promise of drastically reducing other sources which for years have been considered most detrimental.

The three negligible sources are:

Incorrect value of sphere frontal area

Incorrect Mach number determination

Incorrect Reynolds number determination.

Frontal Area

1. The frontal area of each sphere is measured on 7 diameters before packaging. The measurement is made while internal pressure of 20 mb gage is maintained in the sphere. The asphericity must be less than 1% along any 2 diameters. The 7 diameters are averaged and used for the experimental value of frontal area.

Therefore the maximum area error is 1.4% between any two given aspects. In this worst possible case (5 diameters = x, 2 diameters = 1.01x) the average frontal area varies 0.4% from the calculated frontal area. However, in over 80% of the spheres the maximum diameter variation was less than one-half that allowed.

The average error from frontal area measurement is much less than 0.2%. The maximum possible is 0.4%. We have chosen to neglect this error.

2. The area is subject to change if the physical integrity of the sphere is not maintained. We shall describe below how this event is rapid rather than gradual and introduces no error more than 1 km above the abrupt termination.

3. The area is subject to change caused by the capsule weighing 8 g, at -4 g maximum acceleration attempting to deform the sphere. At the nominal internal pressure of 15 mb, the deformation is unmeasurably small. Pressure will be equalizing and skin tension greatly reduced prior to collapse. However, this can only occur in a region with minimum deceleration hence the deforming force is also greatly reduced. Deformation occurs only in the final few hundred meters which data are normally disregarded because of radar smoothing requirements. This source is negligible.

4. The total error due to incorrect frontal area from all sources is believed to be much less than 0.2% on the average and never to exceed 0.4%. It is therefore neglected.

Mach Number and Reynolds Number Determination

Assume that the drag coefficient is known with absolute precision as a function of Mach and Reynolds numbers. Any other error in the entire technique will cause some error in density and temperature. This error will then cause an error in the determination of Mach number and Reynolds number and hence an erroneous drag coefficient will have been chosen.

Fortunately, drag coefficient is only a weak function of Mach and Reynolds number except in the transonic region. Tracking data is processed with an iteration of Mach and Reynolds numbers by assuming the temperature and density in the layer above. Mach and Reynolds numbers are calculated. The drag coefficient is obtained and the density and temperature calculated. Mach and Reynolds numbers are recalculated and a new drag coefficient chosen. A new density and temperature are calculated. The process continues until arbitrarily small corrections are made. This convergence is rapid.

In one region, transonic, the drag coefficient is not such a weak function of Mach number and when processing this region occasional failure to converge has been noted. This happens only when processing unusually poor data, as in the case of an uninflated sphere. In these rather rare instances the process does not diverge, but appears to converge so slowly that the computation is halted for economy's sake.

The error in the final data due to erroneous determination of the Mach and Reynolds numbers is a function of all other errors. It is presently one-to-two orders of magnitude less than the drag coefficient error and may be termed negligible.

IMPORTANT ERROR SOURCES

Four sources of error remain to be reckoned with: incorrect mass, incorrect radar data, incorrect drag coefficient, and vertical wind. Vertical wind will be treated in the next section.

Sphere Mass

The 66-cm sphere weighs about 50 g: 34 g of Mylar, 8 g of aluminum capsule, and 8 g of isopentane. The mass is determined by weighing the deflated, evacuated envelope in a chemical balance and recorded to 1/1000 g. Considerable care is exercised and personal error in this operation has never been considered an error source in the system.

The only other way for a mass error to enter is for the mass to change after weighing, after rocket launch, or after ejection. First we consider the Mylar. If any portion of the Mylar is lost the sphere has no ability to be inflated and if already inflated will collapse under the slightest aerodynamic force. A collapsed or noninflated sphere is useless for density determination. Therefore loss of Mylar is impossible as an error source. Next consider loss of the capsule. This is impossible without a loss of pressure integrity of the sphere and is equally impossible as a mass error source.

Loss of isopentane is the remaining possibility. If the capsule should leak after the sphere is weighed and the liquid (or gas, B.P. 28°C) should permeate the Mylar and escape, a mass error would be introduced. We have tested capsules by oven baking and then weighing daily for weeks, and by storage for five years and have yet to detect a leak. We conclude that such a leak is improbable. Each flight capsule is subjected to a bake test and then weighed daily for one week before being packaged in a flight sphere.

If the capsule should leak after launch and prior to ejection the isopentane would have insufficient time to permeate the Mylar and escape, hence no loss of mass. It would, however, tend to inflate the packaged, unejected sphere at the low ambient pressure and probably cause a sphere failure at ejection. Thus, if the sphere was seen to be properly inflated by the radar, then no mass loss of this type could have occurred.

There remains only one possibility for incorrect mass—loss of isopentane after ejection in a very slow, noncatastrophic manner as if issuing from a pinhole leak. There are three ways this might occur:

1. After pressure test the air is evacuated from the sphere through a

hole which is subsequently taped shut. It is impossible to pressure test this tape for leakage on a flight sphere. Many simulation tests of flight-ready spheres have been conducted and in one case there was such a leak, therefore, it is a definite possibility.

2. After pressure test, the pressurizing hose is removed and the hole taped, similar to (1). Although no leaks have been detected, the same considerations apply.

3. When packaging the evacuated sphere for flight it is folded and squeezed severely to fit inside the sabot. Although accomplished as carefully as possible, a fold-point might become a pinhole. Testing has been limited. Numerous ejection tests in vacuum chambers are useless to prove this point as the high velocity of ejection causes the sphere to rupture upon striking the side of the chamber, even when caught in a net. This occurrence is likewise possible.

However, if pinhole leakage occurred at time of ejection the isopentane would continue to leak during flight and the sphere would lose pressure as well as mass. In this case the sphere will deflate at some altitude considerably above the design deflation altitude. The 66-cm spheres are designed for internal pressure of approximately 15 mb and should deflate at approximately 28.5-km.

If deflation occurs at the design altitude there is no error attributable to incorrect sphere mass. If deflation occurs above the design altitude the logic outlined demands a substantial mass correction. The leak is assumed a sonic jet and the mass change for a 66-cm sphere is given by:

$$\frac{m}{m_{70}} = e^{-\alpha} \qquad \alpha = \frac{t - 70}{t_d - 70} \ln \frac{15}{p_d}$$

where:

m_{70} is mass of gas at 70 sec (ejection)
t is time (sec)
p is ambient pressure (mb)
sub d is at deflation.

The calculation of mass loss at a given altitude as a function of deflation altitude for the 66-cm sphere is shown in figure 2. In figure 3 is given the percent change of sphere mass at any altitude as a function of deflation altitude. If not corrected, this percent change may be thought of as a density error. Figure 4 shows the effect of mass correction for early deflation on NASA 10.265.

The correction of sphere mass for premature deflation is sufficiently important that it is incumbent upon the experimenter to determine the altitude of deflation carefully on each flight. We have found this to be an obvious procedure, although it was once disputed.

The deflation altitude is found by first reducing the data to as low an altitude as possible, neglecting where deflation may or may not occur. Then the fall rate, or vertical velocity is plotted on a semilogarithmic graph. Figure 5 is an example of such a plot. The solid lines represent the standard deviation in fall rate of 12 soundings at Kwajalein Island. Fall rate never departs from this pattern until deflation when it suddenly decreases. It is elementary to note the normal deflation of one sphere (NASA 10.253) and the abnormal 40-km deflation of the other (NASA 10.265).

If the fall rate plot is not sufficiently convincing, the plot of densities should be made. Figure 6 shows the density data from the same two flights. A 30 to 40% density increase in 1-km cannot occur and indicates deflation.

The radar AGC records confirm deflation rather than indicate it. On many occasions the AGC record has a remarkable change of character at deflation, it is often subtle, but always detectable on the FPQ-6. The two flights under discussion are excellent examples of both extremes and are shown in figure 7. The deflation of 10.265 is sufficiently obvious that it may be utilized to pinpoint the exact time and therefore altitude of deflation. Deflation of 10.253 is not immediately obvious but a definite change of character in the signal is there. If several more feet of the record could be shown it would be even easier to verify, since the high frequencies persist to the end of the record and no high frequencies are present in the noise earlier in the flight. Pinpointing deflation time of 10.253 would be hazardous. It may be added that normal and premature deflations have no correlation with AGC signal characteristics.

Summarizing the sphere mass error discussion: There is no error attributable to sphere mass when deflation occurs at design altitude. There is a substantial correction to mass required when premature deflation occurs. Whether this correction is exact depends upon the logical arguments given. No other logical argument has been heard. Since the correction is large, based on ideal flow through an orifice, and since the character of a leak is indeterminate it is important to pay careful attention to sphere sealing and packing as well as an accurate determination of the deflation altitude. This determination is simple and precise.

Radar Tracking Data

1. Discussion

Radar position data has long been credited with contributing a major share of error in the sphere technique. In order to determine the magnitude of the error many computer simulations have been made but sufficiently elaborate radar error functions cannot be supplied. Therefore, these studies proved to be inconclusive.

Recent flights have been made which promise to end the speculation, all involving use of the AN/FPQ-6 radar at Wallops Island, Va. This radar has on the order of 20 db more return signal than the standard AN/FPS-16 radar due to higher gain in transmission and antenna, a smaller angular error specification, and a direct reading range-rate output which is superior to our best computed effort at range differentiation. All told, the performance of the AN/FPQ-6 was such as to be expected to yield the highest quality sphere data yet obtained.

The importance of this high quality data was not in improving the knowledge of the upper-atmosphere over Wallops Island, but in serving as a standard for comparing other radar performance, particularly the AN/FPS-16, and for determining the overall precision of our reduction techniques.

2. Techniques Compared

It has been long recognized that the highest quality data in a passive sphere technique is obtained when the sphere is ejected on the upleg. Since radars are fundamentally a range-measuring device their range data are vastly superior to their angle data. The upleg drag acceleration can then be computed almost wholly by double-differentiation of the range data because the sphere is flying directly away from the radar and angle measurement is of small import.

The FPQ-6 with range-rate output used in conjunction with upleg ejection was expected to and did, provide excellent data to an exceptional altitude and at the same time offered the opportunity to compare three data reduction techniques. The results of sphere 10.253 are shown in figure 8.

The "Ascent-$\dot{R}$ data" plot from 91 to 120-km are densities obtained by differentiating the range-rate data as explained by Peterson, et al. [1965]. This density data represent the best possible as only a single differentiation of the data is required and the angular components of velocity are small.

The "Ascent-R, α, ε data" plot from 95 to 110-km was obtained by our usual upleg technique of singly and doubly differentiating the range-data to provide velocity and acceleration. Again, single differentiation of the angle data is

required but angular components of velocity are small.

The "Descent-R, α, ε data" plot from 100-km down to 30-km are densities obtained from our usual descent technique in which single and double differentiation of the range, azimuth, and elevation data is required at each level at which a density calculation is made.

Agreement of the three techniques is outstanding. The significant results are that all three techniques are practical, that an upper altitude limit for each technique is established with good confidence, and that this radar can provide a standard for comparing other radars and methods.

We conclude from this comparison that considering radar tracking errors alone the limits are 93-km for descent, 108-km for ascent range data, and although no comparison can be made, perhaps 120-km for ascent range-rate based on the lack of scatter. The average difference between ascent techniques from 94- to 108-km is 3.1%.

3. Radars Compared

To compare radars we use the technique comparison above which indicated FPQ-6 ascent range-rate data was an excellent standard. Figure 9 compares FPQ-6 ascent range-rate data with FPS-16 ascent and descent data. The FPS-16 radar involved was equipped with parametric amplifiers. (FPS-16 has no range-rate output.) The flight is 10.254 at Wallops Island, Va. The FPS-16 ascent data show considerable scatter beginning at 104-km. Between 97-km and 104-km the average difference is 5% (from FPQ-6 range-rate data). Descent data is obviously yielding an intolerable error above 93-km, while scatter at 88-km and 81-km looks suspicious. Unfortunately, the FPQ-6 on descent was tracking an uninflated second sphere and no descent comparison below 93-km is possible.

In figure 10 is shown a descent comparison of the two radars tracking sphere 14.386 downwards. The FPQ-6 shows scatter above 94-km almost exactly as predicted by the technique comparison. The FPS-16 shows intolerable scatter above 80-km, which also is consistent with figure 9. The agreement below 80-km looks poor to the eye but the average difference is only 2.8%.

Another comparison is available on our unusual wave-like sounding 10.154. With the FPQ-6, ascent range data is good to about 110 km, descent data to 98-km. The maximum altitude on the FPS-16 is 102-km for ascent and 82-km for descent. The FPS-16 was not equipped with parametric amplifiers at the time of this flight. The descent data comparison is truly phenomonal as the plotted points below 80-km cannot be distinguished at most altitudes. The average difference below 80-km is only 1%.

4. Summary

The comparisons of radar performance and data processing techniques have yielded conclusive results:

a. The fine atmospheric structure shown by the falling sphere technique cannot be dismissed as a problem associated with radar tracking error. This is proved conclusively by the two independent tracks of 10.154 which copy every structural detail. If the small excursions are not atmospheric, they are due to some other error source.

b. The performance of the radar or radar-sphere combination is considerably variable. Compare 1.0% on sphere 10.154 with 2.8% on sphere 14.386.

c. The maximum altitude of satisfactory radar performance with a 66-cm sphere is approximately:

Technique	Max. Alt.
FPQ-6 Ascent (range-rate)	120-km
FPQ-6 Ascent (range, angles)	108-km
FPQ-6 Descent (range, angles)	94-km
FPS-16 Ascent (range, angles)	102-km
FPS-16 Descent (range, angles)	80-km

d. Density errors due to radar tracking errors below 80-km may average on the order of 2% with the FPS-16 and 1% with the FPQ-6. Above 80-km the technique must be carefully chosen to ensure validity. If the tabular values in (c) are observed the error should not exceed an average of 3%.

Drag Coefficient

The knowledge of drag coefficient (C_D) as a function of Mach and Reynolds numbers is essential to relate the experiment results to the ambient atmosphere. The falling-sphere technique yields the product of C_D and density as primary data, hence errors in C_D cause inverse proportionate errors in density.

Aerodynamic drag theory can predict the drag coefficient in certain Mach and Reynolds number regimes with precision but these regimes are limited. Virtually all the drag coefficients required must be experimentally determined. Because experimental data were badly lacking in some regimes required for passive sphere data experimental wind tunnel measurements were conducted [Heinrich, 1965]. These experimental data were soon utilized by most if not all passive sphere experimenters.

All inflated spheres are designed for a minimum mass-to-area ratio, therefore when falling through the atmosphere they quickly lose velocity, pass through the transonic region, and reach a terminal velocity of less than Mach 0.39 at about 58-km altitude for a 66-cm sphere. The spheres continue their flight at smaller Mach numbers thereafter. This Mach number is of interest because the referenced investigator, Heinrich, presented a curve and table for $M \leq 0.39$ implying no Mach number dependence below that number. This curve and tabular values did not agree in slope with his wind tunnel results at higher Mach numbers. Using these data we consistently derived extraordinarily high stratopause temperatures. The temperatures were the result of using the $M \leq .39$ curve as it was exclusively used below 58-km.

In 1968, another series of experiments was conducted in a ballistic range [Goin, 1968]. These results exhibited much the same trends as the Heinrich's $M \leq .39$ curve but were about 10% lower in the Reynolds number range of interest ($2{,}000 < Re < 20{,}000$). Figure 11 presents the results of Goin, Heinrich, Heinrich's $M \leq 0.39$ curve, and some other experimental results of Wieselsberger and Lunnon. Goin's data closely match Wieselsberger's and Lunnon's, while they do not confirm Heinrich's data at higher Mach numbers, even in trend.

We were concerned about the seeming discrepancy at $M \leq .39$ until, checking, no experimental basis for the Heinrich curve was found.

Passive-tracked-sphere experimentalists should use the Goin data. Otherwise, density results will be about 10% low at Mach numbers below $M = .39$. For 66-cm spheres the temperatures will also be erroneous as the curve is entered at a Reynolds number where the slope is incorrect as well.

In the case of 1-meter spheres, the curve is entered at a Reynolds number some 50% higher in a region where the slope is approximately correct. This causes minor effect on temperatures but a large density error will still be encountered.

Further experiments to obtain suitable drag coefficients in the transonic and some supersonic regions are indicated. The small scatter of Goin's ballistic range data (total excursion less than ±1%) affords basis for optimism that the drag coefficients can be measured reliably along the entire trajectory to an accuracy approaching 1% excepting the region very close to Mach 1.0.

Summary

Three major error sources have been discussed. Mass error is nonexistent on properly deflating spheres, but an appreciable correction, implying unknown error, is required in the case of premature deflation. Radar tracking errors

were shown to be intolerable above a limiting altitude which depends on radar type and sphere technique. Below this limit, average errors of 1% to 3% were inherent with the AN/FPQ-6 and AN/FPS-16 respectively. Drag coefficient errors of under 2% were found in the subsonic regime which spans a major portion of each flight when using Goin's data. A major error occurring from use of Heinrich's $M \leq .39$ curve is noted which is unusually important because $M \leq .39$ covers 30 to 40% of the altitude range.

ANALYSIS OF THE UNUSUAL SOUNDING

Error Magnitudes

Figure 1 demonstrated sphere densities from 10.154 which were unusual in having oscillations of 24%, 36%, and 24% peak-to-peak with 10-km vertical wavelength, lying between 30 and 60-km.

The question was apparent: could this wave-like oscillation be erroneous? In the previous discussion all known error sources were examined. Three were found to be negligible. Three more were found to be significant: mass loss, drag coefficient, and radar track. In 10.154 deflation was at the normal altitude and mass loss is ruled out as the source of any error. In the regime below 60-km, drag coefficients are known quite well; interpolation for Mach number between Goin's measurements should add less than 1% and the Goin measurements are on the order of 1%. Radar tracking by two radars was in extraordinary agreement, implying an average error of approximately 1% due to the radar track-errors. These three errors are not necessarily random so the three are added to give a conservative total error of 3%. Therefore the oscillations cannot be due to any error source we have discussed.

Vertical Winds

From our previous analysis it is evident that the wave-like oscillation of density on sounding 10.154 must be atmospheric. The most convincing conformation would be another sounding. Fortunately, the unusual sounding was the first of a series, and was followed by another about nine hours later. Figure 12 shows the density results of both, 10.154 and 10.169. While the wave-like oscillation is of smaller amplitude and shifted somewhat in the vertical scale, 10.169 confirms that the effect was atmospheric and had persisted for hours. It too, viewed alone, would be termed unusual.

In the falling-sphere technique, it is impossible to distinguish density effects from vertical winds. The vertical wind was customarily assumed to be

negligible, and for years most theorists felt that the vertical component would attain a maximum of several centimeters per second. The possibility of vertical motion induced by gravity waves should also be considered. Vertical winds as high as 25 m/s have been estimated from noctilucent cloud observations above 80-km [Witt, 1962]. Short period gravity waves may induce relatively large vertical velocity [C. O. Hines, private communication, 1967]. In analyzing the unusual sounding we found a vertical wind component of 3 m/s would have been sufficient to cause the oscillation presumed to be density. The falling-sphere technique appears to be an excellent detector of a gravity wave, though by its nature must fail to distinguish vertical wind from density. In a strong wave, such as encountered in 10.154 any portion of the density oscillation which was in fact a vertical wind would cause erroneously large temperature oscillations.

CONCLUSIONS

The passively-tracked, inflated, falling-sphere technique is adequate for making routine high-altitude soundings with economy and accuracy, but is limited to sites having a powerful radar. Evaluation of the sphere deflation altitude and the correction of sphere mass is crucial to deriving the correct atmospheric density. Descent density data obtained by tracking a 66-cm inflatable sphere with a AN/FPS-16 radar equipped with parametric amplifiers is questionable above an altitude of 80-km. New drag coefficient data as measured by Goin should be used to derive the proper atmospheric density profile. The inflatable, passive sphere appears to be an excellent detector of a gravity wave, though by its nature must fail to distinguish vertical wind from density.

REFERENCES

Goin, Kennith L.; and Lawrence, W. R.: Subsonic Drag of Spheres at Reynolds Numbers From 200 to 10,000. AIAA J. (Tech. Notes), vol. 6, no. 5, May 1968, pp. 961-962.

Heinrich, H. G.; Niccum, R. J.; Haak, E. L.; Jamison, L. R.; and George, R. L.: Modification of the Robin Meteorological Balloon. Volume II - Drag Evaluations. AFCRL-65-734(II), U.S. Air Force, Sept. 30, 1965. (Available from DDC as AD629775.)

Lunnon, R. G.: Fluid Resistance to Moving Spheres. Proc. Roy. Soc. (London), ser. A, vol. 118, Apr. 2, 1928, pp. 680-694.

Peterson, J. W.; Hansen, W. H.; McWatters, K. D.; and Bonfanti, G.: Falling Sphere Measurements Over Kwajalein. J. Geophys. Res., vol. 70, no. 18, Sept. 15, 1965, pp. 4477-4489.

Wieselsberger, C.: Further Investigations of the Laws of Fluid Resistance. Phys. Z., vol. 23, May 15, 1922, pp. 219-224.

Witt, G.: Height, Structure and Displacements of Noctilucent Clouds. Tellus, vol. 14, no. 1, Feb. 1962, pp. 1-18.

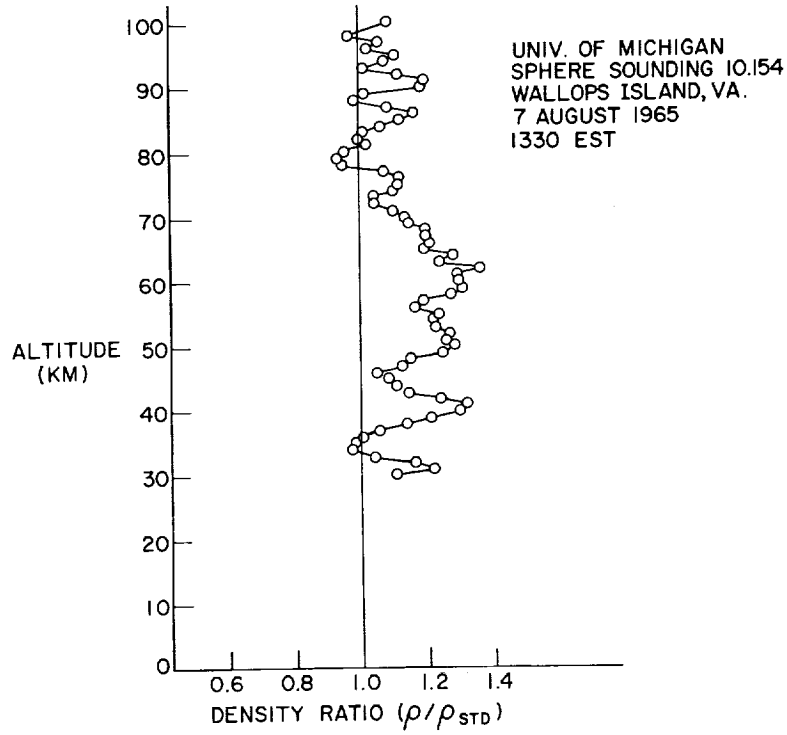

Figure 1.- A very unusual sounding.

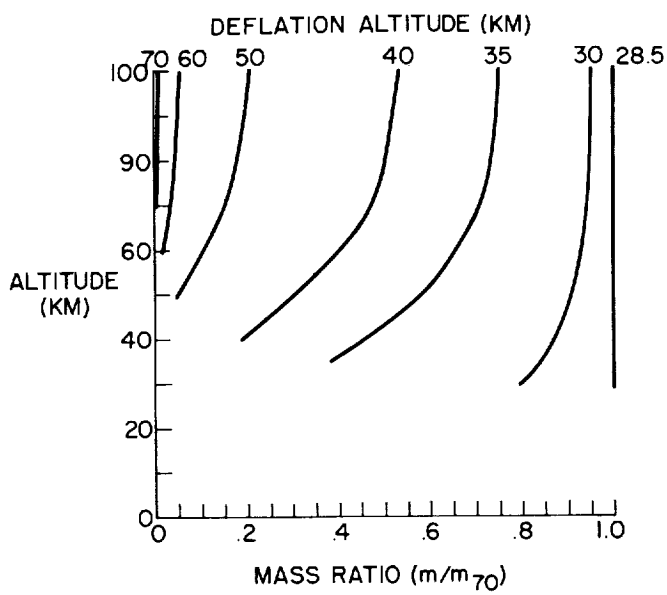

Figure 2.- Ratio of mass of gas in sphere at any altitude to mass of gas in sphere at ejection (70 sec) as a function of deflation altitude.

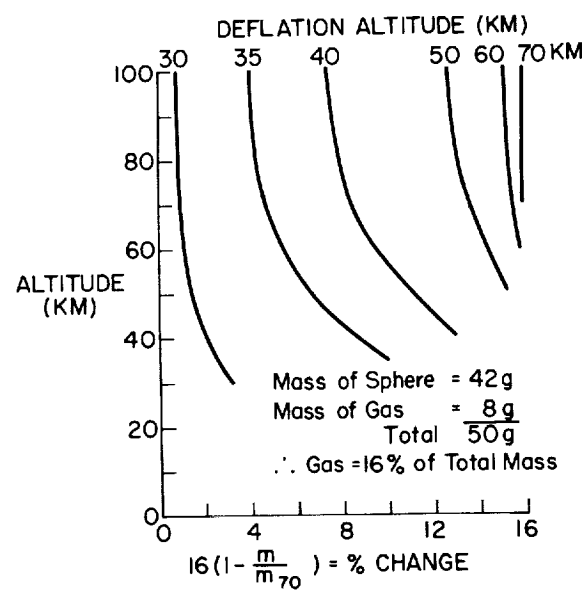

Figure 3.- Percent change in sphere mass caused by a leak.

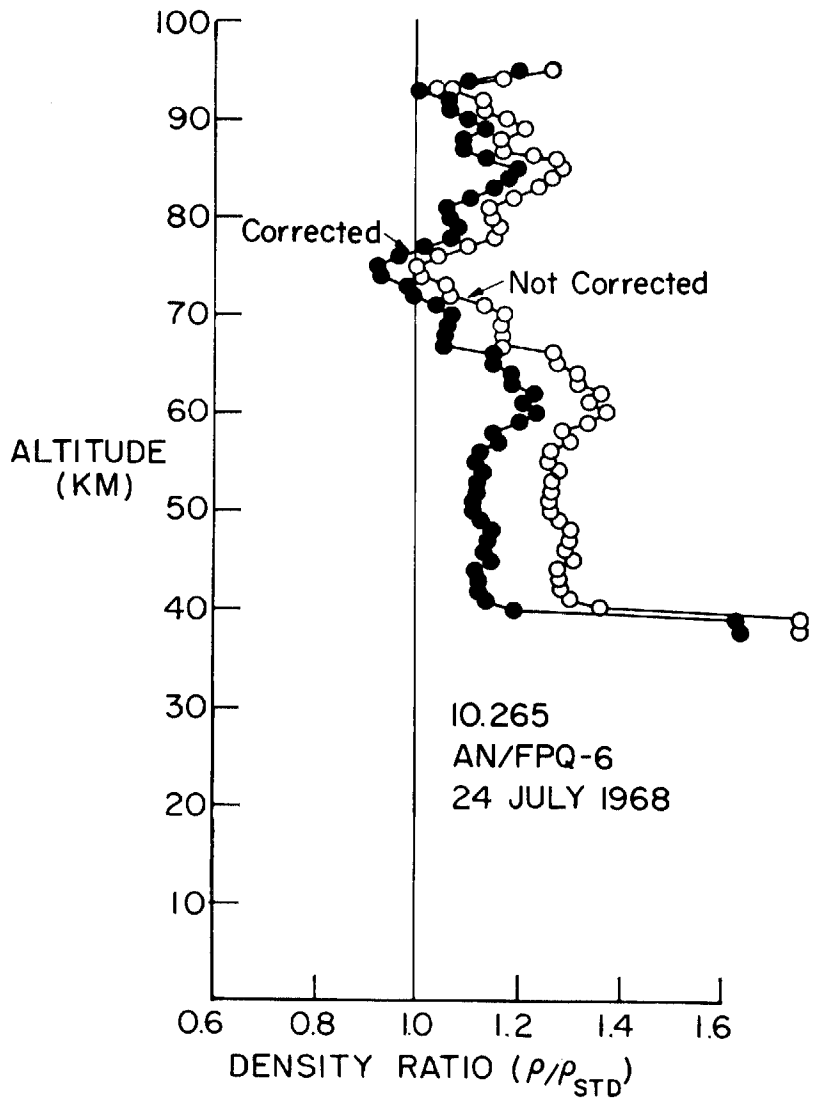

Figure 4.- Effect of mass correction on density in the case of an early deflation.

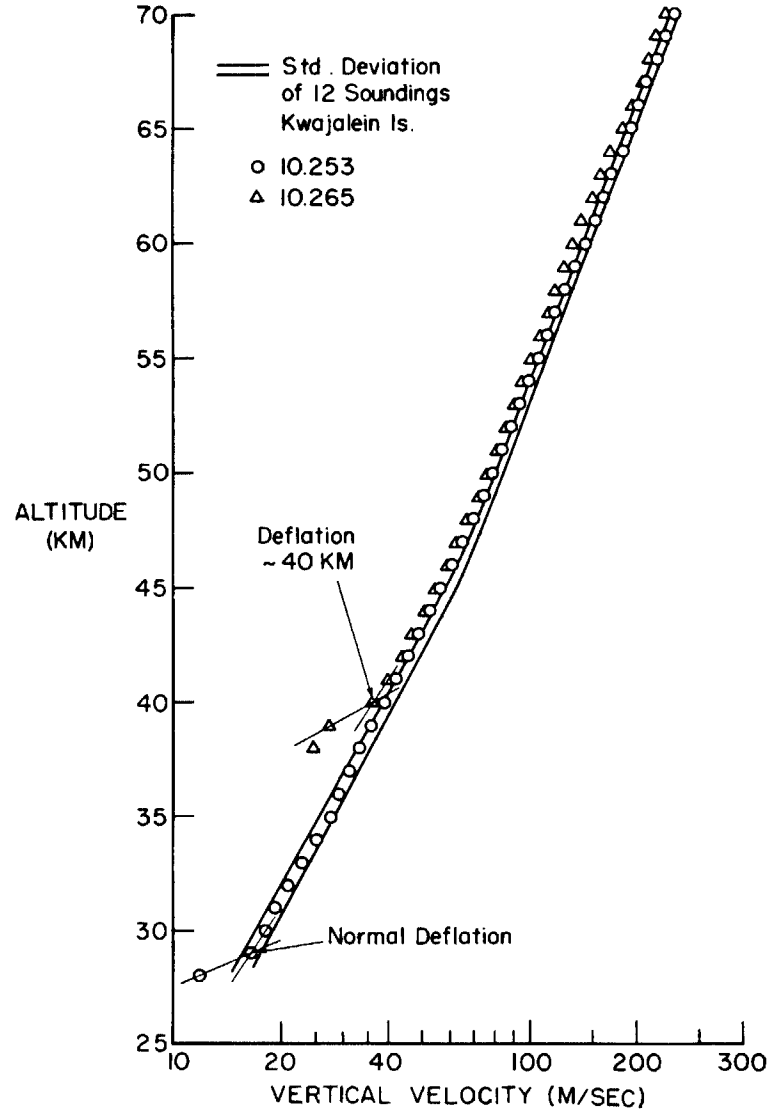

Figure 5.- Fall rate indicates sphere deflation.

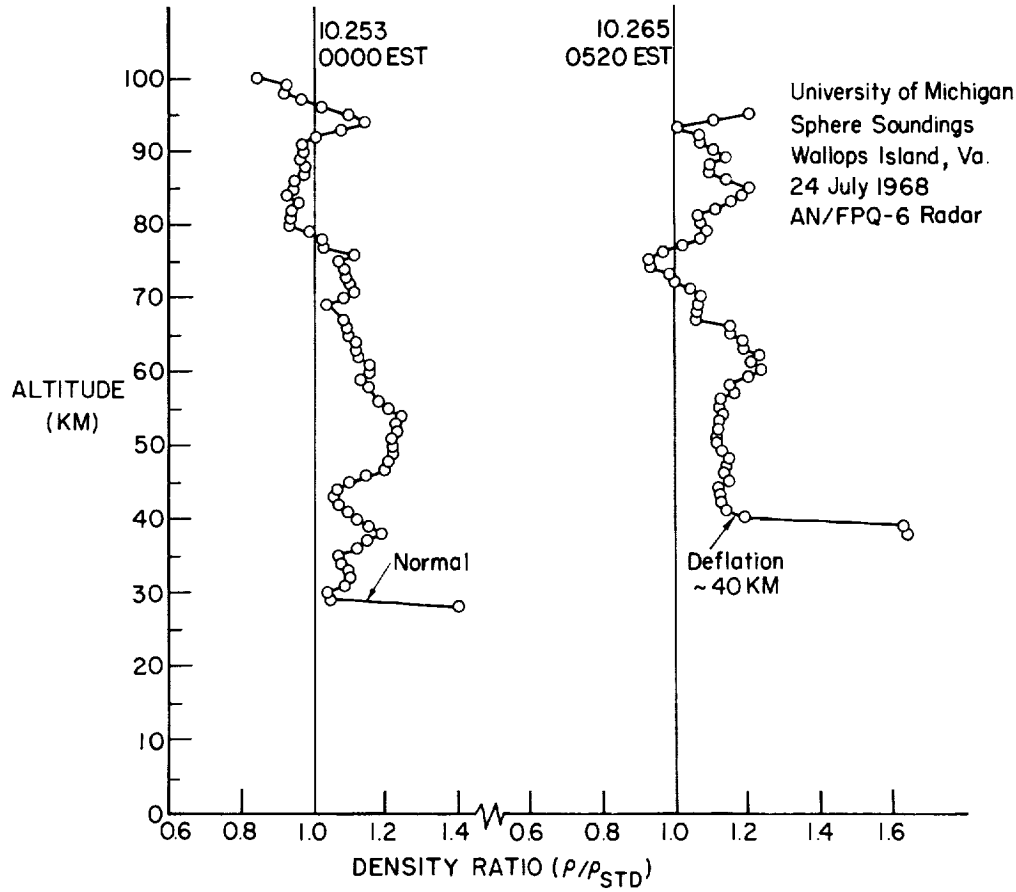

Figure 6.- Density ratio indicates sphere deflation.

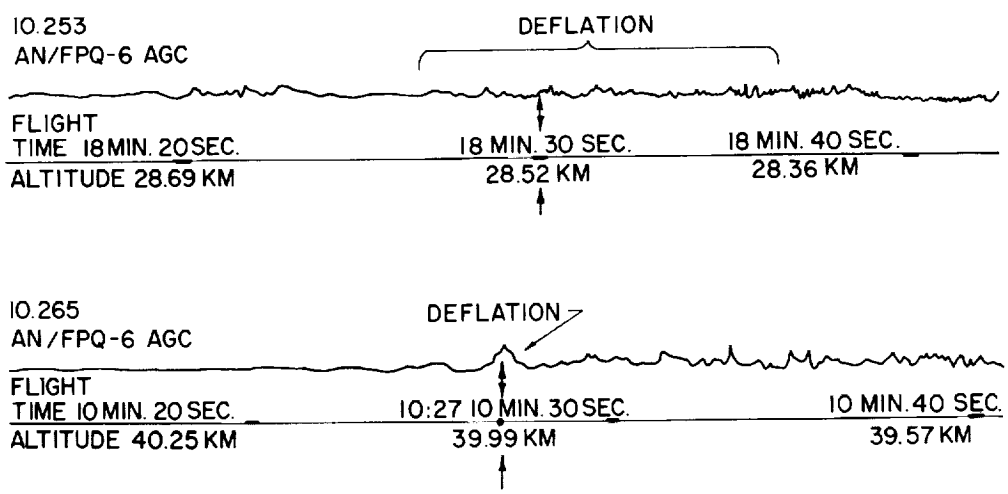

Figure 7.- Deflation observed on AGC records.

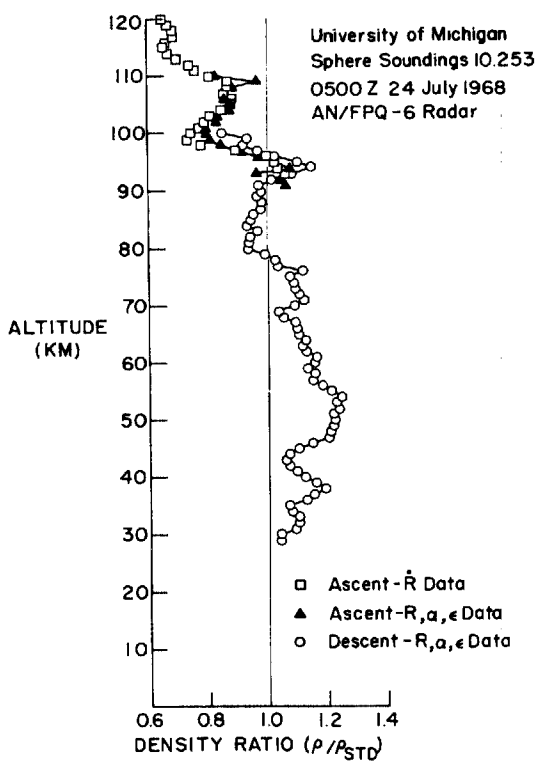

Figure 8.- Three sphere data techniques.

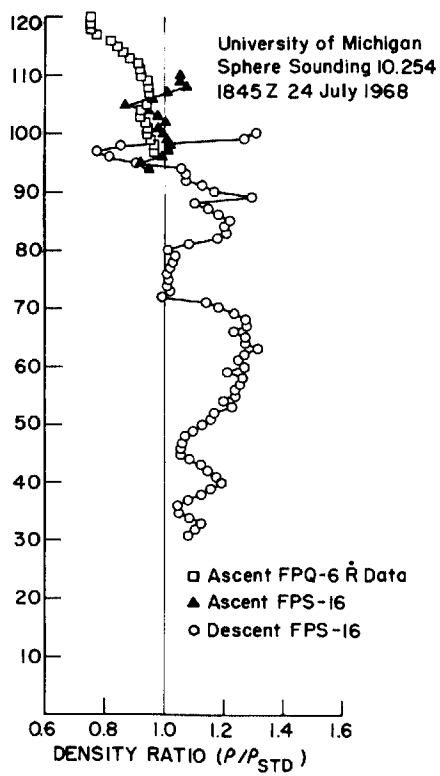

Figure 9.- Comparison of AN/FPQ-6 with AN/FPS-16 in July 1968.

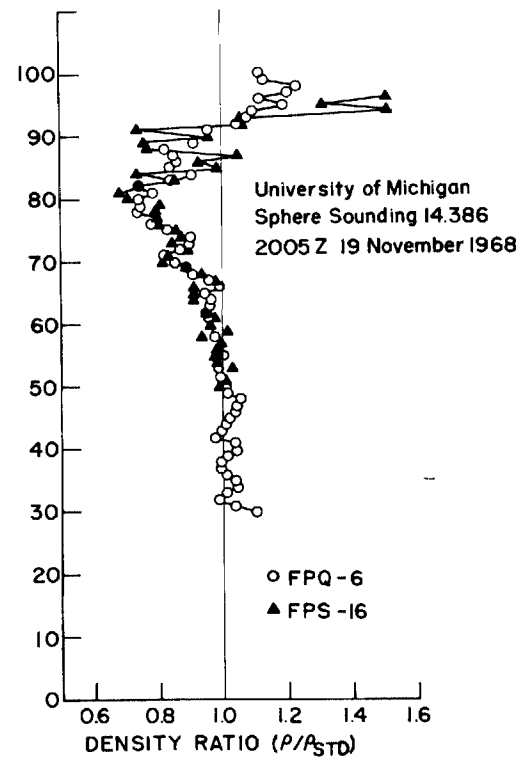

Figure 10.- Comparison of AN/FPQ-6 with AN/FPS-16 in November 1968.

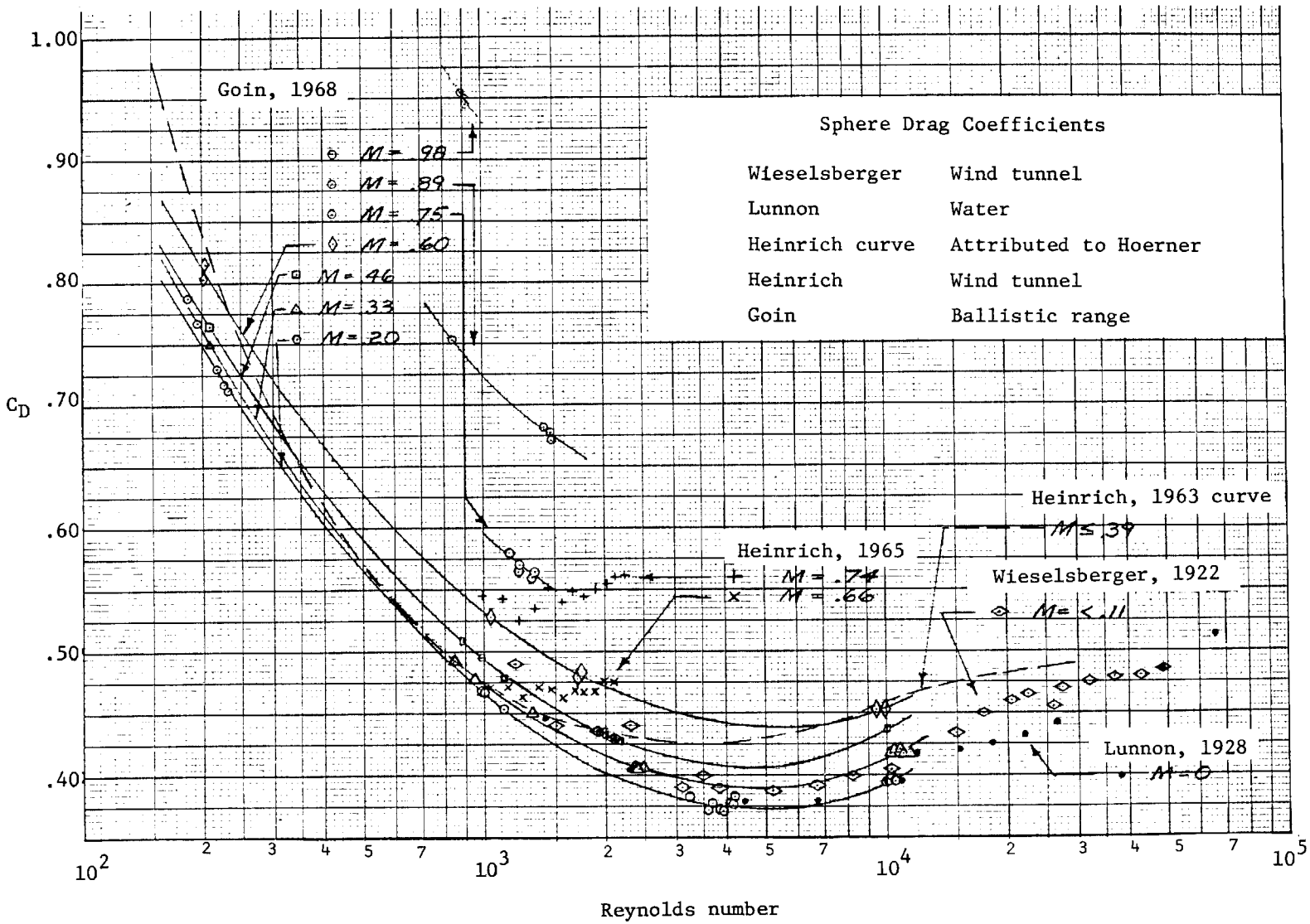

Figure 11.- Sphere drag coefficients.

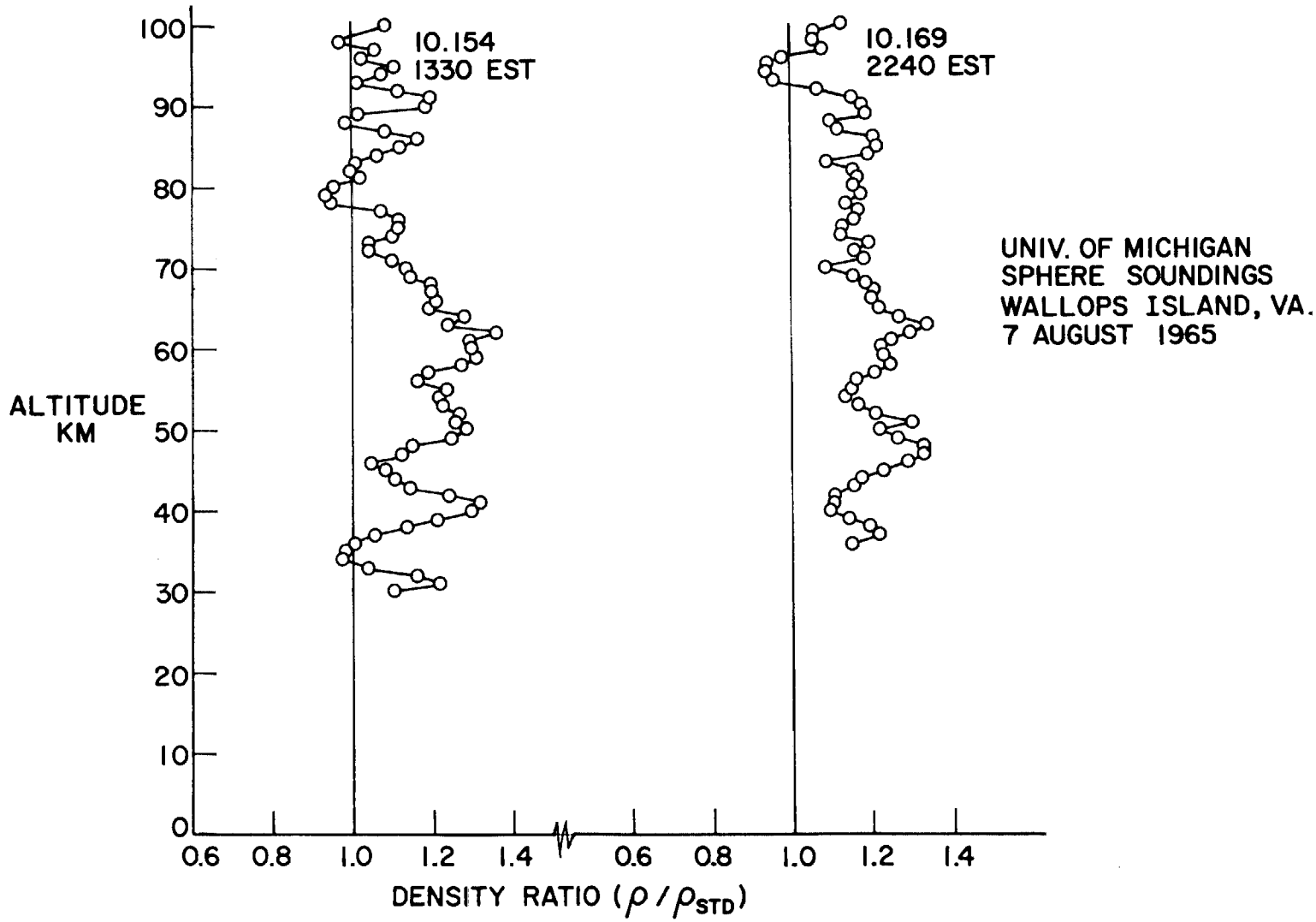

Figure 12.- The unusual sounding and another 9 hours later.

A CAPABILITY MODEL FOR PASSIVE SPHERES AT HIGH ALTITUDES

By Forrest L. Staffanson and R. Gary Phibbs

University of Utah

INTRODUCTION

The motion of a sphere free falling in the high atmosphere deviates from gravitational acceleration according to the drag expression

$$a_V - g_V = a_D = \frac{\rho V^2 C_D A}{2m}$$

where a_V and g_V are the inertial and gravitational acceleration components along the trajectory. (Symbols are defined in the appendix.) Atmospheric density can be deduced from the motion according to

$$\rho = \frac{2m}{C_D A} \frac{a_V - g_V}{V^2}$$

Uncertainty in the result depends on uncertainty in the measured trajectory quantities, assumed drag coefficient, gravitational acceleration, and sphere constants. By assuming random independence, these uncertainties are related as follows:

$$\left(\frac{\delta\rho}{\rho}\right)^2 = \left(\frac{\delta a_V}{a_D}\right)^2 + \left(2\,\frac{\delta V}{V}\right)^2 + \left(\frac{\delta C_D A}{C_D A}\right)^2 + \left(\frac{\delta g_V}{a_D}\right)^2 + \left(\frac{\delta m}{m}\right)^2$$

Atmospheric temperature can be calculated from the deduced density profile within the validity of the hydrostatic equation and equation of state according to

$$T = \frac{M_W}{\rho}\left[\frac{\rho_o T_o}{(M_W)_o} - \frac{1}{R^*}\sum_i (\rho g\,\Delta z)_i\right]$$

Uncertainty in the initial value T_o and mean molecular weight, as well as in the aforementioned quantities, produce uncertainty in the calculated temperature.

$$\left(\frac{\delta T}{T}\right)_k^2 = \left(\frac{\delta\rho}{\rho}\right)_k^2 + \left(\frac{\delta M_W}{M_W}\right)_k^2 + \left(\frac{M_W}{\rho T}\right)_k^2 \left\{\left(\frac{T_o}{(M_W)_o}\,\delta\rho_o\right)^2 + \left(\frac{\rho_o}{(M_W)_o}\,\delta T_o\right)^2 + \left(\rho_o T_o \frac{\delta(M_W)_o}{(M_W)_o^{\,2}}\right)^2\right.$$

$$\left. + \left(\frac{1}{R^*}\right)_k^2 \left[\sum_i^k \left[\left(\frac{\delta\rho}{\rho}\right)_i^2 + \left(\frac{\delta g}{g}\right)_i^2\right](\rho g\,\Delta z)_i^2 + \mu_g\left(\frac{\delta g}{g}\right)^2 \sum_i^k\sum_j^k (\rho g\,\Delta z)_i(\rho g\,\Delta z)_j\right]\right\} \qquad (i \neq j)$$

9

where $0 \leqq \mu_g \leqq 1$ according to the nonindependence of the error in g with altitude. The assumption here of point-to-point independence in other quantities such as C_D is undoubtedly pessimistic in $\delta T/T$. Further investigation and experience with the passive-sphere technique will provide quantitative information concerning independence and correlation in such quantities.

ACCELERATION AND VELOCITY UNCERTAINTY

Uncertainty in the measured acceleration and velocity of a passive sphere is determined by the accuracy of the tracking instrument and by the length of the data-smoothing interval used in computing time derivatives. (We make the tacit assumption that no error is introduced by the smoothing model, which is tantamount to assuming that the sphere trajectory is exactly of the order or form of the polynomial or other function used in fitting the data.) Bases for a general quantitative evaluation of derivative uncertainty from position uncertainty and smoothing interval length are presented herein.

The tracking system measures the position of the sphere to within some volume of uncertainty which, in turn, may vary in size and shape according to sphere position. The dimension of interest in this volume is that along the drag vector, which for the high altitudes under discussion is parallel to the path tangent. By assuming that the tracking system measures sphere position in slant range R, azimuth angle A, and elevation angle E, with uncertainty in each, δR, δA, and δE, the position uncertainty along the path tangent is given by

$$(\delta X)^2 = \left[\frac{(\dot{R}\delta R)^2 + \left(R^2\dot{E}\delta E\right)^2 + \left(R^2\dot{A}\delta A \cos E\right)^2}{V^2}\right]$$

where

$$V^2 = (\dot{R})^2 + (R\dot{E})^2 + (R\dot{A} \cos E)^2$$

Smoothing of data rests on available discriminating knowledge of the signal and noise in the data. The major characteristic of the signal, which immediately suggests itself, is sphere inertia, which implies a cutoff frequency in sphere velocity response.

Linearizing the drag acceleration about a point on the trajectory provides an expression for the local frequency response.

$$\omega_s = \frac{\rho C_D V}{(m/A)}$$

The corresponding minimum altitude wavelength of density structure to which the sphere can respond is

$$Z_s = \frac{2\pi\dot{z}}{\omega_s}$$

The radius Δz of the altitude neighborhood within which a constant ω_s is valid is given by

$$\frac{1}{\omega_s}\left(\frac{\partial \omega_s}{\partial z}\Delta z\right) = \left(\frac{1}{\rho}\frac{\partial \rho}{\partial z} + \frac{1}{C_D}\frac{\partial C_D}{\partial z} + \frac{1}{V}\frac{\partial V}{\partial z}\right)\Delta z$$

The first term in the sum is the reciprocal of the local scale height

$$H = \frac{R^* T}{M_W g}$$

the second is small, and the third is proportional to density according to

$$\frac{1}{V}\frac{\partial V}{\partial z} = \frac{\rho C_D}{2(m/A)}\frac{V}{\dot{z}}$$

The first term dominates at high altitude. By assigning a "validity limit" $\Delta\omega_s/\omega_s$, the altitude interval over which constant ω_s holds is $\pm\Delta z = 2H\left(\frac{\Delta\omega_s}{\omega_s}\right)$. The character of low-order polynomial smoothing routines in the frequency domain is approximated by that of a low-pass filter with cutoff frequency ω_f inversely proportional to smoothing interval W.

$$\omega_f = \frac{\pi}{W}$$

The altitude interval traversed during a "window" time length W is proportional to vertical velocity $\dot{z}$, and the minimum altitude wavelength in density structure passed by such a filter is about twice that interval.

$$Z_f = 2W\dot{z} = \frac{2\pi\dot{z}}{\omega_f}$$

Processing the data with a low-pass filter having a cutoff frequency $\omega_f = \omega_s$ would reject considerable noise without disturbing the signal. As altitude increases, however, $Z_s/2$ exceeds its range of validity $2H(\Delta\omega_s/\omega_s)$. Though approaches are conceivable, by using advanced processing techniques which may effectively enable the use of greater smoothing intervals without exceeding the validity of the associated smoothing model, smoothing intervals are currently limited for practical purposes to those over which ω_s is constant, i.e., to $Z_s/2$ or $2H(\Delta\omega_s/\omega_s)$, whichever is smaller.

Matching W to the frequency response of the sphere but limiting it to $2H(\Delta\omega_s/\omega_s)$ requires

$$W = \frac{\pi(m/A)}{\rho C_D V} \qquad \left[Z_s \leqq 4H(\Delta\omega_s/\omega_s)\right]$$

$$W = \frac{2H}{\dot{z}} \qquad \left[Z_s > 4H(\Delta\omega_s/\omega_s)\right]$$

For the higher altitudes of interest, the window will depend on H, and therefore, the data are filtered less and less with increasing altitude, relative to sphere response. A variable smoothing interval of this maximum length approximates best that can be done with the standard smoothing techniques of low-order polynomial fitting.

Other noise and signal characteristics which permit the identification of certain desired or undesired components in the data sometimes exist. Special techniques designed for specific components are assumed operative in the present discussion to the extent that their respective net noise components do not exceed the assumed measurement uncertainties.

Time derivatives from a low-pass filter are bounded by the cutoff frequency and by input amplitude. If input uncertainty is δX, then uncertainties in the first and second derivatives are approximated by

$$\delta\dot{X} = \omega_f \delta X$$

$$\delta\ddot{X} = \omega_f^2 \delta X$$

The above relations combine and reduce to an error model for the passive-sphere system at high altitudes. By letting $\frac{\Delta\omega_s}{\omega_s} = 1$,

$$\frac{\delta\rho}{\rho} = \left\{4\left(\frac{\omega_f \delta X}{V}\right)^2\left[\left(\frac{\omega_f}{\omega_s}\right)^2 + 4\right] + \left(\frac{\delta C_D A}{C_D A}\right)^2 + \left(\frac{\delta g_V}{g_V}\right)^2 + \left(\frac{\delta m}{m}\right)^2\right\}^{1/2}$$

The first term is

$$20\left[\frac{\rho C_D}{(m/A)} - \delta X\right]^2 \qquad (Z_f = Z_s)$$

$$\left(\frac{\pi}{H}\frac{\dot{z}}{V}\delta X\right)^2\left[\left(\frac{\pi(m/A)}{2H\rho C_D}\frac{\dot{z}}{V}\right)^2 + 4\right] \qquad (Z_f = 4H)$$

A quantitative illustration of this error model, including the associated temperature uncertainty is presented in tables I and II and figure 1.

For reference, a simulated 160-km trajectory in the U.S. Standard Atmosphere 1962 of a 1-meter, 100-gram sphere is used. Arbitrary values for input uncertainties are based on published experience (refs. 1, 2, and 3).

Uncertainty is taken here to correspond to practical limits of error. Uncertainty of the value of a normally distributed random variable is taken as two standard deviations

and that of a uniformly distributed quantity its semirange (radius). Quoted uncertainty values for drag coefficient, for example, are understood to mean the limit within which the true value lies with a high (80- to 90-percent) probability. Inputs and results here may be halved throughout to correspond to the standard deviation.

The uncertainty inputs are as follows:

$$\delta R = 9.0 \text{ meters}$$

$$\delta E = \delta A = 0.0001 \text{ radian}$$

$$\frac{\delta C_D A}{C_D A} = 0.03$$

$$\frac{\delta g_V}{g_V} = 0.01$$

$$\frac{\delta m}{m} = 0.01$$

$$\frac{\delta M_W}{M_W} = 0.03$$

OBSERVATION

The quantitative results of the illustration suggest a significant finding concerning the passive-sphere technique. Deviations between sphere results and results from other atmospheric sounding techniques may be explained in large part as a consequence of the smoothing interval used.

It is recommended that data reduction programs include the automatic calculation of the point-to-point uncertainty and present a measured parameter q from a given sounding in the form of $q \pm \Delta q$, rather than simply as q. Thus, for example, the density profile plot would be a curve with varying width within which the measured density lies with a stated probability. Comparisons between techniques would then be expected to produce overlapping curves.

It is expected that tracking accuracy, δR, δE, δA, will not increase significantly over the assumed values for altitudes considerably higher than 90 km. Therefore, larger data-smoothing intervals would materially enhance the altitude capability of the passive-sphere technique. By assuming successful higher order smoothing models, an upper bound or the maximum possible smoothing interval at a given altitude is the period of the entire trajectory above that altitude including both upleg and downleg portions. Further investigation of the practical capabilities of potential and advanced data processing methods is indicated. The tracking accuracy requirements for a new passive-sphere system must depend on properties of the smoothing interval to be used.

APPENDIX

SYMBOLS

A	sphere cross-sectional area, m^2; radar azimuth angle, radians
a_D	drag acceleration, m/sec^2
a_V	inertial acceleration along the trajectory, m/sec^2
C_D	drag coefficients
E	radar elevation angle, radians or degrees
g	gravity, m/sec^2
g_V	gravitational acceleration along the trajectory, m/sec^2
H	atmospheric scale height, m
M	Mach number
M_W	mean molecular weight
m	sphere mass, kg
N_{Re}	Reynolds number
R	radar slant range, m
R^*	universal gas constant, joules/^{o}K kg-mol
T	atmospheric temperature, ^{o}K
t	time
V	air speed, m/sec
W	smoothing interval, sec

X	position along trajectory, m
Z_f, Z_s	minimum altitude wavelength; passed by smoothing or sensed by sphere, respectively, m
z	altitude, m
δq	uncertainty along trajectory of any parameter q
μ_g	degree of nonindependence of gravity error with altitude
ρ	atmospheric density, kg/m^3
ψ	trajectory angle from horizontal, degrees
ω_f, ω_s	cutoff frequency of smoothing response or of sphere response, respectively, radians/sec

Subscripts:

i,j,k	indices
o	initial

Dots over a symbol indicate the degree of the derivative with respect to time.

REFERENCES

1. Engler, Nicholas A.: Development of Methods To Determine Winds, Density, Pressure, and Temperature From the ROBIN Falling Balloon. AFCRL-65-448, U.S. Air Force, May 1965. (Available from DDC as AD630200.)
2. Peterson, J. W.; Hansen, W. H.; McWatters, K. D.; and Bonfanti, G.: Atmospheric Measurements Over Kwajalein Using Falling Spheres. NASA CR-218, 1965.
3. Smith, Lawrence B.: Observations of Atmospheric Density, Temperature, and Winds Over Kauai. SC-RR-68-523, Sandia Lab., Aug. 1969.

TABLE I

DOWNLEG

t, sec	z, km	V, m/sec	ψ, degrees	R, km	E, degrees	$\dot{R}$, m/sec	$R\dot{E}$, m/sec	$\dot{z}$, m/sec
220	115	960	-72.8	143.9	53.0	-562	-779	-917
225	110	1004	-73.3	140.9	51.3	-575	-821	-963
230	105	1043	-74.2	138.0	49.6	-583	-856	-1004
235	100	1074	-74.8	135.1	47.8	-582	-911	-1037
240	95	1089	-75.9	132.4	45.4	-569	-925	-1055
245	90	1073	-75.7	129.7	43.9	-539	-930	-1042
250	85	986	-76.9	127.2	42.0	-475	-862	-960
255	80	774	-77.4	124.8	39.5	-358	-718	-756
264	75	458	-79.2	122.4	37.8	-208	-406	-450
279	70	254	-83.0	120.1	35.7	-123	-221	-252

z, km	M	N_{Re}	C_D	a_D, m/sec^2
115	2.75	2.41	2.44	0.413
110	3.12	5.99	2.37	.914
105	3.40	14.5	2.20	1.98
100	3.69	38.4	1.84	4.13
95	3.88	101.0	1.51	8.52
90	3.98	277.0	1.29	18.4
85	3.66	645.0	1.19	36.1
80	2.87	1277.0	1.12	53.1
75	1.61	1491.0	1.03	36.8
70	.854	1540.0	.604	13.3

z, km	$\frac{\delta\rho}{\rho}$	$\frac{\delta T}{T}$	δT, °K	δX, m	$\frac{\delta a_D}{a_D}$	$2\frac{\delta V}{V}$	Z_f, km	Z_s, km	W, sec
115	0.758	0.909	275.0	12.8	0.757	0.004	36.9	6.+6	20.1
110	.520	.593	153.0	12.6	.519	.005	31.2	3.+6	16.3
105	.314	.349	81.6	12.5	.313	.005	28.4	1.+6	14.1
100	.199	.214	45.0	12.4	.197	.006	25.4	847	12.2
95	.117	.126	24.0	12.2	.113	.006	23.6	424	12.8
90	.067	.076	13.7	12.1	.059	.007	21.8	191	10.5
85	.041	.052	9.4	12.0	.025	.007	21.8	82.4	11.5
80	.034	.046	8.3	11.8	.011	.007	21.7	34.6	14.3
75	.033	.046	9.2	11.7	.008	.008	24.0	17.6	19.2
70	.034	.046	10.1	11.4	.009	.009	26.3	15.1	30.0

TABLE II

UPLEG

t, sec	z, km	V, m/sec	ψ, degrees	R, km	E, degrees	$\dot{R}$, m/sec	$R\dot{E}$, m/sec	$\dot{z}$, m/sec
23.6	115	962	72.8	119.0	75.0	961.7	-35.9	919
18.4	110	1012	73.8	113.9	75.0	1012.0	-24.7	972
13.4	105	1065	74.4	108.7	75.1	1065.0	-13.8	1026
8.6	100	1124	74.9	103.5	75.1	1124.0	-2.32	1085
4.1	95	1197	75.5	98.2	75.2	1197.0	8.93	1159
0	90	1304	76.0	93.1	75.2	1303.0	20.6	1265

z, km	M	N_{Re}	C_D	a_D, m/sec^2
115	2.76	2.40	2.44	0.414
110	3.15	6.04	2.37	.930
105	3.47	14.8	2.19	.413
100	3.87	40.5	1.82	.442
95	4.27	112.0	1.48	10.2
90	4.84	340.0	1.27	26.8

z, km	$\frac{\delta\rho}{\rho}$	$\frac{\delta T}{T}$	δT, ^oK	δX, m	$\frac{\delta a_D}{a_D}$	$2\frac{\delta V}{V}$	Z_f, km	Z_s, km	W, sec
115	0.535	0.735	223.0	9.00	0.534	0.003	36.9	6.+6	2.04
110	.371	.468	120.0	9.00	.369	.003	31.3	3.+6	16.1
105	.228	.273	63.9	9.00	.226	.004	28.4	1.+6	13.9
100	.148	.166	34.9	9.00	.144	.004	25.4	8.+5	11.7
95	.090	.100	19.6	9.00	.084	.005	23.6	427	10.2
90	.055	.065	11.7	9.00	.045	.005	21.8	193	8.6

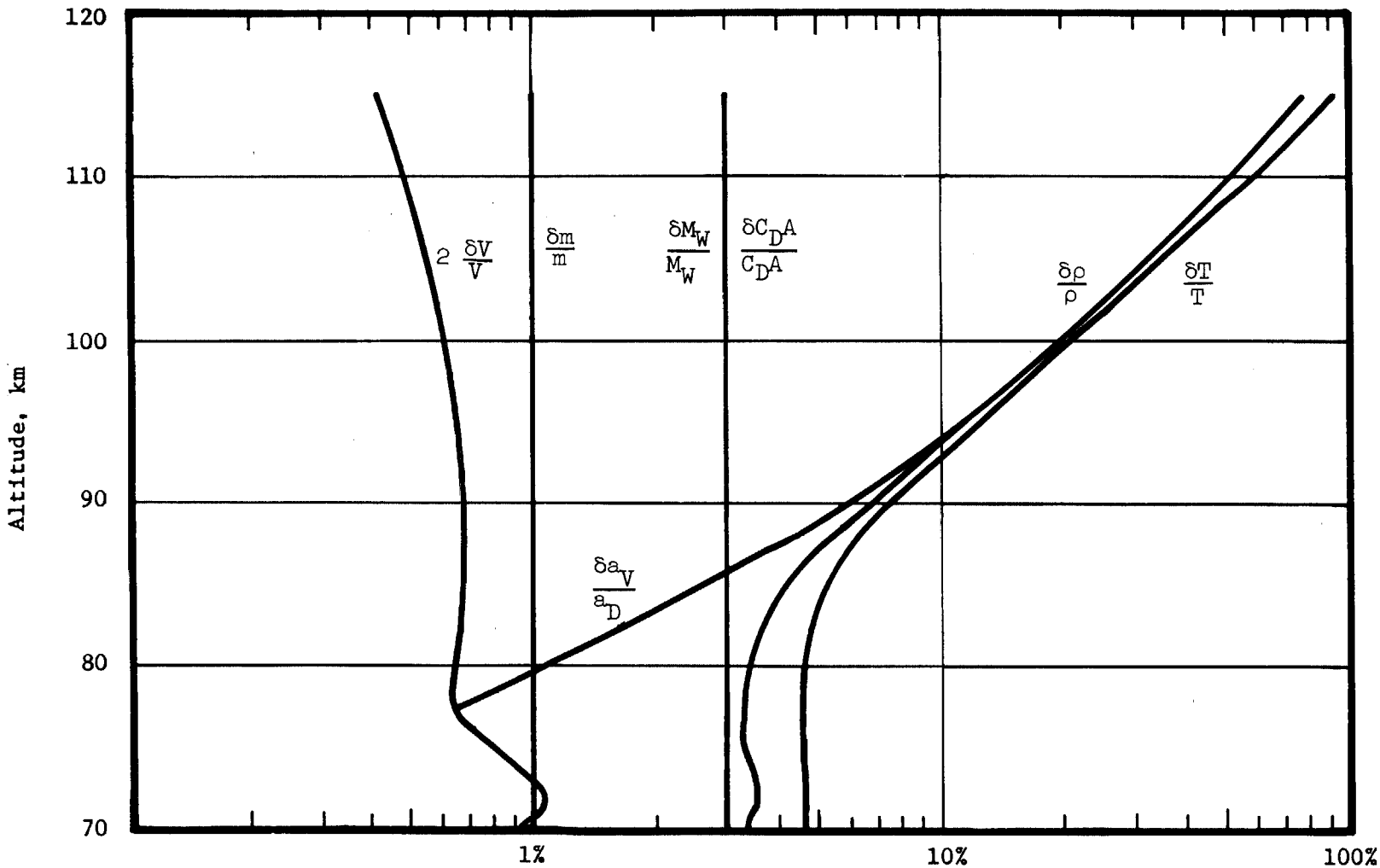

Figure 1.- Uncertainty components and resultants.

REQUIREMENTS FOR TRACKING RADAR FOR FALLING SPHERES

By John L. Hain and William E. Brockman

Booz, Allen Applied Research, Inc.

SUMMARY

As a part of the system design of an upper air synoptic sounding system for NASA Langley Research Center, a technique was developed for expressing explicitly the effect of pertinent radar accuracy limits on the uncertainties in the meteorological data produced by the system. The results of this aspect of the study are briefly reviewed herein.

INTRODUCTION

The passive falling sphere is the lightest and least expensive payload which has been shown to provide satisfactory data in the upper atmosphere, i.e., 30 to 100 km altitude. The payload and the means of lofting it have been well developed and their costs are well understood and manageable. The usable data, however, come from a high-cost ground tracker of limited availability. With few exceptions the data have been obtained using rather expensive trackers procured for and dedicated to significantly different purposes. The purpose of this paper is to explore the relation between the requirements for data on the motion of the sphere and selected sources of error in a radar tracker.

The discussion will consist of three parts, covering: first, the sphere trajectory; second, some pertinent radar accuracy limits; and third, the consequent limits on density and wind accuracies. Since only certain limiting conditions are considered, the results are essentially boundaries rather than explicit statements of accuracies applicable to specific configurations.

A detailed derivation of the equations used in developing these boundaries is included in reference 1.

SYMBOLS

B	Receiver Bandwidth
C_D	Drag Coefficient
E	Elevation Angle of Sphere from Tracker
F_o	Receiver Noise Figure

g	Gravitational Constant
G_t, G_r	Gain of Transmitting and Receiving Antennas
L	Tracker System Losses
N	Number of Independent Data Points
P_t	Radiated Power of Tracker
R	Slant Range Between Sphere and Tracker
$\dot{R}$	Radial Velocity Between Sphere and Tracker
S/N	Effective Signal to Noise Ratio
Δt	Time Interval in Seconds
x,z	x and z Coordinates of Sphere Position
W	Wind Vector
W_z	Vertical Component of Wind
α,β	Angles Defining Line of Sight Between Sphere and Tracker
Δq	Bias Error in Any Parameter q
θ	Antenna Beamwidth
λ	Operating Wavelength of Tracker
ρ	Density
σ	Radar Cross Section of Sphere
σ_q	Standard Deviation of Any Parameter q
σ_q^2	Variance of Random Error in q

τ Tracker Pulse Length

Dots over a symbol denote the degree of the derivative with respect to time.

THE SPHERE TRAJECTORY

Assuming a rocket-lofted sphere, a skewed trajectory envelope such as that depicted in Figure 1 was used. Wind profiles of ±50% and ±99% were included to assure adequacy of spatial coverage. A collocated launcher and tracker were assumed to minimize personnel, logistic and real estate costs for a synoptic system. The initial conditions (at the top of the sphere trajectory) are as follows:

Altitude	140 km
Horizontal displacement	40 km
Horizontal velocity	200 meters/sec
Gravitational acceleration	-9.8 meters/sec
Area/Mass ratio	6.54
Radius of the earth	6,378,388 meters

The resultant theoretical descending trajectory, using the +50% wind profile, is shown in Table 1. If such an actual trajectory can be observed as a suitable set of coordinates vs. time, both density and wind data may be determined.

The density of the atmosphere in the immediate vicinity of the falling sphere may be derived as a function of:

Vertical velocity of the sphere
Vertical acceleration of the sphere
Drag coefficient of the sphere.

The local wind vector may be derived as a function of:

Vertical and horizontal velocity of the sphere
Vertical and horizontal acceleration of the sphere
Gravitational constant.

Thus, if our trajectory is measured as a set of spatial coordinates vs. time, it is apparent that the falling sphere technique is as sensitive to errors in the first and second time derivatives of the coordinates as it is to errors in the coordinates themselves. For ease in exploring these relationships, a two-dimensional flight profile for the sphere was assumed. This is equivalent to aligning the launcher inclination and the effective plane of one of the tracker's angular sensors with the prevailing wind.

If the first and/or second derivatives are obtained by fitting a function to the data points and taking the derivative, the error can be separated into two parts. One part is

the error due to noise in the data, the other due to lack of fit by the function to the physical laws that produced the data points.

The error due to noise is a function of:

Fitting length (number of points)
Data frequency
Noise in measured parameter
Method used (polynomial and degree).

The error due to lack of fit is a function of:

Fitting length (number of points)
Data frequency
Numerical characteristics of the function that produced the data points
Method used (polynomial and degree).

Since the purpose of this discussion is to explore the impact of radar errors, only the error due to noise in the measurements will be pursued.

The expression for the error in density which has been derived (ref. 2) is

$$\left(\frac{\sigma_\rho}{\rho}\right)^2 = \left(\frac{2\sigma_{W_z}}{\dot{z} - W_z}\right)^2 + \left(\frac{2\sigma_{\dot{z}}}{\dot{z} - W_z}\right)^2 + \left(\frac{\sigma_{\ddot{z}}}{\ddot{z} - g}\right)^2 + \left(\frac{\Delta\ddot{z}}{\ddot{z} - g} - \frac{2\Delta\dot{z}}{\dot{z} - W_z} - \frac{\Delta C_D}{C_D}\right)$$

The bias error is the error due to lack of fit and will, as previously stated, not be considered. Uncertainty in the drag coefficient, probably one of the most significant problems relative to the falling sphere technique, is, fortunately, not germane to the tracking accuracy exploration. Eliminating these terms, the expression for error in density may be rewritten as

$$\left(\frac{\sigma_\rho}{\rho}\right)^2 = \frac{4}{\left(\dot{z} - W_z\right)^2}\sigma_{\dot{z}}^2 + \frac{1}{\left(\ddot{z} - g\right)^2}\sigma_{\ddot{z}}^2 + \frac{4}{\left(\dot{z} - W_z\right)^2}\sigma_{W_z}^2$$

Similarly, the variance in the horizontal wind is

$$\sigma_W^2 = \sigma_{\dot{x}}^2 + \left(\frac{\dot{z}}{\ddot{z} - g}\right)^2\sigma_{\ddot{x}}^2 + \left(\frac{\ddot{x}}{\ddot{z} - g}\right)^2\sigma_{\dot{z}}^2 + \left(\frac{\ddot{x}\dot{z}}{\ddot{z} - g^2}\right)^2\sigma_{\ddot{z}}^2$$

where the expression for the horizontal wind is

$$W = \dot{x} - \frac{\ddot{x}\dot{z}}{\ddot{z} - g}$$

PERTINENT RADAR ACCURACY LIMITS

The geometry of a generalized tracker operating on a passive falling sphere is shown in Figure 2. As shown, the definitions are those commonly used for a phased-array tracker. The two-dimensional analysis merely assumes that the wind lies along either the α or β axes. The elevation angle is thus the complement of α (or β). In the case of the usual electromechanical tracker, the analysis assumes no change in azimuth, so that all angular data is again in the elevation angle. The other two measurements of which a radar tracker is capable, range and range rate (or radial velocity), have been shown (ref. 3) to be interrelated through pulse width so that the corresponding accuracy limits are not independent. The standard deviation of range varies directly with the pulse width while that of radial velocity varies inversely. Although not strictly true in the general case, for many applications either may be computed from the other with an accuracy comparable to that which could be obtained by direct measurement. Therefore, the radar measurements which were explored in detail were those of slant range and elevation angle.

The classical radar range equation may be written (ref. 4) in the form

$$\frac{S}{N} = \frac{P_t G_t G_r \lambda^2 \sigma}{R^4 B F_o L}$$

where P_t is in watts, λ is in centimeters, R is in nautical miles, σ is in meters^2, and B is in hertz. The achievable accuracy is a function of the effective signal to noise ratio, and that varies inversely as the fourth power of the slant range. Thus, the quality of the meteorological data will degrade very rapidly with increasing distance to the falling sphere. Thermal noise, an inseparable part of every real signal, establishes a limit beyond which no hardware can extract usable data. The standard deviations for range and angle measurements on a single pulse basis (ref. 4) are

$$\sigma_R = \frac{137\tau}{\sqrt{S/N}}$$

$$\sigma_E = \frac{\theta}{2\sqrt{S/N}}$$

where σ_R is in meters, σ_E and θ are in milliradians, and τ is in microseconds.

Using these basic tools of sphere dynamics and of radar accuracy limits it was then possible to establish certain limits on the quality of meteorological observations.

The obvious trade-offs were those between maintaining vertical resolution and enhancing apparent accuracy by smoothing over a large number of data points. Thus, the length of the smoothing interval became a good indicator of relative merit.

ESTIMATION OF ACCURACY LIMITS

One final simplification: Fully acceptable techniques for separating vertical winds from density variance have yet to be developed, and the radar does not offer a solution. Therefore, the vertical component of the wind vector, like the uncertainty in the drag coefficient, does not appear in the final error model. It simply is not a part of the radar error contribution.

Since the errors in velocities and accelerations are smaller when a quadratic polynomial is fitted to the data points than when successive linear polynomials are used, the quadratic fit was used throughout the study. Velocities were then evaluated from the first derivative and acceleration from the second derivative of this smooth curve.

The error in the first derivative as a function of the error in the parameter is given by

$$\sigma_{\dot{q}}^2 = \frac{12}{N(N+1)(N+2)\Delta t^2}\,\sigma_q^2$$

and the error in the second derivative is given by

$$\sigma_{\ddot{q}}^2 = \frac{720}{(N-1)N(N+1)(N+2)(N+3)\Delta t^4}\,\sigma_q^2$$

The error model consisted of expressions for the error in density and in horizontal winds as functions of the variance of range, range rate, range acceleration, elevation angle, elevation rate, and elevation acceleration, as well as values dependent on the trajectory and smoothing interval.

But since only the range and elevation angle were measured, with the rates and acceleration being derived mathematically, the model was modified by substituting the derived variances of $\dot{R}$, $\ddot{R}$, $\dot{E}$, and $\ddot{E}$. The model then took the form:

$$\left(\frac{\sigma_\rho}{\rho}\right)^2 = F_1\sigma_R^2 + F_2\sigma_E^2$$

$$\sigma_W^2 = G_1\sigma_R^2 + G_2\sigma_E^2$$

where the F's and G's are lengthy functions of the coordinates and of the fitting functions, but not of errors in determining the coordinates.

Since angular accuracy is the most cost-sensitive parameter of a tracker (aside from attaining a workable signal to noise ratio) the relationship of meteorological function error to angular error was explored.

The first method of analysis was to assume a slant range error of 5 meters and to compute the smoothing interval when the elevation angle error was 0.05 mil and the density error was 2%. The density error limit was then increased to 3% and various values of elevation angle error were tried until the resulting smoothing interval was approximately equal to the 0.05 mil, 2% result. The process was repeated for density errors of 4% and 5%. The corresponding wind error was computed at each altitude level, for each combination of elevation angle error and density error. The complete profiles are given in Figure 3.

The following combinations of density error and elevation error yield approximately equal smoothing intervals. The maximum horizontal wind error for each combination is as shown.

Elevation, σ_E (mils)	Density, $\frac{\sigma_\rho}{\rho}$ (%)	Wind, σ_W (meters/sec)
0.05	2	19
0.10	3	37
0.15	4	54
0.20	5	70

The second method was to allow the elevation angle error to assume successively larger values, the only other parameter which was allowed to change as a consequence was the smoothing interval. This has the net effect of increasing the uncertainty as to the altitude at which the computed density was valid and, thus, results in a net uncertainty as to the density profile. The data are shown in Figure 4.

CONCLUSIONS

A method has been developed, programed, and tested for quickly determining the error contours applicable to a passive falling sphere, upper-air sounding system. It was then apparent that a synoptic system using the given trajectory placed stringent requirements on the tracker.

A stated design goal of a vertical resolution of 500 meters, with a standard deviation of 2% in density data and of 5 meters/second in wind velocity (below 70 km altitude) can be met, but it requires a sufficiently high signal to noise ratio in the tracker that the uncertainty due to thermal noise is no greater than 5 meters in range and 0.05 mil in angle.

Relaxation of vertical resolution permits longer smoothing intervals with consequent dramatic reduction in requisite angular accuracy.

REFERENCES

1. Booz, Allen Applied Research, Inc.: System for Upper Atmospheric Sounding (SUAS). Vol. II – Technical Report. NASA CR-66753-2, 1969.
2. Luers, J. K.: Estimation of Errors in Density and Temperature Measured by the High Altitude ROBIN Sphere. Proceedings of the Third National Conference on Aerospace Meteorology, Amer. Meteorol. Soc., 1968, pp. 472-477.
3. Skolnik, Merrill I.: Radar Systems. McGraw-Hill Book Co., Inc., 1962.
4. Barton, David K.: Radar System Analysis. Prentice-Hall, Inc., c.1964.

TABLE 1

TRAJECTORY

Using +50% Wind Profile

ALTITUDE (METERS)	HORIZONTAL DISPLACEMENT (METERS)*	HORIZONTAL VELOCITY (METERS/SECOND)	HORIZONTAL ACCELERATION (METERS/SECOND^2)	VERTICAL VELOCITY (METERS/SECOND)	VERTICAL ACCELERATION (METERS/SECOND^2)	SPEED (METERS/SECOND)**
140,000	41,200	200	−.009	−56	−9.367	208
130,000	49,384	199	−.052	−439	−9.286	482
120,000	53,151	197	−.165	−613	−8.920	644
110,000	56,076	191	−.776	−734	−6.485	759
100,000	58,445	167	−3.415	−756	5.918	774
90,000	60,493	82	−5.575	−472	22.554	479
80,000	61,686	11	.055	−112	1.457	112
70,000	63,065	25	.163	−93	.656	93
60,000	68,279	41	.075	−49	.147	49
50,000	82,110	48	−.036	−26	.042	26
40,000	104,673	34	−.017	−13	.012	13

*FROM A VERTICAL AXIS THROUGH LAUNCH SITE

**WITH RESPECT TO SURFACE OF EARTH

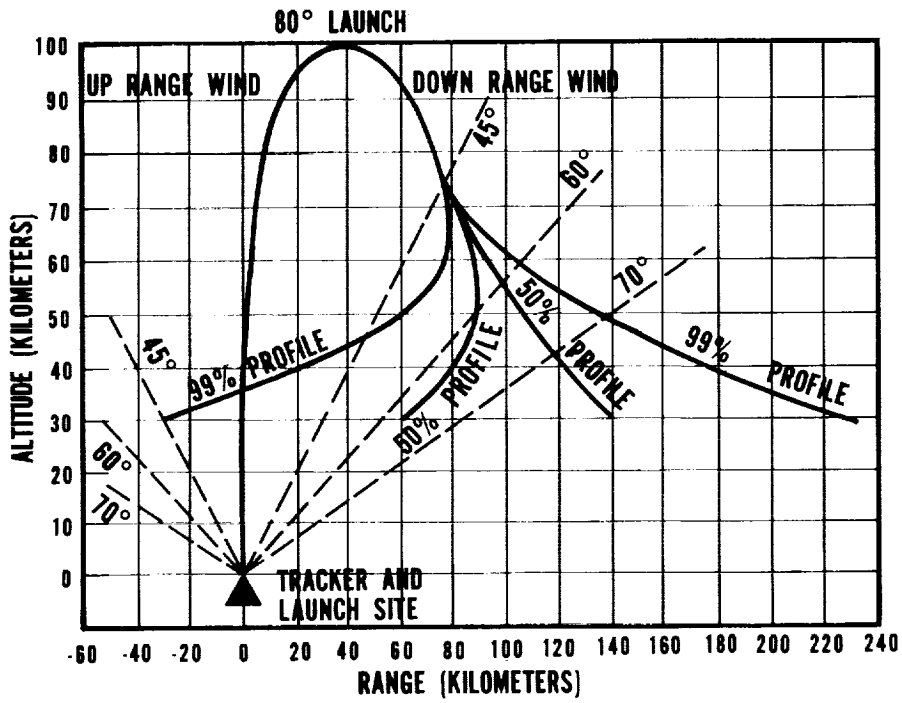

Figure 1.- Flight profile for inclined launch.

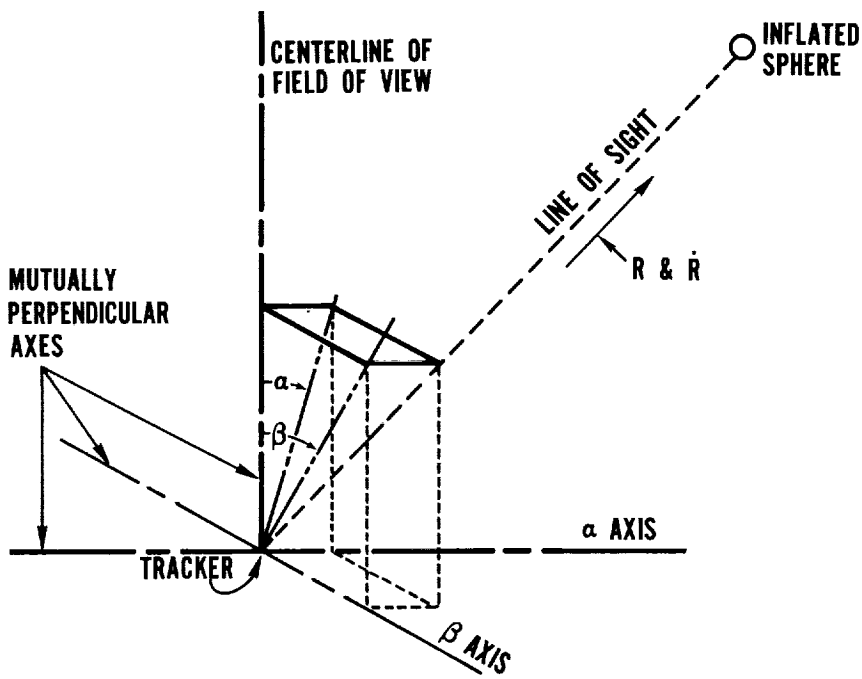

Figure 2.- Geometry of measured quantities.

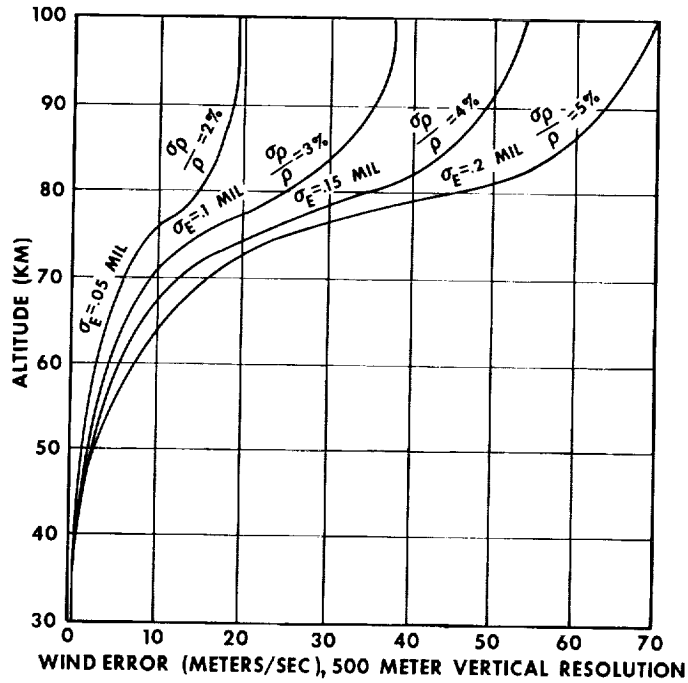

Figure 3.- Wind errors corresponding to various density errors.

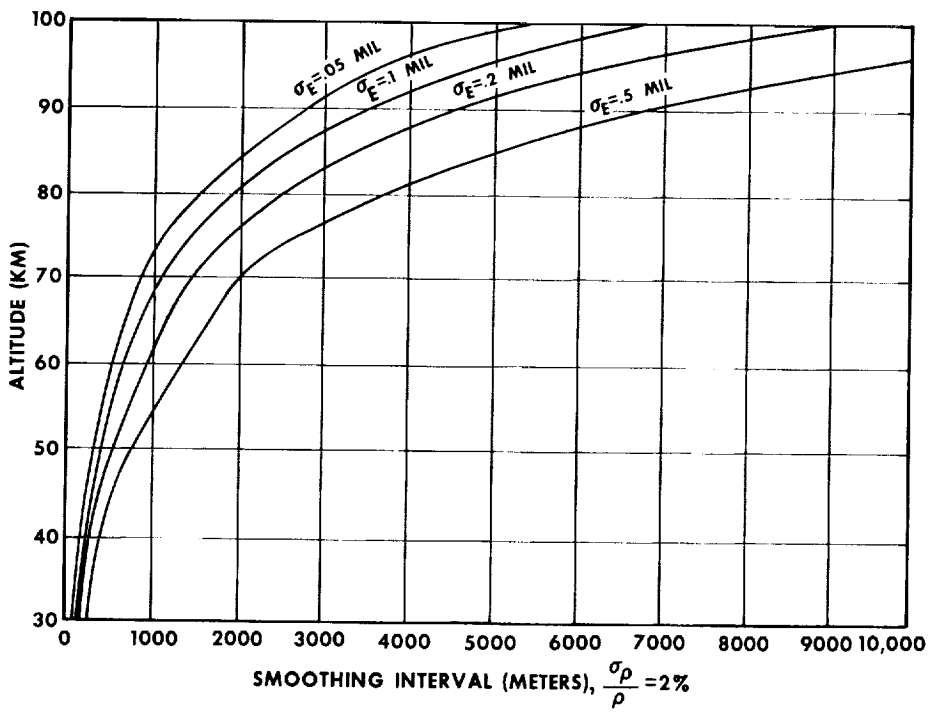

Figure 4.- Requisite smoothing intervals for apparent 2% density error.

THE TONE RANGE/TELEMETRY INTERFEROMETER TRACKING SYSTEM FOR SUPPORT OF SOUNDING ROCKET PAYLOADS

By John I. Hudgins and James R. Lease

NASA Goddard Space Flight Center

SUMMARY

The Tone Range/Telemetering (TM) Interferometer tracking system provides trajectory information for any rocket, balloon, or airborne scientific device which employs telemetry. The system was developed as a back-up and/or replacement for radar to provide the trajectory data of scientific sounding rockets.

This system is comprised of three basic systems: the Airborne, the Tone Range, and the Interferometer. The Airborne system provides ranging reception and telemetry transmission, the Tone Range system provides distance or range data, and the Interferometer system provides angular data.

The Tone Range system derives range by measuring the phase shift experienced by two tones. These tones are radiated from the ground to the Airborne system and reradiated back to the ground by the telemetry transmitter. The tones are then compared in phase with the ground standard. The phase shift of each tone is proportional to twice the slant range to the Airborne system.

The Interferometer system derives angular data by measuring the difference in electrical phase of arriving energy, radiated from the Airborne system, at two ground antennas spaced 16 wavelengths apart. Comparing the phase of the outputs of the two antennas, the azimuth of the Airborne system can be determined with respect to the antenna base line. By using four antennas, two orthogonal base lines, the azimuth and elevation angles can be derived from the electrical phase angles.

The Tone Range/TM Interferometer system has been used to track 22 sounding rockets since 1967. Several of these rockets were also tracked by radar and Radint. A comparison of the trajectories has shown that there is an average difference of 30 meters.

INTRODUCTION

The requirement for determination of the trajectory and position of spacecraft has brought about the development and deployment of many forms of tracking systems. These include tracking radars, such as the MPS-19, FPS-16, and FPQ-6 systems; multi-station Doppler systems, such as Dovap; multi-station interferometer systems, such as Minitrack;

combined Doppler interferometer systems, such as Radint; ballistic camera and theodolite installations; and recently, laser ranging systems. The principal systems used for tracking sounding rockets have been the various radars, although Radint has been used extensively in support of the grenade and pitotstatic probe experiments. Operation of the radar at NASA Wallops Station, Virginia, has been reliable without question. However, the same cannot be said of the tracking radar support at some other ranges, principally because of the lack of a sufficient number of redundant systems.

The Goddard Space Flight Center has long desired to provide some simple form of redundant tracking system to provide backup range and/or positional information. It was decided that the most advantageous and economical solution would combine the telemetry and tracking function. Two approaches were initiated: increasing the telemetry capability of the Radint tracking system, and adding a ranging capability to the standard FM/FM telemetry system. Both approaches have been successfully effected; however, the frequencies allocated to Radint have, up to now, required the use of cumbersome antennas thereby negating popular acceptance.

Several methods to obtain the desired information via standard telemetry were examined with the precision tone-range method being finally selected as the most promising. Several systems using this method had been implemented at the time of this decision. Included in these are the Sandia-AEC DME System (ref. 1) and the NASA-GRARR System (refs. 2 and 3). The techniques used in these systems were analyzed and weighed with respect to their impact on the standard telemetry processes.

A ranging frequency of 100 kHz was selected for precision ranging. Ambiguity removal frequencies of 2 kHz or 4.5 kHz were selected to support the precision ranging frequency. As with the Radint Interferometer system, the range tones are translated, with phase intact, to a frequency of 500 Hz for the ease of phase detection, digitization, and recording.

This report covers the Tone Range system and, to a lesser extent, the Telemetry Interferometer addition to the Radint system. The philosophy of the measurements is investigated, followed by system description. An analysis of data precision, accuracy and resolution is followed in the concluding section by comparisons with FPS-16 radars at Wallops Station and White Sands Missile Range.

SYMBOLS AND ABBREVIATIONS

A_{cc} coupled phase amplitude

$A_{\Delta\phi}$ range phase amplitude

c	velocity of propagation
D	distance
e_{MCV}	demodulated carrier signal
F,G,H	IRIG data channels
$FCN_I(t)$	initial sinusoidal periodic function of time
f_D	Doppler frequency
f_I	initial reference frequency
Δf	maximum carrier frequency swing incurred through modulation
J	Bessel function
M_f	a modulation constant, $2\pi \frac{\Delta f}{\omega_M}$
N	integer
R	range
$(\delta R)_{cc}$	range error as a function of cross coupling
T_I	period of f_I
t	time
t_{DG}	ground equipment delay
t_{DX}	transponder delay time
t_{FM}	time from
t_p	time accumulated between initial transmission and final reception of range tone
t_{TO}	time to
t_{XM}	transmitter delay

v	velocity
X,Y,Z	mutually orthogonal space coordinate axes
x,y,z	distance along the X,Y,Z axes
Z	altitude
θ	angle of arrival
θ_{cc}	intermodulation or cross-coupled component phase relative to $\Delta\phi$
θ_E	resulting phase error, $\tan^{-1} \frac{A_{cc}}{A_{\Delta\phi}}$
λ	wavelength
ϕ	phase
ϕ_I	initial phase
ϕ_o	accumulation of fired phases throughout the system
ϕ_R	range-tone phase
$\Delta\phi$	range-phase difference
$\omega = 2\pi f$	
ω_C	carrier frequency
$\omega_I = 2\pi f_I$	
ω_M	modulating frequency
ω_{MC}	frequency modulated carrier
ϕ_{MCI}	initial modulated carrier phase function
ϕ_{MCR}	received modulated carrier phase function

ϕ_{MCV} dynamic modulated carrier phase function

Abbreviations:

AEC	Atomic Energy Commission
AFC	automatic frequency control
AGC	automatic gain control
Az-El	azimuth-elevation
BCD	binary coded decimal
DME	distance measuring equipment
Dovap	Doppler, velocity and position
GM	Goddard meteorological
GRARR	Goddard range and range-rate system
IF	intermediate frequency
IRIG	Inter-Range Instrumentation Group
LOS	loss of signal
NASA	National Aeronautics and Space Administration
PCM-FM	pulse-coded modulation-frequency modulation
PRF	pulse repetition frequency
Radint	radio Doppler interferometer system
RF	radio frequency
UM	university meteorological

VCO voltage controlled oscillator

WWV National Bureau of Standards time radio station

PHILOSOPHY OF RANGE MEASUREMENT

The system described herein, like radar, uses the "quasi-steady state" Doppler principle (ref. 4) to obtain a range measurement. "Quasi-steady state" Doppler is a distance-propagation velocity relationship and may be thought of as an accumulation of Doppler effects, which occur during the transition from some known point to a second unknown point.

In the Tone Range system, the reference tone, a sinusoidal periodic function, $FCN_I(t) = \sin(\omega_I t + \phi_o)$, is generated and transmitted to a receiver at some fixed unknown distance R. This reference tone is retransmitted and received at the place of generation. This tone propagates over the distance 2R at the constant velocity $c = 2.997928 \times 10^5$ km/sec (the index of refraction will be assumed equal to unity for this derivation); therefore, the time accumulated between the initial transmission and final reception is $t_p = 2R/c$.

The instantaneous phase of $FCN_I(t)$ is $\phi_I = \omega_I t + \phi_o$, where ϕ_o is the accumulation of fixed phases throughout the system. These fixed phases will be assumed constant and equal to zero for the purposes of simplicity of derivation, but will be resurrected during the discussion of accuracy.

While $\phi_I = \omega_I t$, the phase of the returned tone ϕ_R, which has undergone a trip of 2R and been delayed by a period $2R/c$ is $\phi_R = \omega_I(t - 2R/c)$; this ϕ_R shall be called the range tone phase. The term, $2R/c$ is subtracted since ϕ_R is a sample of a phase generated at an earlier time than ϕ_I. In comparing these two tone phases we find ω unchanged, with the phase difference strictly contributed by the propagation time. The range R may be found from a measurement of phase difference:

$$\Delta\phi = \phi_I - \phi_R = \frac{2\omega_I R}{c}$$

$$R = \frac{c\Delta\phi}{2\omega_I}$$

Since $\omega_I = 2\pi f_I = 2\pi/T_I$, where T_I is the period of f_I, ϕ becomes ambiguous at intervals of 2π, that is, $\phi_{2\pi} \equiv \phi_o \equiv \phi_{4\pi} \equiv \phi_{N2\pi}$. On examining $\Delta\phi$ the same periodicity of ambiguity is noted. Rearranging the equation for R,

$$R = \frac{c}{2f_I} \cdot \frac{\Delta\phi}{2\pi}$$

When $\Delta\phi = N2\pi$, R assumes the same value $c/2f_I$. Between these points R is a linear function of $\Delta\phi$. A plot of $\Delta\phi$ with respect to range is shown in sketch (a).

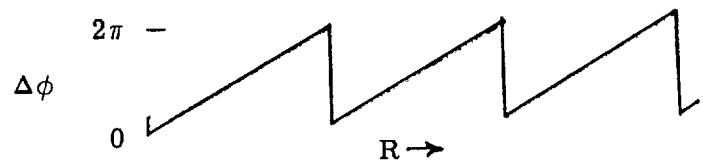

Sketch (a)

This ambiguity points out a necessity of design consideration. The maximum expected change in range may not exceed $c/2f_I$ without incurring a doubt concerning how many ambiguous cycles of $\Delta\phi$ have occurred since the last observation. The choice of a $c/2f_I$ sufficiently large to handle expected changes in range, leads generally to a more coarse measurement of $\Delta\phi$ and thus ΔR. In general, two methods of overcoming this difficulty are used, the first is constant observation and integration of ambiguities, the second is the use of more than one tone to define range. The multiple tone approach selects a high frequency tone for high range resolution plus lower frequency tones to resolve ambiguities in the higher frequency tones. The second approach is, of course, preferable since loss of data or observation time may be beyond the control of the observer.

Earlier it was mentioned that the "quasi-steady state" Doppler was an accumulation of Doppler motion effects, that is, to obtain the observed phase shift, the observed instantaneous frequency must change during a transition in range. This is illustrated by differentiating ϕ_R with respect to time

$$\phi_R = 2\pi f_I\left(t - \frac{2R}{c}\right)$$

and

$$\frac{d\phi_R}{dt} = 2\pi f_I\left(1 - \frac{2}{c}\frac{dR}{dt}\right) = 2\pi f_I\left(1 - \frac{2v}{c}\right)$$

This expression is the classic nonrelativistic Doppler equation, $f_D = \frac{2v}{c} f_I$, where f_D is the Doppler frequency or observed change in frequency resulting from motion.

The ranging frequencies or tones selected for use with the Tone Ranging System were based primarily on noninterference with standard IRIG FM/FM data channels and

conformance with existing system limitations. At present the high resolution or "Fine" ranging tone is 100 kHz (1.5 km) with one ambiguity resolving "Coarse" tone at one of two frequencies 2 kHz (75 km) and 4.5 kHz $\left(33\frac{1}{3}\text{ km}\right)$. Since neither of these "Coarse," or ambiguity removal, tones gives unambiguous range in excess of the expected, deductive logic plus some knowledge of trajectories is required to find the exact range.

Obviously, the frequencies selected are of too long a wavelength to be transmitted directly and instead modulate a carrier frequency. Questions naturally arise with regard to the impact of this "piggyback" mode of transportation on the measurement of interest.

A frequency modulated carrier may be expressed in the following fashion:

$$\omega_{MC} = \omega_C + 2\pi\Delta f \cos \omega_M t$$

where

ω_C the carrier frequency

ω_M the modulating frequency

ω the instantaneous angular velocity or frequency

Δf the maximum carrier frequency swing incurred through modulation

M_f a modulation constant, $2\pi \frac{\Delta f}{\omega_M}$

By integrating we obtain the modulated carrier phase function of time

$$\phi_{MCI} = \omega_C t + 2\pi \frac{\Delta f}{\omega_M} \sin \omega_M t = \omega_C t + M_f \sin \omega_M t$$

The steady-state carrier phase after undergoing the transit to and from a point at range R is

$$\phi_{MCR} = \omega_C\left(t - \frac{2R}{c}\right) + M_f \sin \omega_M\left(t - \frac{2R}{c}\right)$$

The instantaneous dynamic frequency of ϕ_{MCR} is obtained by differentiating ϕ_{MCR} with respect to time

$$\frac{d\phi_{MCR}}{dt} = \omega_C\left(1 - \frac{2v}{c}\right) - M_f\left[\cos \omega_M\left(t - \frac{2R}{c}\right)\right]\left(1 - \frac{2v}{c}\right) = \left(1 - \frac{2v}{c}\right)\left[\omega_C - M_f \cos \omega_M\left(t - \frac{2R}{c}\right)\right]$$

The returned phase for the case of motion ϕ_{MCV} is derived by integrating the above equation

$$\phi_{MCV} = \int_t d\phi_{MCR} = \left(1 - 2\frac{v}{c}\right)\left[\omega_C t - M_f \sin \omega_M\left(t - \frac{2R}{c}\right)\right]$$

The carrier may then be expressed as

$$e_{MCV} = \sin\left\{\left(1 - \frac{2v}{c}\right)\left[\omega_C t - M_f \sin \omega_M\left(t - \frac{2R}{c}\right)\right]\right\}$$

This can be written in the form

$$e_{MCV} = \sin \omega_C t\left(1 - \frac{2v}{c}\right)\cos\left[M_f\left(1 - 2\frac{v}{c}\right)\sin \omega_M\left(t - 2\frac{R}{c}\right)\right]$$
$$+ \cos \omega_C t\left(1 - 2\frac{v}{c}\right)\sin\left[M_f\left(1 - 2\frac{v}{c}\right)\sin \omega_M\left(t - 2\frac{R}{c}\right)\right]$$

This may be manipulated further since $\cos\left[M_f\left(1 - 2\frac{v}{c}\right)\sin \omega_M\left(t - 2\frac{R}{c}\right)\right]$ expanded can be expressed as a Bessel function of argument $M_f\left(1 - 2\frac{v}{c}\right)$, which is written

$$J_0\left[M_f\left(1 - 2\frac{v}{c}\right)\right] + 2J_2\left[M_f\left(1 - 2\frac{v}{c}\right)\cos 2\omega_M\left(t - 2\frac{R}{c}\right) + \ldots\right]$$

Similar expansion of $\sin\left[M_f\left(1 - 2\frac{v}{c}\right)\sin \omega_M\left(t - 2\frac{R}{c}\right)\right]$ yields

$$2J_1\left[M_f\left(1 - 2\frac{v}{c}\right)\sin \omega_M\left(t - 2\frac{R}{c}\right) + 2J_3\left[M_f\left(1 - 2\frac{v}{c}\right)\right]\sin 3\omega_M\left(t - 2\frac{R}{c}\right) + \ldots\right]$$

Reinstating these Bessel functions in the equation for e_{MCV}, using only the first order terms for simplicity of expression, yields

$$e_{MCV} = J_0\left[M_f\left(1 - 2\frac{v}{c}\right)\right]\sin \omega_C t\left(1 - 2\frac{v}{c}\right) + J_1\left[M_f\left(1 - 2\frac{v}{c}\right)A\right]$$

where $A = 2 \sin \omega_M\left(t - 2\frac{R}{c}\right)\cos \omega_C t\left(1 - 2\frac{v}{c}\right)$. Expanding A, it is rewritten in the form

$$e_{MCV} = J_0\left[M_f\left(1 - 2\frac{v}{c}\right)\right]\sin \omega_C t\left(1 - 2\frac{v}{c}\right)$$
$$+ J_1\left[M_f\left(1 - 2\frac{v}{c}\right)\right]\left\{\underbrace{\sin\left[\omega_C t\left(1 - 2\frac{v}{c}\right) + \omega_M\left(t - 2\frac{R}{c}\right)\right]}_{\text{1st upper sideband}} - \underbrace{\sin\left[\omega_C t\left(1 - 2\frac{v}{c}\right) - \omega_M\left(t - 2\frac{R}{c}\right)\right]}_{\text{1st lower sideband}}\right\}$$

The simplest expression for demodulation is translation to zero frequency thus:

$$e_{MCV} = J_1\left[M_f\left(1 - 2\frac{v}{c}\right)\right]\sin \omega_M\left(t - 2\frac{R}{c}\right)$$

The phase $\omega_M\left(t - 2\frac{R}{c}\right)$ is therefore recovered intact!

Any periodic ranging system, such as pulsed radar, operates by the principles outlined above. The principal difference between tone ranging and radar is the trade-off between power and bandwidth. In radar the PRF is the ambiguity removing frequency, with the frequency of the uppermost usable Fourier component of the pulse forming the precision ranging frequency. Due to the wide bandwidth required to accommodate a radar video spectrum and the commensurate noise introduced in this wide bandwidth, signal levels must be high to obtain reasonable signal to noise. Added to this, is the poor "transponder" formed by the almost isotropic reflection from a small object thus forming further demand for high radiated power density to obtain reasonable signal levels at the receiver. To obtain these high power densities and signal levels, the peak power output must be as high as possible, plus antenna gain must be maximized. To obtain the latter, beamwidth is narrowed as much as possible, thus presenting a problem of acquisition. The Tone Range/TM Interferometer system uses hemispheric antenna coverage where feasible, and beamwidths on the order of 60° where some gain is desired. Relative ease of acquisition of Radar and Tone Range/TM Interferometer can be compared with using a searchlight to follow a bird at night versus following a bird in broad daylight with your eyes. In addition, since Tone Ranging and the TM Interferometer systems are both narrow band systems (<10-Hz bandwidth can accommodate the signals) a very favorable signal to noise relationship exists.

PHILOSOPHY OF ANGLE MEASUREMENT

This section of the report will not go into detailed description and analysis of the Interferometer since much of this can be found in reference 5. This reference provides

a detailed description and some accuracy considerations of the Radint system.

The Interferometer system is the radio frequency analog of Fraunhoffer optical interference phenomena. Figure 1 depicts one axis of the interferometer shown at the moment of arrival of a plane wave front at the east antenna. In the time period taken for the wave to arrive at the west antenna, the phase at the east antenna will have changed. If the antennas are spaced exactly 1 wavelength apart, the electrical phase difference of the signals received simultaneously at the two antennas is representative of the cosine of the space angle of arrival of the wave front with respect to the plane of the Interferometer. As the antenna spacing is opened up to 2 wavelengths, ambiguities begin to appear since the same electrical phase, 0°, is present for wave arrivals from the east and west horizons as well as that arriving parallel to the Interferometer axis. Although ambiguous, the electrical phase angle in degrees now represents half the space angle. As the axis increases in numbers of wavelength, ambiguities increase; however, the precision of measurement also increases proportionally. Each ambiguity is termed a "lobe." There are 32 such lobes in a 16-wavelength interferometer. Figure 2 is an attempt to indicate the three-dimensional configuration of the lobe pattern for half the Interferometer pattern. Depicted in this illustration is what might be termed a "core sample" of the lobe pattern. The lobes realistically extend to infinity. Two mutually normal Interferometer axes are used; their combined output defines a vector which includes the center of the Interferometer array, the object being tracked, and results from the intersection of two conical surfaces of constant phase, one associated with each Interferometer. Removing ambiguities by using close-spaced antennas is not at present deemed necessary, since integrated tracking from launch to end of flight or LOS has proven effective and reliable for over 300 Radint operations. However, where ambiguity removal is required, for example, signal not available at launch, this may be accomplished by the addition of one antenna and associated electronics for each axis.

The relationship between measured phase and the space angle of arrival is derived herein. In sketch (b), an equiphase wavefront is shown at the moment it impinges the

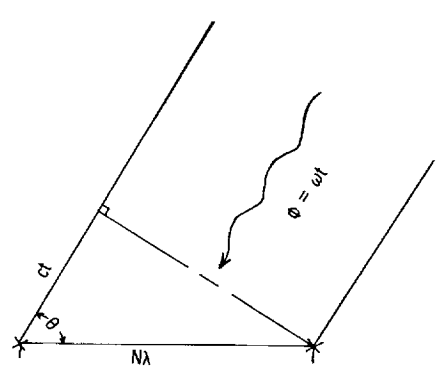

Sketch (b)

right antenna of an interferometer. The phase distribution in the direction of propagation is $\phi = 2\pi ft$ where ct is the distance the wavefront must travel to reach the left antenna and f is frequency of the arriving energy. The Interferometer base is depicted as having a length of $N\lambda$. Geometrically, the desired information, $\cos\theta = \frac{ct}{N\lambda}$. Restating ϕ in terms of λ, $\phi = \frac{2\pi ct}{\lambda}\frac{N}{N}$, and rearranging yields

$$\phi = 2\pi N \frac{ct}{N\lambda} = 2\pi N \cos\theta$$

therefore $\cos\theta = \frac{\phi}{2\pi N}$.

SYSTEM DESCRIPTION

Tone Range System

The Tone Range system is comprised of several subsystems. These are

- Telemetry receiver, antenna, and preamplifier
- Precision tone generator and synthesizer
- Tone reference transmitter and antenna
- Tone translator
- Analog phase comparator and recorder
- Servo phase comparator and grey code to BCD converter
- Airborne receiver and telemetry transmitter

A simplified block diagram of the Tone Range/TM Interferometer system is shown in figure 3. The heart of this system is the precision tone generator. This is normally a Hewlett-Packard HP 5245L counter from which a 1-MHz output is used to synthesize the required frequencies. (Other counter functions include driving the timing and digital systems.)

In the tone frequency synthesizer, the 1-MHz input is applied to divider chains to produce several phase coherent frequencies. The divider chains are commonly reset at a 250-Hz rate to insure against lock-up and undesired noise switching. In the second Tone system, this unit provides

Frequency	To	Purpose
100 kHz	Reference transmitter	Uplink modulation
104.5 kHz	Reference transmitter	Uplink modulation
500 Hz	Reference to analog phase detectors and servo phase detectors	Comparison with range tones

Frequency	To	Purpose
160 kHz	Tone translator	Conversion of 100 kHz range tone to 160 kHz
25 kHz	Tone translator	Conversion of 60 kHz to 35 kHz
31.25 kHz	Tone translator	Conversion of 35 kHz to 3.75 kHz
4.25 kHz	Tone translator	Conversion of 3.75 kHz to 500 kHz + ϕ
3.4 kHz	Tone translator	Conversion of 4.5 kHz range tone to 1.1 kHz
1.6 kHz	Tone translator	Conversion of 1.1 kHz to 500 Hz + ϕ

The tone translator accepts the received mixed video and extracts the 100-kHz and 104.5-kHz range tones from the telemetry data via a 102.5-kHz, 6-percent bandwidth filter. These multiplexed range tones, dc referenced to signal common at the filter output, are applied to a diode limiter. This serves to establish a fixed signal level, as well as to establish the nonlinear function for separation of the coarse 4.5-kHz range tone. The limiter output is applied through buffer amplifiers to a 100-kHz, 2-percent bandwidth filter and a 4.5-kHz, 6-percent bandwidth filter for separation of the Fine and Coarse range tones. The 100-kHz and 4.5-kHz tones are mixed with the phase-coherent translating frequencies as indicated in the above table.

The analog phase detectors generate asymmetrical square waves, the degree of asymmetry of which is linearly proportional to the phase difference $\Delta\phi$ between the 500-Hz reference and 500-Hz + ϕ range tones. This square wave is integrated to form an output voltage linearly proportional to $\Delta\phi$.

The outputs of the analog phase detectors are presented versus time by a Brush MK 280 Analog Recorder. Figure 4 depicts a typical range analog record.

The 500-kHz reference and range tones are also applied to the servo phase detector. Here these two signals are compared in phase by a synchroresolver, the output of which is a voltage proportional to the phase difference. This resolver is coupled by a gear train to a motor, the control of which is derived from the resolver output. Feedback is obtained in this manner and maintains, through mechanical rotation, zero phase difference between reference and range tone resolver windings.

The feedback loop bandwidth is selectable at 0.1, 1, and 10 Hz, thus allowing variable control over dynamic and signal-to-noise characteristics.

The resolver-motor gear train provides other shaft outputs. With their output rotations referenced to the resolver, these are

1-km analog potential output	2:3
500-km analog potential output	1:300
digital encoder	1:600

The potentiometer outputs of the range servo phase detector are not commonly used, however, the 500-km range potential will provide position data for an X, Y, and Z position analog computer now being designed.

The Datex Shaft Encoder provides a special normalized Datex code. Conversion of this code to 8, 4, 2, 1 BCD code is also performed by the servo unit. This is in a form easily processed by the Radint digital system.

In the airborne portion of the system, the only special equipment required is the tone receiver and its associated antenna. The received signal, generally 550 MHz, is demodulated and the resultant range tone signals are multiplexed with the data VCO outputs. The range tone signals are not preemphasized in accordance with their frequency relationship to the VCO frequencies. They are generally accorded 15 to 20 percent of the total telemetry transmitter deviation or ±15 kHz, whichever is less. This is done to limit the effect of tracking on data acquisition, that is, placing the priority on the acquisition of experimental data. Figures 5 and 6 show the airborne components necessary for tone ranging.

Support Subsystems

In addition to the subsystems specific to the Tone Range system, there are several of the Radint support subsystems which are often used in support of the Tone Range/TM Interferometer system. These are

Tape record-playback system
Timing system
Digital system
Data link system
Station multiplex
NASA 28 bit international timing system

Tape record-playback system.- This system, selected for low skew characteristics, provides a permanent record of Tone and Interferometer reference plus phase information. In addition, flight time, voice annotation, and other pertinent information is recorded via the station multiplex.

Timing system.- This system is activated by a launcher-mounted microswitch. The system counts, displays, and encodes flight time. It also provides encoded time for analog records, a visual display, and encoded time for annotation of the tape record. The timing sequence is also activated in the tape playback mode.

Digital system.- This system accepts grey coded Datex information from the Interferometer servo system, BCD time from the timing system, plus other pertinent information. It processes all data to 8, 4, 2, 1 BCD, and provides a punched paper tape containing all information pertinent to the tracking function.

Data link system.- This system accepts paper tape reader output and converts it to a tone format acceptable for transmission of digital data over commercial telephone lines.

Station multiplex.- This system uses multiplexed VCO's to combine several signals, such as receiver AGC levels, voice annotation, and other tracking function events for tape recording.

NASA 28 bit international timing system.- This system incorporates an extremely stable frequency source, from which it derives several forms of coded time for annotation of records. Time synchronization is provided via reception of WWV time signals. The coded time includes day of the year, hours, minutes, and seconds and is usually set to present Zulu time. A slow 28 bit, 2 parts per second code is used for analog record annotation.

Interferometer System

The Interferometer system consists of the antenna subsystem, the receiver subsystem, the servo phase measuring unit, and the Az-El plotter. A magnetic tape recorder and a digital system, which includes a paper tape punch, are used in the operation of both the interferometer and the Doppler portions of the station. Figure 7 depicts this system's functions in somewhat greater detail.

Antennas.- Each axis of the interferometer uses two antennas, 16 wavelengths apart; the antenna elements are spaced 1/4-wavelength above a ground plane. Each antenna is a pair of crossed dipoles, connected in circularly polarized configuration. Circularity of receiving, necessary because of the rotation of the rocket, is achieved by cutting the quarter-wave sections to a length that will cause them to be inductive, and coupling directly to two elements while connecting capacitively to the other two. Connection is made to the coaxial transmission line through a "balun" (balanced to unbalanced) transformer. It is essential for each antenna and transmission line of a pair to have the same phase characteristics. Pairs of antennas are chosen for their similarity of characteristics. Transmission lines are cut to the same integral number of wavelengths. Connections are made to the receivers through coaxial switches, so that a locally generated RF signal can be applied to the receivers for alinement purposes.

Signal processing.- Low-noise preamplifiers provide about 30-dB gain for the incoming 244.3-MHz signals from the antennas plus conversion to 73.6 MHz. The preamplifiers are followed by mixer stages. The local oscillator signal to the north and east mixers is 67.12 MHz; to the south and west mixers it is 67.1205 MHz. The 6.48- and 6.4795-MHz outputs of the north and south mixers, respectively, are combined in an adder and sent through a common IF channel; likewise, the outputs of the east and the west. A second conversion is made, giving IF's of 465 kHz for the north and east mixers and

465.5 kHz for the south and west. The detected output for each axis is 500 Hz ± phase difference between the two signals arriving at the antennas.

Phase measurement.- The phase of each of the two 500-Hz ± phase signals is compared with that of the 500-Hz reference signal by means of two different types of phase-measuring equipment: servo phasemeter tracking filter and electronic, giving an analog output.

Servo phasemeter: The servo phasemeter is an electromechanical system which converts electrical phase differences into shaft angles. These are in turn converted to direction cosines in both analog and digital form.

In this system, the 500-Hz ± phase-shift signal is fed via a motor-driven resolver phase-shifter to an analog-phase detector. Here, any phase difference between the phase-shift signal and the reference 500-Hz input results in a dc voltage. This voltage is amplified and applied to the control winding of a magnetic amplifier. The output of the magnetic amplifier, 400-Hz power level controlled by the amplifier, is applied to a servomotor, which is coupled to the resolver through a gear reduction. The action of this loop is such that the resolver is driven in a direction to bring its output into phase with the reference 500 Hz. If the phase of the incoming signal continues to change, the resolver rotates to track it. Since one rotation of the shaft gives a 360° phase shift, 32 revolutions are required to track a signal source from one horizon to the other. So that unambiguous analog and digital data can be provided, a coarse potentiometer and the shaft encoder are geared down from the resolver shaft so as to give one continuous set of readings from one horizon to the other. The shaft encoder gives outputs which can be converted to decimal numbers, -.9999 to +.9999, corresponding to the direction cosines of the angles of the signals source with respect to the station. Positive and negative voltages are connected to the ends of the potentiometers so the voltage at the center of the pot is zero volts. This corresponds to a signal arriving from directly overhead (90°). The shaft encoder is set to give an output of .0000 under the same conditions. Then for north or east signals, the digital output of the encoder and the voltage output of the potentiometer will be positive, while south or west directions give negative readouts. In each case, the magnitude is proportional to the cosine of the angle. However, since the servo phasemeter would lock in at any one of 32 different readings, it is necessary that the two servo systems be set to the cosines corresponding to the direction of the launch site before the feedback loop is closed.

Electronic phasemeter: An old but effective form of interferometer phase measuring technique is still in use as a redundant readout and signal loss-return code identification. Each interferometer axis 500-Hz signal is fed into an integrating-type phase detector where the signal phase is compared with that of the reference 500 Hz. Any phase difference produces an output voltage whose magnitude and polarity corresponds to the

phase difference. Each of the two analog signals drives a pen of the analog recorder. The data thus obtained are ambiguous, in that a given voltage can indicate any one of 64 different angles. It can be resolved by counting positive slope zero crossings from a known starting point and, thus, would serve as backup data in case of failure to record the other forms of data or as an aid in resolving any difficulties with the digital data.

Data presentation.- The real-time readouts of the interferometer portion of the Radint station are the Az-El plot and the pen recording of the analog data from the electronic and servo phasemeters.

Az-El plotter: An X-Y plotter is an ink recorder having an arm movable in the direction of X-axis, and a pen which moves along the arm in the direction of the Y-axis. It uses a single sheet of paper which is held stationary. The output of the analog potentiometer of the N-S servo phasemeter is applied to the Y-axis and the E-W is connected to the X-axis. A special graph paper is used which, by the geometry of line spacing, performs the conversion from directional cosines to azimuth and elevation coordinates. Because of this ability to transform the data from one set of coordinates to another, the Az-El plotter may be considered as a simple analog computer. This idea can be carried an additional step by any station which is required to furnish Range Safety data. To accomplish this, the course range analog output is processed to provide analog voltages proportional to the slant range. These voltages are used to feed the X-1 analog potentiometers. The outputs of the potentiometers are now directly portional to the X and Y components of the ground range and are used to drive one of the large X-Y plotting boards to display the rocket position in relation to range boundaries, and so on.

The Az-El plot provides an indication that a normal flight has taken place and that the equipment is functioning correctly.

Analog plot: The pen recording of the outputs of the two analog phase detectors indicate flight and equipment performance. It is also an immediately available source of very accurate angular data for on-site data reduction if necessary. Figure 8 is a replica of the continuous Interferometer analog output.

SURVEY OF SYSTEM CAPABILITIES

Tone Range

Four categories define the capabilities of any measurement system:

Accuracy – the ability of the system design to limit random statistical variations, such as noise plus the ability to define and compensate for systematic variations. Accuracy is largely tied to the system output signal to noise and calibration.

Precision – this relates to the granularity of the measuring device. In tone ranging this is governed by the highest frequency tone.

Resolution – the granularity of the system output presentation; the least significant bit in the digital output; the least definable changes in an analog output.

Ambiguity – the ability of a system to make nonambiguous measurement.

Accuracy.- A listing of system problem areas which could affect accuracy follows.

(1) System video and resonant circuit phase effects of Doppler shift and transmitter stability.
   a. Airborne receiver converter, IF, and video filter response.
   b. Airborne transmitter multiplier and output tanks.
   c. Antenna bandwidths.
   d. Ground receiver converter, IF, and video response.

(2) Lack of knowledge of system fixed phase shifts.

(3) Group delay in tone processive circuits.
   a. Those items listed in (1).
   b. Tone translator.
   c. Phase comparator analog output filter.
   d. Servo comparator loop delay.

(4) Reference tone stability. Besides providing a cumulative error with cumulative range, this could also provide additional phase errors in those areas listed in (1) and (3).

(5) Phase shift as a function of dynamic level. Affects all problem areas listed above plus the video limit circuitry.

(6) Cross coupling and intermodulation components creating false phase.

(7) Poor signal to noise at phase comparator.

Referring back to accuracy problem area (1), the following steps have been taken in system video and RF design to eliminate or minimize the problem:

1. Deviation of the Fine Range Tone (100 kHz) at the reference transmitter is limited to a $M_f < 0.5$; thus all but eliminating the 2d and higher order sidebands from contributing to the signal.

2. Airborne IF bandwidth is 500 kHz wide.

3. Ground receiver IF and video-filter bandwidths are 750 kHz and 300 kHz minimum, respectively. AFC is used to maintain center in the IF bandwidth.

The telemetry transmitters and antennas used are standard, but of sufficient bandwidth to limit measured offset frequency phase excursions to negligible amounts.

Problem area (2) concerns the time at which a measurement is recorded versus the time that the measurement was made. Figure 9 illustrates the situation covered by this analysis for a vehicle moving at a constant velocity with respect to the ground station.

Assume that at t_0, the phase ϕ_I is present at the phase comparator and the input to the reference transmitter modulation circuitry. The vehicle traverses the distance to D_1 before the signal is radiated. The time of propagation t_{TO} to point D_2 is part of the measurement that is desired. During the transponder delay time t_{DX} the rocket traverses the distance $D_3 - D_2$, following this, the time of propagation t_{FM} is the second portion of the desired measurement. During the ground processing delay t_{DG} the vehicle traverses the further distance to point D_5. This is the actual position of the rocket when the measurement is recorded with respect to time; however, the range recorded is a function of $\frac{t_{TO} + t_{FM}}{2}$ or the average time of propagation and implies the range corresponds to position D_3, but is recorded at time t_5.

The propagation time from a point $D_3 = 150$ km to ground is 500 μsec. A nominally high radial velocity for a vehicle in the post-burn phase is 1000 m/sec. The error created by propagation time for this example, would thus be 0.5 meter. This error is noncumulative but varies directly with range.

For a motionless payload, the other delays shown are essentially fixed and can be compensated for by adding an equal delay to ϕ_I. However, when the vehicle is in motion, these delays must be limited to minimize the amount of vehicle motion occurring during the measurement process. To obtain a real-time measurement error $\leqq 1$ meter resulting from system fixed delays for a vehicle radial velocity of 1 km/sec, the sum total of the delays must be $\leqq 1$ msec.

Where commercial equipment, such as the telemetry receiver and the analog recorder, is used, delays are fixed, leaving the slack to be taken care of, if possible, in the design of the transmitter modulation circuitry and tone processer.

The 100-kHz delays, measured in the various system components, are as follows:

System components	Delay for –	
	100 kHz	4.5 kHz
Up link (TRF receiver)	42 μsec	1 msec
Down link (DEI receiver)	18 μsec	10 μsec
Tone translator	3 msec	10 msec

Uncompensated differential delays between the Coarse and Fine tones can create unresolvable ambiguity in position of a vehicle, for which the fine range has not been

integrated from a known position. The wide-band video circuitry, the receivers, and the transmitter exhibit phase delays linearly proportional to frequency. The translator circuits do not exhibit this criteria. The determining phase shift is that exhibited by the Coarse translator chain with delay added to the Fine chain to regain proportionality.

The system, besides the space and equipment carrier propagation time delay, also exhibits a group differential phase delay (problem area 3) which results from the passage of the Doppler components through the system. This envelope delay in the RF and video circuitry is negligible. However, the translator and phase detector incorporate narrow bandwidth filters for noise reduction. Large phase errors would result if some means for linearizing the phase versus frequency response of the system were not incorporated. A novel form of translation to the 500-Hz final frequency is used to effect the linearizing process. An equal number of up and down conversions are used with the goal of equating the sum and difference phase delays.

The residual delay is analyzed by the system response to a phase step function. The resultant rise time of 15 msec for the translator and 14 msec for the phase detector, result in an overall rise time of 21 msec. This rise time equates to a frequency response of 17 Hz. For a vehicle traveling at the rate of 1000 m/sec radial velocity, this represents an error in phase of 1.8° or a further error in range of 7.5 m. For the case of the accelerating rocket exhibiting a 50g or 500 m/sec^2 acceleration, this bandwidth represents a cumulative error of 3.8 m/sec^2 during the acceleration time.

The servo system has an adjustable bandwidth up to 10 Hz. Since high acceleration occurs during the launch period at high signal conditions this widest bandwidth is used. The analog record serves to correct high acceleration data when required.

The analog readout device, a Brush MK 280 recorder, has a bandwidth in excess of 60 Hz and, thus, introduces negligible degradation during high dynamic conditions.

In problem area (4), short term statistical variations in tone frequency appear as noise. In general, these are small and are minimized along with system statistical noise by virtue of the very narrow system bandwidth. Any residual can be smoothed in the data reduction process.

The short term drift or an unknown frequency offset can contribute materially to error.

Previously, it was shown that

$$R = \frac{c}{4\pi} \frac{\Delta\phi}{f_I}$$

the error in R as a function of a change in f_I is shown as follows:

$$\frac{\delta R}{\delta f_I} = \frac{c}{4\pi}\left(\frac{f_I \delta\Delta\phi - \Delta\phi}{f_I^2}\right)$$

where $\Delta\phi$ is a measured value and known; therefore, $\delta\Delta\phi = 0$ and

$$\frac{\delta R}{\delta f_I} = -\frac{c}{4\pi}\left(\frac{4\pi f_I \frac{R}{c}}{f_I^2}\right)$$

$$\delta R = -R\frac{\delta f_I}{f_I}$$

This shows that the error is cumulative with range and that the percentage error in range is directly proportional to the percentage error in frequency. The error in measured range incurred by a frequency offset of 1 cycle in the precision range tone at a range of 100 km would be

$$\delta R = \frac{10^5 \text{ meters} \times 1 \text{ Hz}}{10^5 \text{ Hz}} = 1 \text{ meter}$$

Although the tone range system commonly uses an extremely stable, oven-controlled source frequency, very adequate operation can be achieved from a common crystal controlled oscillator.

In problem area (5), the dominant contributions to phase error due to variation in signal level are changes in dynamic loading of tuned circuits as a result of AGC action, variation of conduction angle in mixer circuits, and changes in bias level of ac coupled video circuitry resulting from "Grid Leak" biasing.

Since the tone range system uses standard commercially developed components for the airborne receiver and transmitter plus the ground telemetry receiver, successful operation has been achieved through recognition of the problem accompanied by procurement specifications outlining the maximum acceptable phase deviation over signal dynamic range at a specified carrier deviation. The airborne FM receiver does not use AGC and exhibits extremely good phase stability.

Some insight has been achieved in this area as a result of similar problems encountered in the Radint Interferometer system. AGC variations can be minimized by buffering with follower circuits between a tuned load and the following AGC'd stage. Low Q and broadly tuned loads are used in RF mixer stages.

In the tone translator, filtering, followed by low level limiting and additional filtering, minimizes phase variations resulting from video level change. The use of FM also serves to keep video level constant. Prior to the limiting stage, ac coupled signal processing must be linear class A. Prior to limiting, the video must be referenced to common and direct coupled into the limiter stages. After limiting, the signal is constant, and constant ac coupling will not introduce unknown error.

Closed loop system tests show these variations to be less than 2.2°, which is equivalent to 8 meters for a carrier signal dynamic range of 66 dB, and 2.2°, which is equivalent to 8 meters for a video dynamic level change of 20 dB.

Problem area (6) is in some ways tied to dynamic level errors in that a constant cross-coupled component presents a problem only prior to limiting. After limiting, the cross-coupled component introduces a fixed phase component which can be eliminated. Prior to limiting, the relative resulting phase shift will be a function of the amplitude of the reference tone relative to the cross-coupled component.

The amount of phase offset introduced by cross coupling can be deduced from sketch (c). In this diagram the worst case situation of orthogonality between the undesired component and the desired component is used.

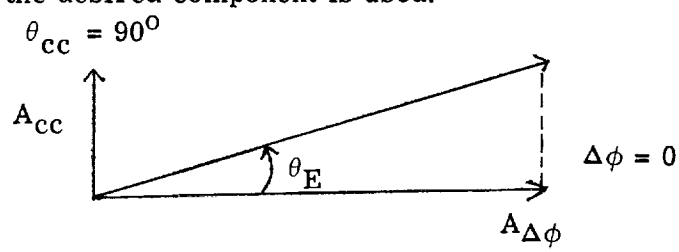

Sketch (c)

where

$\Delta\phi$	range phase difference
$A_{\Delta\phi}$	range phase amplitude
θ_{cc}	intermodulation or cross-coupled component phase relative to $\Delta\phi$
A_{cc}	coupled phase amplitude
θ_E	resulting phase error, $\tan^{-1} \frac{A_{cc}}{A_{\Delta\phi}}$

The following table depicts the range error as a function of relative levels for signal and undesired component:

$\frac{A_{cc}}{A_{\Delta\phi}}$, dB	θ_E, deg	Error, meters, for –		
		Fine tone	Coarse tone	
		100 kHz	2 kHz	4.5 kHz
-10	17.55	73.0	3654	1614
-20	5.72	23.8	1191	526
-30	1.80	7.5	375	166
-40	.57	2.37	119	52
-50	.003	.012	6	3

The results from this table were derived from the following equations. As derived previously

$$R = \frac{c}{4\pi} \frac{\Delta\phi}{f_I}$$

and the resultant range error is

$$(\delta R)_{cc} = \frac{c}{4\pi} \frac{\theta_E \text{ deg}}{f_I} \times \frac{2\pi \text{ rad}}{360 \text{ deg}}$$

$$= \frac{c}{720\, f_I} \theta_E = 4.1639 \times 10^5 \frac{\theta_E}{f_I}$$

Telemetry transmitter intermodulation greater than 1 percent (40-dB voltage) on any IRIG channel is not acceptable for operational use. This criterion is quite sufficient for the tone range introducing a maximum error >3 meters. The intermodulation percentage is, in general, less than that observed on nearby telemetry channels because of the narrower bandwidth of the tone processor. Intermodulation from data channels is, in general, random in nature and any residual can be removed by the data smoothing processes.

The final item, signal to noise, represents a purely statistical distribution of data points centered about the measurement value. The use of narrow band filters in the translator, allows the tracking system to exhibit signal-to-noise characteristics exceeding or identical to those exhibited by the experiment data channels without alloting a large share of the total telemetry transmitter deviation, generally 10 to 20 percent of the total 125-kHz deviation. Under average flight conditions, with the exception of roll induced dropouts, output signal-to-noise conditions are ≧40 dB. This represents a ±1.5 meters

spread which can be reduced to virtually nothing by least squares smoothing. The number of datum samples required to effect adequate accuracy is, of course, an inverse function of the signal-to-noise ratio with the poorest fit occurring during periods of high acceleration. Poor signal-to-noise ratio will, under normal conditions, occur just past apogee and just prior to impact. Fortunately, these are positions of the lowest radial acceleration and thus, materially compensate for any required increase in data smoothing datum points.

In summary, the errors involved are as tabulated in table 1. In the data reduction process, reiterative solutions may be made, incorporating the velocity and acceleration values derived from initial data solution. Tables 2 and 3 indicate the amount of delay error that can be expected in normal flight conditions. Range data from NASA Flight 14.386 GM, a Nike-Apache was processed for velocity and acceleration versus time. The total delay errors were computed under the extreme dynamic conditions shown in table 2 and during a period of general scientific interest, just after apogee, the delay shown in table 2 at $t = 32$ sec decays to 0 at $t = 205$ sec.

Precision and ambiguity.- The precision of a tone range system is a direct function of the highest frequency (Fine) tone. In the previous discussion on accuracy, the frequency of operation has very little impact on the system accuracy, thus, indications are that the Fine Tone may be increased ad infinitum to provide greater and greater precision. There is, of course, the signal-to-noise – bandwidth phase leg trade-off that would indicate an upper limit to the obtainable precision under dynamic conditions. However, these were not the limiting parameters in selection of the Fine ranging tone. Since the requirement for the Tone Range system was based on the need for a redundant means of tracking using the existing FM/FM IRIG telemetry format, the selection of the Fine Range Tone was based on the following considerations:

1. Minimum impact on the telemetry subcarrier format
2. Minimum requirement on telemetry carrier power
3. Use with existing telemetry ground station and airborne equipment (some having bandwidths limited to 100 kHz)

In analyzing the IRIG subcarrier assignments, the notable open frequency slots during the period of initial design were

VCO spectrum	Usable tone	Range ambiguity
Below 370 Hz	None	None
1 828 to 2 127 Hz	2 kHz	75 km
4 193 to 4 995 Hz	4.5 kHz	$33\frac{1}{3}$ km
15 588 to 18 700 Hz	15.8 kHz	9.5 km
Above 80.5 kHz	100 kHz	1.5 km

Rather than take up the space occupied by a data channel, the first system built was designed for a 100-kHz Fine Range Tone and 2 kHz as a Coarse Range ambiguity removing tone. The 75-km ambiguity, although not fulfilling the requirement for range greater than that expected for the vehicle, was sufficient to define position when coordinated with the time into flight and expected vehicle performance. The 2-percent resolution required to remove ambiguity has proved sufficient, although a bit too close to the limit of capabilities under poor signal conditions. The second system built uses a 4.5-kHz $\left(33\frac{1}{3}\text{ km}\right)$ ambiguity removal tone for greater resolution and proves to be a good compromise between resolution under poor signal conditions and selection of an optimal range-length segment for an under- or over-performing vehicle.

With the advent of data channels F, G, and H (upper frequency limit), the 100-kHz tone occupies a position in channel F, just the situation the earlier designs attempted to avoid. The top frequency in this new group is 190 kHz. Future systems will undoubtedly have a choice of 100 kHz or 200 kHz as a Fine tone, although, since future systems must also be capable of working with a PCM-FM telemetry system now being developed, some other frequency may be selected as standard.

The precision of this system at favorable signal to noise and under zero or low dynamic conditions is limited by the resolution of the readout devices. It is a variable under dynamic conditions, being dependent on the amount of improvement made by the reiterative solution process. This has yet to be experimentally determined. However, dynamic errors should be capable of complete elimination since system response under dynamic change is known.

Resolution.- Two readout devices are used to display the range versus time: Brush MK 280 recorder and servo digital readout.

The analog readout device is an 80-mm galvo record subdivided into 50 equal divisions. This record can easily be read to location in 1/3 of a small division or ±5 meters.

The digital readout device is primarily intended for fast computer reduction and is limited in decade capability. It was elected to give this readout an extensive range capability to cover vehicles like the Astrobee 1500 and Javelin rather than greater resolution. The least significant bit represents a change in range of 10 meters.

To summarize, system precision in range equals system resolution; both are analog ±5 meters and digital ±5 meters.

Interferometer Accuracy

From the foregoing system descriptions, one can perceive that the Interferometer suffers identical types of system limitations as those encountered by the Tone Range/TM Interferometer system, inasmuch as the signal processing, measurement technique and display are identical in nature. In fact, since the Radint Interferometer technique had

proven to be very successful at the time of tone range development and the range-phase measurement was recognized to be an identical problem, the Interferometer technique served as a design model for the range processor.

In addition to the system processing errors (those which are covered in the section on tone range accuracy), geometric variations play a dominant role in overall interferometer measurement accuracy. A list of these geometric variations would include such items as

Axis orthogonality and tilt
Axial alinement with respect to geodetic coordinates
Antenna spacing
Antenna element alinement and tilt
Antenna height
Antenna circularity
Antenna cross coupling

Extreme care is taken in the initial layout and installation of the interferometer quadrangle. Geodetic alinement is achieved through observation of the ascension of Polaris (or some other celestial object, if not in the northern hemisphere) and translating by a theodolite to true north. Upon establishing the north-south base leg, the utmost in surveying accuracy is used to establish the other parameters. When completed, the interferometer is essentially "bore sighted" to local zenith. When the antennas are tied into the remainder of the system, extreme care is taken in establishing equal electrical phasing from the antenna through the point of reference phase injection.

For an insight on the procedures used in establishing the interferometer consult reference 5. Preliminary results of an accuracy analysis conducted by James Bassler of the New Mexico State University are presented in table 4. These represent computed standard deviations in position based on range data from a nominal Apache. In this computation of standard deviations, the range values were considered errorless.

Interferometer Precision, Resolution, and Ambiguity

By referring to the "Philosophy of Angle Measurement" section, it can be found that the space angle's θ relationship to electrical phase angle ϕ was

$$\cos\theta = \frac{\phi}{2\pi N}$$

where N is the number of wavelengths encompassed by the interferometer base length.

As N increases, the precision in cosine θ also increases; however, survey tolerance buildups and detrimental environment effects impose a definite limit on the base

length. Sixteen wavelengths for the Radint frequency of 73.6 MHz is near the optimum configuration. Due to its higher operating frequency, the Telemetry Interferometer could conceivably be longer and therefore more precise. However at the present time the two systems are tied to each other for convenience and economy. The precision of the interferometer system is tied to its output resolution, this resolution in direction cosine is analog $\pm 5 \times 10^{-5}$ and digital $\pm 5 \times 10^{-5}$. However, interferometer geometry affects this granularity. Earlier, the relationship of the direction cosine to electrical angle was derived as $\cos \theta = \frac{\phi}{2\pi N}$. Differentiating θ with respect to ϕ one obtains

$$\frac{d\theta}{d\phi} = \frac{(1 - \phi^2)^{-1/2}}{2\pi N}$$

When $(1 - \phi^2)^{-1/2}$ is expanded,

$$(1 - \phi^2)^{-1/2} = 1 + \frac{\phi^2}{2} + \frac{3}{8}\phi^4 + \frac{15}{48}\phi^6 + \ldots$$

is obtained. For $\phi = 0^{\circ}$, source at zenith, the granularity in θ is equal to the granularity in ϕ. For $\phi = 2\pi N$, source at horizon, the granularity in $\theta \approx \infty$. Table 5 gives the computed space angle granularity for several positions of sounding rocket interest. Lobe ambiguities are depicted in figure 10 with their related data tabulated in table 6. Table 7 summarizes the precision of the Tone Range/TM Interferometer system in comparison with other tracking systems.

OPERATIONAL RESULTS

The Tone Ranging/TM Interferometer system has been in semi-operational status since 1967. During this period, the system has been used to track and produce trajectories for 22 sounding rockets. Fourteen of these rockets were parachute-recoverable payloads. The impact point was calculated for all 14 payloads within 15 minutes of impact. The recovery crews, using the Tone Ranging impact point, recovered the majority of these payloads within 24 hours. Prior to 1967, payload recovery took several months, and one payload was never located.

In an effort to determine the accuracy of this developmental system, comparisons have been made with two other types of tracking systems, radar and Radint. The first comparison shown in table 8 was for Nike-Cajun 10.161 GM launched at Wallops Island in May 1967. The comparison shown is the Wallops Island FPS-16 versus the Tone Range/TM Interferometer system. The table shows a typical altitude comparison every 10 seconds for the first 150 seconds of flight.

The second comparison shown in table 9 was for Nike-Apache 14.333 UM launched in Puerto Rico in March 1968. This comparison is of the Tone Range/TM Interferometer system and Radint. The table shows a typical comparison every 10 seconds for the first 160 seconds.

It is difficult to obtain the absolute accuracy of any tracking system. When making comparisons, the accuracy of the system being used as a standard is always questionable. The systems which were used as a standard for the tone ranging comparisons are accepted by most experts as being quite accurate tracking systems. These comparisons between radar, Radint, and the Tone Range/TM Interferometer system are very promising and show that the Tone Range system is capable of providing an accurate trajectory with an average difference, from the standards used, of plus and minus 30 meters.

CONCLUDING REMARKS

The Tone Range/TM Interferometer system has supported 22 firings and is regarded as prime tracking in support of the Dudley Observatory recoverable payloads at White Sands Missile Range. Although the above situation exists, at the present time, the system is regarded as still being in the prototype development stage.

Results from analysis point out areas for improvement and the overall question of point-of-phase comparison has not had sufficient analysis to unquestionably settle on the translation technique.

Recently, a version of Tone Range, called the Wee Track, has been under evaluation. This system makes direct phase measurement at the 100-kHz level and at present does not incorporate ambiguity removal. Laboratory tests of this system are promising. There are also plans for an early test of a single path system using a highly stable 1×10^{-8} oscillator in the vehicle. It is anticipated that the combination of these latter two experimental devices will provide very economical redundant tracking of any vehicle launched with a telemetry transmitter.

With the advent of S-band operation, the interferometer may evolve into a wide beam X-Y mounted tracking antenna from which coarse angles are derived from the shaft position and corrected from the interferometer phase. This type of operation may be required since higher gain antennas must be used. However, this mode of operation would eliminate the high slew rates required of radar mounts.

Taking note of the desirability of immediate post-flight X-Y-Z position plots, the Sounding Rocket Instrumentation Section is developing an analog computer to provide this capability.

Another development in progress is direct digital conversion circuitry. It is anticipated that this will eliminate some dynamic errors presently found in the servo-system and as a side benefit materially reduce the cost. This method, if successful, will be applied to the interferometer digitization, providing the same benefits.

As it is presently comprised, the system may be installed and operating in the field at costs of from $90 000 to $220 000. The difference in costs relates primarily to whether or not digital capability is included.

REFERENCES

1. Laster, J. A.; Scheibner, J. E.; Anderson, D. P.; Martin, B.; and Silverman, M.: Characteristics and Development Report for the Setrac Model 1. SC-DR-64-525, Vol. II, Sandia Corp., Nov. 1964.
2. Vonbun, F. O.: Analysis of the "Range and Range Rate" Tracking System. NASA TN D-1178, 1962.
3. Kronmiller, G. C., Jr.; and Baghdady, E. J.: The Goddard Range and Range Rate Tracking System: Concept, Design, and Performance. GSFC X-531-65-403, NASA, Oct. 1965.
4. Gill, T. P.: The Doppler Effect. Academic Press, Inc., c.1965.
5. Joosten, W. L.; Sabin, R. J.; Lee, E. D.; Gammill, W. G.; and Montz, W. F.: Manual for the NASA/SSD System. PM00171 (Contract No. NAS 5-3068), New Mexico State Univ., Feb. 1963.

TABLE 1.- SUMMARY OF ERROR CONTRIBUTIONS TO TONE RANGING

Source	Effect	Comments
Dynamic level	12.5 meters	Can be calibrated out from correlation with AGC record
Frequency stability offset	Negligible	Frequency source used is stable 5 parts in 10^{10} per day
Cross-coupling intermodulation	3 meters	40-dB separation in level for both cases
Propagation delay	$(R/3) \times 10^{-8}$ meter per m/sec	Can be all but eliminated by reiterative solutions
Equipment propagation delay	10^{-3} meter per m/sec	Can be all but eliminated by reiterative solutions
Differential phase delay:		
Velocity	75×10^{-3} meter per m/sec	Can be all but eliminated by reiterative solutions
Acceleration	7.6×10^{-3} m/sec per m/sec^2	Can be all but eliminated by reiterative solutions

TABLE 2.- CALCULATED COMBINED RANGE DELAY ERRORS, BOOST AND SUSTAINER PERIODS FOR 14.386 GM

Time, sec	Range, km	Radial velocity, m/sec	Radial acceleration, m/sec^2	Combined position delay errors, meters
0	1.085	0	0	0
1	1.100	76.7	123.5	-1.58
2	1.238	302	327	-5.95
3	1.704	631	332	-11.2
4	2.500	805	17.8	-12.8
5	3.313	795	-37.8	-12.5
6	4.089	755	-43.0	-11.8
7	4.822	712	-43.0	-11.1
8	5.512	672	-36.6	-10.5
9	6.165	636	-34.5	-10.0
10	6.784	604	-29.3	-9.5
11	7.373	576	-26.0	-9.1
12	7.936	551	-25.0	-8.7
13	8.475	527	-21.7	-8.3
14	8.991	507	-19.2	-8.0
15	9.489	487	-21.66	-7.6
16	9.965	467	-19.4	-7.3
17	10.4	451	-16.2	-7.1
18	10.9	434	-17.7	-6.8
19	11.3	417	-15.3	-6.6
20	11.7	405	-8.9	-6.4
21	12.1	396	-26.8	-6.1
22	12.5	394	23.5	-6.3
23	12.9	489	166.5	-8.4
24	13.5	662	178.7	-11.2
25	14.2	852	201.3	-14.33
26	15.2	1071	237.3	-18.0
27	16.3	1334	288.5	-22.5
28	17.8	1577	197.0	-26.1
29	19.5	1670	-9.76	-26.9
30	21.2	1654	-23.2	-26.6
31	22.8	1631	-22.0	-26.2
32	24.5	1610	-19.52	-25.9

TABLE 3.- CALCULATED COMBINED DELAY ERRORS FOR PERIOD NEAR APOGEE 14.386 GM

Time, sec	Range, km	Radial velocity, m/sec	Radial acceleration, m/sec^2	Combined position delay errors, meters
205	156.4	-3.5	-8	0
206	156.4	-11.9	-8	.25
207	156.4	-20.1	-8	.39
208	156.4	-28.4	-8	.54
209	156.3	-36.6	-8	.68
210	156.3	-44.5	-8	.82
211	156.3	-52.6	-8	.97
212	156.2	-60.7	-8	1.11
213	156.1	-68.6	-8	1.25
214	156.1	-76.4	-8	1.39
215	156	-84.2	-8	1.52
216	155.9	-92.3	-8	1.67
217	155.8	-100.5	-8	1.81
218	155.7	-109	-8	1.96
219	155.6	-117	-8	2.10
220	155.5	-124	-8	2.24
221	155.3	-133	-8	2.38
222	155.2	-141	-8	2.52
223	155.0	-148	-8	2.66
224	154.9	-156	-8	2.80

TABLE 4.- STANDARD DEVIATION IN X, Y, AND Z COORDINATES WITH RANGE MEASUREMENT ASSUMED PERFECT. (DATA ARE PRELIMINARY RESULTS FROM A RADINT-INTERFEROMETER-ACCURACY SURVEY MADE WITH FLIGHT MODEL NIKE-APACHE 14.386 GM)

Flight time, sec	Elevation angle, deg	Slant range, km	σ_z, meters	$\sigma_x = \sigma_y$, meters
15	77	10.5	0.7	2.9
30	79	21.2	2.1	10.0
50	79	51.1	4.3	21.4
100	77	109	8.2	36.2
150	75	144	9.4	39.7
200	71	157	13.7	39.7
250	64	149	19.8	40.8
300	51	124	36	44
350	21	98	233	110

TABLE 5.- COMPARATIVE DIRECTION COSINE PRECISION GRANULARITY FOR TM INTERFEROMETER, FPS-16 AND FPQ-6 RADARS

Az, deg	El, deg	Least significant value (parts per 10^5)								
		Radint			FPS-16			FPQ-6		
		X	Y	Z	X	Y	Z	X	Y	Z
0	30	5	5	9	8	5	8	4	2	4
0	50	5	5	4	6	7	6	3	4	3
0	70	5	5	2	3	9	3	2	5	2
0	90	5	5	0	0	10	0	0	5	0
30	30	5	5	12	10	8	8	5	4	4
30	50	5	5	6	9	10	6	5	5	3
30	70	5	5	2	7	10	3	4	5	2
30	90	5	5	4	5	8	0	2	4	0
60	30	5	5	12	8	10	8	4	5	4
60	50	5	5	6	10	9	6	5	5	3
60	70	5	5	2	10	7	3	5	4	2
60	90	5	5	4	8	5	0	4	2	0
90	30	5	5	9	5	8	8	2	4	4
90	50	5	5	4	7	6	6	4	3	3
90	70	5	5	2	9	3	3	5	2	2
90	90	5	5	0	10	0	0	5	0	0

TABLE 6.- DIRECTION COSINES AND SPACE ANGLES FOR HALF OF A 16-λ INTERFEROMETER

Lobe	cos θ	Angle from horizon, θ	Lobe	cos θ	Angle from horizon, θ
16	0.99909	2°27'	7	0.43710	64° 5'
15	.93664	20°30'	6	.37466	68° 0'
14	.87420	29° 3'	5	.31222	71°48'
13	.81176	35°44'	4	.24977	75°32'
12	.74932	41°28'	3	.18733	79°12'
11	.68687	46°37'	2	.12489	82°50'
10	.62443	51°22'	1	.06246	86°25'
9	.56199	55°48'	0	0	90° 0'
8	.49954	60° 2'			

TABLE 7.- RELATIVE DESIGN PRECISIONS FOR SEVERAL TRACKING SYSTEMS

TRACKING METHOD		DESIGN PRECISION	
GENERAL	SPECIFIC	RANGE	AZIMUTH & ELEVATION
DOPPLER INTERFEROMETER SYSTEMS	RADINT	± 1 METER	± .0029 DEGREES
	TONE RANGE-T.M. INTERFEROMETER	± 5 METERS (RESOLUTION LIMITED CASE)	± .0029 DEGREES AVERAGE
RADAR	AN/MPS -19	± 25 YDS = ± 22.8 METERS	± 1 MIL = ± .056 DEGREES
	AN/FPS -16	± 5 YDS = ± 4.58 METERS	± 1 MIL = ± .056 DEGREES
	AN/FPQ -11	± 25 YDS = ± 22.8 METERS	± 0.5 MIL = ± .028 DEGREES
	SPANDAR	± 25 YDS = ± 22.8 METERS	± 1 MIL = ± .056 DEGREES
	AN/FPQ-6	± 5 YDS = ± 4.58 METERS	± 0.05 MIL = ± .0028 DEGREES

TABLE 8.- COMPARISON OF TONE RANGE AND FPS-16 TRACKING SYSTEMS

Time, t, sec	Tone Range - FPS-16, ΔZ, meters	Altitude, Z, meters
10	-17.1	5 720
20	-36.6	12 140
30	-38.4	22 620
40	-36.6	31 956
50	-35.3	41 983
60	-35.3	47 013
70	-37.5	53 251
80	-39.6	58 364
90	-40.5	62 650
100	11.3	65 720
110	10.6	68 250
120	-33.5	69 495
130	-39.5	69 750
140	-26.2	69 400
150	-35.8	67 600

TABLE 9.- COMPARISON OF TONE RANGE AND RADINT TRACKING SYSTEMS

Time, t, sec	Tone Range - Radint, ΔZ, meters	Altitude, Z, meters
10	3.9	6 678
20	4.2	11 414
30	19.2	21 756
40	-4.2	37 078
50	-6.1	51 170
60	-3.0	64 250
70	-8.5	76 385
80	-18.5	87 555
90	-21.5	97 767
100	-25.3	107 027
110	-34.8	115 347
120	-40.5	122 713
130	-46.0	129 128
140	-51.5	134 606
150	-44.2	139 140
160	-33.5	143 956

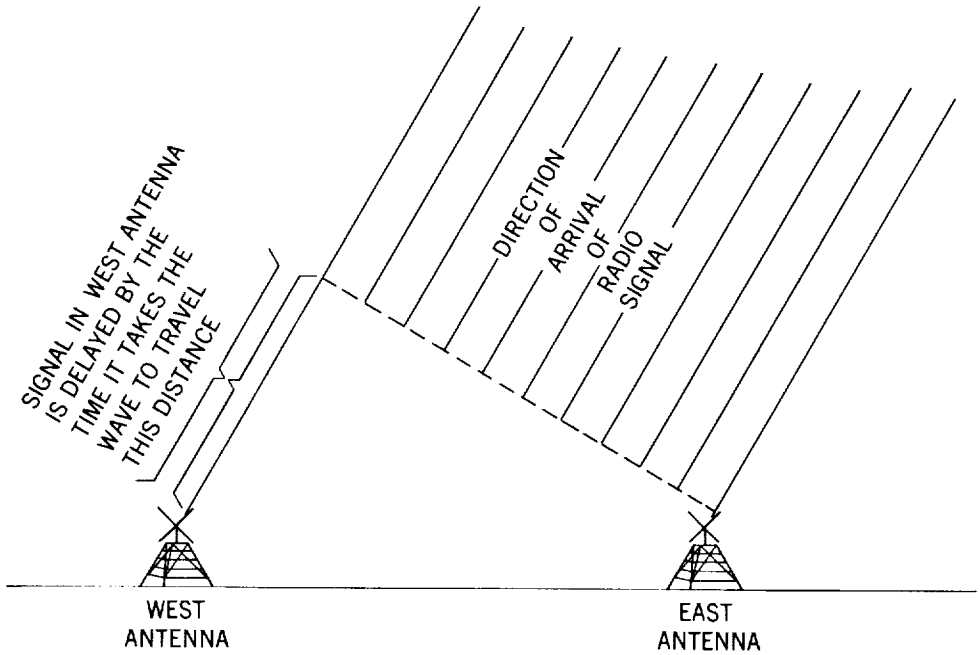

Figure 1.- Interferometer geometry.

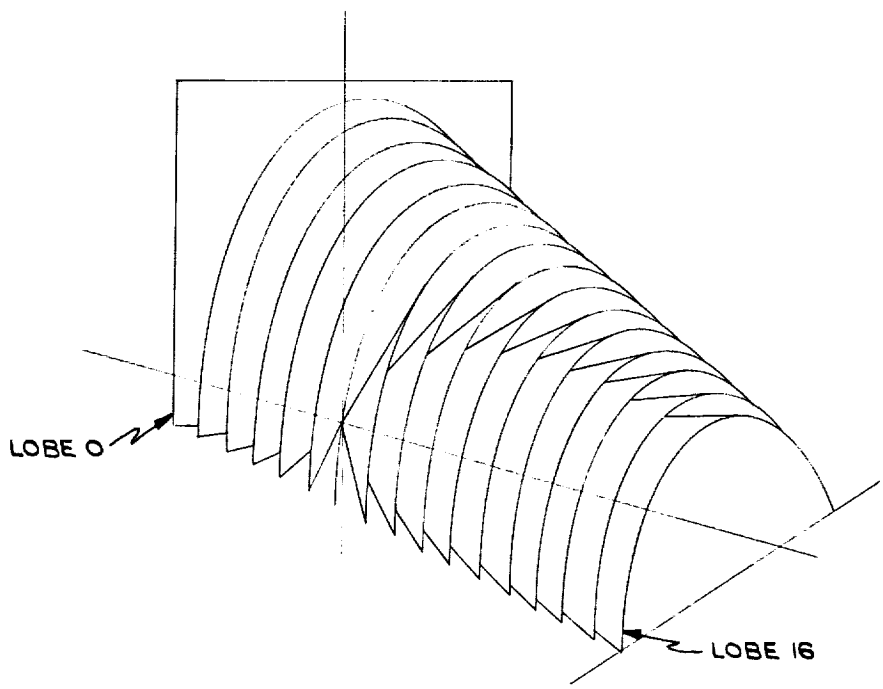

Figure 2.- Spacial distribution of interferometer lobes. (Lobes extend to infinity.)

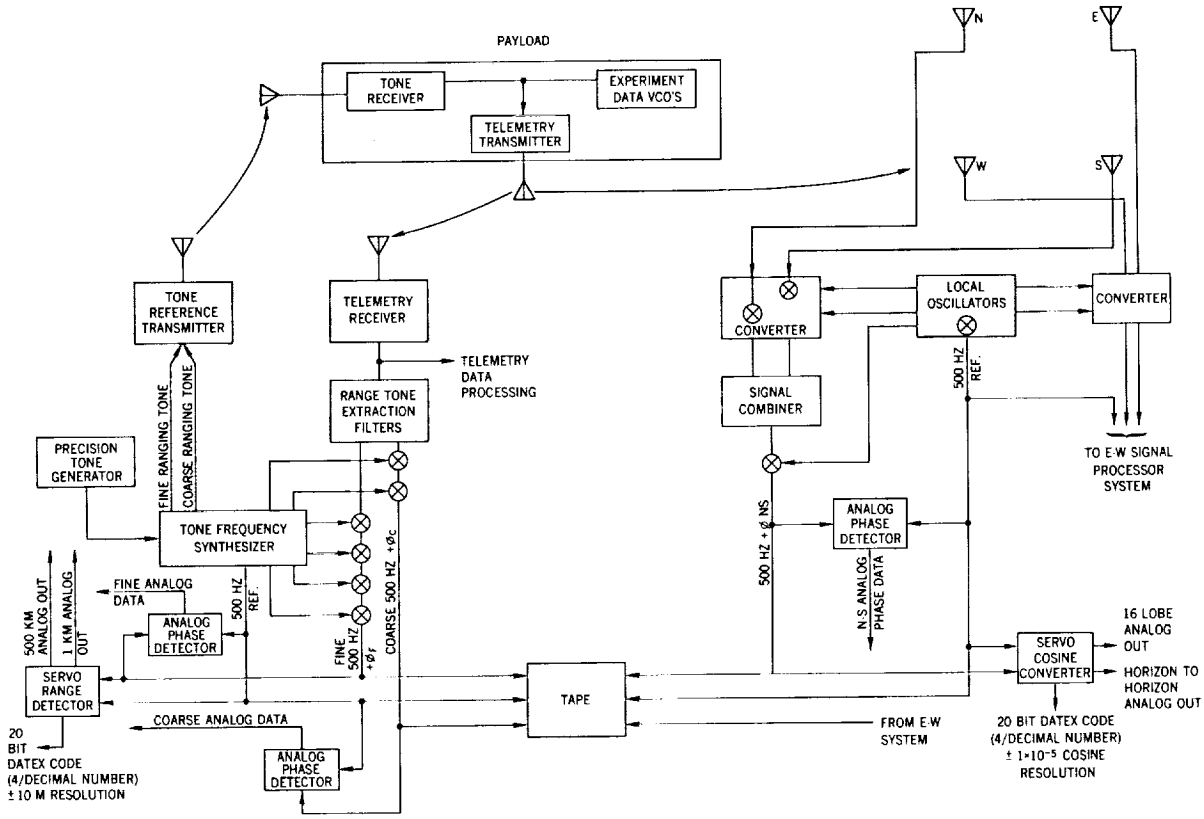

Figure 3.- Tone Range/Telemetry Interferometer systems.

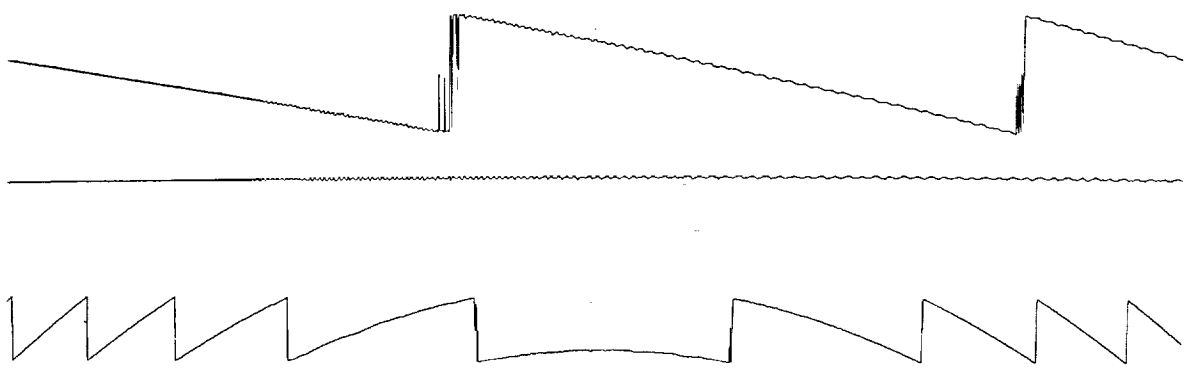

Figure 4.- Segment of a typical range analog record.

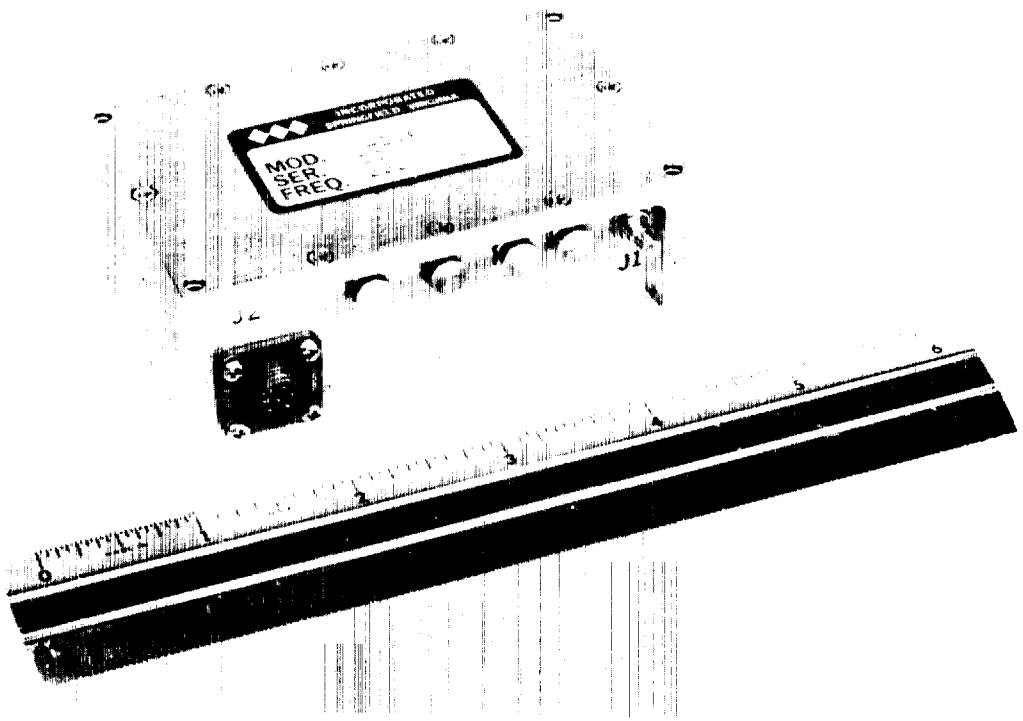

Figure 5.- Airborne range tone receiver.

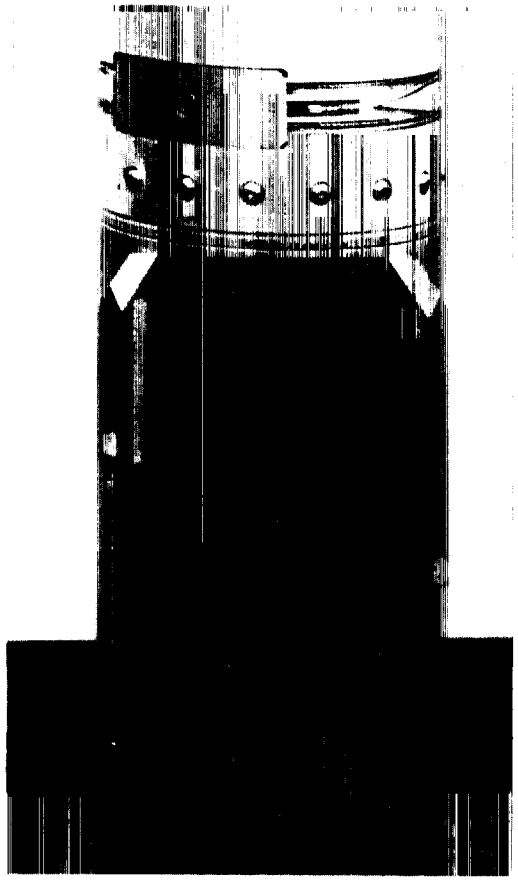

Figure 6.- Telemetry and range receiver antennas mounted on payload.

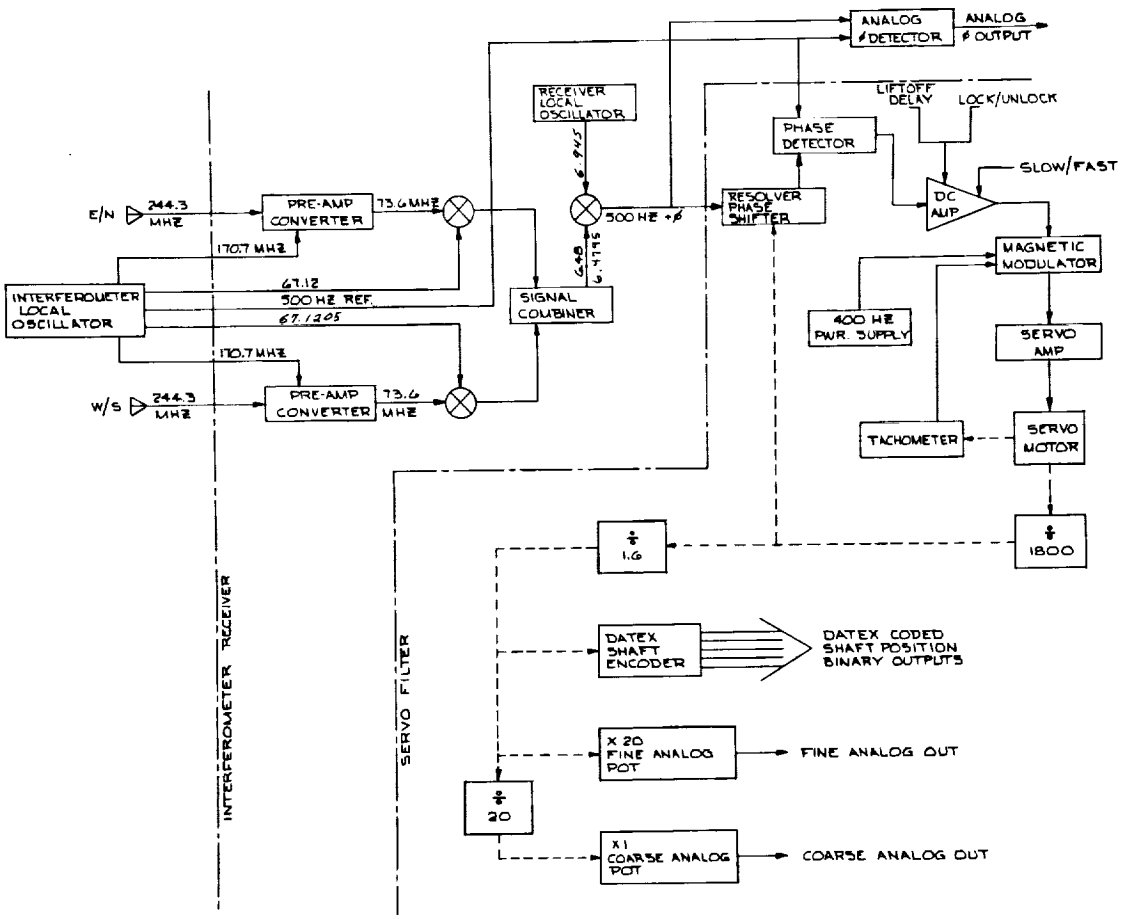

Figure 7.- Interferometer system, simplified block diagram.

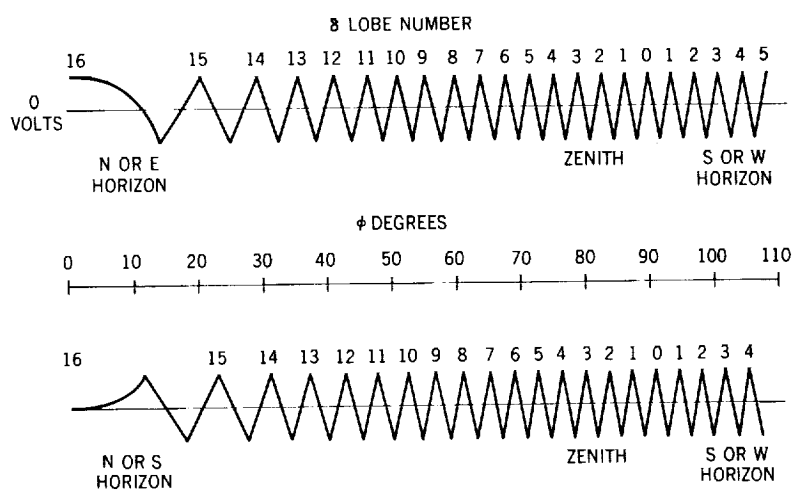

Figure 8.- Continuous analog output of interferometer phase detector.

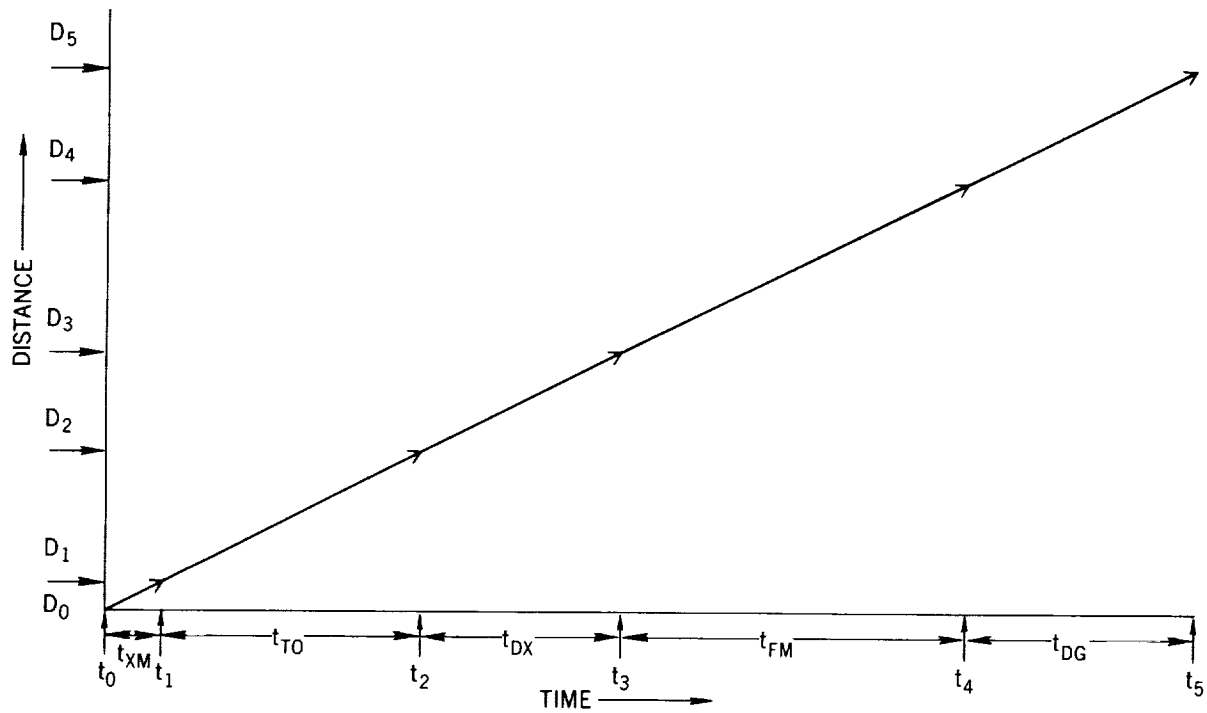

Figure 9.- Impact on measurement accuracy by group delays for a constant velocity.

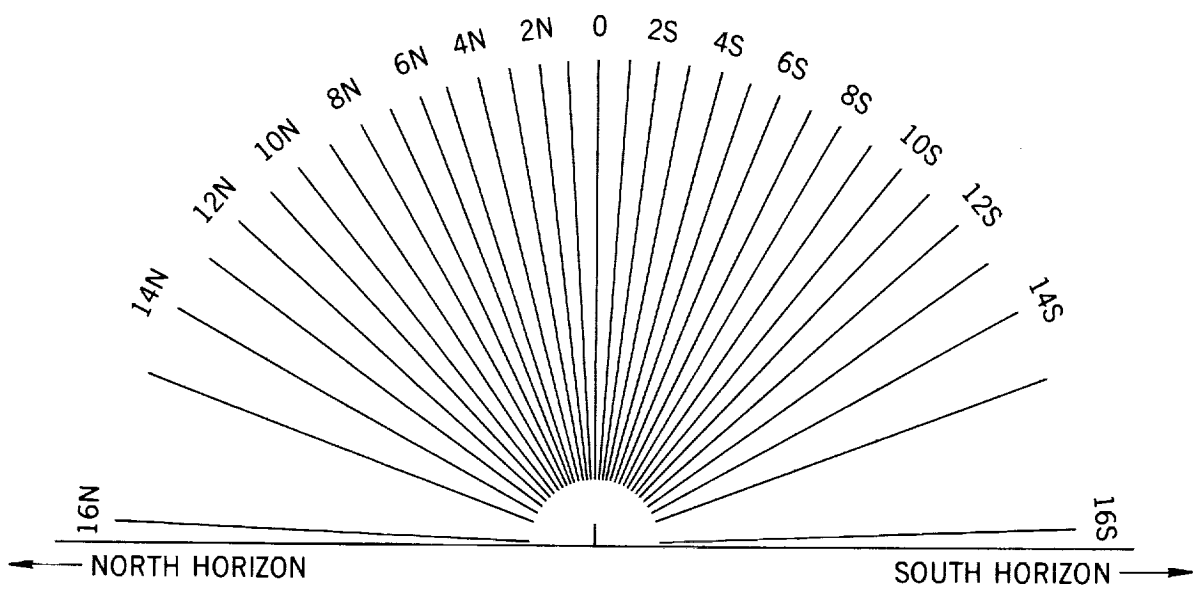

Figure 10.- Slant plane lobe diagram. North-south array.

SOME PROPERTIES OF DATA FROM FALLING SPHERE SOUNDINGS

By R. S. Quiroz

Upper Air Branch, NMC, Weather Bureau, ESSA

12

SUMMARY

Proper use of reduced data from falling sphere soundings requires a detailed knowledge of the many factors affecting their accuracy. Criteria for judging the reliability of ROBIN sphere data (wind and density) are reviewed, and the effect of the data smoothing interval on the suppression of radar tracking error and the retention of real atmospheric detail is briefly considered. The height range of valid temperatures is described in relation to the prevailing pressure scale height and the climatological temperature regime. ROBIN soundings considered valid by stated criteria are presented which illustrate their fidelity to large-scale atmospheric variations. Also shown are rare examples of soundings satisfying the above criteria which indicated physically improbable variations. Special data comparisons include Arcasonde and ROBIN temperatures from Ascension Island, which indicate fair agreement near the stratopause; and densities based on thermistor and sphere data. The latter reveal a systematic difference of about 8%; various explanations are considered, but none is found to account for the full difference. The article concludes with a brief review of past uses of sphere data, together with remarks on persisting problems relevant to all sphere measurements.

INTRODUCTION

Perhaps no method for sounding the upper atmosphere with rockets has required so much study as the falling sphere technique. Much of the commentary has concerned the ROBIN sphere (Engler, ref. 1; Luers, ref. 2), but some of the problems of interest apply to other spheres as well (Jones and Peterson, ref. 3; Salah, ref. 4; Faucher et al., ref. 5; Peterson, ref. 6; Champion and Faire, ref. 7). Nearly 700 ROBIN soundings have been obtained, including a research series of 188 observations in 1960-62 (Lenhard and Kantor, ref. 9) and shorter research series in 1965 and 1966. More than 100 soundings have been taken with other spheres, and these have a proportionally greater value because of the higher altitudes reached. Densities from ROBIN soundings have been obtained generally in the height range 40-70 km, and winds to lower altitudes. Modifications required in the 1965 data reduction program in order to achieve ROBIN measurements above 70 km have been described by Engler (ref.8)

and Luers (ref. 2). Figure 1 indicates in greater detail, according to the author's count, the quantity of data obtained.

This discussion of the data is from the standpoint of the user. In order to ascertain the usability of sphere data in such tasks as the construction of synoptic maps or the analysis of small scales of motion, some review of the data accuracies is needed. It is stressed that odd features encountered in various soundings have been more a matter for explanation than alarm. A few soundings, however, have nearly defied explanation. The discussion of accuracies will therefore be followed by examples of unusual soundings which could be shown to be valid and some which remained suspect. The latter are rare, but they have required special probing by the user in order to judge their acceptability.

THE VALIDITY OF ROBIN WINDS AND DENSITIES

Our experience with ROBIN data indicates that with rare exceptions, the winds and densities are broadly representative of the ambient conditions. The rare exceptions might include conditions of very large vertical motions (neglected in the drag equation for density), or appreciable error in the drag coefficient, or unusual balloon behavior perhaps undetected by Engler's Lambda check (see below) (Jones and Peterson, ref. 3). With regard to small-scale variations of the wind and density, the fidelity of representation must depend greatly (as with any observational method) on the smoothing performed on the original data points.

Criteria for Acceptability

All soundings considered in this article meet the stated criteria for valid data (Engler, ref. 1). These are, as we have understood them:

(1) Densities are within the stated accuracies, to be cited below, for that portion of a sounding satisfying the Lambda check. (Mathematical symbols are listed in the appendix.) Lambda is a measure of the vertical density gradient ($\lambda \approx \rho^{-1} d\rho/dz$), and the check assumes that reliable densities are obtained if Lambda, in practice approximated from the vertical acceleration data, falls within a defined neighborhood of the standard atmosphere value. Any unusual perturbation in the vertical sphere motion is assumed to be due probably to collapse or drastic change in shape of the balloon or perhaps to some unusual aerodynamic behavior. With non-spherical balloons, the C_D and cross-sectional area would not be known and the density could not be ascertained.

(2) When the Lambda check indicates collapse below 50 km,

the densities are considered highly reliable. However, if the Lambda check fails above 50 km, the density data are considered unreliable, in accordance with the inference that the balloon was never fully inflated (Lenhard and Kantor, ref. 9).

(3) Winds are considered broadly reliable at all times after the balloon has accelerated to values of $\ddot{z}$ greater than -3 m sec^{-2}. For a non-rigid balloon, however, the response to the wind is not presently ascertainable from theory (ref. 9), and different error estimates apply (see below).

(4) Temperatures are considered broadly reliable at two scale-heights or roughly 15 km, below the starting altitude (see special section on temperature, below).

Smoothing Interval

The ROBIN data in the University of Dayton printout are given for every second above 50 km and for every 2 seconds below 50 km, but what do these represent? Starting from 0.1-sec. radar positional data, 5 values are averaged to get 0.5-sec. positions. Next, 31 of the 0.5-sec. positions are fitted by one-degree polynomial least squares to give 15-sec. values for velocity (from the slope of the curve). The velocities are recomputed at one-second intervals above 50 and 2-second intervals below 50 km, by dropping and adding data points at top and bottom; and then accelerations are determined by least squares fit to 7 of the velocities. This results in accelerations valid for 22-sec. intervals above 50 km and 28-second intervals below 50 km. For densities, which are proportional to the accelerations, the same time intervals apply. To make this review as self-contained as possible, the pertinent equations for solving for the wind and thermodynamic data have been stated in an appendix.

Thus the velocities are effectively determined over a time interval of 1/4-minute and the accelerations and densities over nearly 1/2-minute. For typical fall rates of the ROBIN one-meter balloon, a time interval of 1/4-minute corresponds to a descent of 2-4 km above 60 km and less than a kilometer below about 50 km. Engler (ref. 1) indicates that the horizontal distance of the balloons had oscillations of period exceeding 1/4-minute, which he regarded as real. His analysis of the effect of varying the number of 1/2-second radar positions used for the basic smoothing interval shows that differences up to several m sec^{-1} are possible in the amplitude of the oscillations, according to the data fit used (Fig. 2). More recently, Boer and Mahoney (ref. 10) have analyzed a research series of ROBIN soundings for March 6, 1965 (White Sands), smoothing over a constant-height interval rather than a constant-time interval. Various thicknesses were tried, from 100 to 500 meters; these are substantially narrower layers than the effective smoothing interval at the higher altitudes of Engler's data. For

these layers, Boer and Mahoney found that if the acceleration term, $\dot{z}\dot{x}/(\ddot{z}-g)$, was included in the wind computations, the correlation between wind profiles based on data from two radars (FPS-16) tracking the same balloon was greatly reduced.

The reduction in one sounding (No. 933, 1500 MST) was so dramatic that it occurred to us to correlate the wind profiles based on the Engler data, which also include the acceleration or "response" correction, but involve a smoothing interval of 22 sec. For the actual fall rates of this sounding, this amounts to a layer thickness ranging from 1.8 km to 3.4 km at 60 km. Figure 3 shows the wind profiles (u component), which are indeed in very close agreement. The correlation between them, on removal of the basic trend, is 0.93[1] in contrast to an extremely low correlation, 0.09, calculated by Boer and Mahoney.

Thus, insofar as it rises above the radar noise level, Engler's smoothing appears more realistic. At altitudes of 45-60 km, Lettau (ref. 11) appears to have made effective use of the White Sands Engler-reduced data in tracking small-scale structure which he interprets as evidence of internal gravity waves. At high altitudes Engler's smoothing interval, however, becomes quite gross (effectively, 4-5 km above 70 km), and consideration should be given to a shorter time interval which would exclude tracking error and yet permit the resolution of small-scale wave structure. Not only would the time interval be critical, but the choice of polynomial fitted to the high-altitude data, whether cubic or linear, for example (Luers, ref. 2), would also be important. Indeed, it appears that various tradeoffs would be necessary to minimize the error in both wind and density, while suppressing radar error.

Mention should be made of small-scale oscillations in the ROBIN density profiles. Unfortunately, there were very few valid thermodynamic data from the White Sands series. Figure 4 is a plot of the two profiles based on radar tracking of the same balloon (sounding no. 933). The curves are in excellent agreement. The indicated oscillations in both curves are of small amplitude, making a more detailed comparison difficult, but the oscillations are clearly in phase and with scarcely detectable divergence. Like the wind profiles, these data indicate that for the smoothing interval used by Engler, there is no apparent distortion from radar error.

---

[1]Correlation is meaningful in first decimal digit only, owing to subjectivity in determining the trend and choice of sampling frequency in the profiles.

Accuracy Estimates

Finally, we need to have in mind the overall error estimates in the ROBIN data, as given by Engler (ref. 1). These are, for an FPS-16 or similar radar and the curve-fit (31-7) commonly used:

TABLE I. ROBIN error estimates[a]

		RMS Error		
		Above 60 km	50-60	Below 50
WIND	Rigid balloon	6 knots	2.5	1
	Non-rigid	10	7	5
DENSITY	Rigid balloon	3.5%	3%	3.5%
PRESSURE	Rigid balloon	3%	3%	2.5%
TEMPERATURE	Rigid balloon	10%	3%[b]	4%[b]

TEMPERATURES FROM SPHERE SOUNDINGS IN GENERAL

The temperature error requires special discussion. As is well known, a relationship based on the hydrostatic equation is used for deriving the temperature when no thermodynamic data other than a density profile are available (eq. 3, Appendix). An initial guess of the temperature T_o, is required at the starting altitude, i.e. the top altitude with density data. The error in temperature is thus a function of two factors, (1) the departure of the initial temperature from the true temperature, and (2) the error in the density throughout the layer of integration.

For an error-free density profile, it is evident that nearly ambient temperatures are not achieved until the ratio ρ_o/ρ becomes negligibly small. This happens typically at an altitude roughly two scale heights, or about 16 km, below the starting altitude. The reduction of the ratio ρ_o/ρ with increasing height separation is shown in Table II. For example, for a height separation of 2 scale heights $\rho_o/\rho = 0.135$, and the temperature error ranges from 0.5 to 3% depending on the error in the temperature guess at the starting altitude. The temperature error itself

---

[a] Based on Table I (ref. 1).

[b] See discussion of temperature error in following section.

TABLE II

Error in temperature T(z) due to error in initial temperature T_o at starting altitude z_o

Δz	$\rho_o/\rho = e^{-\Delta z/H}$	ΔT (°C)[a]			
		±10°	±20°	±40°	±60°
H/2 (4 ≅ km)	0.606	6.1° (2.5%)[b]	12.1° (4.8%)	24.2° (9.5%)	36.4° (14.5%)
H (8 ≅ km)	0.368	3.7° (1.5%)	7.4° (3.0%)	14.7° (6.0%)	22.1° (9.0%)
3H/2 (12 ≅ km)	0.223	2.2° (1.0%)	4.5° (2.0%)	8.9° (3.5%)	13.4° (5.5%)
2H (16 ≅ km)	0.135	1.4° (0.5%)	2.7° (1.0%)	5.4° (2.0%)	8.1° (3.0%)

[a] ΔT is potential error in T_o in a given climatic regime.

[b] Percentages computed from a base temperature of 250°K.

was obtained by evaluating the term, $\left(\frac{\rho_o}{\rho}\right)\Delta T$, where ΔT is identified with the potential error in T_o (eq. 3) for a given climatological regime.

If a certain level of temperature accuracy is desired, say 2.5%, it is thus not generally possible to estimate the first altitude of "good" data without some preconceived idea of the temperature variability at the station of interest. In low latitudes, we know from rocket grenade observations, for example, that if the temperature in the U.S. Standard Atmosphere Supplements, 1966 (ref. 12), is used for T_o, the true temperature will not likely differ by more than 20°. Thus, from Table III it can be seen that nearly ambient temperature would be achieved at a height separation of about 10 km. In high latitudes in winter, however, the temperature variability is typically much greater, and it is doubtful that ambient temperatures will be sensed at separations less than 2 scale heights. The summer mesopause is known to have very cold temperatures associated with it, with the scale height possibly as low as 4-5 km, so that near 80 km real temperatures might be sensed in relatively short order.

The other error source for temperature is error in the densities themselves and it should be noted that it is the error over the layer of integration that matters, not just the error at altitude (eq. 3, Appendix). According to Engler (ref. 1) various density error profiles are possible. However, it may not always be possible to describe the height configuration of the density error in individual profiles, so that in some cases the total error in temperature may not be ascertainable. At the very least, Table III clearly illustrates that the temperatures provided in the first few kilometers below the first level of density data should not be construed as real temperatures. At times the reported temperatures may fortuitously come close to the real values, but we know of no way to readily distinguish these cases. The practice of publishing complete temperature profiles in the data books of the Meteorological Rocket Network thus seems questionable, at least without some qualification as to the validity of the data at the topmost levels. Jones and Peterson (ref. 3), however, consider publication justifiable on the grounds that although the absolute values of the temperature may be in error, "valid trends can often be seen."

For the height range in which reasonably accurate temperatures may be expected, comparison with data obtained by other techniques is desirable. Since this topic was to be considered in depth by other speakers, only a few remarks will be made here.

Jones and Peterson (ref. 3) have discussed the extent of agreement of data obtained with the aid of the University of Michigan 66-cm sphere, with grenade (layer-average) temperatures

and with HASP rocketsonde data in August 1965, at Wallops Island. Initially, the sphere and grenade measurements differed appreciably, the sphere temperatures being warmer. Improvements in the microphone array for the grenade measurements and in the sphere drag coefficients resulted in better agreement. In a combined sounding in which grenade and sphere measurements were separated at most by 10 minutes, the temperatures were found to agree generally within a few degrees. Oscillations in the sphere temperature curve were not present in either the grenade data nor in the HASP rocketsonde data at lower altitudes. Certain oscillations should, of course, not be expected in the grenade temperatures, in view of the layer-averaging; their absence in the HASP data, however, suggests that the oscillatory part of the sphere data may be erroneous. Jones and Peterson gave several possible explanations, namely, a poor radar track, a deflated sphere, peculiar aerodynamics of the sphere, or the effect of large vertical motions in the atmosphere. The first two were not judged to be the cause in this case; there were arguments against aerodynamic behavior as a cause; and the vertical motion effect could not be evaluated owing to a lack of suitable information.[2]

In the case of temperatures from ROBIN soundings, S. Teweles (private communication to N. Engler, Jan. 7, 1964) pointed to an apparent discrepancy between ROBIN and grenade temperatures but subsequently Engler determined that the ROBIN data used for comparison did not meet the criteria for acceptability (balloon collapse above 50 km). Indeed, even now, there is no extensive set of ROBIN and grenade data available, to our knowledge, obtained under similar observing conditions, which would permit definitive comparison. The situation with respect to rocketsonde thermistor data does not seem much better, since in the altitude region where ROBIN temperatures should be most reliable, about 45-60 km (assuming the thermodynamic data commence at $\sim$70 km), the thermistor temperatures are subject to increasing error with height. The results of comparisons of ROBIN and Arcasonde temperatures at altitudes near 50 km will be presented in the next section.

---

[2] The subject of vertical motions was to be considered by another speaker; it is generally agreed that vertical motions are important only if they are of the order of m sec^{-1}. Although perhaps rare, motions of this magnitude may be possible, above 30 km. In the stratosphere vertical motions of cm or mm sec^{-1} have been generally found (Miller, ref. 13), but during a stratospheric warming in 1966, upward motions as high as one-half meter sec^{-1} were estimated (Quiroz, ref. 14). Above the mesopause motions near 10 m sec^{-1} have been reported. Thus the effect of vertical motions may be a difficult problem to evaluate until better statistical knowledge of the motions is obtained.

ILLUSTRATIVE DATA

Cape Kennedy, Dec. 7, 1964

A ROBIN sounding for Dec. 7, 1964 has been selected to illustrate the broad agreement of the ROBIN data with atmospheric measurements by other methods (Fig. 5). On this date the zonal wind indicated by the sphere increases at an extraordinary rate between 30 and 55 km; the local vertical shear near an altitude of 33 km is about 20 m sec^{-1} km^{-1}, a value which may be considered statistically rare. At 55 km the westerly wind component exceeds 100 m sec^{-1} and is three times as great as the tropospheric wind maximum at the same station. So unusual a sounding might be questioned, especially in view of the westerly firing angle (to the east) at Cape Kennedy.

Later the same day, however, a wind profile based on the tracking of a parachute indicated close agreement with the ROBIN profile (the observed differences are probably due to real atmospheric variation). Figure 6 shows the synoptic situation on Dec. 9 (maps were not analyzed for Dec. 7); a very strong jet is found at the 0.4 mb level (about 55 km over Florida), with strong winds observed as far west as Hawaii. At the 5-mb level (about 35 km), the winds are light over Florida and to the south, in agreement with the data for Dec. 7.

The temperature and density profiles for this date are also of some interest. In view of our earlier discussion, realistic sphere temperatures would be expected at Kennedy some 10 km below the starting altitude and indeed, good agreement with rocketsonde thermistor temperatures can be seen just above 50 km. Near 55 km, comparison is precluded by the likelihood of increasing error with height in the thermistor measurements (Quiroz, ref. 15). The reality of the temperature difference at 42-44 km would be difficult to ascertain. It seems reasonable to conclude that reliable temperatures are indicated by both methods of observation at least in the height range 44 to 52 km. A statistical comparison of sphere and thermistor temperatures will be described below.

The ROBIN densities are 7-10% lower than the Arcasonde densities, for which the observation time is in mid day. Part of this difference may be due to diurnal variability. The possibility of a systematic bias will be explored below.

Ascension Island Temperature Comparison, March-June 1964-65

The period March-June 1964-65 was chosen for the comparison of temperatures from Arcasonde thermistors (1965) and from ROBIN sphere soundings (mainly 1964). The comparison was limited to three altitudes, 46, 50, and 54 km, where data from both sources should be considered reasonably reliable. The thermistor data have

not been corrected for possible aerodynamic, radiational, and conduction heating errors, which have been estimated at about 2 degrees (total) at 46 km, increasing to about 5 degrees at 54 km (Drews, ref. 16). The number of ROBIN soundings (18) is small, but nevertheless represents one of the densest clusters of such soundings available, save for the experimental series at Eglin AFB in 1960-62.

The observed temperatures are plotted in Figure 7 and relevant statistics are given in Table III. Inspection of this table shows that:

(1) Average temperatures from the two sources agree within about three degrees if the thermistor data are uncorrected.

(2) Sphere temperatures are warmer by a few degrees if compared with corrected thermistor data.

(3) The dispersion of the sphere temperatures, as given by the values of standard deviation, is greater than for the thermistor temperatures. (No attempt was made to smooth the oscillations present in the sphere data; smoothing would have brought the standard deviations into closer agreement.)

While the sample is probably too small to give stable statistics, these data indicate that over a definable height range the sphere average temperatures are at least realistic. Further comparison in a regime of greater variability (middle or high latitudes in winter) is desirable. Moreover, the influence of oscillations of large amplitude needs to be examined further.

An interesting feature in Figure 7 is the indication of a diurnal temperature increase from 04-05 GMT to 16-18 GMT in three pairs of observations. At 46 km, the two thermistor pairs on May 23 and 26 indicate a diurnal range of about 10°C; this range is also indicated by the pair of sphere observations on April 8, which are not subject to any direct radiational error. At 50 km a similar behavior is observed; part of the large temperature increase in the sphere pair, however, may be due to non-diurnal effects

Enigma in Ascension Island Density, August 1964.

Figure 8 depicts the observed densities at Ascension Island in 1964 at two altitudes, 46 and 60 km, based on ROBIN sphere soundings, together with comparative data obtained by other methods. The lower altitude was chosen because at this height the sample of thermodynamic data from descending spheres was still appreciable and would permit comparison with values derived from thermistor measurements; as previously indicated, the error in the latter has been considered small in the upper stratosphere.

TABLE III

Comparison of temperatures from sphere and thermistor soundings, Ascension I., March-June 1964-65

Altitude (km)		SPHERE	THERM.	THERM. IF CORRECTED	SPHERE MINUS CORR. THERM.
54	$\bar{T}$	1.0°C	2.5°C	-2.9°C	+3.9°
	S_T	6.3	4.6		
	N	17	30		
50	$\bar{T}$	6.1	3.5	0.0	+6.1
	S_T	7.6	4.0		
	N	18	31		
46	$\bar{T}$	1.6	1.6	-0.7	+2.3
	S_T	5.1	3.6		
	N	16	31		

Figure 8 shows a number of interesting features, of which the most striking is the unusual and highly improbable behavior in mid-August. A density increase by 35% at 46 km and by 43% at 60 km is indicated by the sphere data in a period of 31 hours. These values greatly exceed the maximum density change in 24 or 48 hours previously indicated from rocketsonde data, namely a change of 19% occurring at a high-latitude station (Quiroz, Lambert, and Dutton, ref. 17). Yet by the criteria for acceptability stated earlier, the soundings in August must be considered reliable soundings. It is noteworthy that the extraordinarily high density on August 17 was again observed two days later, and the low value of August 16 was similar to the value observed earlier on August 12. Correspondence with the Air Force office responsible for the observational program at Ascension Island did not reveal any irregularity in data reduction. Subsequently, Engler (ref. 1) applied his time-of-fall test for suspect balloons and judged the soundings to be valid. Thus, while the values observed on August 17 and 19 were too extreme to inspire credibility, there seemed to be no way of showing that the data were incorrect. In preparing this review, it occurred to us to examine, insofar as possible, the internal consistency of the thermodynamic data with the observed winds. The temperature change from August 16 to 17 amounted to only a few degrees at 46 km. Thus a large pressure increase was associated with the increase in density. Fortunately, pressure data were also available for another rocket station, Antigua (17°N), on August 17. A geostrophic computation, assuming a linear pressure change between the two stations[3], indicates that if the pressures and densities at Ascension are valid, the zonal wind at Ascension should exceed 400 m sec^{-1}. The wind obtained from radar tracking of the ROBIN sphere was at most 25 m sec^{-1} in the vicinity of 46 km. We therefore conclude, on the basis of purely physical reasoning, that the soundings of August 17 and 19 are invalid. Rocket grenade observations were also taken on August 16 and 17, though the results were not available until much later (Smith et al., ref.18). These data, entered on Figure 8, are completely at variance with the sphere results.

This case is but one, although possibly the most dramatic, of several extraordinary sphere soundings encountered by the author, and it emphasizes the need for careful scrutiny of all data by the user. Indeed, all rocket soundings by whatever method require careful review, since the many aspects of data reduction and transcription may increase the possibility for error.

---

[3] A non-linear pressure distribution would require an even greater wind than that computed, at some point between the two stations.

Densities from Sphere Soundings Compared with Other Measurements

Another feature of interest in Figure 8 is an apparent discrepancy in densities based on sphere soundings and on thermistor measurements. Ascension Island offers a useful opportunity for comparison because at the end of September 1964 the observational program reverted from an exclusively sphere schedule to a predominantly Arcasonde schedule. Also available for comparison in 1964 are a few grenade and Pitot-static tube measurements at Ascension and several University of Michigan sphere soundings at Kwajalein (9°N, 168°W). From other years, tropical grenade soundings at Natal, Brazil (6°S, 35°W) (1966-67) and Guam (14°N, 145°E) (November 1958) are also entered.

Two points are readily apparent:

(1) The sphere densities are, with rare exceptions, lower than the mean based on thermistor densities; e.g. in September-December, 1964, the mean sphere density is nearly 10% less than the mean based on thermistor measurements.

(2) A greater dispersion is indicated by the sphere measurements.

At the upper altitude, the difference between sphere and thermistor measurements is partly due to the error in the latter, which increases strongly above 55 km, and no attempt has been made to enter individual thermistor values for 60 km.

It is therefore meaningful to concentrate on the data for 46 km, where the error in either set of data should be minimal. Various possible explanations of the observed difference merit considerations, such as unsuspected temperature error in the rocketsonde measurements, error in the drag coefficient used for the sphere reduction, etc.

The effect of a thermistor temperature error may be evaluated with the aid of the integrated hydrostatic equation in the form[4]

$$\rho = \rho_o \left(\frac{T}{T_o}\right)^{-\left(\frac{g}{R\gamma}+1\right)} \qquad (1)$$

[4] In practice, pressures and densities based on rocketsonde temperature are obtained through use of the approximation $p = p_o \exp(-g\Delta z/R\,\overline{T})$, but as has been shown by Ballard (ref. 19), the departures from results based on the more exact Eq. (1) are negligibly small.

Introducing an error, ΔT, in temperature, held constant over the layer of integration, the density at the upper altitude becomes

$$\rho + \Delta\rho = \rho_o\left(\frac{T + \Delta T}{T_o + \Delta T}\right)^{-\left(\frac{g}{R\gamma} + 1\right)} \tag{2}$$

and the ratio of (2) to (1) is

$$R = \frac{\rho + \Delta\rho}{\rho}\left[\left(\frac{T}{T_o}\right)\left(\frac{T_o + \Delta T}{T + \Delta T}\right)\right]^{+\left(\frac{g}{R\gamma} + 1\right)} \tag{3}$$

For a temperature structure approximating the conditions at Ascension Island[5] and for a hypothetical temperature bias, ΔT, in the thermistor soundings, sustained over the 20-km layer from 26 to 46 km, the solution of Equation (3) yields a density error of approximately +3% if $\Delta T = +3°$, increasing to +8% if $\Delta T = +8°C$. (Over a 10-km layer from 36 to 46 km, a temperature error of 16° would be required to explain a discrepancy of 8% in the density at 46 km.) The rocketsonde temperatures are generally believed to be quite accurate below about 50 km, although some disagreement with radiosonde temperatures near 30 km has yet to be explained (Quiroz, 1969). Since an unreasonably large temperature error is required to explain the density difference in Figure 8, it appears that we must look to some other error source, or more likely, a combination of sources.

According to Engler (ref. 1) uncertainty in the drag coefficient for ROBIN spheres is less than about 2% below 50 km, but improved knowledge of this factor is needed. Luers (ref. 2) and Peterson (ref. 6) have pointed to inconsistencies in the available drag tables and have re-emphasized the need for improved data. An interesting series of measurements with hypersonic rigid spheres (Kwajalein, 1965-1968) has been obtained under conditions for which a high degree of confidence can be placed in the drag data used, according to Salah (ref. 4, 21). Comparative ROBIN and hypersonic sphere measurements, if feasible, might shed light on the drag data used for the inflatable, subsonic spheres.

It is interesting to note in Figure 8 that measurements by the grenade method tend to lie between the sphere and thermistor values. Almost without exception, the grenade densities are lower than the thermistor values. It is therefore our belief that the discrepancy between the sphere and Arcasonde data must be due to error in both methods of measurement.

---

[5]Supplemental Atmosphere data for 15°N were used.

Diurnal series, Eglin AFB, May 9-10, 1961

Another example of unusual sphere data is found in the diurnal series for May 9-10, 1961 (Figure 9). The 2000 GMT observation indicates a density increase of nearly 30% from 1600 GMT. This sounding and two soundings at 1015 and 1115 were not used by Cole and Kantor (ref. 20) in their harmonic analysis for data at 60 km. Summing the first two harmonics, Cole deduced a daily range of 12% in the density. The inclusion of the three unused soundings, in particular the data for 2000 GMT, would probably have had a strong influence on the results. To the author's knowledge, these data have not yet been shown to be invalid. Lenhard's (ref. 22) analysis of the wind data for this observational series indicated a weakening of the easterly flow in parallel with the afternoon rise in density, suggesting a diurnal advective effect, but careful study would be required to show a relationship.

USES OF SPHERE DATA AND FINAL REMARKS

Data from falling spheres have already proved useful in a variety of ways, but their full potential has not been exploited. They have already been used in:

(1) the construction of high-level synoptic maps.

(2) preliminary determinations of diurnal variability of density and wind: in the lower mesosphere from ROBIN data, in the stratosphere and mesosphere from Australian spheres (Rofe et al. ref. 23), and in the quasi-isopycnic layer at about 90 km from Michigan spheres (Jones and Peterson, ref. 3).

(3) exploratory studies of small-scale variability (Newell, Mahoney, and Lenhard, ref. 24, Lettau, ref. 11; Mahoney and Boer, ref. 25; Cole and Kantor ref. 26 and others).

(4) models of the density structure in the important region 90-120 km (U.S. Standard Atmosphere Supplements, 1966, ref. 12).

(5) climatological data processing (e.g., Brockman, ref. 27, Salmela and Sissenwine, ref. 28).

With regard to (1), the synoptic analysis program of the Upper Air Branch, National Meteorological Center, has resulted in a continuing series of weekly constant-pressure charts at levels centered at about 36, 42, and 55 km (5, 2, and 0.4 mb), beginning in 1964. (Constant-level density charts have also been produced though less frequently.) Because of the preponderance of rocket-sonde data (Quiroz, ref. 15), the utilization ratio of sphere data is small. The analysis technique requires wind and temperature for input, and not surprisingly the temperatures from ROBIN spheres

could be used only infrequently. This was due to (1) the typically small height range of valid temperatures and (2) untenable departures from the otherwise smooth temperature fields depicted in the analyses. These departures were at times associated with oscillatory features in the sphere profiles and would have been minimized if smooth profiles had been used. Nevertheless, the sphere data have at times provided missing links in a rocket network of sparse coverage, and they have a strong potential utility in future work, particularly if the height range of valid data is extended.

One of the most promising uses of the data is for better defining the complex density structure from 90 to 120 km. Only a handful of soundings have been used as a basis for deriving structural models of the thermosphere, yet as Figure 1 shows there has been a large increase in the number of soundings obtained in recent years. In addition to providing a better grasp of boundary conditions for thermospheric models (Thomas, ref. 29), improved knowledge will permit more definitive investigation of the influence of variable solar activity at these altitudes (Lindblad, ref. 30; Ellyett, ref. 31).

We have sought to indicate, through a few examples, that the sphere density and wind data are, with rare exceptions, reliable over definable ranges of altitude. Temperatures should be reliable at two scale heights below the first altitude of density data, but the oscillations in temperature, which either are of greater amplitude than those encountered in rocketsonde profiles or are sometimes not present in the latter, need further study. It is recommended that this problem be given special attention, since the full utility of the temperature data cannot be achieved until the reality of the oscillations is ascertained. Other problems for investigation are the apparent systematic difference in densities based on sphere versus thermistor soundings, the accuracy of the available drag data, and the possibility of large vertical motions which might at times affect the sphere results. With regard to high-altitude data from spheres with fast descent rates, consideration should be given to determining an optimum smoothing interval which at the same time suppresses radar error and preserves small-scale atmospheric structure. Finally, it is recommended that comparative experiments in the future be conducted preferably in winter in high latitudes, under conditions which favor the unambiguous separation of observational error from true variability.

REFERENCES

1. Engler, Nicholas A., 1965: Development of methods to determine winds, density, pressure, and temperature from the ROBIN falling balloon. Univ. of Dayton Res. Inst., Contract AF19(604)-7450, Final Report.

2. Luers, J.K., 1968: Estimation of errors in density and temperature measured by the high altitude ROBIN sphere. Proc. Third Nat. Conf. on Aerospace Meteorology, New Orleans, 472-477.

3. Jones, L.M. and Peterson, J.W., 1968: Falling sphere measurements, 30 to 120 km. Meteor. Mon., vol. 9, no. 31, 176-189.

4. Salah, Joseph E., 1967: Atmospheric measurements at Kwajalein using hypersonic spheres. J. Geophys. Res., vol. 72, no. 21, 5389-5393.

5. Faucher, G.A.; Morrissey, J.F.; and Stark, C.N., 1967: Falling sphere density measurements. J. Geophys. Res., vol. 72, no. 1, 1967, 299-305.

6. Peterson, John W., 1967: Falling sphere method for upper-air density, temperature, and wind. COSPAR Technique Manual Series, Paris, Appendix 7.

7. Champion, Kenneth S.W. and Faire, A.C., 1964: Falling sphere measurements of atmospheric density, temperature, and pressure, up to 115 km. AFCRL, Env. Res. Paper no. 34.

8. Engler, Nicholas A., 1967: Report on high altitude ROBIN flights October 1966. Univ. of Dayton Res. Inst., Contract AF19(628)-4796, Sci. Report no. 1.

9. Lenhard, Robert W. and Arthur J. Kantor, 1965: A catalogue of ARCAS-ROBIN soundings. AFCRL Env. Res. Paper no. 113.

10. Boer, George J. and James R. Mahoney, 1968: Further results on the velocity structure in the 30-60 km region deduced from paired ROBIN soundings. M.I.T. Contract AF19(628)-5075, Final Sci. Report, 1968.

11. Lettau, Bernhard, 1966: Persistence of small-scale features in the mesospheric wind field. AFCRL, Env. Res. Paper no. 198.

12. U.S. Standard Atmosphere Supplements, 1966. Government Printing Office.

13. Miller, Alvin J., 1967: Note on vertical motion in the lower stratosphere. Beitr. Physik Atmos., vol. 40, no. 1-2, 29-48.

14. Quiroz, Roderick S., 1969: The warming of the upper stratosphere in February 1966 and the associated structure of the mesosphere. Mon. Wea. Rev., vol. 97, no. 8, 541-552.

15. Quiroz, Roderick S., 1969: Meteorological rocket research since 1959 and current requirements for observations and analysis above 60 kilometers. NASA CR-1293.

16. Drews, William A., 1966: Final report on research and development to improve temperature measurements at high altitudes. Atlantic Res. Corp., Contract NAS1-1611, TR-PL-8876.

17. Quiroz, Roderick S.; J.K. Lambert; and J.A. Dutton, 1965: Density and temperature variability in the upper stratosphere and the mesosphere. AIAA Second Aerospace Sciences Meeting, New York, Jan. 25-27, 1965, AIAA Paper no. 65-12.

18. Smith, Wendell E.; et al., 1966: Temperature, pressure, density, and wind measurements in the upper stratosphere and mesosphere, 1964. NASA TR R-245.

19. Ballard, Harold N., 1968: A parachute-borne beta ray densitometer. Proc. Third Nat. Conf. on Aerospace Meteorology, New orleans, May 6-9, 1968, 86-93.

20. Cole, Allen E. and Arthur J. Kantor, 1964: Horizontal and vertical distributions of atmospheric density, up to 90 km. AFCRL, AF Surveys in Geophys., no. 157.

21. Salah, Joseph E., 1969: Tropical air density below 80 km from hypersonic sphere measurements. J. Appl. Meteor., vol. 8, no. 4.

22. Lenhard, Robert W., 1963: Variation of hourly winds at 35 to 65 kilometers during one day at Eglin Air Force Base, Florida. J. Geophys. Res., vol. 68, no. 1, 227-234.

23. Rofe, B; W.G. Elford; and E.M. Doyle, 1966: Diurnal variations in density, temperature, pressure, and wind, between 40 and 90 km, in the sub-tropical latitudes of the Southern Hemisphere. Australia Weapons Res. Est., TN PAD-116.

24. Newell, Reginald E.; J.R. Mahoney; and R.W. Lenhard, 1966: A pilot study of small scale wind variations in the stratosphere and mesosphere. Quart. J. Roy. Meteorol. Soc., vol. 92, no. 391, 41-54.

25. Mahoney, James R.; and George J. Boer, 1968: Horizontal and vertical scales of winds in the 30 to 60 kilometer region. Proc. Third Nat. Conf. on Aerospace Meteorology, New Orleans, May 6-9, 1968, 457-464.

26. Cole, Allen E.,and Arthur J. Kantor, 1968: Spatial variations in stratospheric and mesospheric wind fields. Proc. Third Nat. Conf. on Aerospace Meteorology, New Orleans, May 6-9, 1968, 465-471.

27. Brockman, William E., 1964: Summaries of meteorological data from ROBIN flights of 1960-1962. Univ. of Dayton Res. Inst., Contract AF 19(604)-7450, Report no. 1.

28. Salmela, Henry A., and Norman Sissenwine, 1969: Distribution of ROBIN sensed wind shears at 30 to 70 kilometers. AFCRL, Env. Res. Paper no. 298.

29. Thomas, Gary E., 1968: The influence of lower boundary conditions on thermospheric models. Meteor. Mon., vol. 9, no. 31, 213-214.

30. Lindblad, B.A., 1968: A long-term variation in mesosphere and lower thermosphere density and its relation to the solar cycle. In: Space Research VIII; North-Holland Publ. Co. (Amsterdam), 835-844.

31. Ellyett, C.D., 1968: Influence of atmospheric density variations of solar origin on meteor rates. ESSA TR ERL 71-ITS-61.

32. Staff, Upper Air Branch, National Meteorological Center, 1967. Weekly Analyses, 5-, 2-, and 0.4-mb surfaces for 1964. ESSA TR WB-2.

A P P E N D I X

PHYSICAL EQUATIONS FOR REDUCTION OF SPHERE DATA

Atmospheric Variable	Complete Equation		Simplified Equation	
WIND	$u = \dot{x} - \dfrac{(\dot{z} - w)\left(\ddot{x} + C_x - B_x\right)}{\ddot{z} + C_z - B_z}$	(1a)	$u \cong \dot{x} - \dfrac{\dot{z}\,\ddot{x}}{\ddot{z} - g}$	(1b)

u, horizontal west-east component
w, vertical motion (atmospheric)
g, acceleration of gravity
C,B Coriolis, buoyancy forces

Equation for v, the horizontal south-north component, is similar. The total wind, $V = (u^2 + v^2)^{1/2}$. For generality, the Coriolis and buoyancy forces in (1a) are retained in the ROBIN program. C is judged significant above 90 km (ref. 1). The buoyancy force $B = (v)_B \rho g$, may be large below about 30 km. In the simplified equation (1b), vertical motion and horizontal Coriolis and buoyancy forces are neglected. This eq. is used after collapse of ROBIN balloon.

Under certain conditions, the acceleration or "response" term, $\dot{z}\,\ddot{x}/(\ddot{z} - g)$, might be neglected if $u \cong x$, but Engler shows that error due to neglect of this term may be very large at high altitudes and does not recommend the use of the approximation.

DENSITY

In general, $F_D = 1/2\rho V_B^2 C_D A = ma_D$

i.e., $$\rho = \frac{2ma_D}{V_B^2 C_D A}$$

For ROBIN $$\rho = \frac{2m\left(g_z - \ddot{z} - C_z\right)}{C_D AV(\dot{z} - w) + (v)_B g_z} \qquad \rho \sim \frac{-2m(\ddot{z} - g)}{C_D AV\dot{z}}$$

(2a) (2b)

In (2b), Coriolis and buoyancy forces and vertical motion are neglected. This is form of eq. commonly used.

TEMPERATURE In general, $\partial p/\partial z = -\rho g$; $p = \rho RT$.

Integrated hydrostatic equation,

$$T = \frac{1}{\rho R}\int_{z}^{z_o} \rho g \, dz + \frac{\rho_o}{\rho} T_o \qquad (3a)$$

$$T \cong \frac{1}{\rho R}\sum \bar{\rho} g \, \Delta z + \frac{\rho_o}{\rho} T_o \qquad (3b)$$

z_o is starting altitude. Eq. (3b) is used.

Mathematical symbols not defined above:

$\dot{x}$, $\ddot{x}$	dx/dt, d^2x/dt^2, etc.
A	sphere cross-sectional area
a_D	drag acceleration
C_D	drag coefficient
γ	temperature lapse rate, dT/dz
H	pressure scale height ($H = RT/g$)
m	sphere mass
p	pressure
R	gas constant for dry air
ρ	air density
S_T	standard deviation of temperature
$T, \bar{T}$	temperature, mean temperature
V_B	sphere velocity
$(v)_B$	sphere volume

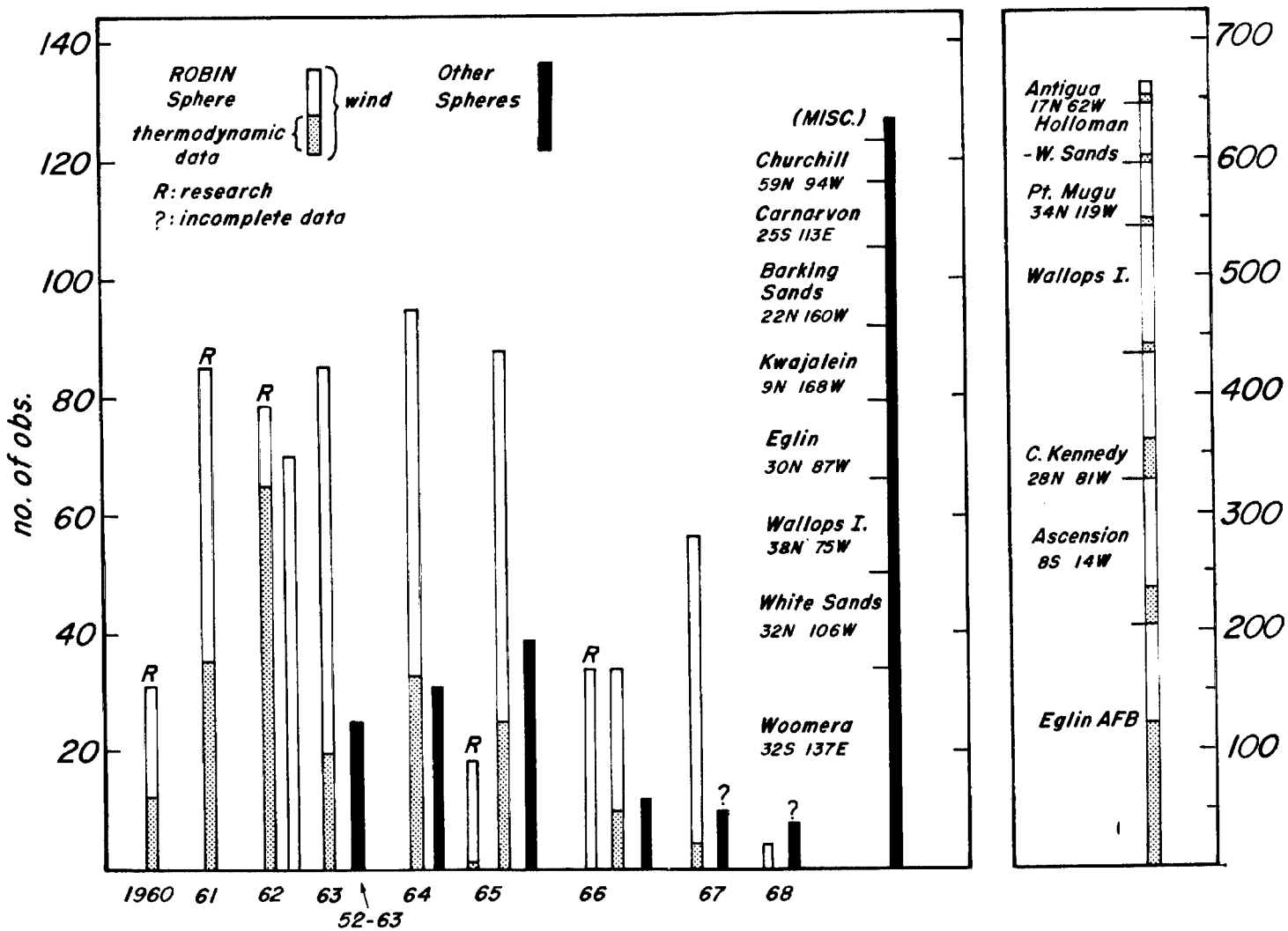

Figure 1.-Number of atmospheric soundings obtained with ROBIN spheres (passive) and with other spheres, both passive and instrumented. Statistics are based on published reports and may be incomplete in the last 2-3 years shown.

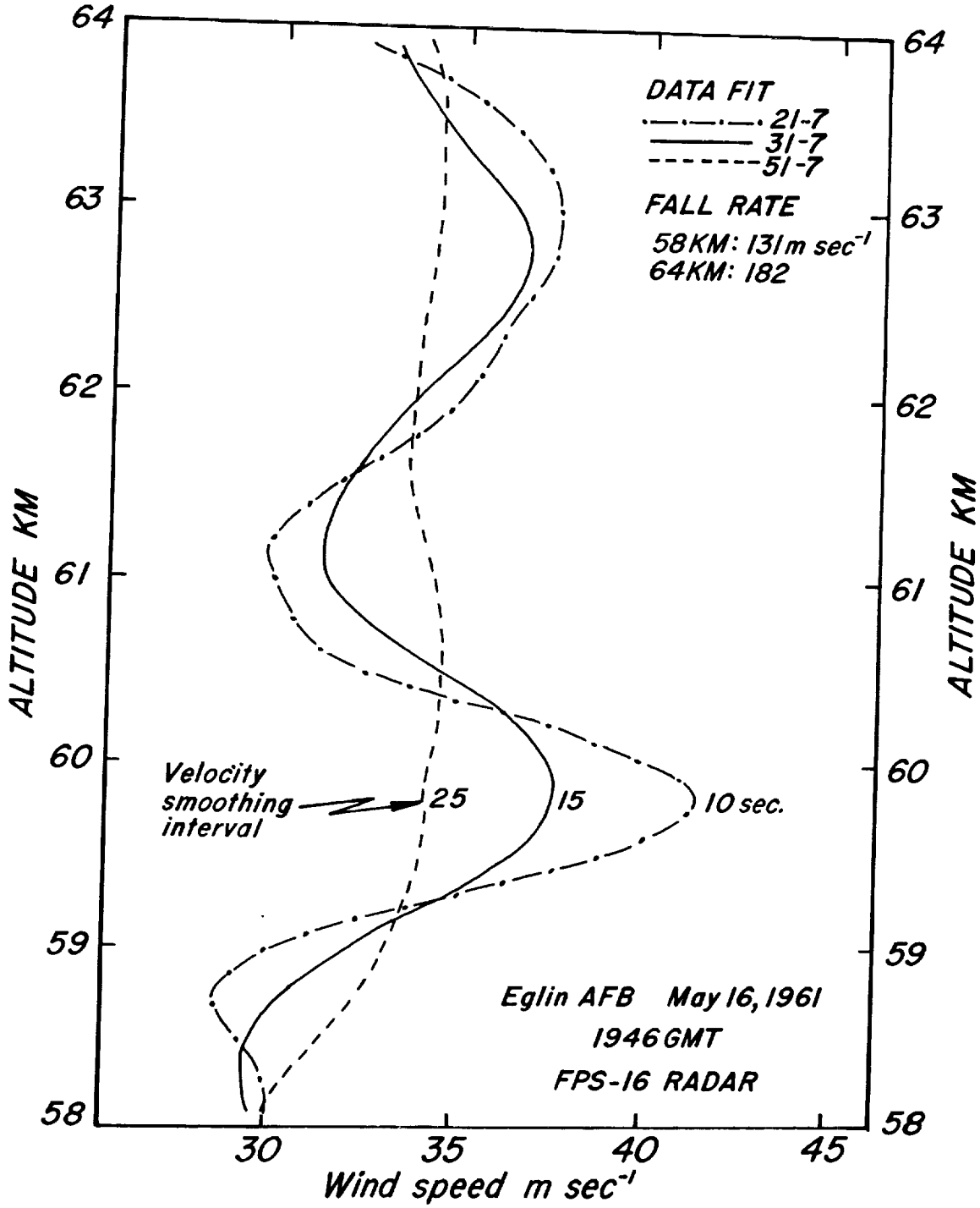

Figure 2.-Variation in amplitude of indicated wind oscillations due to choice of data fit. (Adapted from Figure 9, Engler, ref. 1, which shows additional curves for other fits.)

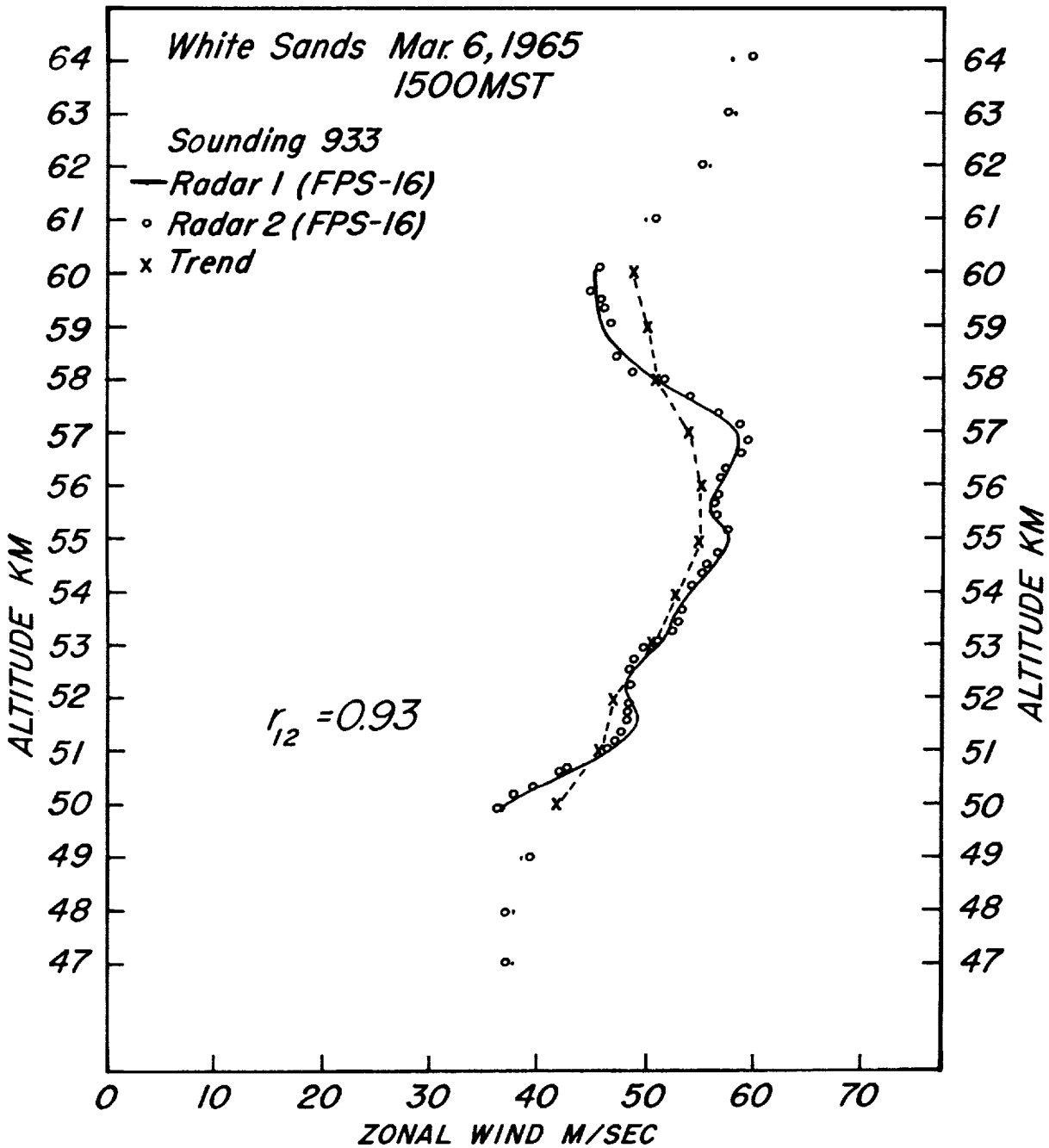

Figure 3.-Plot of wind profiles determined from data of two radars tracking same sphere, indicating high correlation for Engler smoothing interval.

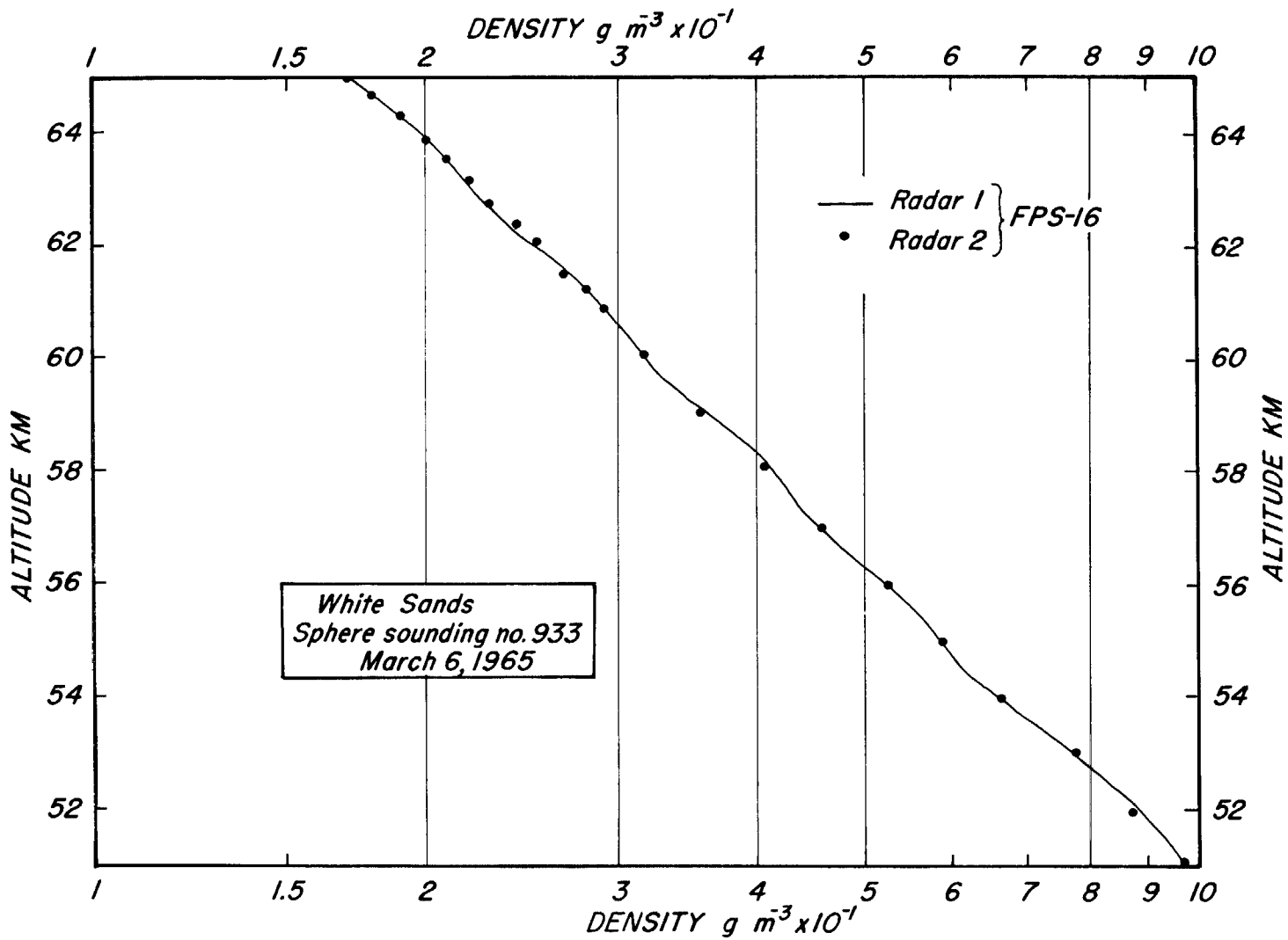

Figure 4.-Density data for same sounding as in fig. 3, showing excellent agreement in values based on data from two radars.

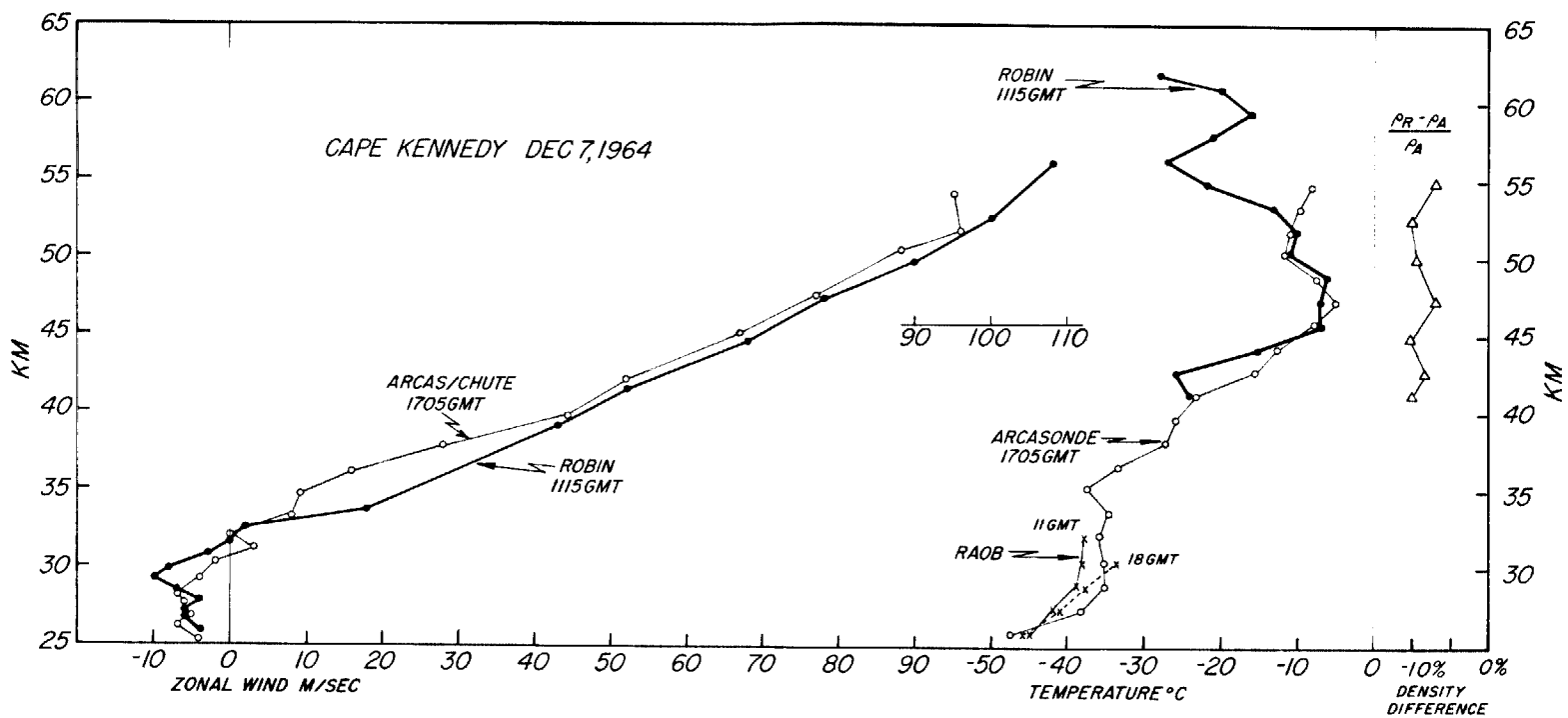

Figure 5.-Wind, temperature and density profiles from sphere sounding at C. Kennedy, Dec. 7, 1964, compared with data from Arcasonde launching 6 hours later.

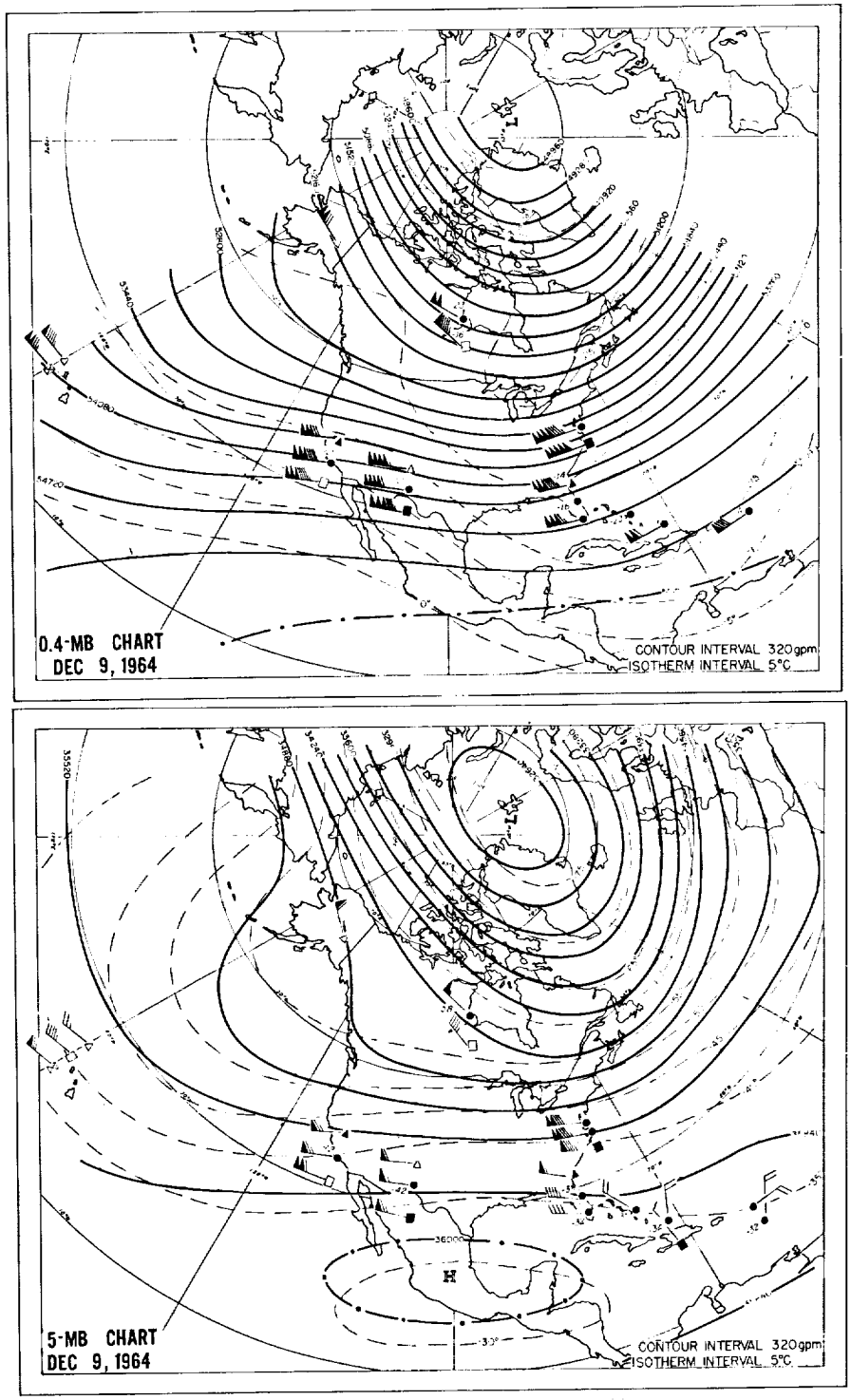

Figure 6.-Constant-pressure maps for the 0.4- and 5-mb levels, Dec. 9, 1964 (Staff, Upper Air Branch, NMC, ref. 32).

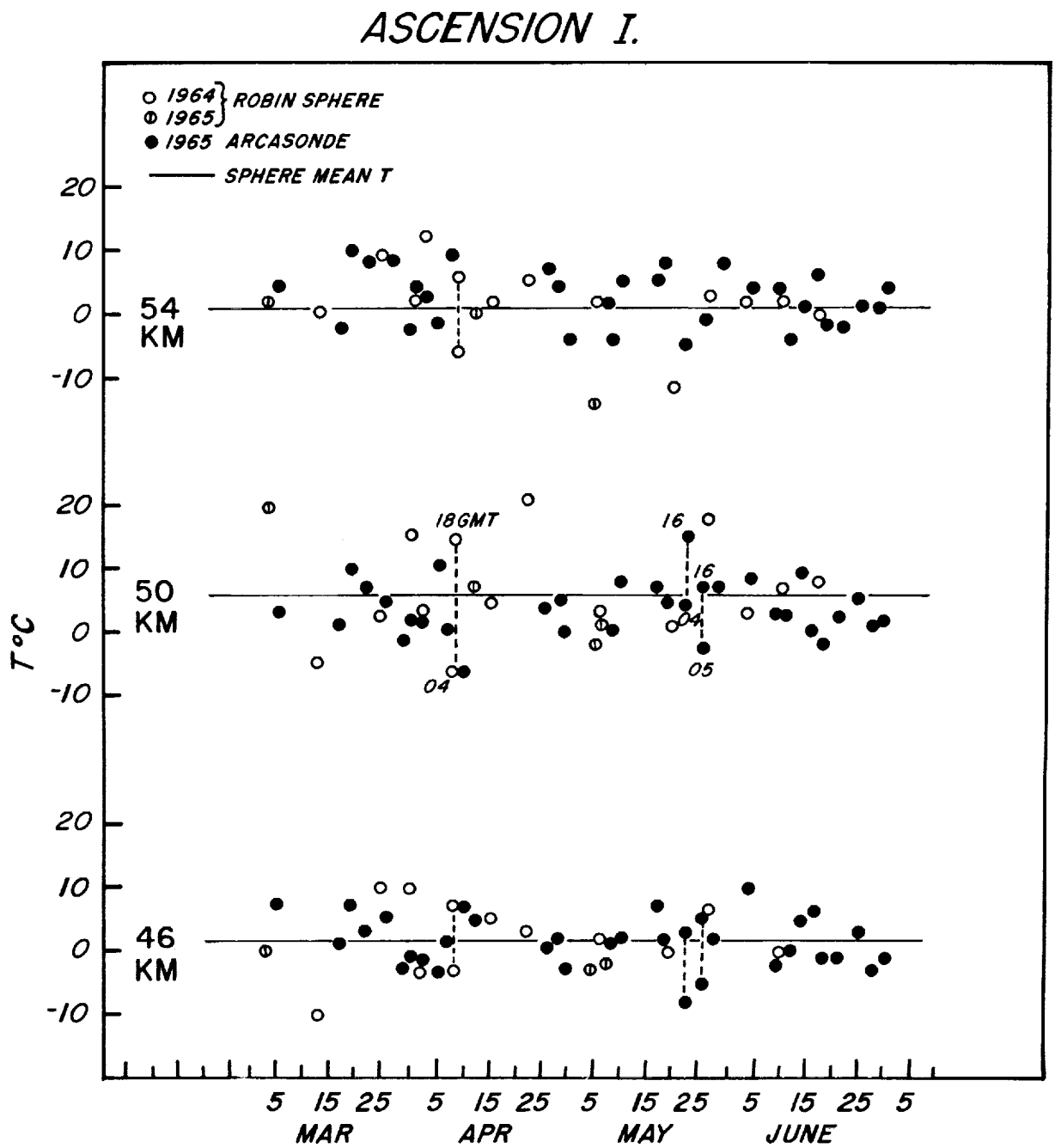

Figure 7.-Comparison of temperatures from sphere soundings, 1964-65, and thermistor soundings, 1965, at Ascension Island. See statistics in table III.

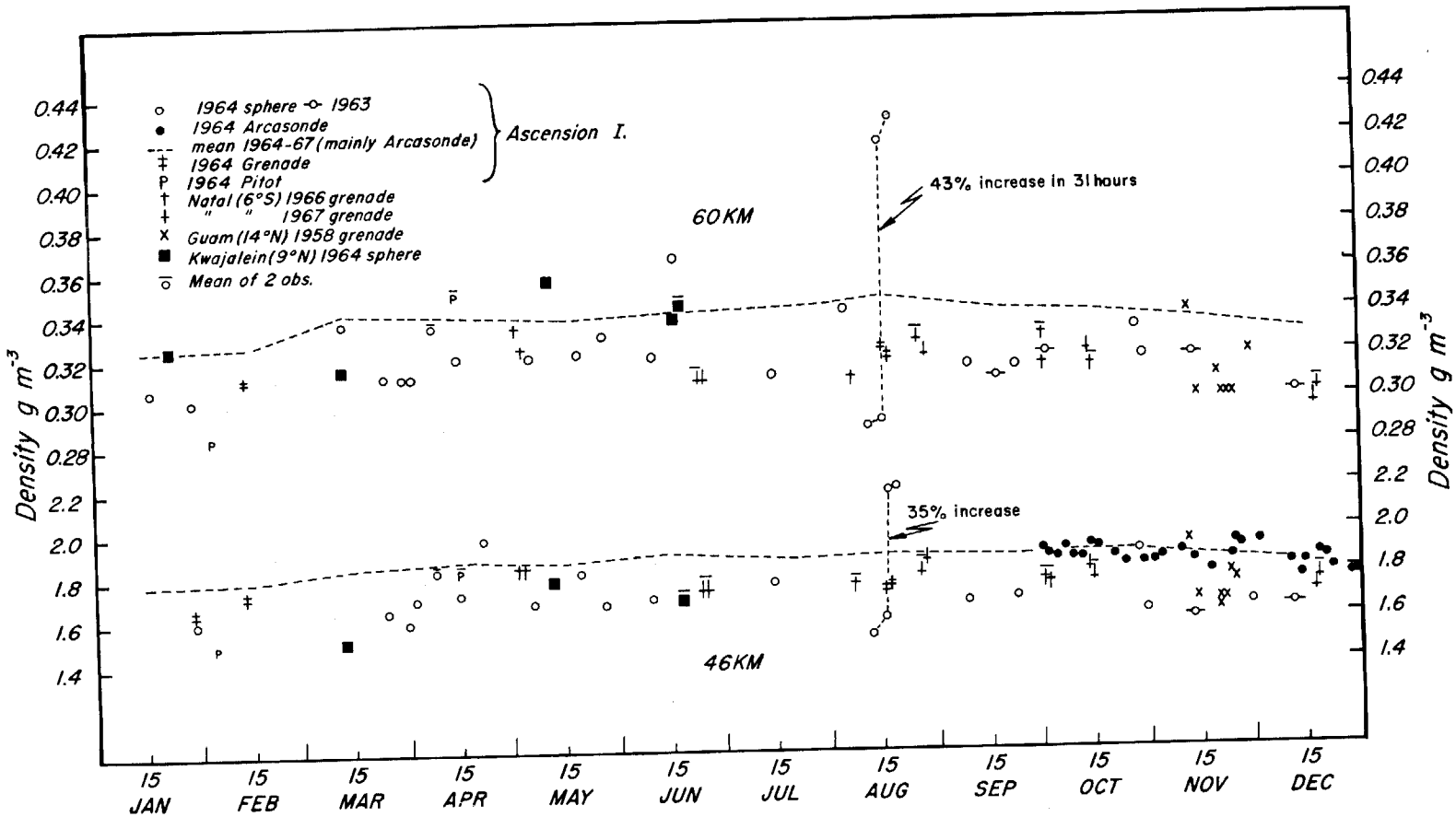

Figure 8.-Densities at 46 and 60 km, Ascension Island, based on sphere soundings (open circles), as compared with values based on thermistor, grenade, and Pitot soundings. Comparative data for other tropical locations are also entered, including University of Michigan spheres for Kwajalein. Spurious density change from Aug. 16 to 17 is discussed in text.

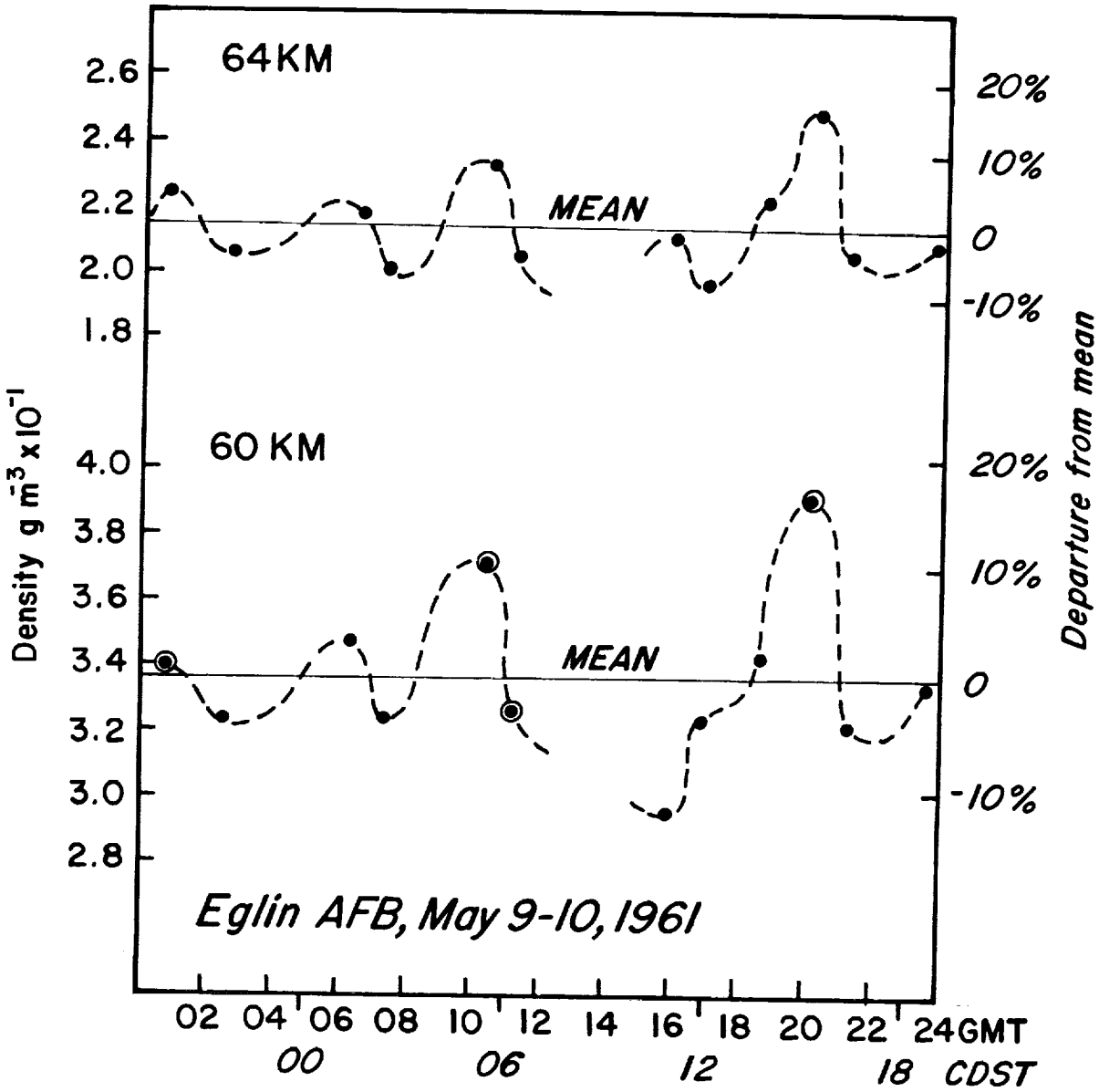

Figure 9.-Densities indicated in May 1961 diurnal series of sphere soundings. Circled values were apparently not used in harmonic analysis of 60 km data by Cole and Kantor (ref. 20).

DATA FROM FALLING SPHERE EXPERIMENTS INCLUDING COMPARISON TESTS BETWEEN DIFFERENT SYSTEMS*

Lawrence B. Smith

Sandia Laboratories
Albuquerque, New Mexico

13

SUMMARY

A discussion is given of the falling sphere program conducted by Sandia Laboratories. The 30 experiments conducted between October 1964 and June 1969 are categorized according to their results. The results from a series of comparison tests made in May 1968 between a variety of systems used to measure density are also discussed with emphasis on possible system errors. It is concluded that more effort needs to be expended to determine the size of errors arising from drag coefficient uncertainties and velocity and acceleration measurements.

INTRODUCTION

The falling sphere program at Sandia started in October 1964 with units provided by the U.S. Navy from a discontinued program at Kwajalein. Since that time we have conducted 30 such experiments mainly launched from Kauai, Hawaii, but also from Johnston Atoll and Tonopah Test Range, Nevada. This system uses the 66-cm diameter passive sphere designed and developed by Peterson, et. al., at the University of Michigan.[1] Although there are 3 spheres per Nike-Cajun payload, it has not been possible to obtain simultaneous data from all three because of a lack of precision radars. Thus at Kauai the NASA FPS-16 man-in-space radar at Kokee has been our primary tracking unit. Contiguous to the Sandia launch site is the Navy Bonham Air Landing Field which has a number of less precise radars and usually one MPS-25. Position data from radars other than the FPS-16 or MPS-25 have not been usable for density calculations, although I do hope to combine their output with the other tracks for study on atmospheric dispersion. In an operation the Kokee unit is requested to track the first sphere, the MPS-25 to follow the second, and an MPS-26 or equivalent to track the third.

From October 1964 through June 1969 we have conducted 30 falling sphere experiments. The results have been:

---

*This work was supported by the Atomic Energy Commission.

21 experiments where density, temperature, and wind data were obtained from at least one sphere

3 experiments where radars did not acquire sphere (all three at Johnston Atoll)

5 experiments with improper sphere inflation

1 experiment with radar computor malfunction

Of the 5 spheres listed as improperly inflated, 2 were ejected at too low an altitude as a result of rocket or payload malfunction, and the other 3 showed slow fall rates indicating underinflation. As with most sphere experimenters we verify the fall rate versus altitude of each sphere with a mean from many observations. Underinflation was also implied by the fact that these spheres were from a new group whose shelf life had not been verified. A check of the remaining units in the group indicated several with less than the original 8 grams of isopentane.

In the 3 experiments where the FPS-16 radars did not acquire any spheres, the problem was believed to be operator and not sensor related. With all 3 the radar operators were inexperienced in sphere operations. A signal-to-noise ratio of greater than 10 db is usually observed. A description of these operations and a compilation and analysis of the data from 15 of these experiments is provided by reference 2.

SYMBOLS

C_D	drag coefficient
λ	mathematical technique for checking sphere inflation
ρ	density
σ_R	root-mean-square range error
σ_ϵ	root-mean-square angle error

COMPARISON TESTS

On May 16, 17, and 23, 1968, a series of 14 individual rocket systems were launched from Kauai on a closely coordinated schedule. The purpose was to measure atmospheric density by several different techniques and compare results. The following schedule was maintained:

	System	Identification	Date	Launch Time (LST)	Altitude (km)
1.	Rocketsonde	Arcasonde	May 16, 1968	2130	20-60
2.	Instrumented Sphere (AFCRL)	154-106	May 16, 1968	2300	72-110
3.	Rocketsonde	Arcasonde	May 17, 1968	0530	20-60
4.	Passive Sphere	154-110	May 17, 1968	0015	30-110
5.	Rocketsonde	Arcasonde	May 17, 1968	1437	20-60
6.	Passive Sphere	154-111	May 17, 1968	1530	30-110
7.	Ionization Gages	152-112	May 17, 1968	1633	125-300
8.	Rocketsonde	Arcasonde	May 23, 1968	1030	20-60
9.	Passive Sphere	154-102	May 23, 1968	1000	30-110
10.	Instrumented Sphere (AFCRL)	154-103	May 23, 1968	1100	72-110
11.	Passive Sphere	154-105	May 23, 1968	1510	----
12.	Ionization Gages	154-113	May 23, 1968	1515	125-300
13.	O_2 Absorption	152-115	May 23, 1968	1745	80-160
14.	Pressure Probe	154-104	May 23, 1968	1200	30-100

In the above, the Arcasonde and the passive and instrumented falling spheres are operational systems. The ionization gage payload on a Nike-Tomahawk contains 3 cold cathode and one hot cathode gage. The O_2 absorption experiment used photometers aboard a Nike-Tomahawk to observe the attenuation in the 1600 Å and 1216 Å lines of the solar spectrum on both ascent and descent. This system included an automatic pointing system (ACS). The O_2 profile with height was converted to mass density by assuming a N_2/O_2 rate of 4 to 1. The ram and static pressure system was the standard instrumented probe on a Nike-Apache. Pressure inside the probe was measured by Metro-Physics thermocouples and related to ambient pressure across the shock wave from wind tunnel tests on this probe geometry.

Figure 1 shows observations of density taken over a 4 hour time interval by the instrumented sphere, the passive sphere, the radiosonde and the Arcasonde. Between 72 and 95 km the sphere data differ by as much as 30 percent. Results on the second day are indicated in Fig. 2 where measurements by the optical and the probe pressure techniques are also included. At these altitudes quoted uncertainties in the optical data are of the order of ± 20 percent and those of the probe data are 10 to 15 percent with the greater uncertainty in these probe results on the positive side. In Fig. 2 data from other systems fall between the density profiles from the instrumented sphere as a lower limit and the passive sphere as the upper limit. Except for the region above 100 km all measurements indicate a notable similarity in their variation with altitude. Above 100 km the sphere data diverge significantly. Between 70 and 100 km comparison with the other measurements is not conclusive because of the large error bars. Below about 60 km, comparison between passive sphere, pressure probe, Arcasonde, and radiosonde shows very good agreement. All differences are less than 10 percent, a result which can easily be attributed to small time and space variations. Such variations have been observed by a variety of other sounding techniques in most of the altitude region between 30 to 110 km.

Passive sphere experiments 154-110 and 154-111 indicated normal flights on the basis of their fall rate versus altitude as shown in Fig. 3 and on the basis of their acceleration and velocity on an expanded altitude scale as shown in Fig. 4. A λ check as suggested by Engler[3] was also made on both flights at the altitude of acceleration maximum. The results of 1.6 and 1.2 x 10^{-4} m^{-1} were well within the limits proposed by Engler for slightly lower altitudes. It is thus assumed both Sandia spheres were properly inflated. No such checks were made on the AFCRL sensor but the experimenter expressed confidence that the sphere inflated properly.

In an attempt to at least indicate the reason for the observed density differences in the sphere data, comparisons between pertinent parameters from four sphere flights are listed in Table I. The four flights consisted of two instrumented spheres (IS) and two passive spheres (PS). Differences between the two types of systems are given as percent difference in density but as absolute difference (Δ) in other parameters.

TABLE I

Launch 2300 and 0015 LST on 16 and 17 May 1968

Altitude km	Density $gm/cm^3 \times 10^9$			Mach No.			Reynolds No.		
	IS	PS	% Diff	IS	PS	Δ	IS	PS	Δ
99	0.6	0.8	-25	4.9	3.3	1.6	17	35	18
95	1.2	1.0	20	5.2	3.1	2.1	33	46	13
90	2.9	3.9	-24	5.5	3.5	2.0	86	203	117
85	7.2	7.0	3	5.6	2.9	2.7	209	270	61
80	16.6	20.3	-18	5.6	2.6	3.0	578	765	187
75	37.1	47.7	-22	5.4	1.6	3.8	1090	1070	20

	C_D			Drag Accel. m/sec^2			Fall Speed m/sec		
	IS	PS	Δ	IS	PS	Δ	IS	PS	Δ
99	1.6	1.9	0.3	0.2	-4.9	5.1	1417	951	466
95	1.4	1.8	0.4	0.4	0.7	0.3	1443	964	479
90	1.2	1.3	0.1	0.8	10.3	9.5	1472	945	527
85	1.1	1.3	0.2	2.0	19.0	17.0	1499	873	626
80	1.0	1.2	0.2	4.4	32.6	28.2	1519	702	817
75	1.0	1.1	0.1	9.6	17.0	7.4	1525	427	1098

Launch 1000 and 1100 LST on 23 May 1968

Altitude km	Density $gm/cm^3 \times 10^9$			Mach No.			Reynolds No.		
	IS	PS	% Diff	IS	PS	Δ	IS	PS	Δ
100	0.4	0.5	-19	4.9	1.6	3.3	14	12	2
95	1.5	1.3	15	5.2	2.2	3.0	33	65	32
90	2.0	3.4	-41	5.5	2.1	3.4	86	98	12
85	6.6	9.2	-28	5.6	2.2	3.4	209	297	88
80	15.4	18.8	-18	5.7	1.8	3.9	508	465	43
75	34.2	42.3	-19	5.4	1.3	4.1	1092	766	326

	C_D			Drag Accel. m/sec^2			Fall Speed m/sec		
	IS	PS	Δ	IS	PS	Δ	IS	PS	Δ
100	1.6	2.4	0.8	0.2	-8.5	8.7	1411	520	891
95	1.4	1.6	0.2	8.9	-5.9	14.8	1446	568	878
90	1.2	1.5	0.3	4.1	-2.1	6.2	1474	605	869
85	1.1	1.3	0.2	1.8	6.2	4.4	1500	598	902
80	1.0	1.2	0.2	0.8	10.1	9.3	1522	517	1005
75	1.0	1.0	0.0	0.4	10.8	10.4	1529	374	1155

For the altitude region of interest the spheres are in transitional flow between continuum and free molecular flow. The literature shows quite a variance or scatter of the drag coefficient data in this regime and accordingly this parameter is the most readily suspected as the cause of the differences. The Sandia program uses University of Michigan[1] derived drag tables which are based on measurements by Ashkenas[4] and May[5] for the transitional region and on measurements by Goin[6] in the subsonic region. From Mach 2.5 to 4 these coefficients are considered independent of Mach number. The AFCRL coefficients were taken from measurements by Sims[7] and Aroesty.[8] These appear to be quite independent of Mach number although this is not so stated by the authors.

If drag coefficient uncertainties are not the fundamental cause of the differences, the problems must be in the determination of velocity and acceleration since the only other parameters are area and mass and both are carefully measured. The passive sphere depends upon position versus time coordinates provided by the radar to determine velocity and acceleration.

At the time of this writing no empirical data were available on the magnitude of radar tracking errors in the 100 km region. However, if the results quoted by Engler[3] can be extrapolated to the 80- to 100-km layer, the contribution to the density from radar tracking errors is less than 3 percent. This estimate resulted from a comparison of densities calculated from two independent FPS-16 radar tracks of the same balloon. The validity of this extrapolation is enhanced by the fact that Engler's data show the variation increases with decreasing altitude. Thus the maximum difference in densities was found in the 50-60 km layer rather than in the higher 60-70 km layer implying it may be less above 80 km. Also, the difference was nearly independent of the type of smoothing. A similar experiment for altitudes between 80 and 110 km is to be conducted at White Sands this month.

An attempt was made to compute the effect of tracking errors by generating a fictitious set of position data which incorporated random radar errors. The regular computer program then used these fictitious data to compute new accelerations and velocities from which new densities were calculated for comparison with the real time data. Each new coordinate was generated by a Monte Carlo process that algebraically added to the real time range and angle value the product of a random number and an assumed RMS radar error. The random numbers were taken from a normal distribution with zero mean and unit standard deviation.

The above technique was tried with 2 sphere experiments with results as shown in Table II. Although errors frequently quoted for a well maintained FPS-16 are $\sigma_\epsilon = 0.1$ mil in angle and $\sigma_R = 5$ meters in range, the tabulated results are based on more conservative errors as given. Each coordinate was assumed to be independent of the others and no correlation was assumed between the measured parameters or with themselves, i.e., range error was not assumed to depend on distance or angle to target, etc.

Table II shows the percent deviation in density as computed using random number generation of sphere position data relative to densities obtained from original real time data. Radar errors are given as RMS percent for ϵ = angle error in degrees and R = range error in meters. Apogee altitudes for experiments 154-110 and 154-111 were 144 km and 152 km, respectively.

TABLE II

Altitude km	Percent deviation in density			
	Experiment			
	154-110	154-111	154-110	154-111
	$\sigma_\epsilon = 0.001^\circ$ and $\sigma_R = 10$ m		$\sigma_\epsilon = 0.0005^\circ$ and $\sigma_R = 10$ m	
100		1.9	0.2	-4.7
99	-0.1	4.5	0.4	-2.3
98	3.1	11.0	-0.4	7.6
97	-0.5	3.8	0	-1.5
96	-2.6	3.4	-0.6	0
95	-2.8	3.6	-0.2	0
94	-3.0	2.2	-0.4	0.5
93	-2.2	3.7	0.2	1.2
92	-0.8	2.2	0.2	0.7
91	0.6	1.6	-0.2	0.2
90	0.7	1.2	0	0.3
<90	≤1	<0.6	≤0.2	≤0.4

On the basis of Table II random radar tracking errors are generally less than 3 percent. It is, of course, possible that a fixed bias causing errors may exist. However, in view of the excellent equipment and operating personnel at the NASA Kokee site it appears unlikely that these real time coordinate data were so skewed.

One other possibility exists. The velocity-position data from the instrumented sphere reduction is obtained from integration of the telemetered acceleration measurements. The beginning altitude results from a radar track while each subsequent position and sphere velocity is a sum of previous values. An error in each such determination would be cumulative with an unknown magnitude.

CONCLUSIONS

The comparison tests described in this paper have shown that the falling sphere technique provides atmospheric data in good agreement with other systems from 30 to about 70 km. The technique is also capable of altitudes much above 70 km although these tests indicate the errors in density so derived may be as great as 20 to 30 percent, significantly greater than the usual 5 to 10 percent error quoted. It is not apparent what causes such errors nor is it apparent whether they are unique to one of the two types of spheres described here or if they result from an accumulation of several small errors.

The literature provides a variety of drag coefficient data for the transitional region. One highly desirable product of this conference would be to standardize such data so that sphere experimenters would at least have a common input. The new technique of computing coefficients by a Monte Carlo calculation shows promise and could be used.

Additional studies are needed on the accuracy of radar tracking and the possibility of cumulative errors in the velocity-position data from the instrumented sphere.

REFERENCES

1. Peterson, J. W., W. H. Hansen, K. D. McWatters, and G. Bonfanti, "Falling Sphere Measurements Over Kwajalein," J. Geophy. Res., 70 4477-4489, 1965.

2. Smith, Lawrence B., "Observations of Atmospheric Density, Temperature, and Winds Over Kauai," SC-RR-68-523, Sandia Laboratories, August 1969.

3. Engler, Nicholas A., "Development of Methods to Determine Winds, Density, Pressure, and Temperature from the Robin Falling Balloon," Contract AF19(604-7450), University of Dayton Research Institute, 1962.

4. Ashkenas, H. I., "Sphere Drag at Low Reynolds Numbers and Supersonic Speeds," Jet Propulsion Laboratory Research Summary, No. 36-12, Vol. I, 1962.

5. May, A., "Supersonic Drag of Spheres at Low Reynolds Numbers in Free Flight," J. Applied Physics 28, 910-912, 1957.

6. Goin, Kennith L., and W. R. Lawrence, "Subsonic Drag of Sphere at Reynolds Numbers from 200 to 10,000," AIAA Journal 6, 961-962, 1968.

7. Sims, William H., Rarefied Gas Dynamics, Vol. I, p. 751, Academic Press, New York (1969).

8. Aroesty, J., "Sphere Drag in a Low Density Supersonic Flow," University of California Tech. Rept., HE - 150-192, Berkeley, 1962.

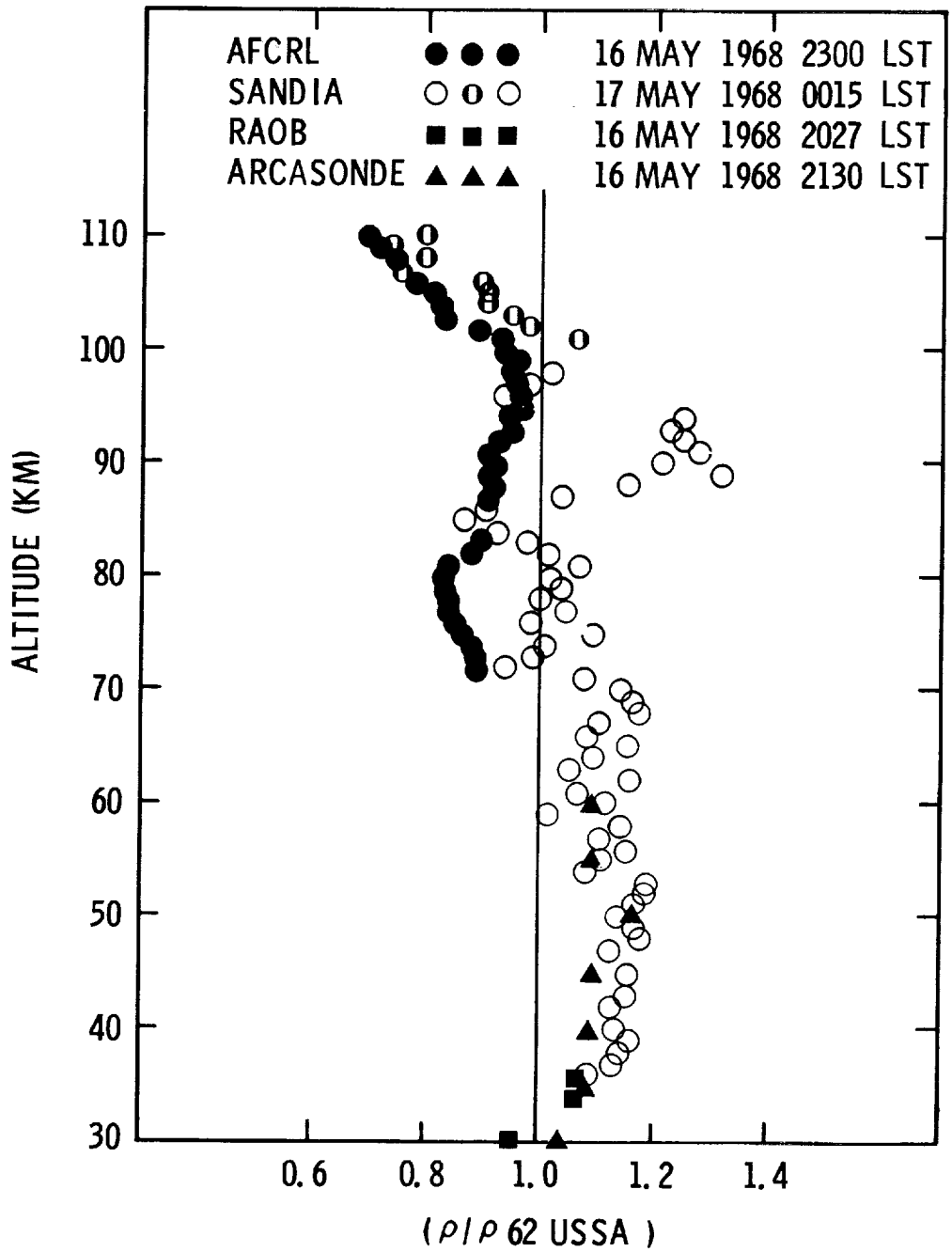

Figure 1.- Atmospheric density measurements on May 16-17, 1968, at Kauai, Hawaii, with the data normalized to the 1962 U.S. Standard Atmosphere (USSA). (Data listed as AFCRL and Sandia pertain to falling spheres of the instrumented and passive type, respectively.)

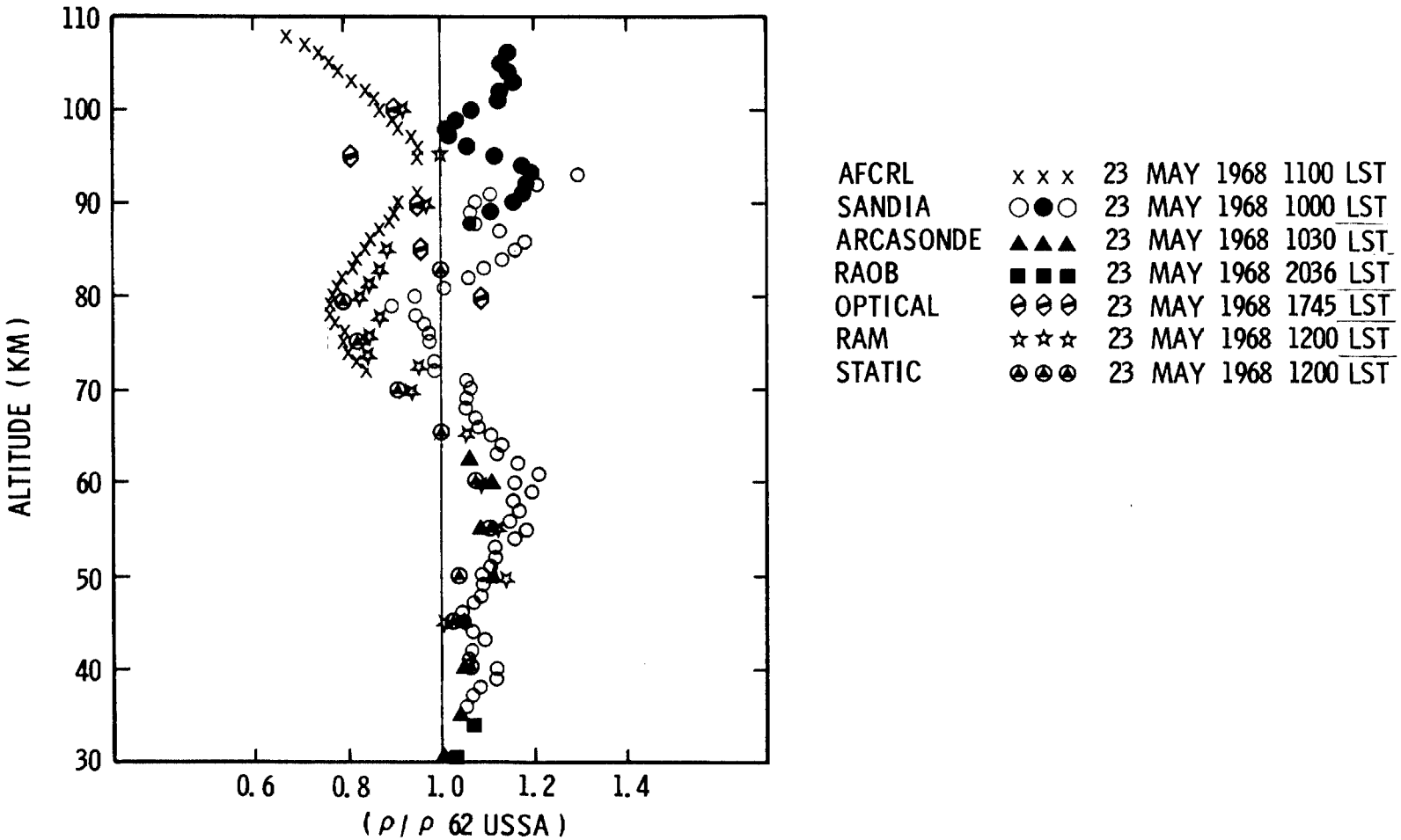

Figure 2.- Atmospheric density measurements on May 23, 1968, at Kauai. (See text for brief description of the measurement techniques listed.)

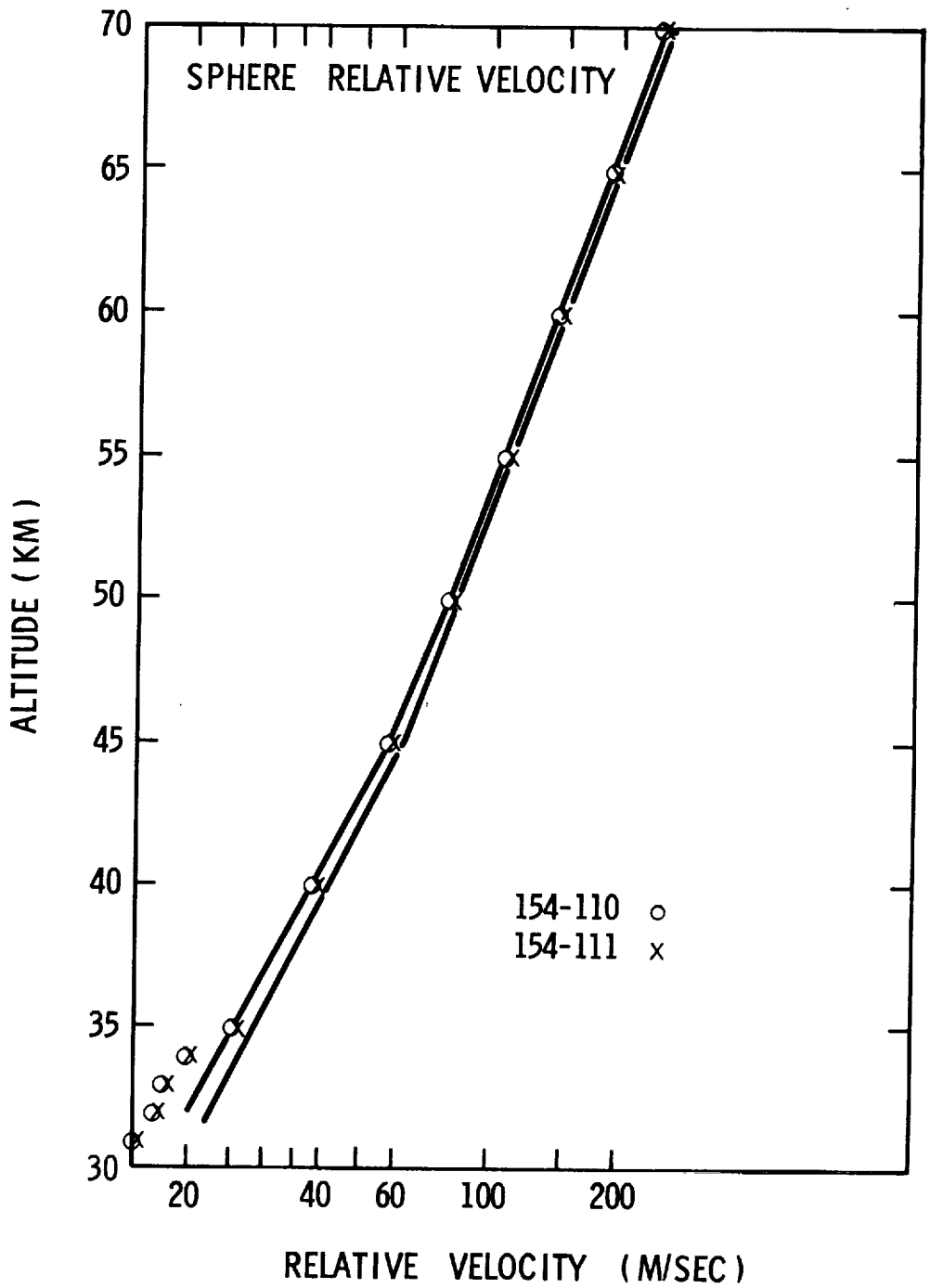

Figure 3.- Fall rate data from passive sphere experiments on May 17, 1968. (The two parallel segmented straight lines include the mean and ± one standard deviation of the fall rates from 12 previous sphere flights.)

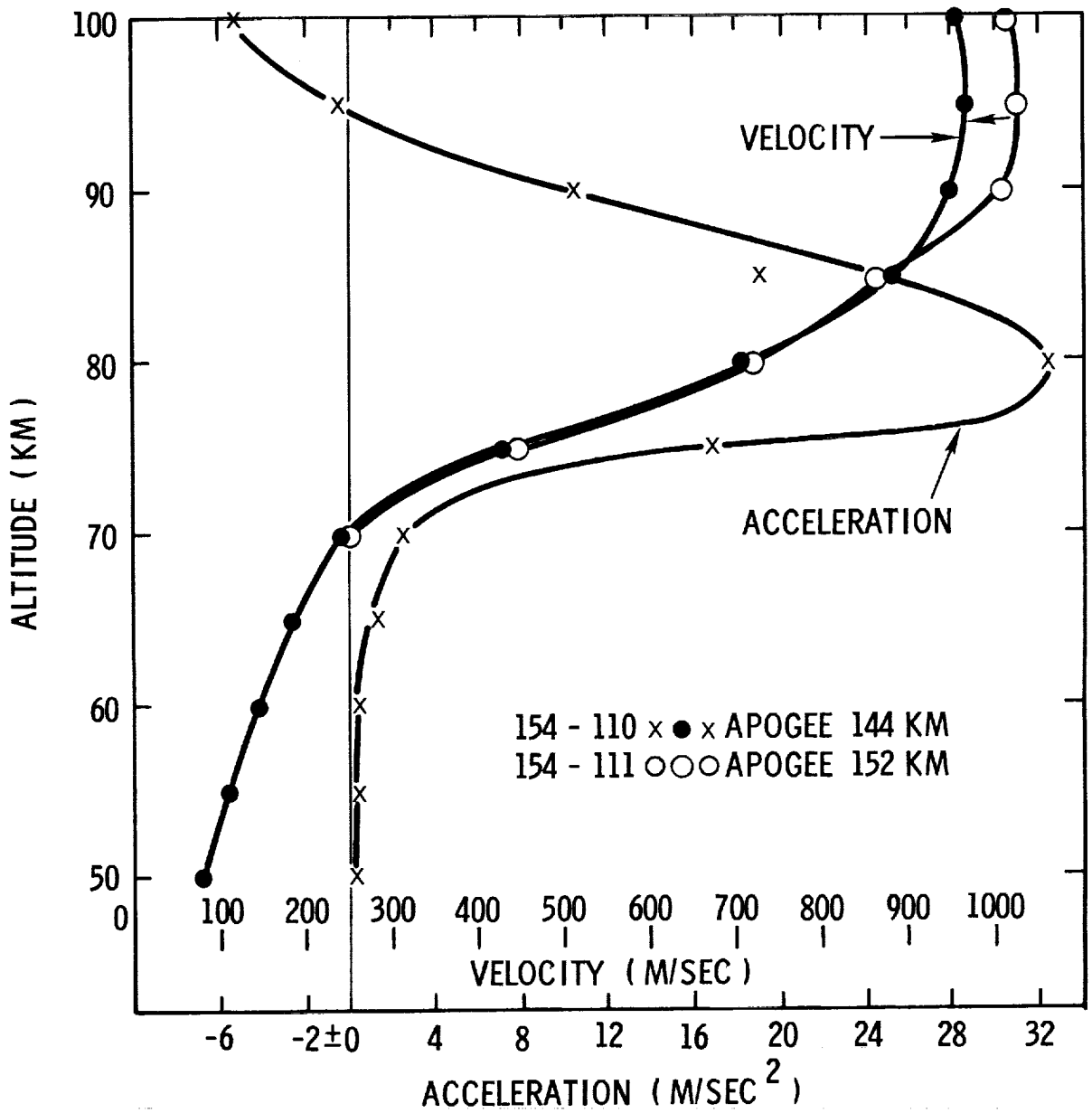

Figure 4.- Acceleration and velocity curves for two spheres released at 144 and 152 km over Kauai in May 1968.

RESULTS FROM SEVERAL EXPERIMENTS AT WHITE SANDS MISSILE RANGE AIMED AT ASSESSMENT OF FALLING-SPHERE DENSITY DATA

By Robert Olsen
Atmospheric Sciences Laboratory
U.S. Army Electronics Command
White Sands Missile Range, New Mexico

SUMMARY

Density measurements utilizing inflatable passive falling spheres were made at White Sands Missile Range. Two different rocket vehicle systems, the Viper balloon dart system and the Super Loki balloon dart system, were used to deploy the sphere at apogee to demonstrate the capabilities of each of these systems in providing high-altitude data. Five sets of density data computed from a total of fourteen flights were compared with density data derived from rocketsonde soundings and the 1966 Standard Atmosphere. A negative density departure from the 1966 Standard Atmosphere was shown to exist between 70 and 80 km. Two sets of density data were derived from each flight, with the exception of the first flight, one utilizing the Sandia drag table the other the University of Minnesota drag table. The difference between the density values using the two tables can be as great as 12%. Density data computed from these flights were compared with density data derived from rocketsonde soundings and the 1966 Standard Atmosphere. These comparisons indicate varying agreement; however, no conclusions can be made because of the limited number of comparisons. One flight compared density differences derived from the radar tracks of two FPS-16 radars tracking the same sphere. These differences were within $\pm$ 1% throughout the vertical profile. Some of the problems encountered in acquiring density data from approximately 40 to 100 km and some of the areas in which the sphere data may be questionable are discussed.

14

INTRODUCTION

The Atmospheric Sciences Laboratory at White Sands Missile Range provides upper atmospheric data to Range Projects. In support of these missions, surface observations, radiosonde releases, and rocketsonde launches are made to provide a vertical profile of the atmosphere from the surface to 65 km.

Recently, several of these programs, particularly those involved in reentry studies, have specified a requirement for density data up to 100 km. This increased altitude is beyond the capabilities of the usual low cost operational sensors and vehicles; thus, a different technique or method must be developed to meet the new requirements.

The system which demonstrated the most promise as a density measuring tool at altitudes above 65 km is the passive falling sphere being developed by the Air Force Cambridge Research Laboratory (ref. 1). Its advantages as an operational system for use at a missile range are low cost relative to other density measuring systems, basic operational simplicity, and tracking by AN/FPS-16 radars, which are the radars utilized at missile ranges. Two different rocket vehicle systems were available, the Viper and Super Loki (ref. 2) which can deliver the inflatable 1/2-mil Mylar sphere to apogees in excess of 125 km at White Sands Missile Range. The apogee performance of these rocket vehicles is aided by the higher launch elevation of approximately 1200 meters mean sea level (MSL) at the Range. This performance satisfies the apogee altitude of approximately 125 km required to derive density data from 40 to approximately 100 km.

Plans were made to flight test both configurations and establish the upper limits of density data that could be derived from both systems. The advantage in utilizing the smaller Super Loki rocket motor rather than the larger Viper rocket motor was lower cost. It was believed that the Super Loki system could be used when there was no stringent requirement for density data to 100 km, and data between 90 and 95 km would suffice.

Nine Viper and five Super Loki balloon dart systems were employed in determining the operational characteristics and density measuring capabilities of these systems. Two computer programs were provided by the University of Dayton Research Institute (ref. 3) through the U. S. Air Force Cambridge Research Laboratory. The first program contained the drag values derived at the University of Minnesota hereafter termed the Minnesota drag table (ref. 4), a second program contained the sphere drag values from the Tullahoma ballistic range hereafter termed Sandia drag table (ref. 5). It was necessary to derive densities using both programs since there was a difference in the drag coefficients reported by the two investigations resulting in differences in derived densities using the same input data.

FLIGHT TEST PROGRAM

For comparison purposes, each sphere launch (table I), except the second Super Loki and second Viper, was made with a supporting rocketsonde. In most cases, two FPS-16 radars were used with each launch to determine whether radars tracking the same falling sphere would yield similar results. Comparisons were also made between two sphere flights when the time lag between launches did not exceed 48 hours. In all cases when density data were derived, a comparison was made with the seasonal 1966 Standard Atmosphere. These comparisons were made with both sets of drag values, those derived from the Minnesota drag table and those derived from the Sandia drag tables.

Each of the launches from which density data were collected is discussed, beginning with the Viper launches, and following with the Super Loki launches.

Viper 1 was launched 14 January 1969, at 1205 hours MST, followed by a rocketsonde launch at 1310 MST. Two FPS-16 radars were used to track the sphere; however, good radar track data were received from only one of the radars, and one set of density data was derived by using the Minnesota drag table. These data were compared with the 1966 Standard Atmosphere, January 30°N, a mean wintertime density profile derived from eight rigid falling spheres (ref. 6) and the rocketsonde densities (fig. 1). The dominant features exhibited by this sounding when compared with the 1966 Standard Atmosphere are the positive density departures at approximately 90 and 58 km and the negative departure in the 74 km region. This type of oscillatory pattern has been noted by other researchers both in theory and empirical data (ref. 7) and could be attributed to the diurnal effects of the upper atmosphere, or to the data from the Standard Atmosphere. Upon inspection of figure 1 it can be seen that, in the upper portions of the data, the trends or slopes are in agreement, with the positive-to-negative departures crossing near the same altitudes. The sphere data show a large negative departure, whereas the mean density data are negative but to a lesser degree.

The large negative departure between 80 and 70 km may be due to the inaccuracies in the drag coefficient for spheres in the transonic region, since it is very difficult to determine drag values accurately in this region.

The comparison between the sphere and rocketsonde data indicates good agreement from 51 to 48 km, at which point the two sets of data diverge markedly. At approximately 42.5 the sphere collapses and cannot be used to compute densities because it is no longer a sphere. A graph of the density ratio between the sphere and sonde is shown in figure 2, where the density departure becomes as much as 12 percent. This difference becomes somewhat difficult to resolve as the sonde should have an increased accuracy at levels below 50 km. Densities using the program with the Sandia drag tables were not derived because the original data tapes were mistakenly degaussed before this was accomplished.

Viper 2 was launched the following day at 1230 MST, with one FPS-16 radar scheduled to track the falling sphere. The apogee altitude and point of deployment of the inflatable sphere was 147 km. Density data could not be derived at an altitude of 97.5 km, when the resultant accelerations of drag and gravity became greater than -3 m sec^{-2}. At 94 km the first density value was derived because of the limitation of the drag table in the low Reynolds number regime at the higher altitude. After this point, density data were derived to an altitude of 78.5 km, where the radar track data appeared to become erratic down to 66 km. Densities were again able to be computed from 66 to 54 km where the sphere collapsed. Figure 3 is a plot of the density departures derived from the Viper 2 launch and utilizes the Minnesota and Sandia drag tables compared with the 1966 Standard Atmosphere. From 94 to 90 km some variation is shown; from 90 to 80 km, both programs yielded identical results; and below 78 km, data are not available from either program until 66 km, after which point the departure values exceed a density ratio greater than two. The density data throughout the vertical

profile appears questionable because of the high density values, this being particularly true below 66 km. This may have been due to the poor quality of radar data which indicated some type of radar tracking problem between 66 and 78 km.

Although the density data from Viper 2 appear to be questionable, the densities computed by the two different drag tables were compared to determine at what point the derived densities deviated. Figure 4 shows some disagreement at the upper end of the data and then identical results from 90 to 78 km; at 66 km, the two drag tables begin to give different density values, with maximum departures of 12 percent from 58 km to balloon collapse at 54 km.

Flights of Viper 8 and 9 were the next analyzed. These two rounds were launched as part of a special series (ref. 8). This series consisted of nine rocketsonde and two sphere launches over a four-hour period. Viper 8 was launched at 1100 hours Mountain Daylight Time (MDT) on 9 May with a supporting rocketsonde launched at 1300 MDT and Viper 9 was launched the next evening (10 May, 2000 MDT).

The density data from Viper 8 (fig. 5) indicate a negative departure from the 1966 Standard Atmosphere. Two sets of density data were plotted by utilizing the different drag tables. The first density value computed from the Minnesota drag table was at an altitude of 76 km, whereas the first value computed from the Sandia drag table was at 82 km. The differences in altitude of the computed densities are possibly due to the more complete Sandia drag table in the particular flow regime experienced by the sphere which was deployed at a lower altitude (92 km) than normal. When the density departures are compared, it can be seen that from 76 to 72 km, the density departures from the Minnesota data are less negative than those computed from the Sandia data. At 70 km, this trend is reversed and continues downward to 42 km, the difference between the values increasing to 14 percent at 42 km. Figure 6 depicts the density ratio between Minnesota and Sandia drag tables and indicates more clearly the difference in density data derived from each of the tables.

Figure 7 shows the density departure determined from data obtained by two FPS-16 radars tracking the same sphere. The difference in derived densities from both radars does not exceed $\pm$ 1 percent. Figure 8 shows the results of the two sets of density data compared with density data computed from the supporting rocketsonde measurement. The data derived from the Sandia table appear to agree more favorably, although the region from 49 to 44 km exhibits rather large positive departures. The density data using the Minnesota drag values show poorer agreement, the values being less than the rocketsonde measurements throughout the same region of measurement.

Results from the comparison of data from Viper 9 to the 1966 Standard Atmosphere are plotted in figure 9. This profile shows mostly negative departures, the largest departure occurring at 76 km. Figure 10 compares both sets of density data derived from the sphere with the rocketsonde

density data. In this case there is better agreement between the densities derived from the Minnesota drag table, with departures from the sonde data being no greater than 5 percent. As mentioned previously Viper 9 was launched in conjunction with a short-term density variability study. The results of this investigation indicated the average density difference in a vertical layer from 58 to 40 km to be 4 percent over a four-hour period, and the variability between two rocketsondes fired almost simultaneously was less than 1 percent. Therefore, a conclusion may be drawn that the variability due to the instrumentation is small and the density varied approximately 3 percent; however, the variation between the density data derived utilizing the Sandia drag and the rocketsonde densities at the same altitudes is from a minimum of approximately 5 percent to a maximum of 13 percent. Figure 11 provides a comparison of the variation between the day and night soundings, the two systems being compared with each other. The sonde data indicate that daytime densities were greater than nighttime densities, whereas the sphere data show a negative departure at 58 km and then a positive departure at 60 km. The sonde data agree with a previous study made at the White Sands Missile Range which indicated the maximum densities at these altitudes to occur during the daytime (ref. 9).

The set of densities from Super Loki 2 was compared to the seasonal 1966 Standard Atmosphere and the mean densities from the rigid sphere with the results plotted on figure 12. Density values were derived beginning at 91 km because above this altitude the Reynolds numbers were too low. Both sets of density data are plotted and are the same down to 72 km, at which point the two sets begin to deviate. There is a large negative departure throughout most of the profile, the maximum departure being at 74 km.

DISCUSSION

The results from the flights of the Viper and Super Loki balloon dart systems at White Sands Missile Range have demonstrated a capability of increasing the heights of atmospheric measurements from 40 km to an altitude between 90 and 100 km. The available density data from the flights, except that of Viper 2, appear to have reasonable values when compared with the Standard Atmosphere. There are some areas in which additional investigation should be made to improve the density measurements. The amount of density data derived from these flights was small, but this condition was due to several factors which can be minimized in the future.

Of the fourteen sphere launches, nine utilized the Viper system and five, the Super Loki system. Four of the Viper systems achieved a dart apogee of under 60 km; this low performance resulted from a mechanical problem which caused poor dart separation. Once this problem was rectified, the remaining vehicles performed satisfactorily. For each of the Viper launches, two FPS-16 radars were scheduled to track the vehicle. This step was found to be absolutely necessary because in the five Viper launches that reached the required altitude, only one launch received good radar track from the assigned FPS-16 radars. In three of the launches, one good

radar track was received from the two radars, and in the case of Viper 6, both radars lost track near apogee and did not reacquire the sphere until it was down to an altitude of 38 km. It is believed that the problem of radars losing a track on the dart can be reduced once the radar personnel become familiar with the performance of the Viper system.

A similar radar problem was encountered with the Super Loki and perhaps intensified since the acceleration of this dart vehicle is the same as that of the Viper but the radar cross-sectional area of the dart is smaller. The radars were able to track only one of the five Super Loki flights successfully. On the first flight, the target was lost by the radars at 69 km and was not reacquired until it was at about 44 km. On the second flight, a good radar track was obtained with one of two FPS-16 radars scheduled to support this flight. The vehicle achieved an apogee of 129 km, and density data were derived from 91 to 58 km; thus, the Super Loki system proved to be capable of collecting high-altitude density data. On the next flight, the radars did not acquire the target, and on the two remaining flights, the radars acquired the spheres below 60 km. Although these initial results were not completely satisfactory, it is believed that they can be vastly improved with experience.

One of the problems exhibited by the sphere itself was the variation in altitude at which the sphere collapsed; this collapse occurred anywhere between 58 and 42.5 km.

Density values could not be computed at altitudes above 94 km even though the resultant acceleration was greater than -3 m sec^{-2} because no drag numbers were available at Reynolds numbers below 150. This situation proved to be the case with Viper 2 and 9 where the spheres were deployed at approximately 147 and 146 km. The same condition occurred with the Super Loki launch where the sphere was deployed at 129 km, and densities were not computed until the sphere reached an altitude of 91 km.

When the densities derived from the two drag tables were compared, there was no difference above 72 km. From that altitude downward, the differences became greater with an average difference of 12 percent between 40 and 50 km. In most cases, the sphere had collapsed at altitudes above 40 km, but the data could still be used to indicate the difference in densities due to use of the two different drag tables although the absolute density values were incorrect after the sphere collapsed.

One of the dominant characteristics of the sphere density data as compared with the 1966 Standard Atmosphere is the negative density departure between 70 and 80 km. This particular characteristic may be due to the error in determining the drag coefficient under transonic flow conditions.

The agreement was generally unsatisfactory when a comparison was made between the sphere densities derived from the two different drag tables and from the rocketsonde. The Sandia values were a little better for one sounding than those derived from the Minnesota drag table; for the other sounding, the opposite was true.

The lack of agreement in the overlap region could be attributed to errors associated with both systems. In the case of the sphere system, there might be some disagreement due to incorrect drag numbers, not precise enough radar data or some other factor associated with computing densities from passive falling spheres. The rocketsonde could also contribute errors to the density due to temperature and height differences in the rocket and radiosonde soundings or to errors in the observed thermistor temperature (ref. 10). In a recent investigation, M. Kays and P. Avara found that a height difference of 300 meters could bias the density at the upper levels by 4 percent, while a temperature error of 2°C could result in an error of less than 1/2 percent.

These results are preliminary, and additional launchings would be required to determine the overall performance characteristics of this system. Since these are required data, effort should be put into this program which provides density measurements between 100 and 65 km.

CONCLUDING REMARKS

Some specific areas which require further research are discussed below.

Discrepancies in the density measurements between the falling-sphere and rocketsonde techniques should be investigated. Careful consideration should be given to the accurate determination of the radiosonde height for tie on to rocketsonde by a radar track to eliminate possible bias error in the computed density data. Another possible method of circumventing the problem of errors in computing densities at rocketsonde altitudes is to incorporate a pressure sensor into the rocketsonde. This would eliminate the requirement of a radiosonde pressure measurement for computing densities.

The drag curves from the wind tunnel and ballistic ranges should be studied to determine their validity experimentally. This might be accomplished by varying the ballistic coefficient and deployment altitude of several spheres. These spheres would be deployed almost simultaneously in approximately the same space so that each sphere would experience essentially the same atmosphere. The spheres would be at different Mach and Reynolds numbers at a given altitude, but each sphere should yield similar density values at the same altitudes. Another method of testing the drag curves would be to compare the density derived from the spheres and the rocketsonde and use this overlap region to check other portions of the curve. For example, the present sphere is transonic at an altitude between 70 and 80 km; it might be advantageous to have the sphere become transonic at a level at which density data are available from the rocketsonde. This would enable the drag data to be checked against some other measurement, and possibly an empirical determination could be made of some of the drag values. If this cannot be accomplished, at least it could point to certain areas in the drag curves which might require additional work.

The sphere itself might be more closely examined to determine its sphericity.

More drag data should be made available at the lower Reynolds numbers to compute density data to 100 km.

A study should be made to determine which sphere drag coefficients are valid in the subsonic regime, those values measured by Sandia Corp. or those by the University of Minnesota.

Most important comparison flights with other systems and techniques should be made. This would include such systems as the active falling sphere, Pitot probe, grenades and other systems capable of making high-altitude density measurements. A measurement program of this type could aid in determining the validity of the density measurement and could also point out possible areas where the measuring techniques of the various systems might be improved.

REFERENCES

1. Bollerman, Bruce; and Walker, Robert L.: Design, Development and Flight Test of the Viper Dart Robin Meteorological Rocket System. AFCRL-68-0418, U.S. Air Force, June 30, 1968. (Available from DDC as AD675608.)

2. Bollerman, Bruce; and Walker, Robert L.: Super Loki Dart Meteorological Rocket System (Final Report). NASA CR-61238, 1968.

3. Engler, Nicholas A.: Development of Methods To Determine Winds, Density, Pressure, and Temperature From the Robin Falling Balloon. AFCRL-65-448, U.S. Air Force, May 1965. (Available from DDC as AD630200.)

4. Heinrich, H. G.; Niccum, R. J.; Haak, E. L.; Jamison, I. R.; and George, R. L.: Modification of the Robin Meteorological Balloon. Volume II - Drag Evaluations. AFCRL-65-734(II), U.S. Air Force, Sept. 30, 1965. (Available from DDC as AD629775.)

5. Goin, Kenneth L.; and Lawrence, W. R.: Subsonic Drag of Spheres at Reynolds Numbers From 200 to 10,000. AIAA J. (Tech. Notes), vol. 6, no. 5, May 1968, pp. 961-962.

6. Olsen, R.; Thiele, O.; and Faire, A.: Seasonal and Diurnal Variability from 30 to 110 km Above White Sands Missile Range. Presented at AMS Conf. on Composition and Dynamics of the Upper Atmosphere, El Paso, Tex., November 1968.

7. Theon, J. S.; Nordberg, W.; and Katchen, L.: Some Observations on the Thermal Behavior of the Mesosphere. JAS vol. 24, July 1967, pp. 428-438.

8. Miers, B.; and Olsen, R.: Short Term Density Variations Above White Sands Missile Range. ECOM 5275, U.S. Army Electronics Command, White Sands Missile Range, New Mexico, 1969.

9. Thiele, Otto W.: Observed Diurnal Oscillations of Pressure and Density in the Upper Stratosphere and Lower Mesosphere. ECOM 5047, U.S. Army Electronics Command, White Sands Missile Range, New Mexico, 1966. (Available from DDC as AD634884.)

10. Ballard, H.; and Rubio, R.: Corrections to the Observed Rocketsonde and Radiosonde Temperatures. J. Applied Meteor. Volume 7, 1968, pp. 919-928.

TABLE I

SUMMARY OF LAUNCH DATA

Flight	Date	Launch time, hr	Radars	Apogee altitude, km	Altitude of sphere collapse	Density data, km	Remarks
Viper 1	14 Jan 69	1205	2 FPS-16	147	42.5	94 to 42.5	Good flight
Viper 2	15 Jan 69	1230	1 FPS-16	147	54.0	Data questionable	Good flight
Viper 3	19 Mar 69	1200	2 FPS-16	51	Undetermined	None	Poor dart separation
Viper 4	20 Apr 69	2000	2 FPS-16	43	Undetermined	None	Poor dart separation
Viper 5	25 Apr 69	0930	2 FPS-16	46	Undetermined	None	Poor dart separation
Viper 6	27 Apr 69	2219	2 FPS-16	146 (est.)	Undetermined	None	Radars lost track at 110 sec at 118 km
Viper 7	28 Apr 69	0007	2 FPS-16	18	Undetermined	None	No dart separation
Viper 8	9 May 69	1100	2 FPS-16	94	42.5	83 to 82.5	Low dart apogee
Viper 9	10 May 69	2000	2 FPS-16	145	55.5	92 to 55.5	Good flight
Super Loki 1	24 Jan 69	2000	2 FPS-16	126 (est.)	Undetermined	None	Radars lost track at 55 sec at 69 km
Super Loki 2	27 Jan 69	1500	2 FPS-16	127	58.5	92 to 58.5	Good flight
Super Loki 3	19 Feb 69	1230	1 FPS-16	Unknown	Undetermined	None	No radar acquisition
Super Loki 4	20 Apr 69	2115	2 FPS-16	Unknown	Undetermined	None	No radar acquisition
Super Loki 5	11 May 69	0100	2 FPS-16	126 (est.)	50.0	56 to 50.0	Late radar acquisition at 34.5 sec at 58 km

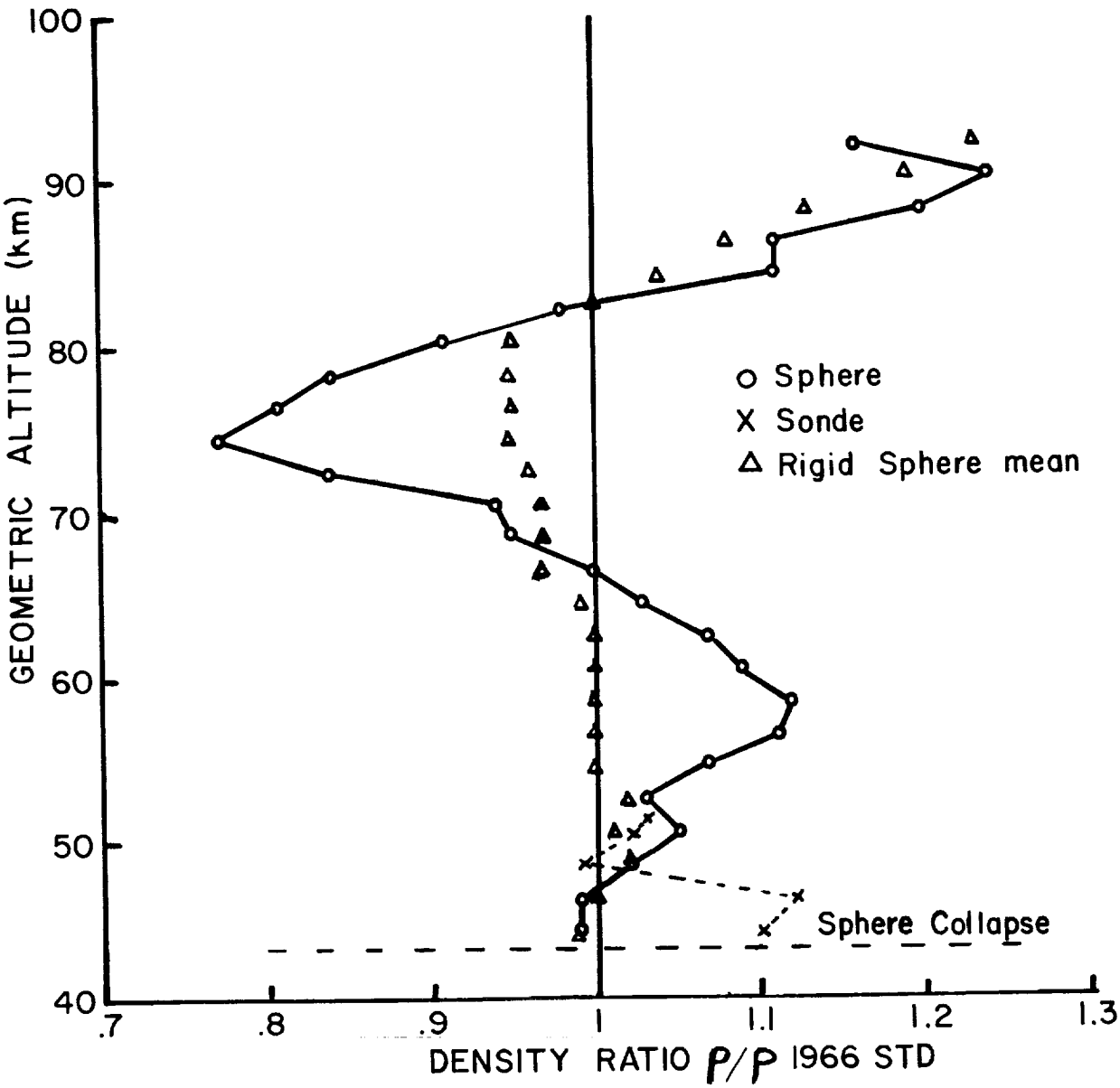

Figure 1.- Viper 1, 14 Jan 1969, Density Departures from 1966 Standard Atmosphere, January, 30°N.

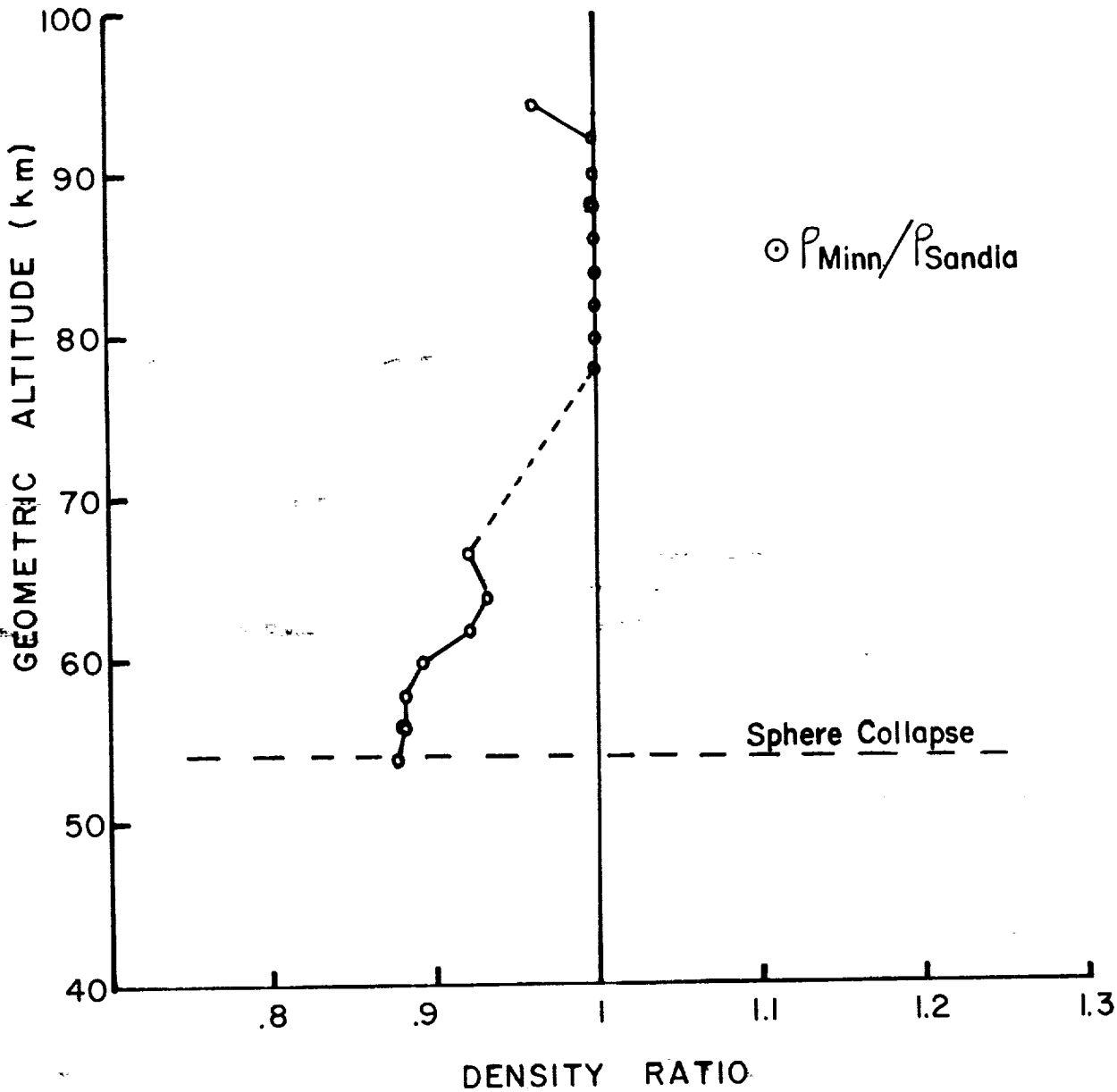

Figure 4.- Viper 2, Comparison of Densities Using Different Drag Tables.

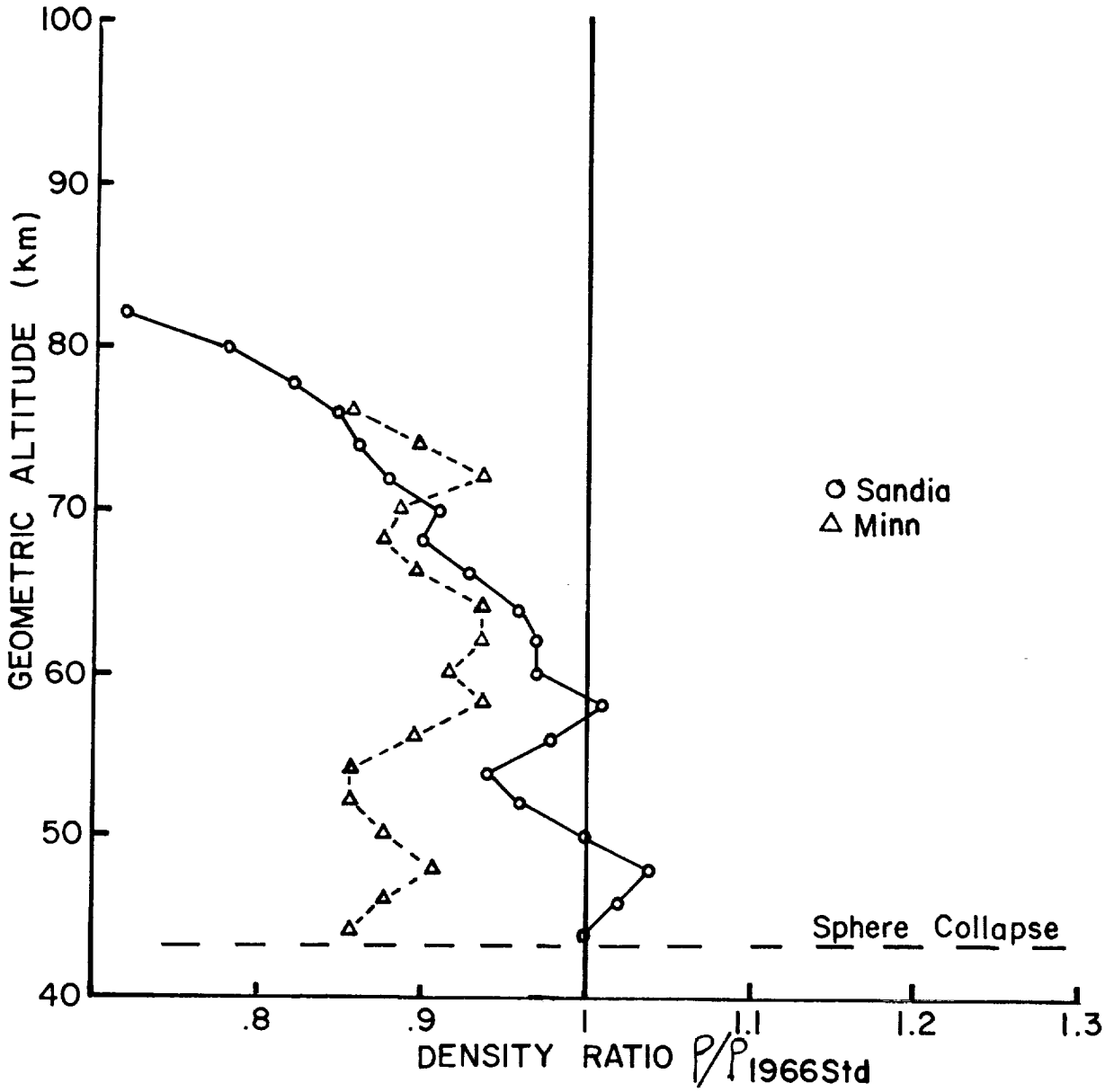

Figure 5.- Viper 8, 9 May 1969, Density Departures from 1966 Standard Atmosphere, July, 30°N.

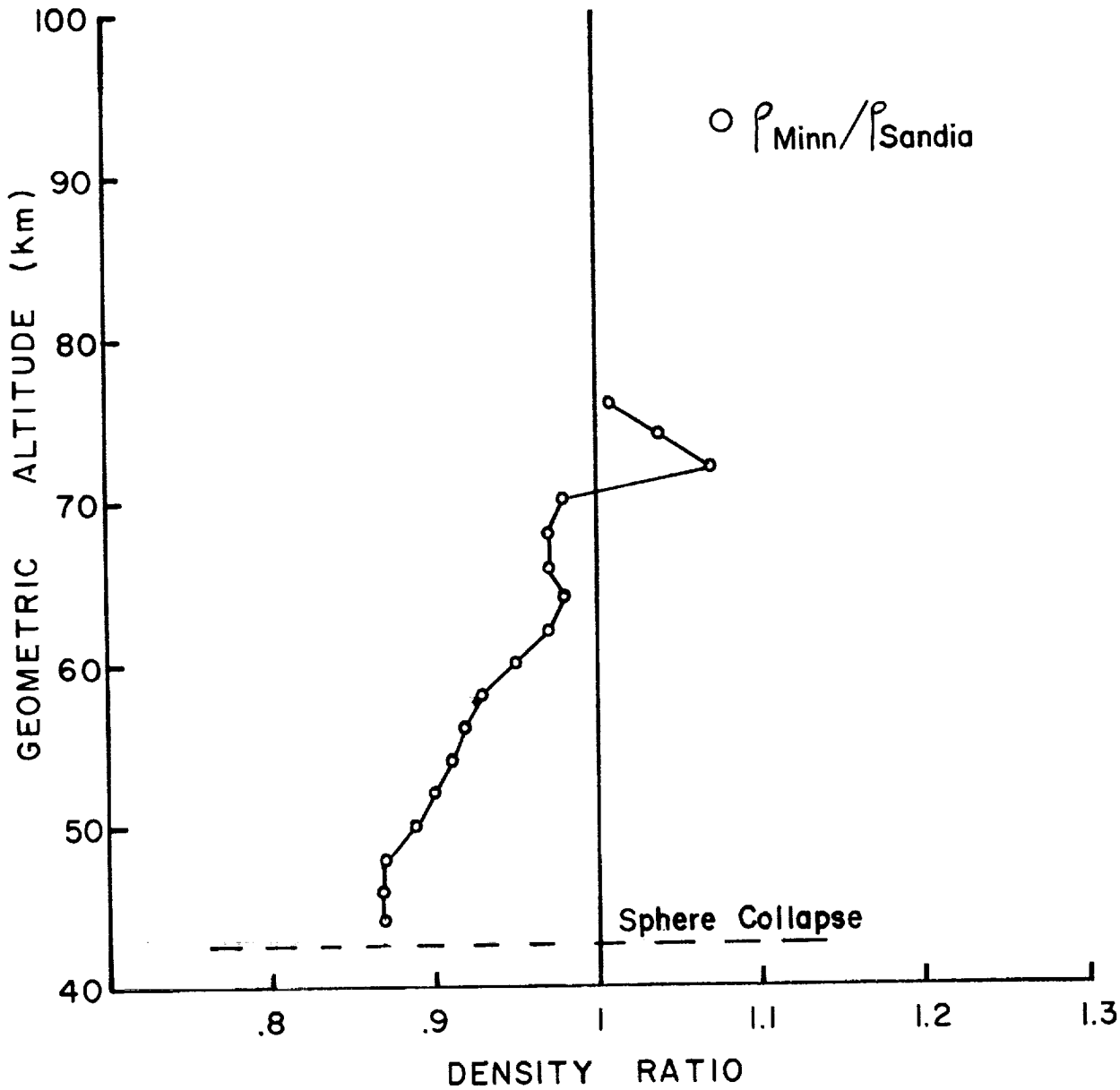

Figure 6.- Viper 8, Comparison of Densities Using Different Drag Tables.

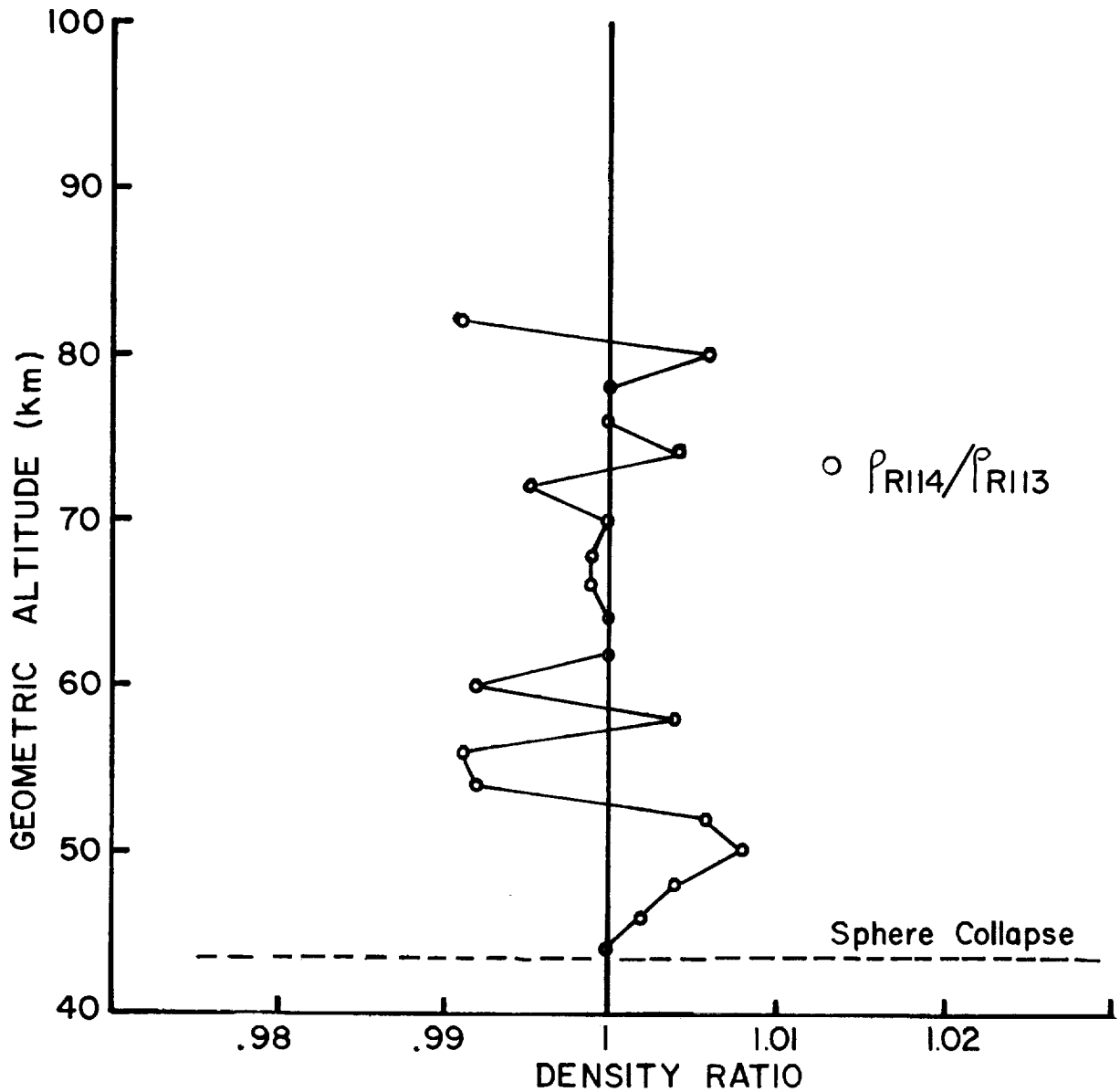

Figure 7.- Density Ratio Between 2 FPS-16 Radars Tracking the Same Sphere.

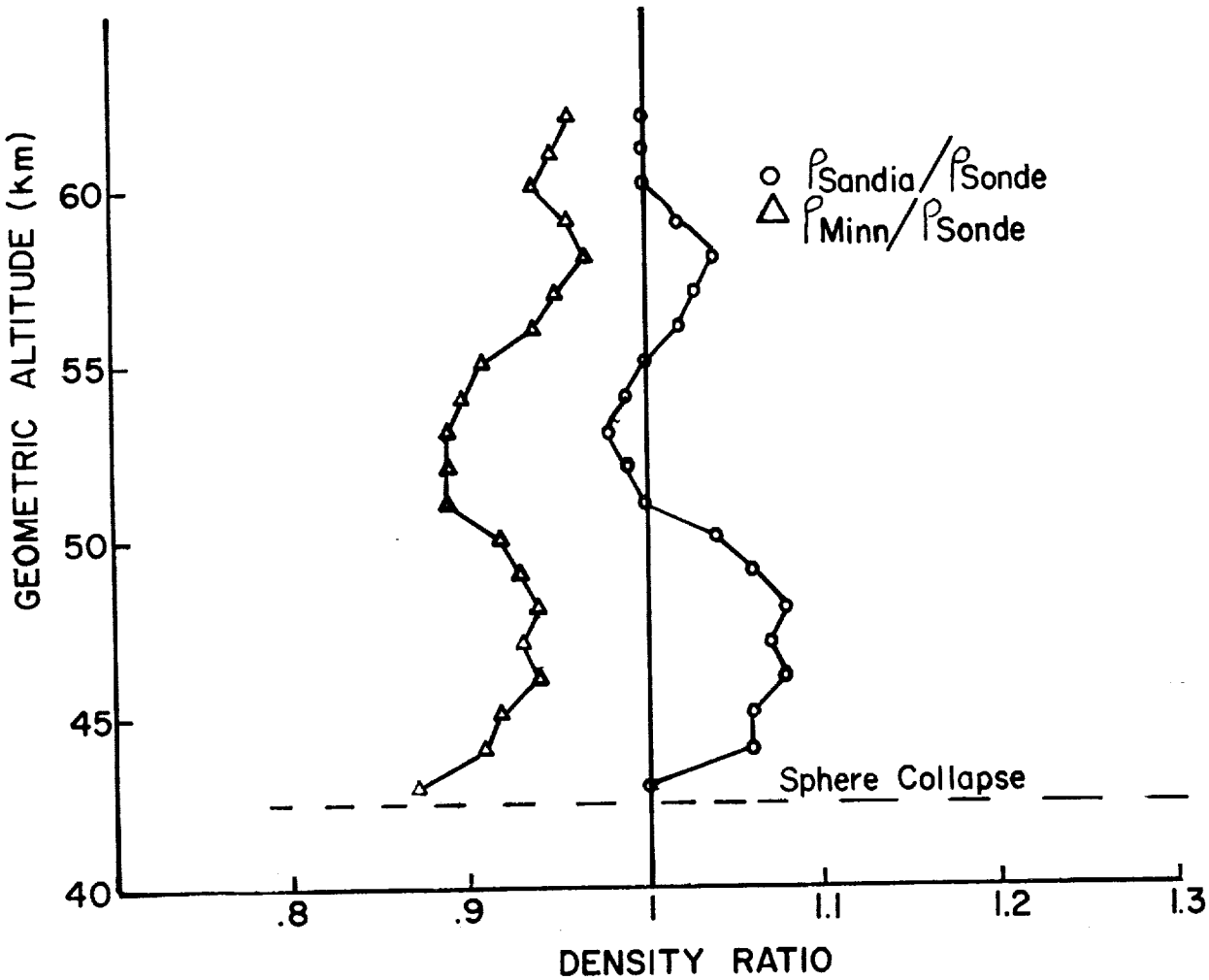

Figure 8.- Viper 8, Comparison of Density Between Sphere and Rocketsonde.

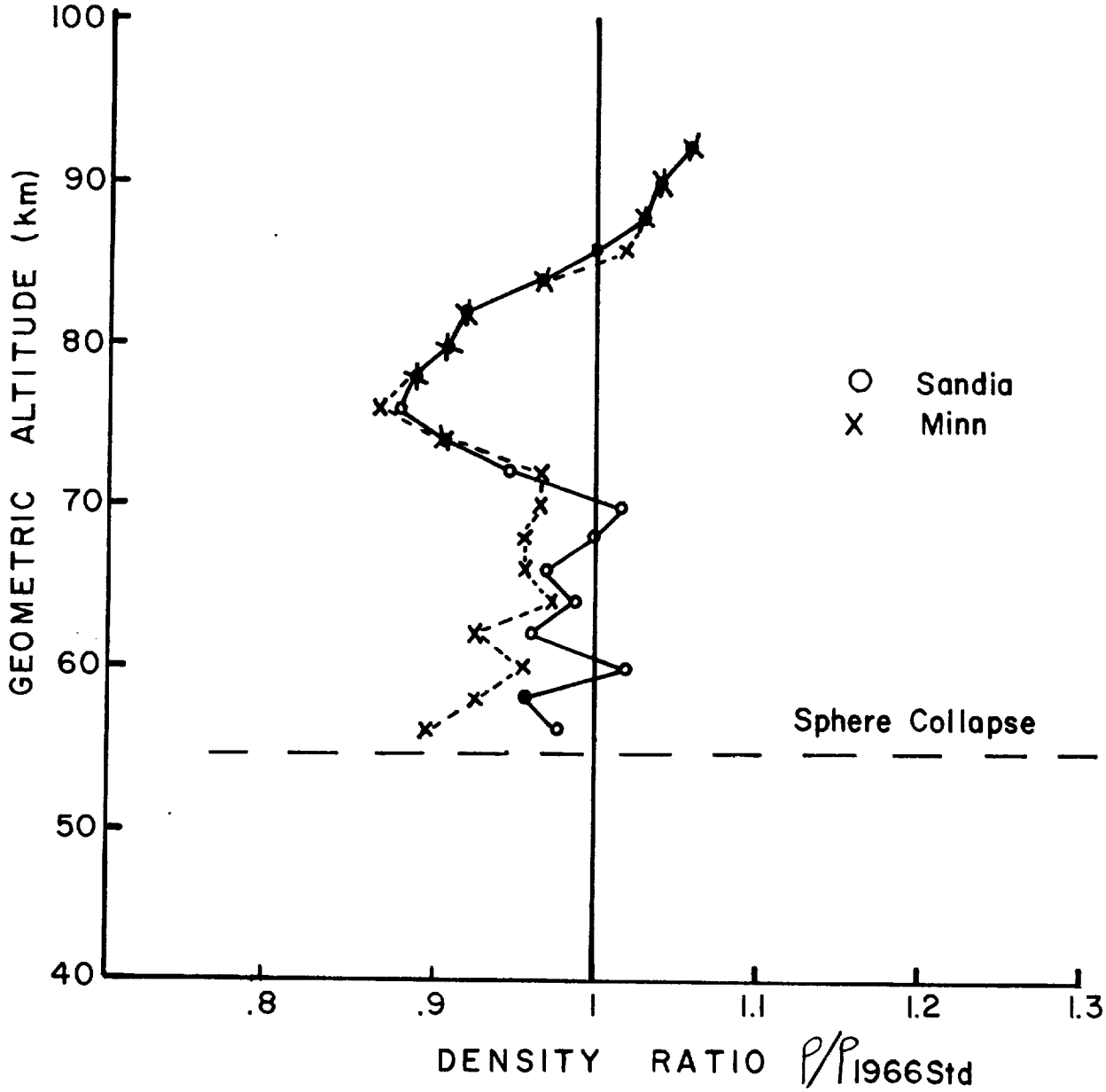

Figure 9.- Viper 9, 10 May 1969, Density Departures from 1966 Standard Atmosphere, July, 30°N.

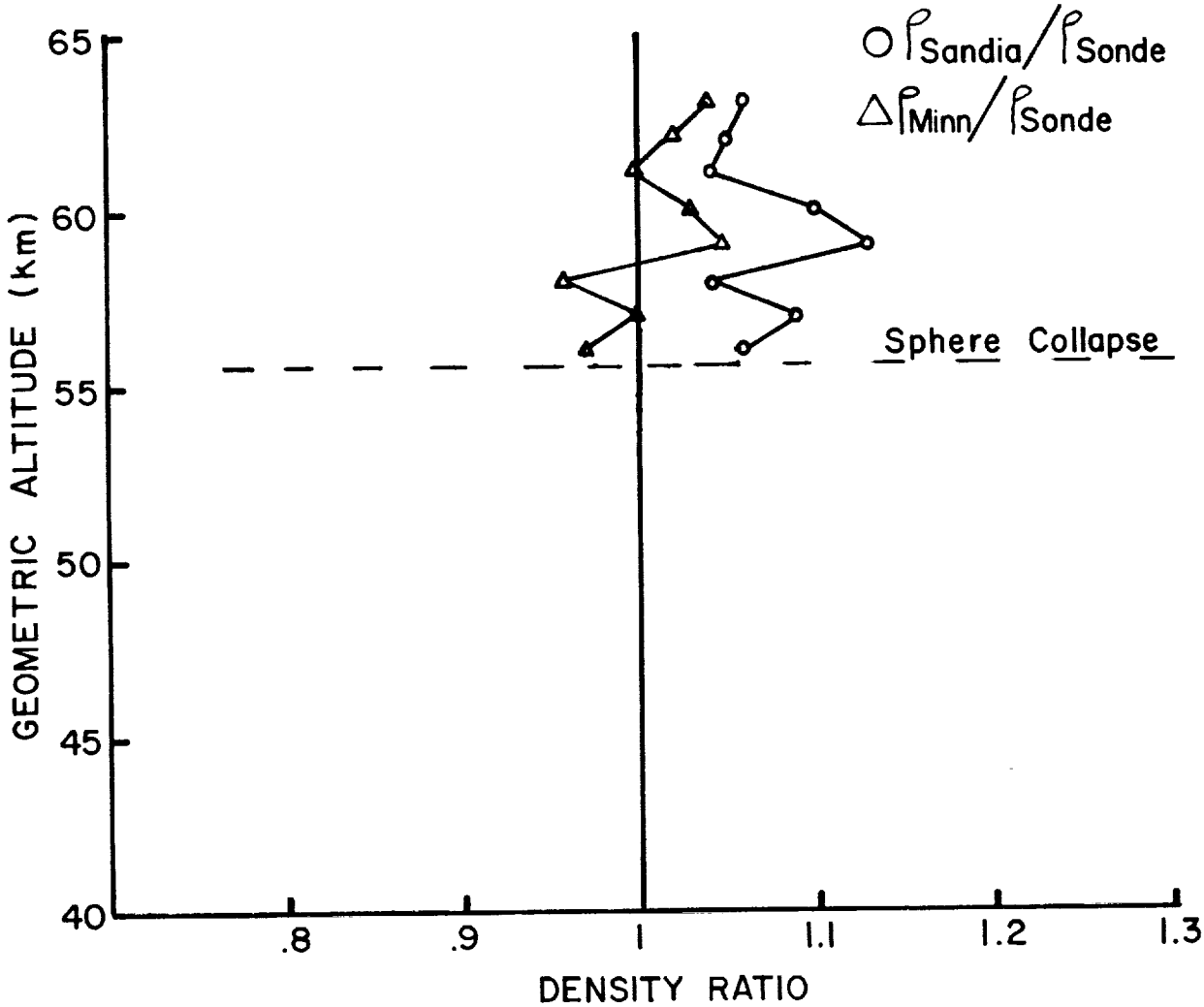

Figure 10.- Viper 9, Comparison of Densities Between Sphere and Rocketsonde.

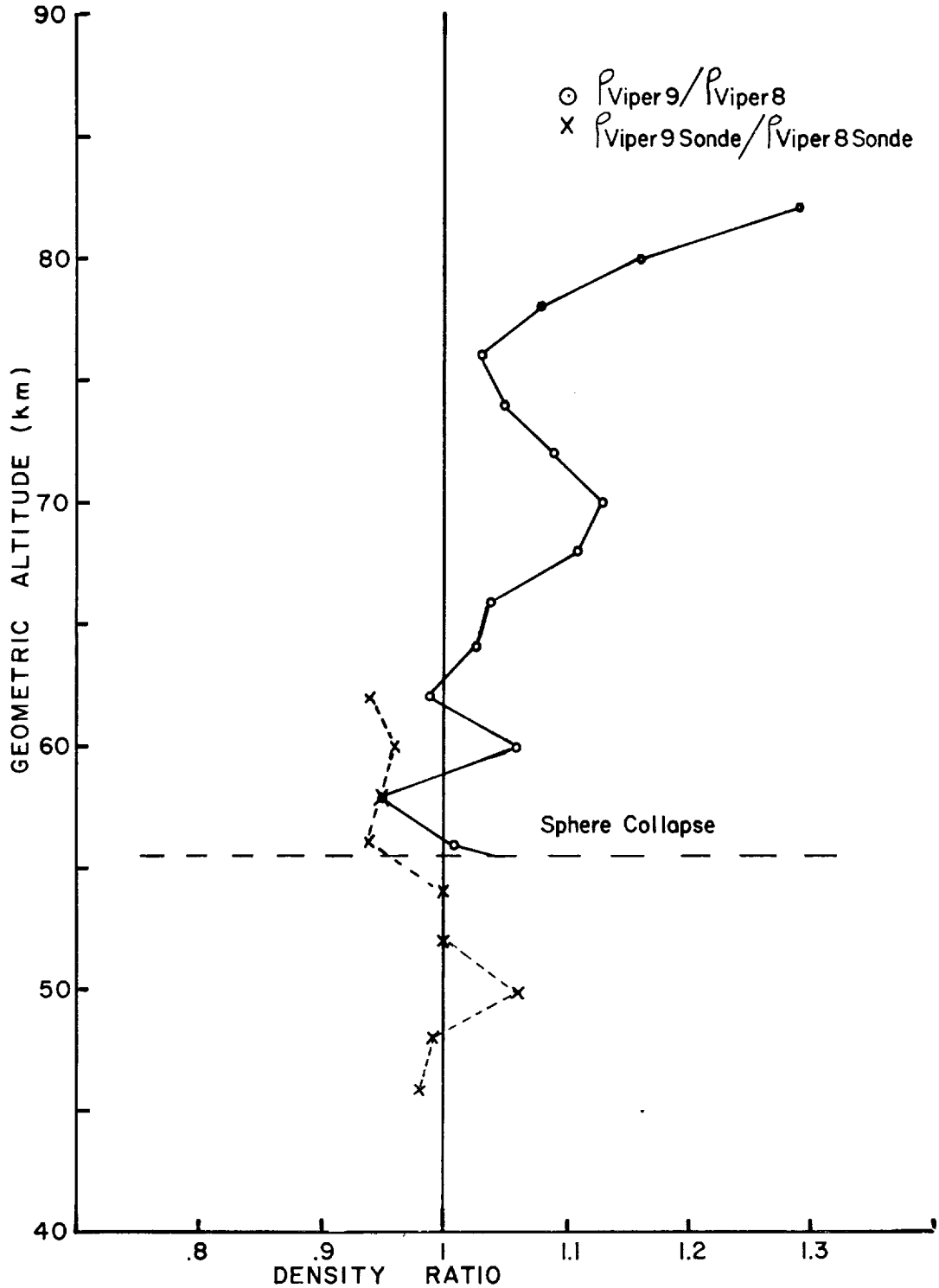

Figure 11.- Comparison of Day and Night Density Soundings.

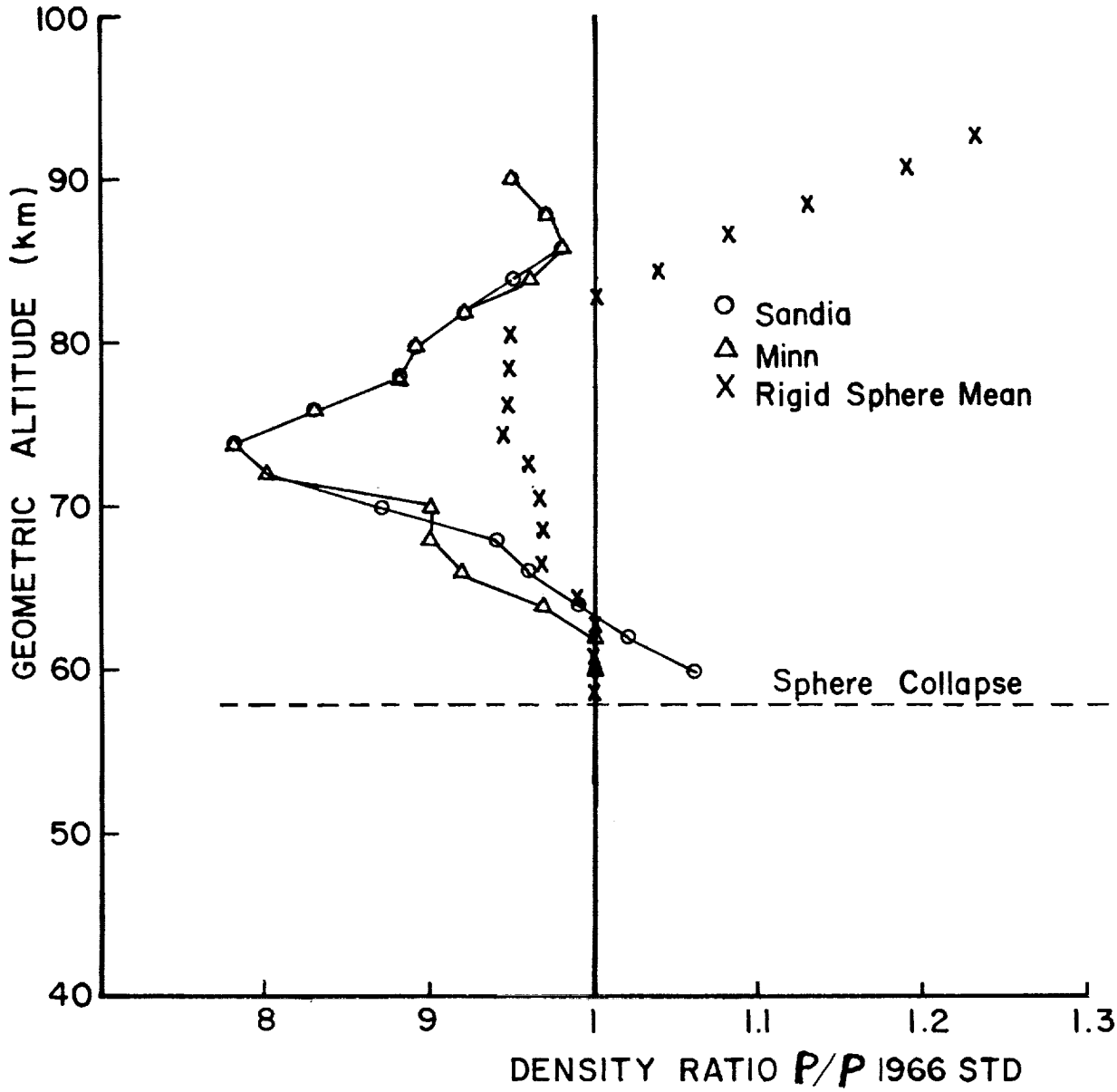

Figure 12.- Super Loki 2, 27 Jan 1969, Density Departures from 1966 Standard Atmosphere, January, 30°N.

METEOROLOGICAL DATA FROM FALLING SPHERE TECHNIQUE COMPARED WITH DATA FROM OTHER SOUNDING METHODS

By Wendell S. Smith

NASA Goddard Space Flight Center

SUMMARY

The objective of the Goddard Space Flight Center's Meteorological Sounding Rocket Program is the launch and operation of sounding rocket experiments for making synoptic global measurements of the physical parameters of the atmosphere between 60 and 150 km and to relate the measurements to those obtained from experiments conducted directly above and below this region. In the pursuit of this objective, approximately 50 soundings per year are made of the stratosphere, mesosphere and lower thermosphere utilizing primarily rocket grenade and pitot-tube experiments. It has been recognized that the falling sphere technique offers some potential advantage over these other techniques in terms of economy and operational flexibility provided that the basic accuracy of the sphere technique can be established and maintained. Opportunities to obtain comparative data have been sought, most recently utilizing a sphere which is deployed from a pod mounted to the tail-fin assembly of a Nike Cajun or Nike Apache rocket carrying either a grenade or pitot-tube experiment. The experiments conducted thus far indicate an average density difference of 3 percent above 70 km where the fall rate of the sphere is supersonic and 8 percent below 70 km where the fall rate is subsonic. The difference above 70 km would appear to be largely random (though the sample is smaller) while below 70 km the sphere yields results which are consistently closer to the standard atmosphere than the results of either the grenade or the pitot-tube experiments.

INTRODUCTION

The potential advantages of the falling sphere experiment over other techniques for mesospheric and lower thermospheric soundings have been recognized for many years. The sensor cost is small when compared with payload instrumentation required to conduct grenade or pitot-tube experiments. The small volume and weight required permit the consideration of a less expensive rocket delivery system. The simplicity of the airborne portion of the system would mean an inherently reliable system. In spite of these potential advantages, the sphere system has not been widely incorporated as a tool in NASA's research program owing largely to the fact that we have not yet developed confidence in the accuracy or the repeatability of the sphere experiment. For the past decade,

we have attempted to obtain comparative data either through the nearly simultaneous launch of sphere and other payloads, through the deployment of spheres from grenade payloads, or most recently through the use of a "strap-on" sphere pod which is positioned on the tail-fin assembly of a rocket carrying another experiment. The results of the earlier work have been reported by Jones and Peterson (ref. 1).

The "strap-on" version of the sphere experiment is an inflatable, 26-inch-diameter mylar sphere. It is carried aloft on a Nike Cajun or Nike Apache rocket and, during the ascent portion of the flight, is housed in a cylindrical pod which is about $1\frac{3}{4}$ inches in diameter and about $23\frac{1}{2}$ inches long. The mounting arrangement is shown in figure 1. Each pod (two are required to balance the aerodynamic drag) is capable of housing a sphere, an ejection system, a timer, and a power supply. Thus the entire sphere experiment is self-contained, requiring no connections to the payload. The increased aerodynamic drag and weight of the pods degrade the rocket performance by about 10 to 15 percent. Upon reaching the desired time during the flight, the black powder charge in the ejection system is fired and the sphere is expelled rearward out of the pod. The acceleration of the sphere causes the puncture of a small isopentane capsule that releases the gas required to fully inflate the sphere. The radar systems, which up to this point in the flight have been tracking the rocket, are then switched to track the sphere.

During 1968 inflatable spheres were successfully deployed from three rockets carrying grenade experiments, and from one rocket carrying a pitot-tube experiment. The falling sphere experiments and the pitot-tube experiments were performed by the High Altitude Engineering Laboratory and the Space Physics Laboratory, respectively, of the University of Michigan under contract with GSFC. These combined experiments (one in February, two in July and one in November) were conducted from Wallops Island and utilized either FPS-16 and/or FPQ-6 radar systems in order to track the spheres. In each case the grenade or pitot-tube experiment was conducted on the upleg of the trajectory and the sphere experiment primarily on the downleg of the trajectory. Thus, the time elapsed between the sphere and other measurements is reduced to a few minutes (on the order of 3 minutes at 100 km, lengthening to about 15 minutes at 30 km). Heretofore, the temporal variation in the atmospheric parameters, in all but a few cases, has been an uncertain factor in comparisons of two or more techniques.

RESULTS

The data from the four comparative rocket-borne experiments of 1968 are presented in figures 2, 3, and 4. Figure 2 contains density (in terms of percent of deviation from the 1962 standard atmosphere) versus altitude information. In the first 3 plots of figure 2 the sphere data are compared with data from rocket grenade experiments, while

in the 4th plot the sphere data are compared with a pitot-tube experiment. If one takes an average of the absolute value of the difference over the entire height range, one finds that the sphere data agree with those from other techniques within about 6 percent. Further, one finds that the two techniques display different characteristics above and below 70 km. Above 70 km, where both the grenade and pitot-tube error functions are increasing slightly with altitude, the difference between the sphere data and those from other techniques is only about 3 percent. Below 70 km, the average difference between the data from the spheres and the other techniques is about 8 percent. Whereas the 3 percent difference above 70 km appears to be largely random in nature, the 8 percent difference below 70 km appears (within the confidence level that can be obtained with 3 samples) to be biased in a consistent manner. That is, the sphere data consistently show less deviation from the standard atmosphere than do those from the other techniques. Presuming that the data from these experiments are not coincidental, an additional examination of the sphere data handling and reduction appears warranted in an attempt to remove the bias in the subsonic regime, as has apparently been done in the supersonic regime above 70 km.

The density data are used in the falling sphere experiment to derive temperatures. These temperatures are compared with the temperatures measured by the grenade and derived from the pitot-tube experiment in figure 3. Since the sphere temperatures are derived by a differentiation process, the temperature differences do not automatically "track" the density differences. However, the gross features emerge. In the firing conducted on 1 February, the region where the density comparison is very good, naturally, yields the best temperature comparison, an average difference of 4° K. The two firings in July, in which grenade densities are greater than sphere densities, yield sphere temperatures which tend to be higher than the grenade temperatures. The pitot-tube and sphere temperatures are consistent; the pitot-tube densities are lower than the sphere densities, which results in a lower sphere temperature. The average temperature difference between the four experiments conducted is 7° K.

The zonal and meridional components of wind are shown in figure 4 for the three grenade and sphere experiments. The pitot-tube experiment, which was the 4th experiment in the density and temperature comparisons, does not have a wind measuring capability. In general, the wind profile from the falling sphere displays a greater amount of small-scale structure. This is a predictable result, since the grenade experiment averages the winds over a 2 or 3 km layer. The averaging process would be expected to increase the difference between the two techniques to a greater extent with winds than with the other parameters due to the more variable nature of the winds. In spite of this, the average difference between the grenade and sphere winds is about 6 meters per second. Contrary to the density data, the agreement is very good (differences of only 2 to

3 meters per second) at 60 km and below, with the differences increasing to 10 to 15 meters per second between 60 and 70 km.

CONCLUSIONS

The results of the four sphere and grenade or pitot-tube experiments are summarized in figure 5. The salient features of this figure are:

1. Sphere winds which show very good agreement with grenade winds at 60 km and below, and fair agreement at 65 and 70 km.

2. Sphere temperatures which on the average differ 7° K from grenade and pitot-tube experiments. The recognized error in the grenade and pitot-tube experiment accounts for 1.5 to 4° of the total difference.

3. Sphere densities which are closer by about 6 percent to the standard atmosphere than densities derived from either grenade or pitot-tube experiments. The agreement above 70 km is markedly better than below.

It is further offered that the primary obstacle toward the incorporation of the falling sphere experiment in a program of synoptic measurements rests not with the accuracy of the data, but with the requirement for an FPS-16 radar system or one that is better. It is for this reason that GSFC is currently investigating the concept of utilizing the relatively low-cost doppler tracking systems with the relatively low-cost falling sphere payload through the use of a transponder sphere.

REFERENCE

1. Jones, L. M.; and Peterson, J. W.: Falling Sphere Measurements, 30 to 120 km. Meteorol. Monogr., vol. 8, no. 31, Apr. 1968, pp. 176-189.

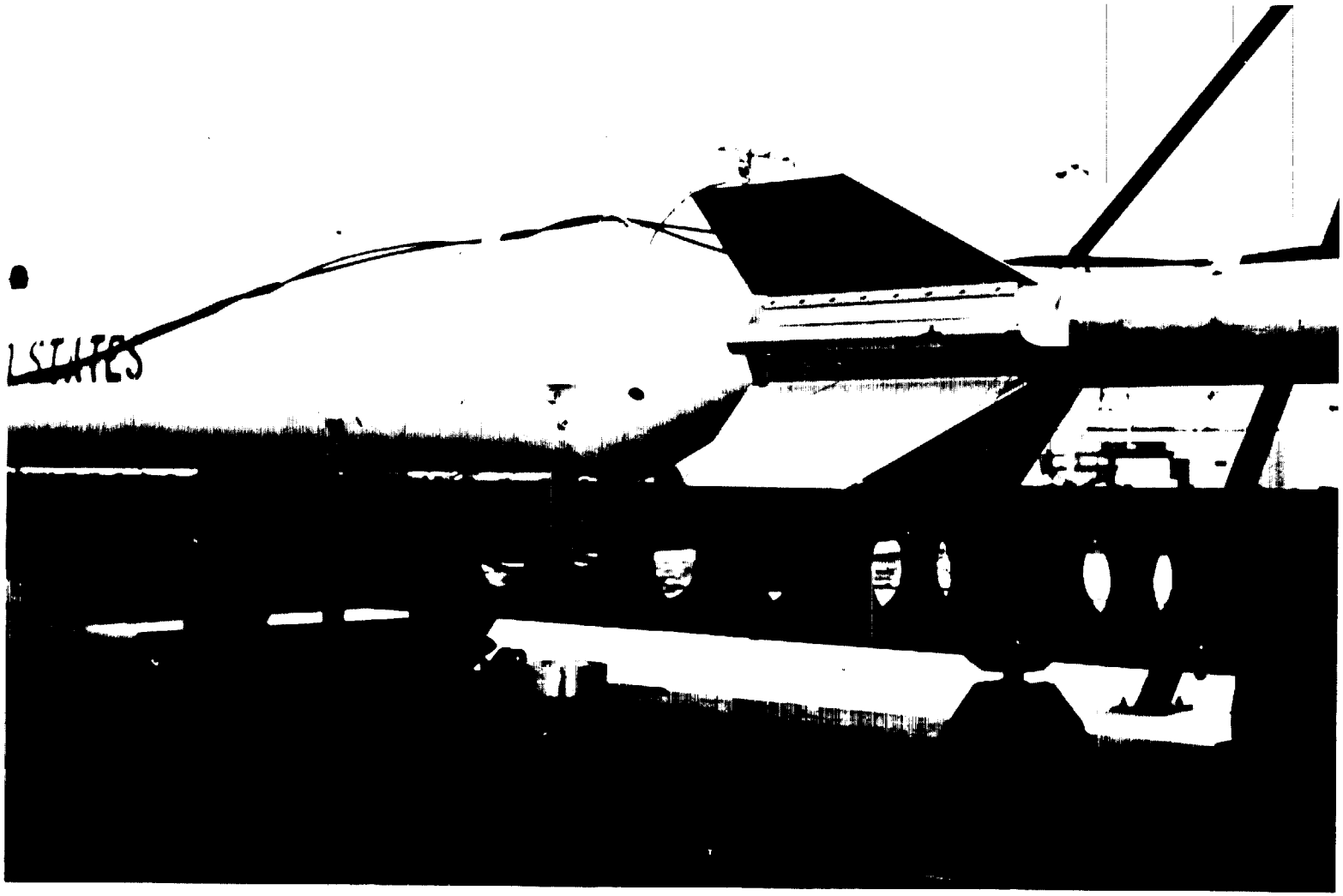

Figure 1.- Tail-fin assembly of an Apache rocket showing one of the pods containing an ejectable sphere.

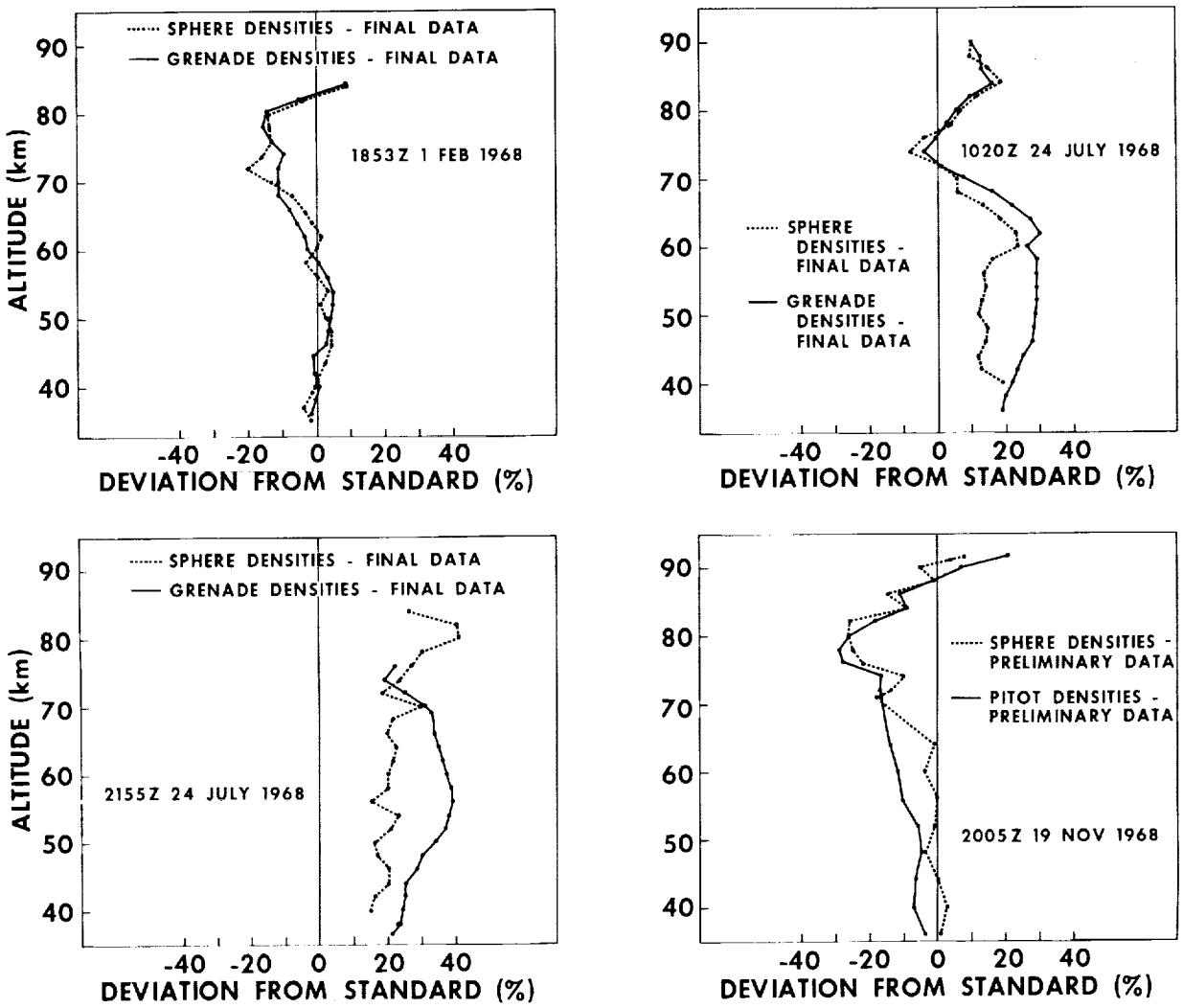

Figure 2.- Density data, in terms of percent of deviation from 1962 U.S. Standard Atmosphere, as derived from sphere and grenade or pitot-tube experiments versus altitude.

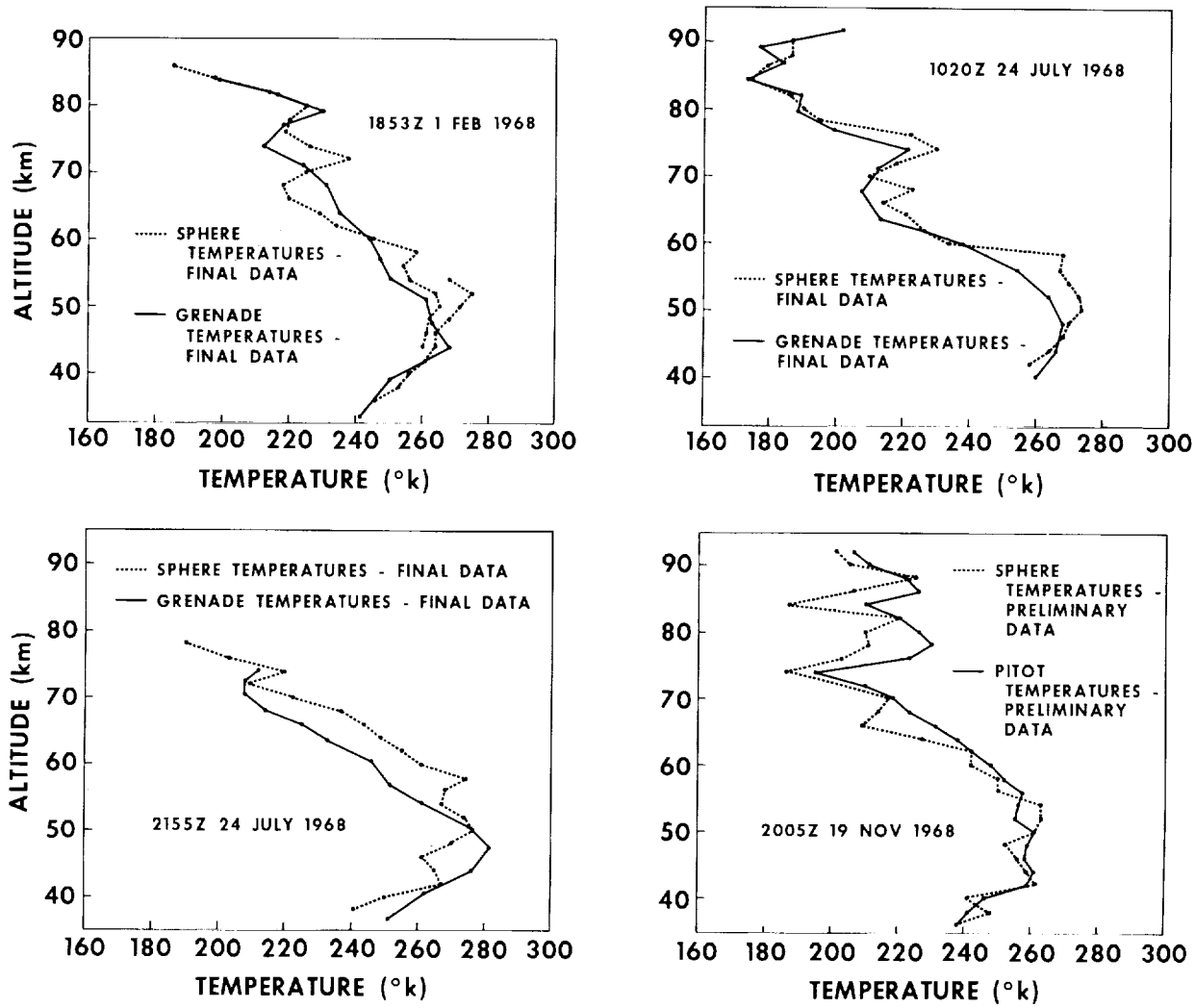

Figure 3.- Temperature data as derived from sphere and grenade or pitot-tube experiments versus altitude.

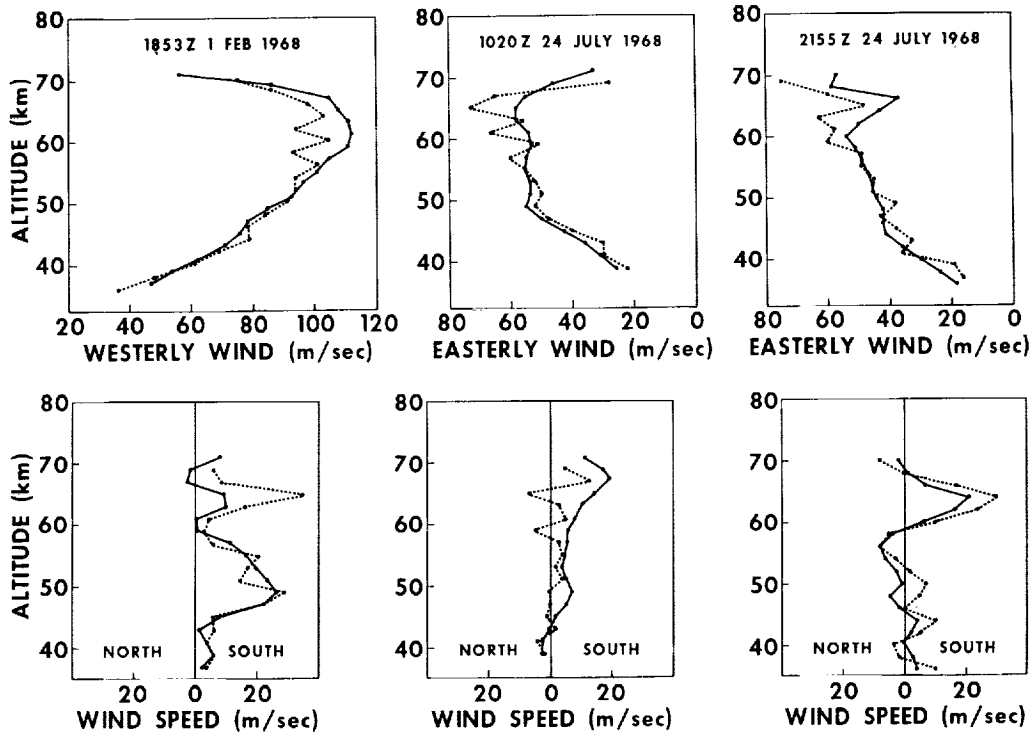

Figure 4.- Wind data, in meridional and zonal components, as derived from sphere and grenade experiments versus altitude.

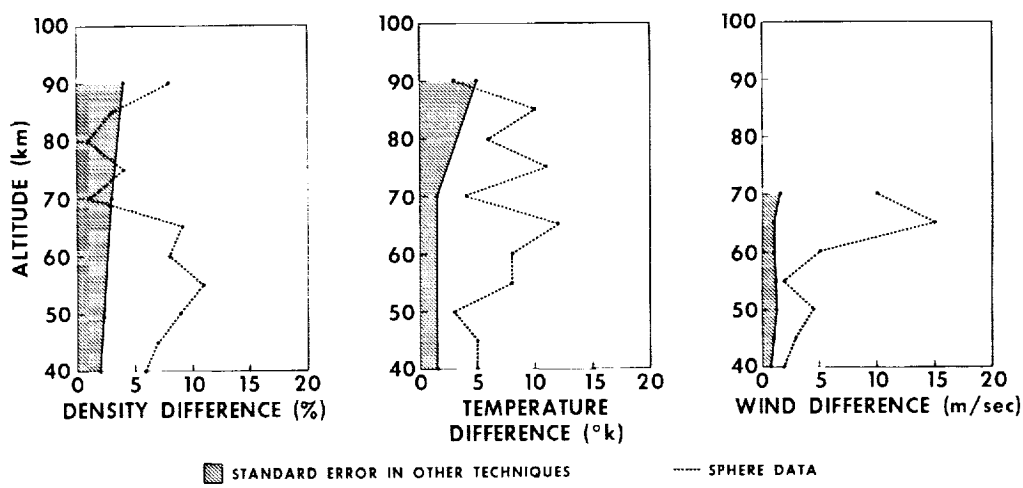

Figure 5.- Summary of density, temperature, and wind data differences. The zero-line data are an average of the grenade and pitot tube, the cross-hatched area represents the error estimated with these data, and the dotted line represents the data from the sphere experiments.

LIST OF ATTENDEES

BABER, Hal T.	NASA Langley Research Center
BAILEY, Alan B.	ARO, Inc.
BOLLERMAN, Bruce	Space Data Corporation
BROCKMAN, William E.	Booz, Allen Applied Research, Inc.
BROWN, Clarence A., Jr.	NASA Langley Research Center
BUSH, Kenneth S.	NASA Langley Research Center
COLE, Alan E.	Air Force Cambridge Research Laboratories
CONRAD, George R.	New Mexico State University
DANIEL, Orville H.	Pan American World Airways, Inc.
DANZEISIN, Richard	Booz, Allen Applied Research, Inc.
DUKE, Joseph R.	NASA Wallops Station
ENGLER, Nicholas A.	University of Dayton
FISHBACK, Frederick F.	University of Michigan
GORDON, Stuart A.	Space Research Corp.
GRAHAM, John	Goodyear Aerospace Corp.
GREENE, George C.	NASA Langley Research Center
GROGINSKY, Herbert L.	Raytheon Company
HAIN, John L.	Booz, Allen Applied Research, Inc.
HENRY, Robert M.	NASA Langley Research Center
HORVATH, John J.	University of Michigan
HOUGHTEN, Robert L.	NASA Headquarters
HUDGINS, John I.	NASA Goddard Space Flight Center
JOPLIN, Sammie D.	NASA Langley Research Center
KEATING, Gerald M.	NASA Langley Research Center
LASSITER, William S.	NASA Langley Research Center
LEITAO, Clifford D.	NASA Wallops Station
LUERS, James	University of Dayton
LYONS, W. Carson, Jr.	U.S. Naval Ordnance Laboratory
MANNING, James C.	NASA Langley Research Center
McGEE, Donovan E.	G. T. Schjeldahl Co.
McWATTERS, Kenneth D.	University of Michigan
MILLER, Robert W.	NASA Langley Research Center
MOLZ, Kenneth F.	RCA
MORRISSEY, James F.	Air Force Cambridge Research Laboratories

MULLINS, James A.	NASA Langley Research Center
MURROW, Harold N.	NASA Langley Research Center
NESSMITH, Josh	RCA
NOREEN, Robert A.	University of Minnesota
OLSEN, Robert	White Sands Missile Range
PREISSER, John S.	NASA Langley Research Center
PRIOR, Edwin J.	NASA Langley Research Center
QUIROZ, Roderick S.	ESSA
REED, Wilmer, III	NASA Langley Research Center
REESE, David E.	NASA Ames Research Center
SCHMIDLIN, Frank	ESSA
SHEARIN, John G.	NASA Langley Research Center
SLOAN, George J.	U.S. Naval Ordnance Laboratory
SMITH, Lawrence B.	Sandia Laboratories
SMITH, Orvel E.	NASA Marshall Space Flight Center
SMITH, Wendell S.	NASA Goddard Space Flight Center
SOMMER, Simon C.	NASA Ames Research Center
SPURLING, John F.	NASA Wallops Station
STAFFANSON, Forrest L.	University of Utah
THEON, John S.	NASA Goddard Space Flight Center
TOLEFSON, Harold B.	NASA Langley Research Center
WELINSKI, Bernard R.	Space Data Corporation
WRIGHT, John B.	Air Force Cambridge Research Laboratories

NASA-Langley, 1970 —— 1

NATIONAL AERONAUTICS AND SPACE ADMINISTRATION
WASHINGTON, D. C. 20546

OFFICIAL BUSINESS

FIRST CLASS MAIL

POSTAGE AND FEES PAID
NATIONAL AERONAUTICS AND
SPACE ADMINISTRATION

POSTMASTER: If Undeliverable (Section 158 Postal Manual) Do Not Return

"The aeronautical and space activities of the United States shall be conducted so as to contribute . . . to the expansion of human knowledge of phenomena in the atmosphere and space. The Administration shall provide for the widest practicable and appropriate dissemination of information concerning its activities and the results thereof."

— NATIONAL AERONAUTICS AND SPACE ACT OF 1958

NASA SCIENTIFIC AND TECHNICAL PUBLICATIONS

TECHNICAL REPORTS: Scientific and technical information considered important, complete, and a lasting contribution to existing knowledge.

TECHNICAL NOTES: Information less broad in scope but nevertheless of importance as a contribution to existing knowledge.

TECHNICAL MEMORANDUMS: Information receiving limited distribution because of preliminary data, security classification, or other reasons.

CONTRACTOR REPORTS: Scientific and technical information generated under a NASA contract or grant and considered an important contribution to existing knowledge.

TECHNICAL TRANSLATIONS: Information published in a foreign language considered to merit NASA distribution in English.

SPECIAL PUBLICATIONS: Information derived from or of value to NASA activities. Publications include conference proceedings, monographs, data compilations, handbooks, sourcebooks, and special bibliographies.

TECHNOLOGY UTILIZATION PUBLICATIONS: Information on technology used by NASA that may be of particular interest in commercial and other non-aerospace applications. Publications include Tech Briefs, Technology Utilization Reports and Technology Surveys.

Details on the availability of these publications may be obtained from:

SCIENTIFIC AND TECHNICAL INFORMATION DIVISION

NATIONAL AERONAUTICS AND SPACE ADMINISTRATION

Washington, D.C. 20546